

Fracture and Hydraulic Fracture Initiation, Propagation and Coalescence in Shale

by

Omar AbdulFattah AlDajani

B.S., Petroleum Engineering (2012)
Texas A&M



Submitted to the Department of Civil and Environmental
Engineering
in partial fulfillment of the requirements for the degree of
Master of Science in Civil and Environmental Engineering
at the

MASSACHUSETTS INSTITUTE OF TECHNOLOGY

February 2017

© Massachusetts Institute of Technology 2017. All rights reserved.

Author..... **Signature redacted**
Department of Civil and Environmental Engineering
January 20, 2017

Certified by ... **Signature redacted**
Herbert Einstein
Professor of Civil and Environmental Engineering
Thesis Supervisor

Accepted by **Signature redacted**
Jesse Kroll
Professor of Civil and Environmental Engineering
Chairman, Department Committee on Graduate Theses

Fracture and Hydraulic Fracture Initiation, Propagation, and Coalescence in Shale

by

Omar Abdulfattah AlDajani

Submitted to the Department of Civil and Environmental Engineering
on January, 20, 2017 in Partial Fulfillment of the
Requirements for the Degree of Master of Science in
Civil and Environmental Engineering

Abstract

Even though hydraulic fracturing has been in use for more than six decades to extract oil and natural gas, the fundamental mechanism to initiate and propagate these fractures remains unclear. Moreover, it is unknown how the propagating fracture interacts with other fractures in the Earth. The objective of this research is to gain a fundamental understanding of the hydraulic fracturing process in shales through controlled laboratory experiments where the underlying mechanisms behind the fracture initiation, -propagation, and -coalescence are visually captured and analyzed. Once these fundamental processes are properly understood, methods that allow one to produce desired fracture geometries can be developed.

Two different shales were investigated: the organic-rich Vaca Muerta shale from the Neuquén Basin, Argentina and the clay-rich Opalinus shale from Mont Terri, Switzerland, which were shown to vary in mineralogy and mechanical properties. Specimen preparation techniques were developed to successfully dry cut a variety of shales and produce prismatic specimens with pre-existing artificial fractures (*flaws*).

The Vaca Muerta shale specimens were subjected to a uniaxial load which induces fractures emanating from the flaws. Two geometries were tested: a coplanar flaw geometry (2a-30-0) resulting in indirect coalescence and a stepped flaw geometry (2a-30-30) resulting in direct coalescence. These “dry” fracture experiments were analyzed in detail and corresponded well to the behavior observed in the Opalinus shale. This result shows that the fracture behavior in Opalinus shale can be extended to other shales.

A test setup capable of pressurizing an individual flaw in prismatic shale specimens subjected to a constant uniaxial load and producing hydraulic fractures was developed. This setup also allows one to monitor internal flaw pressure throughout the pressurization process, as well as visually capture the processes that occur when the shale is hydraulically fractured. Three fracture geometries in Opalinus shale were tested using this developed setup: single vertical flaw (SF-90) for the proof of concept of the test setup, stepped flaw geometry (2a-30-30) which resulted in no coalescence, and stepped flaw geometry (2a-30-60) which resulted in indirect coalescence.

Of particular interest were the observed lag between the crack tip and the liquid front as well as the way the hydraulic fracture propagates across and along bedding planes. A systematic difference was observed when comparing crack interaction behavior for “dry” and hydraulic fracture experiments for various flaw geometries. The result of this thesis will add to fundamental knowledge of how fractures behave and interact under various loading conditions, flaw geometries, and materials serving as a basis for predictive fracture models.

Thesis Supervisor: Herbert H. Einstein

Title: Professor of Civil and Environmental Engineering

Acknowledgements

Let it be noted that these acknowledgements come from my heart!

I would like to express my sincerest, utmost gratitude to my advisor, Professor Herbert H. Einstein, for his guidance, encouragement, and enthusiasm for this work. He has been, and always will be, more than a research or an academic advisor to me. He is a compassionate friend who has been supportive in good and bad times, both in academics and life in general. He is truly an inspiration and a role model that I hope to one day live up to. I'll never forget the first time I walked into your office; I was unsure of whether to apply, and was only three days away from the deadline. If it was not for you, I would not even have applied to MIT!

I am also grateful to Professor John (Jack) Germaine (Dr. G!) for his never-ending support throughout my research. He has stood firmly by my side through thick and thin, and for that, I am sincerely thankful. Never have I met anyone with such hands-on expertise in every aspect of laboratory experiments, from electronics to equipment design. Our early Monday group meetings are so much more productive with you, where you just casually spout solutions like it was nothing!

I must also thank Stephen Rudolph who trained me to be a master machinist! He has spent countless hours in the lab selflessly teaching me skills I lacked and was there to help me whenever things went wrong. I also must thank Professor Brian Evans, who is the one who kick-started my research and helped facilitate my experimental needs. My thanks also go out to Carolyn Jundzilo-Comer who took care of my colleagues and always showered us with cookies. I cannot forget to give my gratitude to Kiley Clapper, who not only takes care of administrative logistics, but is also kind, caring, and compassionate towards my colleagues and me.

Special thanks must go to my friends at MIT, who have made this rigorous journey a tolerable one. Mauro Sotille was my first friend at MIT and was always there to supplement my lack of knowledge in Civil Engineering, but also always made himself available for me to just talk about life. Stephen Morgan, my predecessor, my mentor, my friend, who taught me the ins and outs of our dirty lab work and helped me to carry on his research to higher levels, but never forgot to keep me smiling and laughing throughout the process. Wei Li inspired and amazed me since day one with his incredible work ethic and is arguably the smartest guy I know, but is also one of the humblest and compassionate people I know; always dropping in and ask me how I was doing or if I needed anything. Bing Li is one of the most practical people I have ever met, and although he can be extremely candid, taught me with tough love the life-lessons of "figure it out" and "get it done"! Amer Deirieh was there for me when things were rough and seemed hopeless to bring my spirits up and give me some much needed confidence. I must thank my office mates: Chunwei Ge, Nina Panagiotindou, and Vaso Founta who are all incredibly courteous and were always there to help when I needed them. I must also thank my colleagues Bruno Gonçalves da Silva, Hao Kang, Rafael Villamor Lora, Ivo Rosa Montenegro, Eva Ieronymaki, Zhandos Orazalin, Steve Palkovic, Murat Uzun, Grace Gu, and Talal Al-Mulla who each have a special place in my heart. On a final note to my MIT friends, Khalid AlKaabi has been my greatest friend of all, a brother even. My MIT experience has not been, and will never be the same without you.

I can't possibly forget my Aggies. Dmitry Andreev was the one who took me out of my sheltered comfort zone and exposed me to so much unforgettable life experience. You've always had my back and I'll

always have yours. Jose Martinez is one of the most laid back serious people I have ever met. Only you could have taken tedious studying and made it fun and memorable. Drew Wellsfry was the one who showed me how easy it was to be serious at school and somehow still make time for whatever I'd like. Erin Bergeron Whitely is the most amazing baker I have ever met and you always made me feel welcomed and at home when I needed it the most. Cole Chavey had two daughters when he went back to school, and seriously accelerated my desires of fatherhood. Tony Kamenov was the upperclassman who always lent a hand and always made me laugh. You are all deeply missed and my memories with you are cherished.

Changing gears to my Saudi Aggies, you are all without a doubt invaluable. Atallah AlHarbi in my eye is a curious, humble genius who will never let you down. Khalid AlOthman, I have never had a workout partner I was more in sync with in the gym, and you're not too bad outside the gym either. Majid Rafie, the laziest smartest guy in the world who I love getting burgers with at 2 AM. Finally, Tariq AlMubarak, my clutch, the guy who has my back throughout all turns of life, is honestly the most talented person I know who is just naturally good at anything he does. I love you all from the bottom of my heart!

All these acknowledgements and thanks are meaningless without my family. My aunts and uncles are each uniquely amazing and have the biggest hearts. My Grandfather, Saleem, is the wisest man I know. I am blessed to have shared so many memories with him and look forward to many more. Every time I see him, my amazement only increases when I see that his heart is as full of kindness as his mind is wisdom. My late grandmother, Waleedah, is extremely missed. I always imagine her smile when she used to see me and play with me in her garden when I was just a boy. I am also grateful for my late grandfather, Ahmed, and grandmother, Mariam, who did not witness me grow up. They were amazing, strong people whose stories live on through their kids and on to their grandkids.

I am grateful and lucky to have the privilege of having four fantastic brothers in my life. Ahmed, you and I would always fight when we were growing up, but I can't imagine how I would have turned out without you. Believe it or not, you have steered me right whenever I took a wrong turn without you even realizing it. Now you're a doctor to be proud of! Saleem, I have always seen you as the genius among us, but what I also see, even today, is your kind, compassionate heart. I have told you before, you have great potential, but you can always lean on me when you need to. There is no need for you to carry the weight of the world on your shoulders alone. Mohammed, you never ceased to amaze me. I don't know anyone as strong as you. You bounced back from those dark days when you were really sick and you showed the world. I honestly believe you are capable of anything, so keep on doing what you're doing and prove me right! Basheer, my baby brother whom I carried in my arms who then grew up to be this fierce talent, waiting to let the world see what he can do; you astonish me with all that you do. I pray with all my heart that your pure heart remains uncorrupted no matter the circumstances. To all of you, each and every one of you has influenced me in ways you'll never know, and for that I am sincerely grateful. You guys make me so proud to be your brother.

My father, Abdulfattah, and mother, Raidah, deserve words that I am not even capable of. I may be biased when I say this, but I have the best parents in the world who I constantly want to make proud. Having you in my life from the day I was born until now has been the greatest blessing ever granted to me. You are both inspirations and role models who have achieved so much greatness, and still managed to always be there for my brothers and me. Never in my life did I ever feel that I needed you and didn't find you. I am so proud to call myself your son, and hope to make you as proud of me as I am of you.

Nothing I can ever do will compare to how much you have both sacrificed for me, and I am infinitely grateful.

Last but most definitely not least: Lubna, the love of my life. Meeting you was the highlight of my life. Marrying you is a blessing I thank God for every single day. My first year at MIT was hell without you. When you decided to join me, MIT became a calmer, happier hell! You inspire me and motivate me to work my hardest every single day (working hard is not hard work if it is for the ones you love). You are always there to help me whether I need it or not. You put me before yourself and always have my best interest at heart. For all this and so much more, you have my sincerest gratitude from the bottom of my heart. I just wanted you to know that I appreciate the unconditional love and affection that you have given me. You are not just my wife; you are my life...

Table of Contents

1. Introduction	20
1.1 Context – Hydraulic Fracturing of Unconventional Resources	21
1.2 Research Objective	23
2. Background	25
2.1 Shale	25
2.1.1 Geologic Details	25
2.1.2 Unconventional Resource	27
2.2 Material Studied	30
2.2.1 Opalinus Shale	30
2.2.2 Vaca Muerta Shale	32
2.2.3 Mineralogy	33
2.2.4 Mechanical Properties	36
3. Uniaxial Compression Experiments	38
3.1 Specimen Preparation	38
3.1.1 Cutting Prismatic Samples	39
3.1.2 Cutting Flaws	42
3.1.3 Sample Preservation	46
3.2 Experimental Procedure	48
3.2.1 Testing Setup	49
3.2.2 Analysis	54
3.3 “Dry” Fracture Results	57
3.3.1 Flaw Pairs in Vaca Muerta Shale	58
3.3.1.1 Coplanar Flaw Geometry	59
3.3.1.2 Stepped Flaw Geometry	68
3.3.2 Comparison	76
4. Hydraulic Fracture Experiments	79
4.1 Experimental Procedure	79
4.1.1 Test Setup	80
4.1.2 Test Procedure	98
4.2 Results	106
4.2.1 Single Vertical Flaw	106
4.2.2 2a-30-30	116

4.2.3	2a-30-60	128
4.3	Discussion	144
4.3.1	Lag Between Crack Tip and Liquid Front	144
4.3.2	Propagation Process of a Hydraulic Fracture	145
5.	Conclusions	148
	Characterization	148
	Specimen Preparation	148
	“Dry” Fracture Experiments	149
	Hydraulic Fracture Experiments	149
	Flaw Interaction in Hydraulic Fracture versus “Dry” Fracture	150
	Summary	151
	Bibliography	152
Appendix A –	Analysis of Shale Fracture Experiments	155
Appendix A1 –	Analysis of “Dry” Fracture Experiments on Vaca Muerta Shale	156
VM1-2a-30-30 (0)	156
VM2-2a-30-30 (0)	161
VM3-2a-30-0 (0)	169
Appendix A2 –	Analysis of Hydraulic Fracture Experiments on Vaca Muerta Shale	178
OP-HF-SF-90-A	178

Table of Figures

Figure 1 – schematic of prismatic specimen with prefabricated flaws subject to uniaxial loading to induce fractures and study fracture mechanisms and flaw interaction.	21
Figure 2 - Diagram of structural and stratigraphic trap formations (from www.glossary.oilfield.slb.com)	28
Figure 3 – Diagram of the petroleum system elements and processes. (Hagenmana, 2014)	29
Figure 4 – Map of Switzerland showing the location of the Mont Terri Underground Research Laboratory where the Opalinus shale samples are extracted.	31
Figure 5 - Geologic section showing the locations where each core was extracted from within the Mont Terri URL. (Modified from www.mont-terri.ch)	32
Figure 6 - Left: Map of Neuquén Basin, Argentina which contains the Vaca Muerta formation. Right: stratigraphy of the Neuquén Basin. (Sagasti et. al, 2014).....	33
Figure 7 – Mineralogy ternary plot of Vaca Muerta shale (Askenazi et. al, 2013) overlaid with data points from Table 1.	35
Figure 8 - Intact test setup diagram. Data acquisition includes load frame vertical load and displacement data, and lateral displacement data from proximity sensors.	36
Figure 9 - Example of data acquired from intact tests on shale specimens. The example shown is for a Vaca Muerta shale prismatic specimen with horizontal bedding planes. Left axis: stress, bottom axis: axial strain, right axis: lateral strain.	37
Figure 10 – Objective of sample preparation is to produce a prismatic shale specimen with double flaws with the dimensions listed in the figure. From Morgan (2015).	39
Figure 11 - Vaca Muerta Shale cylindrical core samples. Bedding planes are approximately perpendicular to the major axis of the cylindrical core. Specimens were cut along the dashed lines. Left: side view of core. Right: top view of core.	39
Figure 12 - Lubricant investigation on Opalinus clayshale. Table shows shale submerged in solutions of various salts and concentrations. Right top: shale submerged in untreated water. Right bottom: shale submerged in non-ferrous, vegetable oil-based anhydrous lubricant. Solutions with higher valency salts at higher concentrations showed the least swelling, spalling, and disintegration of shale sample. Oil showed no sign of these reactions.	41
Figure 13 – Specialized diamond wire band saw to cut Vaca Muerta core samples. Left: Photograph of diamond wire saw. Right: Close up of diamond wire cutting Vaca Muerta shale.	42
Figure 14 - Cutting flaw pairs in prismatic shale samples. Flaws were drawn on the specimen using a laser-cut stencil. A hole was drilled at each flaw tip. A scroll saw blade was inserted into the hole to cut the flaw. Modified from Morgan (2015).....	43

Figure 15 - Electroplated diamond twist drill bits for micro-drilling Vaca Muerta Shale.	44
Figure 16 - Hand-feeding sensitive chuck adapter for micro-drilling.....	45
Figure 17 - Left: drilling holes at flaw tips using 0.75 mm electroplated diamond twist drills, sensitive hand-feeding chuck adapter, and peck drilling. Right: cutting flaws by connecting flaw tip holes using a scroll saw with 0.7 mm diamond wire.	46
Figure 18 - Documentation station to keep track of everything that happens to the Vaca Muerta Shale core samples.	47
Figure 19 - Documentation of cut specimen and cut pieces of Vaca Muerta Shale.	47
Figure 20 – Shale sealing and storage. Left: shale is stored in vacuum sealed bags to preserve in-situ water content. Right: cooler container for added protection. From Morgan (2015).....	48
Figure 21 – Definition of flaw pair geometries. Flaw pair geometries are defined by ligament length (L), flaw inclination angle (β), bridging angle (α), and bedding plane angle (ψ). A geometry is reported in the format L- β - α (ψ).....	49
Figure 22 - Photograph of the test setup used for specimens with flaw pairs. From Morgan (2015).....	50
Figure 23 – Uniaxial compression on shale specimen with flaw pairs setup schematic. Central data acquisition saves vertical load and displacement data from load frame as well as high-speed camera trigger to relate observed crack events to stress-strain-time data.	50
Figure 24 – Nikon™ D90 high-resolution camera with a 105-mm lens used to take a 2 second time-lapse from beginning of loading until catastrophic failure of specimen. Taken from Morgan (2015). ..	52
Figure 25 - Photron™ SA-5 high-speed camera which was used to capture high-speed cracking events. For this study, it was set to 7,000 fps and 600x800 pixel resolution to allow 1.6 seconds of recording time. Taken from Morgan (2015).	53
Figure 26 - Dolan-Jenner Fiberlite™ MI-150 fiber optic lighting. Two lighting units, each fitted with dual branch fibers, were used for optimum luminescence of specimen surface. Taken from Morgan (2015).	53
Figure 27 – Analysis workflow of uniaxial compression fracture experiments.....	54
Figure 28 - Seven crack types proposed by Wong and Einstein (2009b) and an eighth crack proposed by Morgan (2015). T=Tensile Cracks, S=Shear Cracks.....	56
Figure 29 - Nine coalescence patterns proposed by Wong and Einstein (2009a). These observations were made on molded gypsum and Carrara Marble subjected to unconfined compression.	57

Figure 30 – Geometries of flaw pairs tested on Vaca Muerta Shale specimens. Left: coplanar flaw geometry with horizontal bedding planes 2a-30-0 (0). Right: Stepped flaw geometry with horizontal bedding planes 2a-30-30 (0).58

Figure 31 – Fracture analysis legend. Cracks are labeled alphabetically in chronological order of initiation. Crack mode is either tensile or shear. Crack type is defined based on Wong and Einstein (2009b) and Morgan (2015).59

Figure 32 – Stress-Strain curve for Vaca Muerta shale with coplanar flaw pair subjected to uniaxial loading. Yellow “x” indicates crack initiation. A red triangle indicates a sketched frame while the boxed number indicates sketch number, where the detailed sketches are shown next from Figure 33 to Figure 39. Orange circle indicates maximum stress. Green “*” indicates coalescence stress.60

Figure 33 – Sketch 0 as referred to in Figure 32. Left: sketch of cracks. Right: photograph of the specimen at this point in the experiment. Right: frame-time-stress-strain data as well as observations.....61

Figure 34 – Sketch 1 as referred to in Figure 32. Left: sketch of cracks. Center: photograph of the specimen at this point in the experiment. Right: frame-time-stress-strain data as well as observations.....62

Figure 35 – Sketch 2 as referred to in Figure 32. Left: sketch of cracks. Right: photograph of the specimen at this point in the experiment. Right: frame-time-stress-strain data as well as observations.....63

Figure 36 – Sketch 3 as referred to in Figure 32. Left: sketch of cracks. Right: photograph of the specimen at this point in the experiment. Right: frame-time-stress-strain data as well as observations.....64

Figure 37 – Sketch 4 as referred to in Figure 32. Left: sketch of cracks. Right: photograph of the specimen at this point in the experiment. Right: frame-time-stress-strain data as well as observations.....65

Figure 38 – Sketch 5 as referred to in Figure 32. Left: sketch of cracks. Right: photograph of the specimen at this point in the experiment. Right: frame-time-stress-strain data as well as observations.....66

Figure 39 – Sketch 6 as referred to in Figure 32. Left: sketch of cracks. Right: photograph of the specimen at this point in the experiment. Right: frame-time-stress-strain data as well as observations.....67

Figure 40– Stress-Strain curve for Vaca Muerta shale with stepped flaw pair subjected to uniaxial loading. Yellow “x” indicates crack initiation. A red triangle indicates a sketched frame while the boxed number indicates sketch number, where the detailed sketches are shown next from Figure 41 to Figure 46. Orange circle indicates maximum stress. Green “*” indicates coalescence stress.69

Figure 41 – Sketch 0 as referred to in Figure 40. Left: sketch of cracks. Right: photograph of the specimen at this point in the experiment. Right: frame-time-stress-strain data as well as observations.....70

Figure 42 – Sketch 1 as referred to in Figure 40. Left: sketch of cracks. Right: photograph of the specimen at this point in the experiment. Right: frame-time-stress-strain data as well as observations.....71

Figure 43 – Sketch 2 as referred to in Figure 40. Left: sketch of cracks. Right: photograph of the specimen at this point in the experiment. Right: frame-time-stress-strain data as well as observations.....72

Figure 44 – Sketch 3 as referred to in Figure 40. Left: sketch of cracks. Right: photograph of the specimen at this point in the experiment. Right: frame-time-stress-strain data as well as observations.....73

Figure 45 – Sketch 4 as referred to in Figure 40. Left: sketch of cracks. Right: photograph of the specimen at this point in the experiment. Right: frame-time-stress-strain data as well as observations.....74

Figure 46 – Sketch 5 as referred to in Figure 40. Left: sketch of cracks. Right: photograph of the specimen at this point in the experiment. Right: frame-time-stress-strain data as well as observations.....75

Figure 47 – Comparison of coalescence behavior observed in Vaca Muerta and Opalinus shales, both showing Category 2: indirect coalescence by multiple cracks.77

Figure 48 – Comparison of coalescence behavior observed in Vaca Muerta and Opalinus shales, both showing Category 5:one or more Type 2 S crack(s) and Type 2 T crack segments between inner flaw tips.78

Figure 49 – Planned testing procedure for experimental results. (Gonçalves da Silva, 2016)79

Figure 50 - Experimental setup for uniaxial compression tests with hydraulic fracturing on shale specimens. The shale specimen has the flaw pressurizing device clamped externally by polycarbonate window from the front and a steel bar from the rear. The central data acquisition system collects vertical load, feedback pressure, hydraulic volume injected, internal flaw pressure, and trigger time data.....80

Figure 51 – Three-dimensional rendering of flaw pressurization device components (oblique front view) showing transparent polycarbonate window and flaw seal with front injection needle inserted into flaw. Note: example specimen in figure has a single vertical flaw. Other geometries possible by simply rotating flaw seal to same orientation of the pressurized flaw.....81

Figure 52 – Three-dimensional rendering of flaw pressurization device components (oblique rear view). Transparency is not a priority for the rear components. Both needles are inserted into the flaw. The bottom needle is the rear injection needle (runs through center of steel bar and flaw seal) while the top needle is the pressure measurement needle (0.15” away from injection needle). For other flaw orientations, the flaw seal is rotated and holes are drilled into the steel bar to accommodate the pressure measurement needle.....82

Figure 53 - Transparent silicon rubber membrane after laser-cutting from 1.6 mm thick sheet. This membrane is pressed against the specimen surface with the front injection needle passing through its center hole into the flaw. The membrane is optically transparent.....83

Figure 54 – Transparent polycarbonate housing after machining followed by vapor polish. Left: specimen-facing side (front) of housing where transparent membrane fits in recess. Right: outside-facing side (back) of housing where O-ring seal fits in recess.84

Figure 55 - O-ring seal which sits in the circular recess on the back side of the housing. When pressure is applied, the O-ring seals around the injection needle, preventing needle movement or leakage.84

Figure 56 - Transparent polycarbonate window machined to be greater than the specimen width that allows one to see the specimen. It acts as the front external clamp and holds the membrane and housing against the specimen face.85

Figure 57 - Silicon rubber membrane after laser-cutting from 1.6 mm thick sheet. This membrane is pressed against the backside of the specimen. The central hole is for the rear injection needle and the offset hole is for the pressure measurement needle. Transparency is not needed.....85

Figure 58 – Steel housing from original design by Gonçalves da Silva (2016) with three holes. Only two are used for this modified design. Left: specimen-facing side (front) of housing where membrane fits into recess. Right: outside-facing side (back) of housing where O-ring seals fit in recesses...86

Figure 59 – Steel plates with three needle sized holes from original design by Gonçalves da Silva (2016). Only two holes are used for this modified design. Left: specimen-facing side (front) of plate where it presses against the O-ring and steel housing. Right: outside-facing side (back) of plate where it is supported by the rear steel bar clamp.87

Figure 60 – Rear steel bar clamp machined to be greater than the specimen width and threaded holes to receive screws from front transparent polycarbonate window. It acts as the rear external clamp and holds the membrane and housing against the specimen face. Various holes drilled around center hole to give the flaw pressure measurement needle access to the other components and the flaw.....87

Figure 61 - Picture of injection needle. Needle tip passes through pressurization device components and into the flaw. Opposite end screws into copper pipe.88

Figure 62 – Schematic of closed-loop feedback process of a PID controller.91

Figure 63 - An example of the pressure response (red curve) in a granite hydraulic fracture experiment using the enclosure device. The target pressure is increased at 0.5 MPa increments. Pressure converges to target pressure with no overshoot and minimum offset.94

Figure 64 – Result of PID algorithm prior to any tuning. PID parameters are same as those used by Gonçalves da Silva (2016) in granite hydraulic fracture experiments using enclosure device. When applied to new pressurizing device on a single flaw only, overshoot, offset, and ringing is observed and is more pronounced as pressure is increased.95

Figure 65 – 3/8” thick acrylic specimen with a hairline crack laser-cut through it used for PID tuning of hydraulic fracture apparatus.....96

Figure 66 - Final PID parameters determined for modified pressurization device for single flaw pressurization in a 3/8” thick acrylic specimen. Pressure response shows minimized overshooting, offset, and ringing. Undershooting is a result of escaping the program to input a new target pressure command.96

Figure 67 – Testing tuned PID Parameters on a shale specimen with a single vertical flaw oriented perpendicular to bedding planes. Offset is constant at each pressure increment. There is no overshooting. Pressure is stable after it converges. Note: red “x” is when specimen fractured. .97

Figure 68 - First crack initiation stresses in Opalinus shale with horizontal bedding planes observed by Morgan (2015). Each bar refers to a first crack initiation stress in a specimen (each geometry was tested three times).99

Figure 69 - Effect of varying bedding plane orientation on first crack initiation in Opalinus shale with 2a-30-30 geometry flaws.....100

Figure 70 - Dual functionality of third needle which uses feedback pressure transducer initially, then internal flaw pressure transducer after closing system.....101

Figure 71 - Schematic of elastic boundary value problem for an inclined, pressurized elliptical hole subjected to biaxial applied stress (Pollard and Fletcher, 2005).102

Figure 72 - Normal stress component, $\sigma_t = \sigma_{\eta\eta}(\xi = \xi_0)$, acting tangential to the hole boundary with varying internal pressures for the case of: $\sigma_3 = -3.5$ MPa, $\sigma_1 = 0$ MPa, $\beta = \pi/2$, $\rho = 0.35$, $a = 4.23$, $b = \rho \cdot a = 1.22$ 103

Figure 73 - Test data collected from PVA pressure transducer, feedback pressure transducer, and PVA LVDT on Opalinus shale prismatic specimen with a single vertical flaw. Test starts when system is closed by attaching flaw pressure transducer to third needle. Test ends after fracture stops propagation.107

Figure 74 - Test data from Figure 73 zoomed in to time of specimen failure to clarify curve trend and show sketch data points.....108

Figure 75 – Sketch 0: initial configuration of the specimen with saturated flaw.109

Figure 76 - Sketch 1: crack initiation within flaw seal boundaries.....110

Figure 77 - Sketch 2: crack initiation, A(T) propagates past flaw seal.....111

Figure 78 - Sketch 3: crack initiation, B(T) propagates past flaw seal boundary.112

Figure 79 - Sketch 4: crack propagation, lag between crack tip and fluid front.113

Figure 80 - Sketch 5: crack propagation, end of crack B(T) propagation.114

Figure 81 - Sketch 6: end of crack A(T) propagation.115

Figure 82 – Summary of all uniaxial compression with hydraulic fracture tests of a single vertical flaw showing observed fracture behavior, breakdown pressure, and total injected volume at breakdown.116

Figure 83 – 2a-30-30 geometry where the bottom flaw is pressurized and right flaw is not pressurized. The blue rectangle indicates the flaw seal boundary of the rubber membrane.117

Figure 84 - Test data collected from PVA pressure transducer, feedback pressure transducer, and PVA LVDT on Opalinus shale prismatic specimen with flaw pair geometry 2a-30-30. Test starts when system is closed by attaching flaw pressure transducer to third needle. Test ends after fracture stops propagation.118

Figure 85 – Close- up (range from t=835 – 890 seconds and P=3.75 – 4.05 s) of pressure drop from test data shown in Figure 84 - Test data collected from PVA pressure transducer, feedback pressure transducer, and PVA LVDT on Opalinus shale prismatic specimen with flaw pair geometry 2a-30-30. Test starts when system is closed by attaching flaw pressure transducer to third needle. Test ends after fracture stops propagation.119

Figure 86 – Sketch 0: initial configuration of the specimen OP-HF-2a-30-30-D after flaw saturation.120

Figure 87 - Sketch 1: crack initiation within flaw seal boundaries.121

Figure 88 - Sketch 2: crack initiation, A(T) propagates past flaw seal.122

Figure 89 - Sketch 3: crack initiation, B(T) propagates past flaw seal boundary.123

Figure 90 - Sketch 4: crack propagation, lag between crack tip and fluid front.124

Figure 91 - Sketch 5: crack propagation, end of crack B(T) propagation.125

Figure 92 - Sketch 6: end of crack A(T) propagation.126

Figure 93 – Summary of all uniaxial compression with hydraulic fracture tests on flaw pair geometry 2a-30-30 showing observed fracture behavior, breakdown pressure, and total injected volume at breakdown.127

Figure 94 – 2a-30-60 geometry where the bottom flaw is pressurized and right flaw is not pressurized. The blue rectangle indicates the flaw seal boundary of the rubber membrane.129

Figure 95 - Test data collected from PVA pressure transducer, feedback pressure transducer, and PVA LVDT on Opalinus shale prismatic specimen with flaw pair geometry 2a-30-60. Test starts when system is closed by attaching flaw pressure transducer to third needle. Test ends after fracture stops propagation.129

Figure 96 – Close-up of pressure drop from test data shown in Figure 95 used to determine specimen breakdown.	131
Figure 97 – Sketch 0: initial configuration of the specimen OP-HF-2a-30-60-C after flaw saturation.....	132
Figure 98 - Sketch 1: crack initiation within flaw seal boundaries.....	133
Figure 99 - Sketch 2: crack propagation within flaw seal boundary, B(T) _i arrests at boundary.	134
Figure 100 - Sketch 3: crack propagation with flaw seal boundary, A(T) _i arrests at flaw seal boundary.	135
Figure 101 - Sketch 4: crack propagation past flaw seal boundary, A(T) _i	136
Figure 102 - Sketch 5: crack propagation past flaw seal boundary, B(T) _i	137
Figure 103 - Sketch 6: crack propagation.....	138
Figure 104 - Sketch 7: crack propagation, B(T) _i arrests.....	139
Figure 105 - Sketch 8: crack propagation, C(T) _i branches off B(T) _i	140
Figure 106 - Sketch 9: crack propagation, A(T) _i arrests.....	141
Figure 107 - Sketch 10: coalescence.	142
Figure 108 – Summary of all uniaxial compression with hydraulic fracture tests on flaw pair geometry 2a-30-60 showing observed fracture behavior, breakdown pressure, and total injected volume at breakdown.	143
Figure 109 – examples of crack tip propagating ahead of driving pressurized liquid. Left: hydraulic fracture propagating from pressurized single vertical flaw. Right: hydraulic fracture propagating from pressurized flaw interacting with non-pressurized flaw in 2a-30-60 geometry. 1: location of fluid front. 2: location of crack tip.....	145
Figure 110 – Schematic of fracture propagation schemes in a horizontally layered material subjected to vertical uniaxial load. Modified from Fisher and Warpinski (2012).....	146
Figure 111 - Final sketch of specimen OP-HF-2a-30-60-B.....	147

List of Tables

Table 1 – Bulk mineralogy of various shale samples measured with XRD, highlighting quartz, carbonate (calcite + dolomite), and clay (chlorite, illite+illite/smectite-mixed layers, kaolinite) mineral contents.....	34
Table 2 – Mechanical properties of different rocks subjected to fracture tests at MIT CEE Rock Mechanics Group (Wong, 2008, Miller, 2008, Gonçalves da Silva, 2009, and Morgan, 2015) highlighting the materials tested in this study.....	37
Table 3 – Summary of all cracks, types, image origin, frame number, initiation time, initiation stress, initiation strain, and sketch.....	68
Table 4 – Summary of all cracks, types, image origin, frame number, initiation time, initiation stress, initiation strain, and sketch.....	76
Table 5 – Summary of the crack coalescence behavior, as defined by Wong and Einstein (2009b), observed in Opalinus Shale and Vaca Muerta Shale with the flaw geometries described in the table.	77
Table 6 - Effects of increasing PID parameters (Zhong, 2006)	92
Table 7 - Input parameters that describe loading conditions and geometry of the experiment.	102
Table 8 - Dimensions of specimen OP-HF-SF-90-A.....	107
Table 9 - Summary of test loads and volume.....	108
Table 10 – Dimensions of specimen OP-HF-2a-30-30-D.	118
Table 11 - Summary of test loads and injected volume for OP-HF-2a-30-30-D.....	119
Table 12 – Dimensions of specimen OP-HF-2a-30-60-C.....	130
Table 13 - Summary of test loads and injected volume for OP-HF-2a-30-30-D.....	130
Table 14 – Comparison of coalescence category observed in “dry” fracture experiment (uniaxial loading to failure) with hydraulic fracture experiment (pressurize an individual flaw to failure in an Opalinus shale specimen subjected to a constant uniaxial load) for two flaw pair geometries.	151

Introduction

Since the 1940's, hydraulic fracturing has been extensively used as one of the main stimulation techniques to enhance the productivity of oil and gas wells (Montgomery & Smith, 2010, Trembath et al., 2012, Wells & Wells, 2016). More recently, precise horizontal drilling combined with multi-staged hydraulic fracturing have unlocked the potential of previously unextractable resources in unconventional reservoirs. Shale constitutes a prominent type of such unconventional reservoirs, and is the most common type of rock found to hold fragments of organic material required to produce oil and gas. Due to its low permeability, this rock needs to be hydraulically fractured to release and retrieve the trapped hydrocarbons. As a consequence of enhanced extraction, proven natural gas reserves in the US have increased more than 50% throughout the last 20 years (Cook and Perrin, 2016). Moreover, it is expected in the next 10 years that 60-80% of wells drilled in the US will require fracturing to produce commercially. Given that hydraulic fracturing of shale is necessary to extract the trapped hydrocarbons to meet energy demands, it is important to understand the mechanisms of hydraulic fracturing. Hence, the proposed research is an experimental program that explores hydraulic fracturing of shale in a controlled laboratory environment.

Extensive work has been done at MIT to study fracture initiation and propagation (Reyes, 1991, Bobet, 1997, Wong, 2008, Miller, 2008, Gonçalves da Silva, 2009, and Morgan, 2015). Many of these studies were done on prismatic specimens with two pre-existing artificial fractures (*flaws*). The specimens were subjected to uniaxial compressive loading, then fracture initiation and propagation mechanisms were captured and analyzed while varying the geometry of the flaws. Such experiments were done on gypsum, marble, granite, as well as shale. In the latter, another parameter that was recently investigated is the bedding plane angle (Morgan, 2015). The fracture mechanism was captured using a high-speed video camera and a high-resolution camera and then analyzed frame by frame. The eventual

objective of this research is to continue the experiments on shale with the added step of hydraulically pressurizing the flaws and capturing the behavior of fluid-driven fracture initiation and propagation.

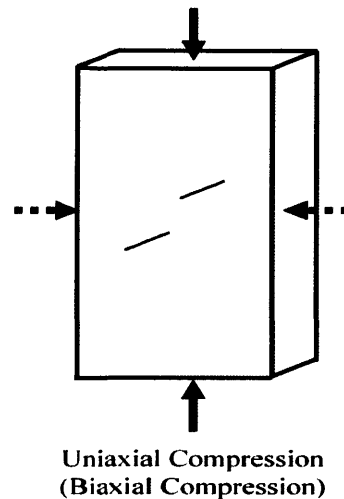


Figure 1 – schematic of prismatic specimen with prefabricated flaws subject to uniaxial loading to induce fractures and study fracture mechanisms and flaw interaction.

1.1 Context – Hydraulic Fracturing of Unconventional Resources

Hydraulic fracturing was first documented to have been used to separate granite blocks from bedrock at Mt. Airy Quarry in North Carolina in 1903 (energy4me, 2015). It was only in 1947 when this technique was experimented on in oilfield fracturing in the Hugoton field in Southwestern Kansas, and only in 1949 when hydraulic fracturing treatments were first commercialized by Halliburton Oil Well Cementing company (Montgomery & Smith, 2010). Since then, hydraulic fracturing treatments were used mostly in vertical wells in conventional sandstone or limestone reservoirs to stimulate the flow of natural gas or oil, increasing the volumes than can be extracted.

Significant gas deposits in shale were known to geologists since the 1820's (Trembath et al., 2012).

However, engineers had neither the technology nor the knowledge base to cost effectively map shale

expanses, drill horizontally the formations, initiate fractures that were productive and predictable, and recover the gas resources locked in the formations (Trembath et al., 2012). It required the combination of technological advancements in different areas to unlock this potential. The most important developments are discussed below:

- Directional shale drilling techniques were first patented in 1976 (NETL, 2011). This allowed operators to span larger radial expanses of shale deposits, and eventually led to horizontal well drilling which would make it cost effective for extracting more natural gas (NETL, 2011).
- Diamond studded drill bits were developed by General Electric and the Energy Research and Development Administration for application in geothermal energy to drill in hot dry rocks, but were also found to be effective for drilling shales (Fri, 2006).
- Sandia National Laboratories developed three-dimensional microseismic imaging technology for work in coal mines, which were used for applications in shale gas drilling. This technology allowed shale drillers to visualize the shale formations along with existing natural fractures and unevenly distributed gas deposits as drilling advanced (National Research Council, 2001).

Without microseismic, shale drillers were blind.

The first multi-stage hydraulic fracture, where the rock was fractured multiple times at incremental distances along a wellbore, was demonstrated in 1986, but was too costly for commercial application (Yost, 1988). It was not until 1998 that 'slick water fracturing' (or 'light sand fracking') that brought costs of hydraulically fracturing an individual well down from \$300,000 to \$100,000 (Trembath et al., 2012). This is widely considered as the milestone that made shale gas fracture operations economically feasible. As a result of the adaptation and integration of these major technologies and many more into the petroleum industry over the course of 30 years, shale gas went from inaccessible deposits locked in unfamiliar geologic formations to the fastest growing contributor to the US's energy portfolio.

The most effective implementation of hydraulic fracturing is to contact as much rock as possible with a fracture or network of fractures of high conductivity. In this context, fracture conductivity is determined by many factors such as fracture geometry, proppant type and size, fracturing fluid system, and placement techniques (Saldungaray & Palisch, 2012). Looking into all this is beyond the scope of this research. While hydraulic fracture completion (downhole tubulars and equipment) design accounts for many of the previously stated parameters, the produced fracture geometry is assumed rather than known, and is challenging to optimize because it is not truly understood (Saldungaray & Palisch, 2012). What this research aims at understanding is the underlying mechanisms involved in initiating and propagating hydraulic fractures in shales, and how these fractures interact with pre-existing fractures within the formation. Once this fundamental process is properly understood, methods that allow one to produce the desired fracture geometry may be developed.

1.2 Research Objective

This research aims at better understanding the fracture mechanisms involved in hydraulic fracturing of shales in the field through controlled experiments in the laboratory. Such experiments need to visually capture fracture initiation, -propagation, and -coalescence. To achieve this, the following objectives were met and presented in this thesis:

- Develop specimen preparation techniques that can be used to prepare prismatic shale specimens with flaws. These techniques have to be adaptable and can handle shales of various mineralogies, textures, and strengths.
- Subject Vaca Muerta shale specimens with two distinct flaw pair geometries to uniaxial load to visually capture the fracture process. The objective of this experiment is to observe fracture initiation and propagation and relate these observations to stress-strain data. Another aspect is to observe the interaction between the two flaws.

- Comparison of the fracture behavior in Vaca Muerta shale to that which was observed in Opalinus shale. The Vaca Muerta shale cores were extracted from a deep petroleum reservoir in the Neuquén Basin whereas the Opalinus shale cores were extracted from a shallow clay-rich facies in Mont Terri.
- Develop a test setup capable of pressurizing an individual flaw in prismatic shale specimens subjected to uniaxial load and produce hydraulic fractures, while allowing one to monitor the internal hydraulic pressure in the flaw as well as visually capture the processes that occur when the shale is hydraulically fractured.
- Analyze and interpret the fracturing processes and mechanisms of the produced hydraulic fractures that are visually captured while relating them to hydraulic pressure and volume injected data.
- Study the effect of flaw geometries on the observed fracturing processes, including the interaction of hydraulic fractures with a pre-existing flaw.

2. Background

2.1 Shale

Shales are usually defined as fine-grained, siliciclastic sedimentary rocks, made up dominantly of silt-sized (1/16-1/256 mm) and clay-sized (<1/256 mm) particles (Tourtelot, 1960, Potter et. al, 1980, Boggs, 2006). These authors classify all fine-grained siliciclastic sedimentary rocks as shales, but divide them into several types depending on percent of clay-size constituents and the presence or absence of lamination (Boggs, 2006).

Some authors prefer to classify all fine-grained rocks as mudrock, but divide them into shales (if laminated) or mudstones (if non-laminated) (Blatt et. al, 1980). This thesis will use the latter classification when describing the material studied.

2.1.1 Geologic Details

Shales are primarily composed of fine-sized quartz and feldspars as well as clay minerals (Tourtelot, 1960, Blatt et. al, 1980, Potter et. al, 1980, Boggs, 2006). They may also contain other minerals such as carbonates (calcite, dolomite, siderite), sulfides (pyrite, marcasite), iron oxides, as well as organic carbon (Boggs, 2006). Many factors affect the composition of shales, such as depositional environments, grain size, tectonic setting and burial diagenesis (Boggs, 2006). Some minerals, such as carbonates and sulfides, form in the shales during burial as cements or replacement minerals (Boggs, 2006). Quartz, feldspars, and clay minerals are mainly detrital, but some fraction of these minerals may form during burial diagenesis (Boggs, 2006). Clay minerals are strongly affected by diagenetic processes, as it has been shown that older rocks have higher proportions of illite and chlorite at the expense of kaolinite and smectite (Singer & Muller, 1979).

Shales form under environmental conditions in which fine sediment is abundant and water energy is sufficiently low to allow the sediments to settle (Boggs, 2006). Prime examples of this are marine environments adjacent to major continents, lakes, as well as the quiet-water parts of rivers, lagoons, tidal-flats, and deltaic environments (Boggs, 2006). The fine sediments in these low-energy environments settle to form a single layer of bedding in the shale prior to burial. This leads to what may occur next, and that is a change in depositional environments.

Change in the depositional environment can happen for many reasons, but can be attributed overall to a relative change in water level (Boggs, 2006). For example, if the environment being discussed is a deep marine environment that becomes a shallow marine environment due to relative water level drop, this will change the depositional environment as well as the rock being formed in that area. A shallow marine environment will usually have higher energy which will make it more difficult to settle fine sediments, so there might be larger grain sedimentation. It might also host more biological life due to the increased oxygen levels in the water, which may disturb the already settled fine grained sediments by burrowing and feeding activities. This is important to realize this when discussing shales since the depositional regime affects bedding plane formation.

A bed is defined as a layer of sedimentary rock that have lithological, textural, or structural unity that clearly distinguishes them from strata above and below, while bedding planes are defined as the upper and lower surfaces of these beds (Campbell,1967). Bedding planes are one of the major characteristic of shales in this study. The fine laminations observed in shales are results of successions of changing depositional environments, which cause variations in grain size, clay content and organic material, mineral composition, or microfossil content of sediments (Campbell,1967). Once formed, laminae have the greatest potential for preservation in anoxic or toxic environments, where organic activity is minimal, or where deposition is so rapid that the sediment is buried below the depth of active organic activity (Boggs, 2006).

2.1.2 Unconventional Resource

Before discussing details of unconventional resources, it is important to understand the petroleum system. A petroleum system is defined as the geologic components and processes necessary to generate and store hydrocarbons. "Petroleum" is a term used to describe these hydrocarbons, and it includes crude oil, natural gas, condensates, and bitumen while "system" describes the independent elements and processes that form the functional unit that creates hydrocarbon accumulations (Magoon & Beaumont, 2003). The petroleum system includes the following elements:

- source rock: a rock that is rich in organic matter (1-10% total organic content) which, if heated sufficiently, will generate oil (120° F – 250° F) or gas (250° F – 350°) (Selley, 1985).
- reservoir rock: a rock that has sufficient porosity and permeability to store and transmit fluids, commonly sedimentary rocks (Selley, 1985).
- seal rock: rock that is relatively impermeable that forms a barrier or cap above and around the reservoir rock such that fluids cannot migrate beyond the reservoir, commonly shale, anhydrite, or salt (Selley, 1985).
- overburden rock: rock overlying the reservoir and seal rocks (Selley, 1985).

and have two processes:

- Trap formation: a configuration of rocks suitable for containing hydrocarbons and sealed by a relatively impermeable formation through which hydrocarbons will not migrate. Traps are described as structural traps in deformed strata such as folds and faults, or stratigraphic traps in areas where rock types change such as unconformities, pinch-outs, and reefs (Figure 2) (Selley, 1985).

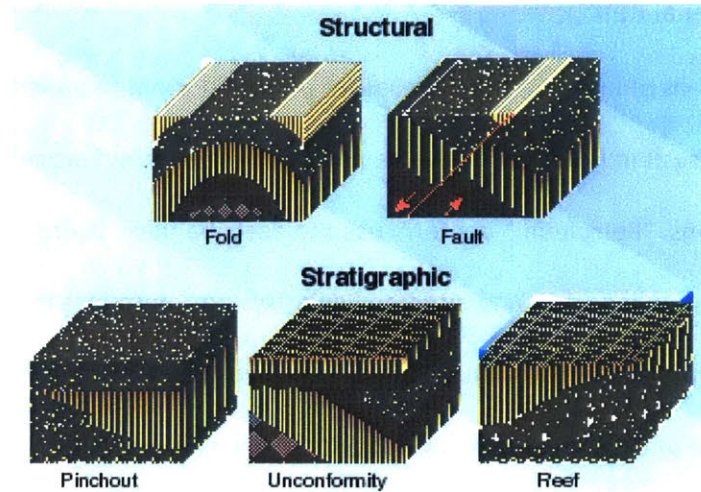


Figure 2 - Diagram of structural and stratigraphic trap formations (from www.glossary.oilfield.slb.com)

- Generation-migration-accumulation of hydrocarbons: Generation is the formation of hydrocarbons from a source rock. Migration is the movement of hydrocarbons from the source rock into the reservoir rock. Accumulation is the phase in which the hydrocarbons migrate into and remain trapped in the reservoir rock due to encountering a trap formation (Selley, 1985).

These elements and processes must be correctly placed in time and space so that organic matter in the source rock can be converted into a petroleum accumulation (Magoon & Beaumont, 2003). A diagram of the petroleum system and its elements are shown in Figure 3.

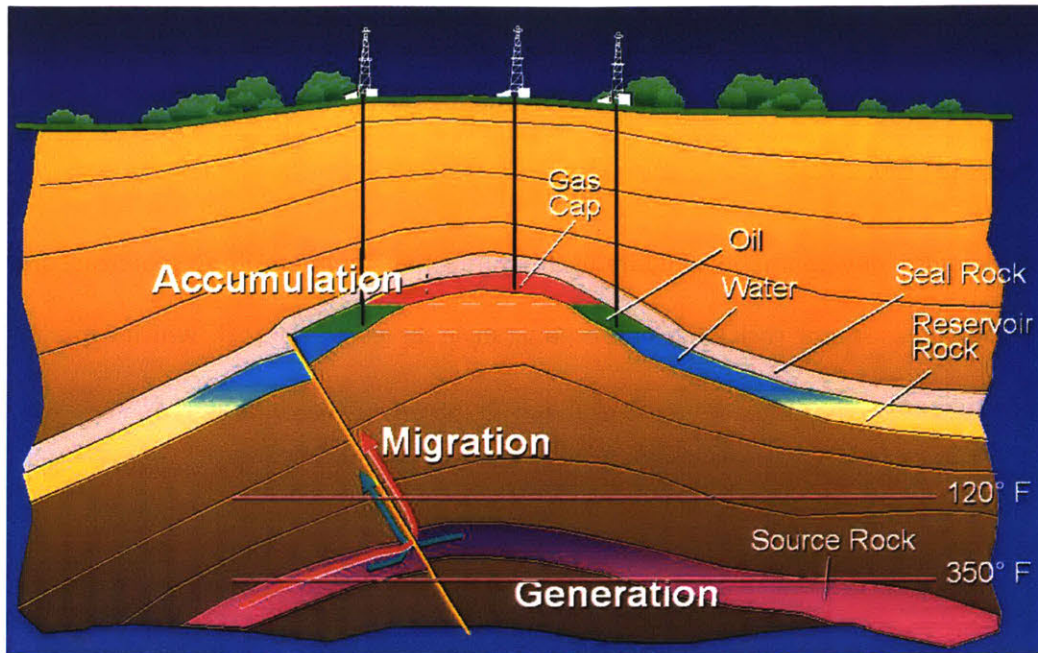


Figure 3 – Diagram of the petroleum system elements and processes. (Hagenmana, 2014)

Unconventional oil and natural gas are essentially the same as their conventional counterparts, where the term “unconventional” refers to the methods used for extraction as well as the type of rocks from which oil and natural gas are produced (AER, 2017). Unconventional oil refers to “tight oil”, which is oil found in low-permeability rock including sandstone, siltstone, shale, and carbonates (AER, 2017).

Unconventional gas refers to the following:

- “tight gas” which is natural gas found in low-permeability rock including sandstone, siltstone and carbonates
- “shale gas” which refers to natural gas found in organic-rich shales
- “coalbed methane (CBM)” which refers to natural gas found in coal (AER, 2017).

One of the materials studied in this thesis is related to shale gas, so it will be discussed in further detail.

Putting shale gas in the context of a petroleum system, such organic-rich shale is typically the source rock that also functions as reservoir rock and seal rock simultaneously (Zou, 2013). Overburden rock includes all the overlying strata that have buried the shale to sufficient pressure and temperature to

convert the organics to natural gas (Zou, 2013). Trap formation is not necessary, as more than 50% of total hydrocarbon generation remains trapped in the nano-scaled pore spaces and micro-fractures, unable to migrate (Zou, 2013).

Prior to technological developments of hydraulic fracturing that commercialized shale gas, organic-rich shale mainly served as source rock while non-organic shale served as seal rock, which were important in identifying petroleum systems but were avoided in exploration and development. Now, the organic-rich shale is sought after to exploit its trapped potential.

2.2 Material Studied

The two materials used in this thesis are Opalinus shale and Vaca Muerta shale. Morgan (2015) did extensive research on Opalinus shale where prismatic specimens with pre-existing flaws were subjected to uniaxial load and fracture behavior was visually captured and analyzed. He studied the effects various flaw geometries as well as bedding plane angles. This thesis may be regarded as an extension of that work to investigate if the observations made by Morgan (2015) on Opalinus shale could be extended to other shales, as well as to study the mechanisms behind hydraulic fracturing in shale.

Vaca Muerta shale was used to carry out the investigation of fracture behavior in a different shale than Opalinus shale. Opalinus shale was then used to study the mechanisms of hydraulic fracturing in shale.

2.2.1 Opalinus Shale

Opalinus shale is a clay-rich shale from the Dogger Formation in the Jura Mountains, located in Northwest Switzerland, France, and Southern Germany (Figure 4). The Opalinus shale cores used by Morgan (2015) and in this research comes from the Mont Terri Underground Research Laboratory for radioactive waste disposal.



Figure 4 – Map of Switzerland showing the location of the Mont Terri Underground Research Laboratory where the *Opalinus* shale samples are extracted.

The Swiss government organization, Swisstopo, which is responsible for the Mt. Terri URL provided MIT with 3 meters of 11 cm diameter *Opalinus* shale core (FE-A) for the study carried out by Morgan (2015). They then provided 3 meters of BSO-36 and 1 meter of BSO-34, of which the BSO-36 was used in this study. As seen in Figure 5, FE-A and BSO-36 were extracted from the shaly facies while the BSO-34 was extracted from the carbonate-rich facies.



Figure 5 - Geologic section showing the locations where each core was extracted from within the Mont Terri URL. (Modified from www.mont-terri.ch)

2.2.2 Vaca Muerta Shale

The Vaca Muerta shale is an organic-rich shale formation located in the Neuquén Basin, Argentina (Sagasti et. al, 2014). Figure 6 shows a map of the Neuquén Basin as well as a stratigraphic column. The Vaca Muerta Formation and the overlying Quintuco Formation were carbonate-siliciclastic sediments deposited in successions of shallow to deep marine, where the Quintuco Formation represents the shallow marine deposits and the Vaca Muerta Formation represents the deep marine (Sagasti et. al, 2014). There is no solid boundary between the two formations as the transgressive-regressive cycles created a diachronous contact which attributes to the Vaca Muerta shale heterogeneity (Sagasti et. al, 2014). The lower Vaca Muerta formation is primarily a result of deep marine deposition undisturbed by the transgressive-regressive cycles which occurred above it, and so it has a high total organic content (TOC) as organic matter deposited in this part of the shale was better preserved (Sagasti et. al, 2014).

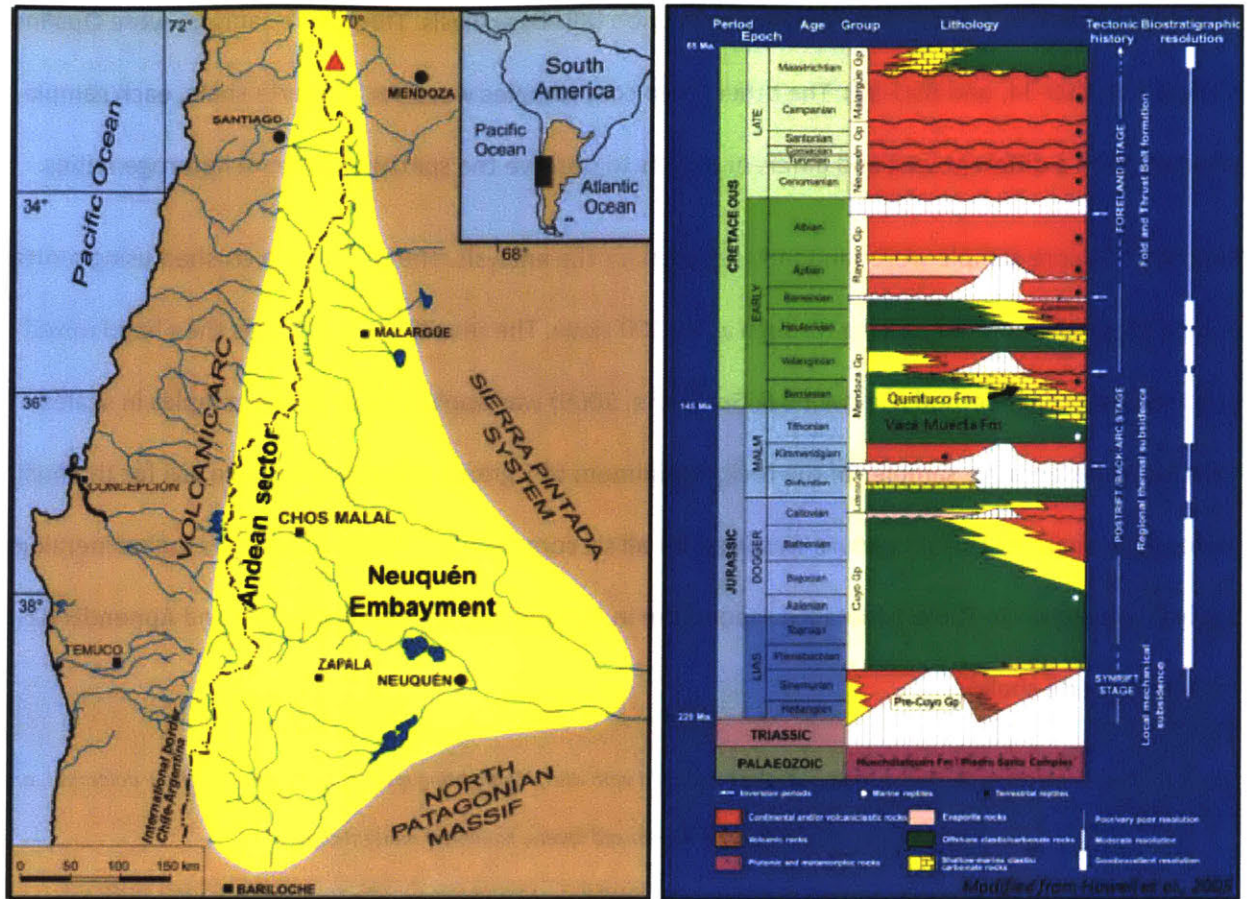


Figure 6 - Left: Map of Neuquén Basin, Argentina which contains the Vaca Muerta formation. Right: stratigraphy of the Neuquén Basin. (Sagasti et al, 2014).

A total of 10 core samples, 6 cm in diameter, were provided by Total to the Multi-Scale Shale Gas Collaboratory (MSGC) project at MIT. Four of these cores are used in this study, one to test its mechanical properties and three for fracture experiments. These core samples came from five wells (locations undisclosed) and various depths. Small cylindrical plugs were also provided from various wells and depths. These plugs were used for the mineralogic analysis.

2.2.3 Mineralogy

One of the key parameters to be studied when dealing with rocks is mineralogy. Getting a close look at a material's constituents can significantly increase our understanding when characterizing fracture types and behaviors. Hence, the mineralogy of six core samples was investigated by sending them to Macaulay

Scientific Consulting LTD for X-ray powder diffraction (XRPD) analysis. Three core samples were Opalinus shale (FE-A, BSO-34, and BSO-36). The other three core samples were Vaca Muerta shale, each sample selected from a different well and different depths to observe the spatial and lateral heterogeneities.

Sections of a core sample were randomly selected for the analysis. The rocks were crushed using mortar and pestle to the point of passing through a No. 100 sieve. The resulting powder was then hand mixed and the quartering method (Germaine & Germaine, 2009) was applied to place the samples in sealed vials for representative samples of the rock. A minimum of 5 grams were collected in a vial for the bulk mineralogy analysis. This procedure was used for all six core samples. The results of the bulk mineralogy analysis are shown in Table 1 (detailed reports are in Appendix B1 for Opalinus shale and Appendix B2 for Vaca Muerta shale).

Table 1 – Bulk mineralogy of various shale samples measured with XRD, highlighting quartz, carbonate (calcite + dolomite), and clay (chlorite, illite+illite/smectite-mixed layers, kaolinite) mineral contents.

Sample	Opalinus Shale FE-A	Opalinus Shale BSO-34	Opalinus Shale BSO-36	VM-X3 2596 m	VM-X4 2897 m	VM-X5 2686 m
Quartz	13.5	34	15.9	82.6	37.6	25.7
K-Feldspar	0.5	2.3	0.5	2.9	1.8	0
Plagioclase	1.1	1.4	0.9	4.8	13.4	9.6
Calcite	12.8	6.5	5.4	0.2	15.1	14.4
Dolomite	1.3	0.7	0.5	0.3	1.2	1.5
Siderite	0.7	0.7	0.3			
Gypsum	0	0.3	0			
Halite	0	0	0	0.8	0.1	0.2
Anatase	0.4	0.4	0.5	0	0.1	0.1
Apatite	0.9	1.1	1.1	0.5	1.5	0.9
Pyrite	0.9	1.2	2.2	0.2	2.6	1.3
Chlorite	3.4	2.6	3.6	0.4	0.7	5.6
Muscovite	2.2	2	2	0	3.6	0
I+I/S-ML	44.2	31.5	45.4	3.6	20.9	40.6
Kaolinite	18.1	15.6	21.6	0	0.6	0
Carbonate*	14.1	7.2	5.9	0.5	16.3	15.9
Biotite						
Granophyre						
Hematite				3.7	0	0.1
Marcasite				0	0.7	0.1
Clay**	65.7	49.7	70.6	4	22.2	46.2

The Opalinus shale is generally high in clay content, but varies slightly in quartz and carbonate content. The BSO-34, specifically, has about double the quartz content than the other Opalinus shale samples and was more challenging to prepare specimens for experiments because of this. The Vaca Muerta shale, on the other hand, seemed to vary more steeply.

Figure 7 shows a mineralogy ternary plot of Vaca Muerta shale (Askenazi et. al, 2013). The data in Table 1 were also plotted as an overlay onto Figure 7. This plot shows the wide range of heterogeneity observed in Vaca Muerta shale where clay content is generally less than 40%, but a wide distribution of quartz and carbonate contents is observed. Although one cannot say that Opalinus shale is homogeneous, it can be seen that Opalinus samples occupy the clay corner of the triangle, varying slightly in quartz and carbonate contents.

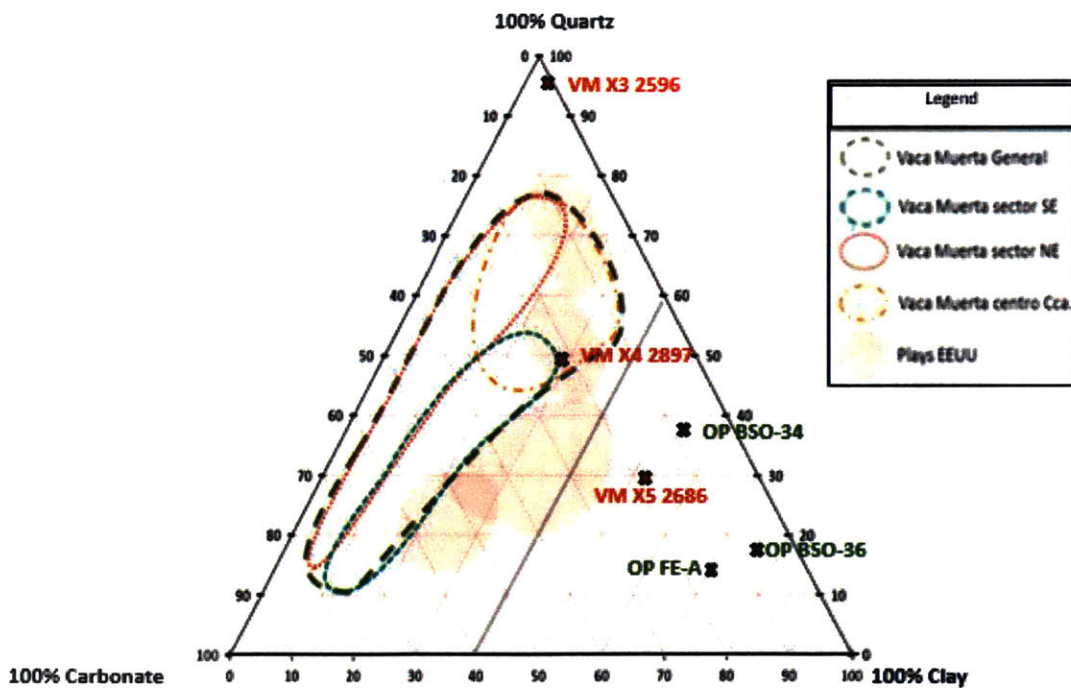


Figure 7 – Mineralogy ternary plot of Vaca Muerta shale (Askenazi et. al, 2013) overlaid with data points from Table 1.

2.2.4 Mechanical Properties

Mechanical properties of the BSO-36 and Vaca Muerta shales were measured in the laboratory. Figure 8 shows the experimental setup where data acquisition includes vertical load applied and vertical displacement from the load frame, as well as lateral displacement from proximity sensors adjacent to aluminum foil placed onto the sides of the specimens tested. This is the same setup used by Morgan (2015) to determine mechanical properties of intact prismatic shale specimens. The specimens are loaded at 1024 lbs/min until failure.

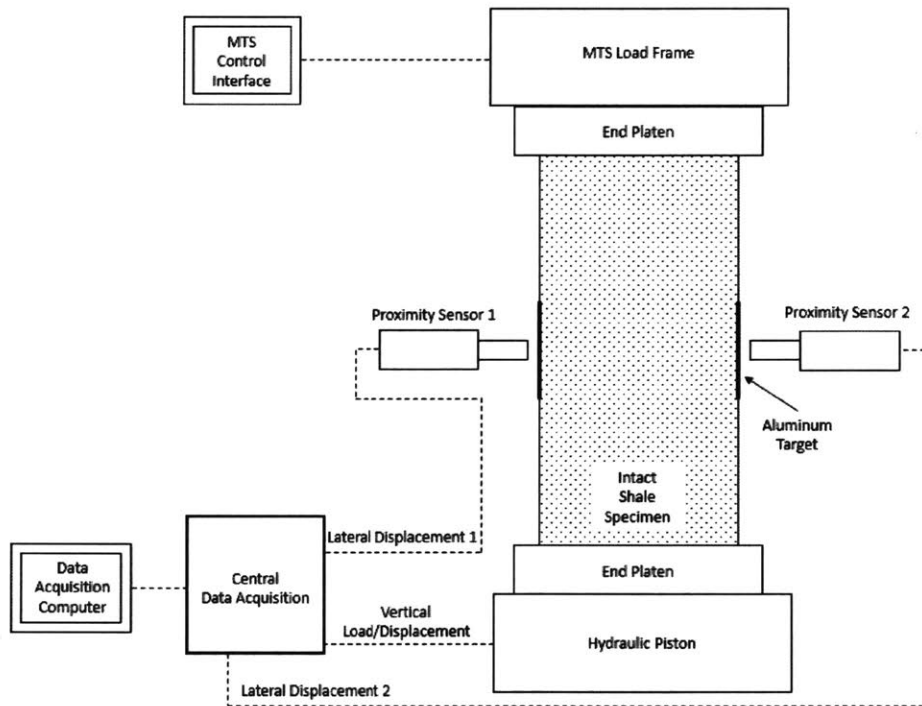


Figure 8 - Intact test setup diagram. Data acquisition includes load frame vertical load and displacement data, and lateral displacement data from proximity sensors.

From these experiments, stress and strain is calculated from the load and displacement data. Figure 9 shows an example of the collected data. The example in Figure 9 is for the Vaca Muerta shale specimen (shown in Table 2) with horizontally oriented bedding planes, from which the ultimate strength, stiffness, and Poisson's ratio are determined.

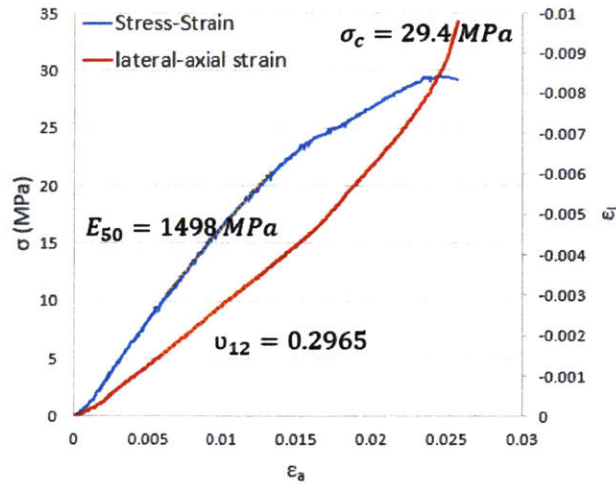


Figure 9 - Example of data acquired from intact tests on shale specimens. The example shown is for a Vaca Muerta shale prismatic specimen with horizontal bedding planes. Left axis: stress, bottom axis: axial strain, right axis: lateral strain.

Uniaxial compression tests were also carried out on Opalinus shale from the core BSO-36. In the case of BSO-36, the prismatic specimens were prepared with horizontal bedding planes (perpendicular to loading direction) and vertical bedding planes (parallel to loading direction). Table 2 summarizes the results of the mechanical properties of the different rocks tested by the MIT CEE Rock Mechanics Group.

Table 2 – Mechanical properties of different rocks subjected to fracture tests at MIT CEE Rock Mechanics Group (Wong, 2008, Miller, 2008, Gonçalves da Silva, 2009, and Morgan, 2015) highlighting the materials tested in this study.

Characterization Parameter	Molded Gypsum	Barre Granite	Opalinus Shale FE-A	Opalinus Shale BSO-34	Opalinus Shale BSO-36	VM-X3 at 2528 m
Density, ρ [g/cc]	1.54	2.61	2.71			
Natural Water Content, w_c [%]			6	2.90	7.52	2.73
Young's Modulus, E [GPa]	5.96	11.9 _{min} / 23.1 _{max}	1.08 _⊥ /4.54 _∥		1.33 _⊥ /1.95 _∥	1.49 _⊥
Uniaxial Compressive Strength, σ_c [MPa]	33.85	170 _⊥ / 192.5 _∥	19.4 _⊥ /14.4 _∥		17.26 _⊥ /5.76 _∥	29.4 _⊥
Uniaxial Tensile Strength, σ_t [MPa]	3.2	5.08 _{min} / 10.65 _{max}				
Poisson's Ratio, ν	0.15		0.25 _⊥ /0.27 _∥		0.33 _⊥ /0.26 _∥	0.29 _⊥

3. Uniaxial Compression Experiments

The uniaxial compression experiments discussed in this chapter were done on Vaca Muerta shale specimens with flaw pairs. By applying uniaxial stress on the prismatic specimen, fractures initiate at the flaws, which then propagate and may or may not interact with the neighboring flaw, depending on the flaw geometry.

First, the specimen preparation techniques, challenges, and solutions are discussed. Next, the details of the experimental setup are described. Finally, the results of the experiments are presented, and then compared to what was observed in Opalinus shale by Morgan (2015).

3.1 Specimen Preparation

The objective of the specimen preparation techniques is to produce a prismatic specimen with a pair of artificial cracks (referred to as *flaws*) shown in Figure 10, causing as little mechanical or chemical disturbance as possible to the natural state of the rock throughout the preparation process.

Traditionally, most rocks are cut involving a variation of a water cutting techniques such as a water jet or water flooding the cutting blade. Because of the presence of water-sensitive expandable clay minerals, this is not an option as this may induce clay swelling in the specimen, disturbing the natural state of the rock both chemically and mechanically. A dry cutting process was developed for Opalinus Shale by Morgan (2015). However, the Vaca Muerta Shale presented new challenges that Morgan's techniques could not handle.

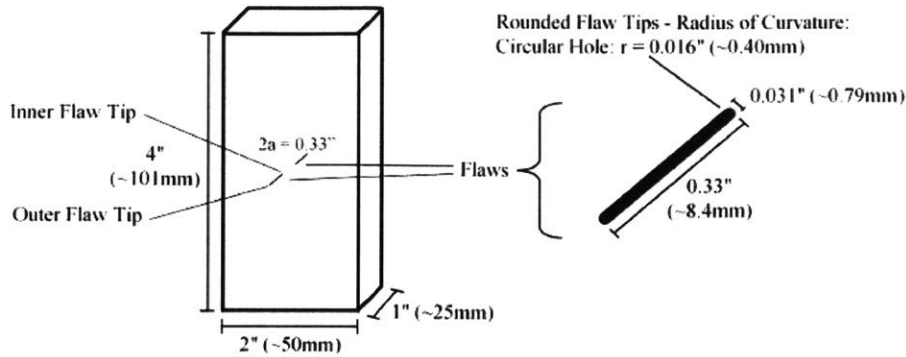


Figure 10 – Objective of sample preparation is to produce a prismatic shale specimen with double flaws with the dimensions listed in the figure. From Morgan (2015).

3.1.1 Cutting Prismatic Samples

The objective is to produce prismatic specimens that are 4" long, 2" wide, and 1" thick out of the 2.5" diameter cylindrical Vaca Muerta core samples, shown in Figure 11.

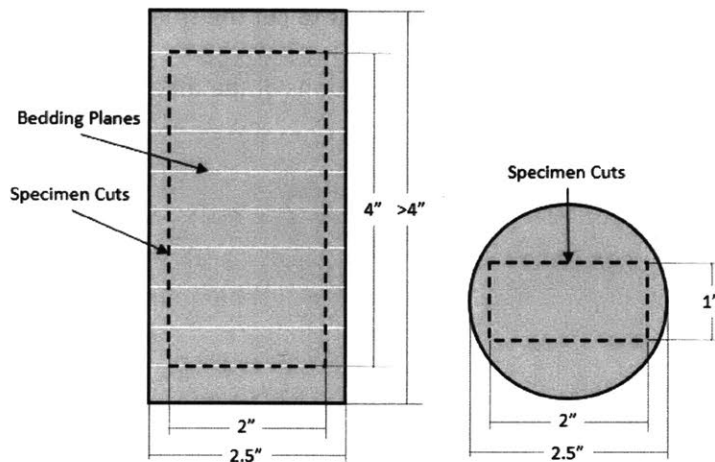


Figure 11 - Vaca Muerta Shale cylindrical core samples. Bedding planes are approximately perpendicular to the major axis of the cylindrical core. Specimens were cut along the dashed lines. Left: side view of core. Right: top view of core.

Previously, Morgan (2015) cut Opalinus Shale into prismatic specimens with a traditional tabletop band-saw with specialized carbide-tipped abrasive saw blades. The Opalinus shale was soft enough to cut without the use of lubrication, which can prevent the blade from over-heating. However, the Vaca Muerta Shale's hardness/abrasiveness caused the carbide-tipped blades to over-heat and snap.

Also, the Vaca Muerta Shale core samples were 2.5" in diameter while the Opalinus Shale cores were 4" in diameter. As shown in Figure 11, there are tight tolerances for each cut given the core geometry. Also, the thick blade (~0.1") made it difficult to produce the desired dimensions.

Many alternatives were investigated. First, the carbide-tipped abrasive saw blades were replaced with diamond-tipped abrasive blades. Next, lubrication of the blade was studied qualitatively and is shown in Figure 12. Shale samples were soaked in water of various salinity of different salt valencies. It was shown that increased salinity and valency reduced clay swelling. However, these saline solutions are corrosive to the blade and the machinery. So a non-ferrous, vegetable oil-based, anhydrous metal-cutting lubricant was investigated; it showed no swelling in the clay and is machine friendly. Also, a mist spraying pump was installed for dispersing a small amount, yet sufficient lubrication to the blade alone. This combination of equipment allows one to cut harder shales without compromising their mechanical or chemical integrity. However, it still was not sufficient to cut the smaller diameter Vaca Muerta Shale cores given the thickness of the blade, the heavy vibrations of the machine, and tight tolerances.

Lubricant tests

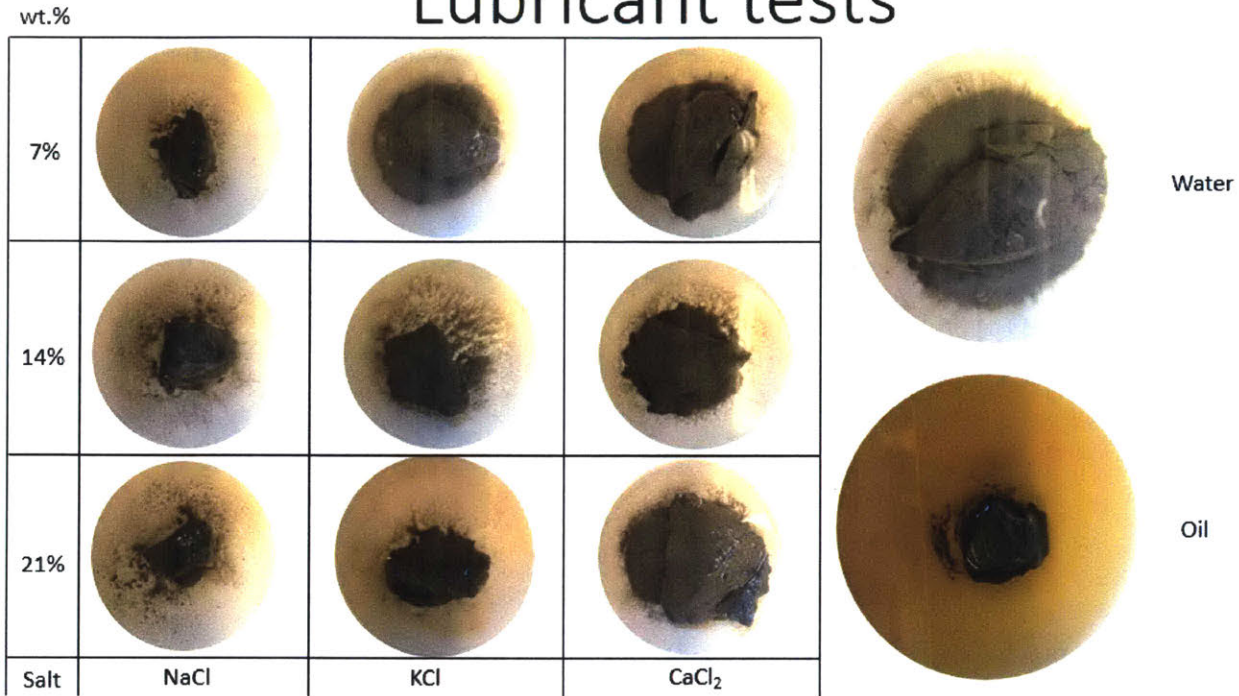


Figure 12 - Lubricant investigation on Opalinus clayshale. Table shows shale submerged in solutions of various salts and concentrations. Right top: shale submerged in untreated water. Right bottom: shale submerged in non-ferrous, vegetable oil-based anhydrous lubricant. Solutions with higher valency salts at higher concentrations showed the least swelling, spalling, and disintegration of shale sample. Oil showed no sign of these reactions.

The solution to these challenges was to use a specialized diamond wire band saw, shown in Figure 13. This type of band saw produces very little vibrations, helping to keep the sample intact throughout the cutting process. The diamond wire is 2 thousandths of an inch (50 μm) in diameter, producing the precision cuts required by the tight dimensional tolerances. The table and saw have variable speed motors. The sample is fixed in position, the saw speed and table speed are set, then a single straight cut is made. After much investigating, it was found that a moderate saw speed (3-6 m/s) combined with a slow table speed (2-5 mm/min) produce the cleanest and most precise cuts. The table has attachments that can fix the sample in any orientation. To produce the prismatic samples of the desired dimensions, one only needs six perpendicular cuts (see Figure 11). Finally, the surfaces of the prismatic specimen are

hand polished using multiple sheets of sand paper increasing in fineness (grit sizes: 80, 220, 400, 600, and 800). Polished surfaces are better at visually capturing features such as bedding planes or beef.

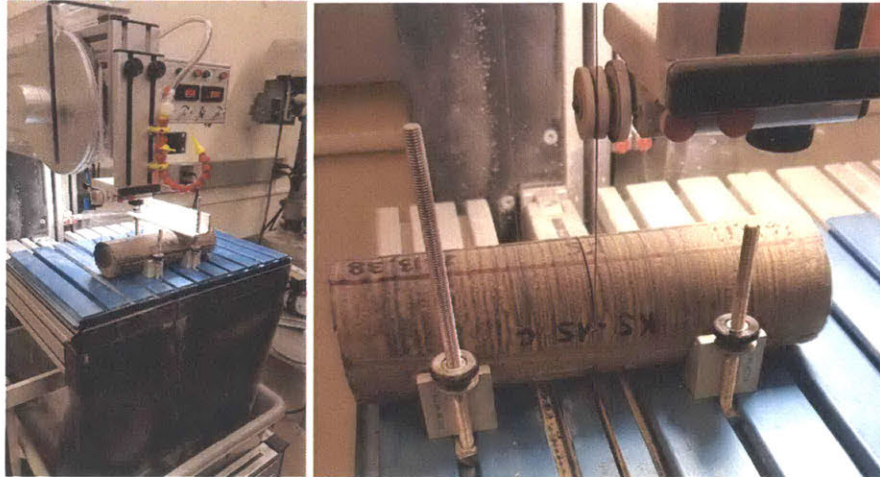


Figure 13 – Specialized diamond wire band saw to cut Vaca Muerta core samples. Left: Photograph of diamond wire saw. Right: Close up of diamond wire cutting Vaca Muerta shale.

3.1.2 Cutting Flaws

Many of the challenges associated with cutting flaws are similar to cutting prisms. Previously, molded gypsum was cast with removable shims to produce flaws. Materials such as granite or marble had flaws cut into them using a water jet. Again, since shale is sensitive to water, the flaws need to be dry cut. Morgan’s technique for dry cutting flaws (2015) was to drill small diameter holes using a drill press at the locations of the tips of the flaws using a standard table top drill press. Afterwards, a scroll saw is used to cut the flaws. This process is shown in Figure 14.

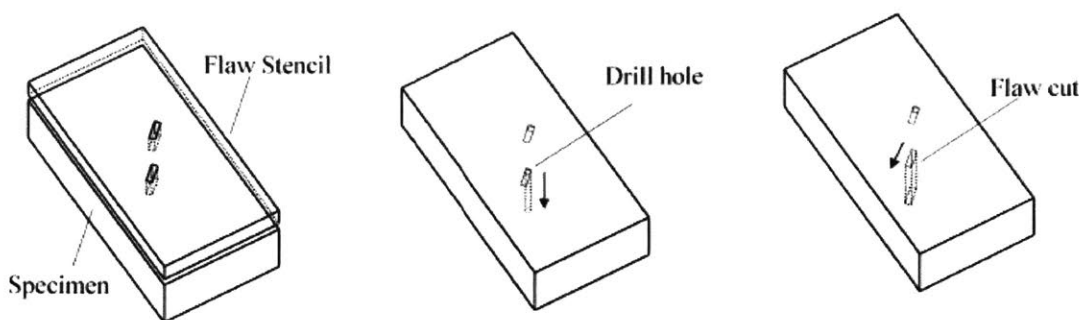


Figure 14 - Cutting flaw pairs in prismatic shale samples. Flaws were drawn on the specimen using a laser-cut stencil. A hole was drilled at each flaw tip. A scroll saw blade was inserted into the hole to cut the flaw. Modified from Morgan (2015).

Morgan's technique did not work for the harder Vaca Muerta Shale. To drill holes in Opalinus Shale, standard steel drill bits (#68 – 0.031" diameter) were used. When using these to drill through Vaca Muerta Shale, their cutting edge dulled within the first 0.1" depth of cut, then they broke. As for the scroll saw blades, Morgan used scroll saw blades 0.015" (0.381 mm) in thickness and 0.032" (0.813 mm) in width with serrated teeth on one edge. The width of the blade makes it self-correcting for straight cuts. However, when using these blades in Vaca Muerta, the cutting edge immediately dulls and cannot cut even 1 mm. The technique of drilling holes and cutting with a scroll saw is sound for cutting dry flaws, but upgrades were required in order to implement this technique on hard shale specimens.

First, the drill bits were investigated. Steel drill bits wore down too fast and usually broke in the hole leading to losing an entire specimen. The drill bits were replaced with 0.029" (0.75 mm) diameter electroplated diamond twist drills, shown in Figure 15. These bits are coated with a matrix that has layers of diamonds, allowing new diamonds to act whenever the cutting diamonds wear down or are plucked out. The twist drill bit shape has flutes twisting around the side of the bit allowing the cut material to be removed.



Figure 15 - Electroplated diamond twist drill bits for micro-drilling Vaca Muerta Shale.

These drill bits were effective in drilling through Vaca Muerta Shale but posed some challenges. They have a length of 1.2", leaving a small tolerance of 0.2" to be inserted into the chuck and drill through the 1" thick specimen. Also, the spindle on the drill press does not allow the user to know when the drill bit has reached the bottom of the hole; hence it was common to apply more force than needed and cause the bit to break. For these two reasons, a hand-feeding sensitive chuck adapter for micro-drilling was installed, shown in Figure 16. This adapter has a keyless chuck that tightens on the drill bit as it drills, and only requires a very short length of the drill bit to be held. Also, the thumb press allows the user to feel when the drill bit has reached the bottom of the hole and prevents exerting high forces that may break the drill bit. Finally, the "peck drilling" technique is used, where one lightly yet rapidly pushes the thumb press down and releases repeatedly, making small incremental cuts into the material. This technique keeps the flutes unclogged and cools the bit. The combination of the electroplated twist drill bits, the hand-feeding chuck adapter, and the peck drilling technique allows one to effectively drill clean micro-holes in shales as hard as the Vaca Muerta.



Figure 16 - Hand-feeding sensitive chuck adapter for micro-drilling.

After successfully drilling the holes all the way through at the locations of the flaw tips, the next step is to cut the flaws. With the success of the diamond wire in cutting the prismatic specimen, a diamond wire replaced the rectangular steel scroll saw blades. After experimenting, it was found that using a 0.002" diameter wire made it difficult to cut straight. Applying extra tension on the wire to ensure a straight cut often caused the wire to break. This issue was solved by using a thicker diamond wire of 0.027" (0.7 mm) diameter, which was more rigid and easier to control.

Using the above upgrades and modifications to Morgan's technique to dry cutting flaws in shale, flaws were successfully cut into the harder Vaca Muerta Shale, as shown in Figure 17.

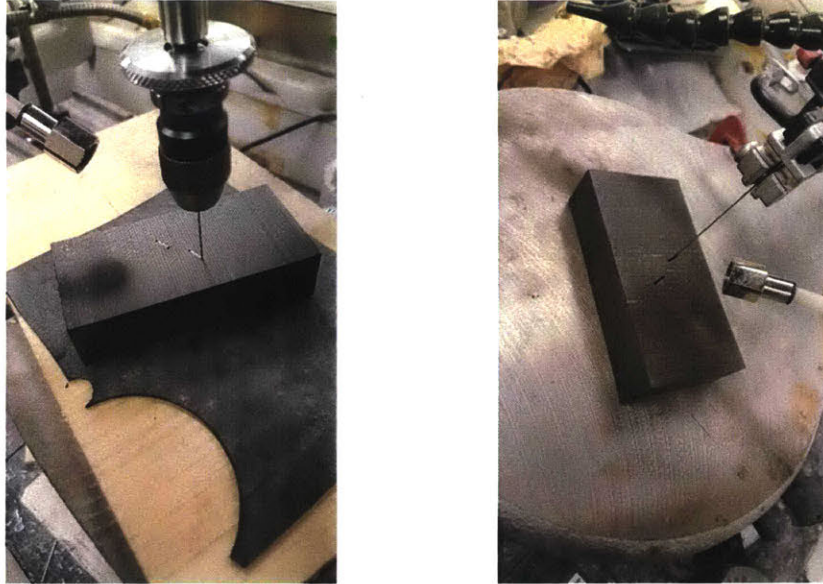


Figure 17 - Left: drilling holes at flaw tips using 0.75 mm electroplated diamond twist drills, sensitive hand-feeding chuck adapter, and peck drilling. Right: cutting flaws by connecting flaw tip holes using a scroll saw with 0.7 mm diamond wire.

3.1.3 Sample Preservation

The Vaca Muerta Shale core samples come from cored reservoir sections and are of high value. A documentation station was setup to keep track of everything that happened to a core sample, shown in Figure 18. This station consisted of a stage for the specimen, a number of lights to best capture the features of the specimens, a DSLR camera with a telescoping zoom lens attached to the stage with a jointed arm providing maneuverability, and a computer. The images captured are saved on the computer, and a photo editing software is used to save the specimen information in the meta-data of the saved image.

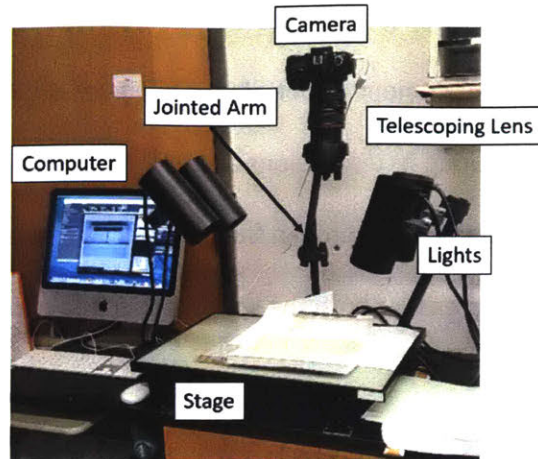


Figure 18 - Documentation station to keep track of everything that happens to the Vaca Muerta Shale core samples.

Figure 19 shows an example of a photo taken to document the cuts required to produce a prismatic specimen. The meta-data of this folder has information such as: who made the cuts, when the cuts were made, name of core, depth of core, purpose of cuts.

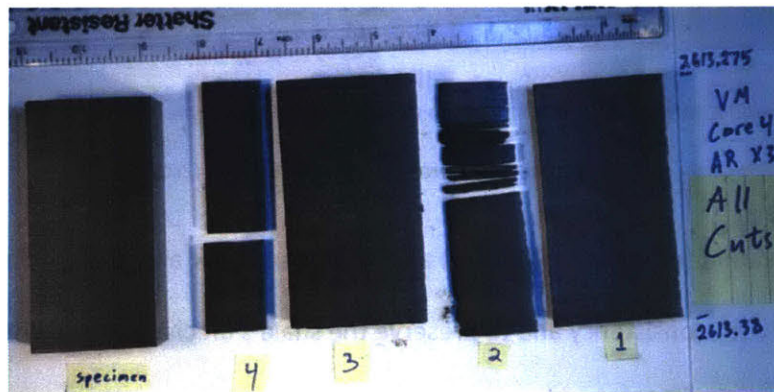


Figure 19 - Documentation of cut specimen and cut pieces of Vaca Muerta Shale.

Whenever the specimen preparation is finished, or between the stages of cutting prisms, drilling holes, and cutting flaws, the shale is carefully preserved and stored. This is to preserve the natural water content as much as possible, as the degree of saturation may affect the strength, stiffness, and other properties of the shale. All specimens and cut pieces are each individually placed in a vacuum sealed bag. Each vacuum sealed bag containing a test specimen is placed in its own cardboard box for added

protection. Vacuum sealed bags containing cut pieces are put in a separate cardboard box. Then the cardboard boxes are placed in a containment cooler, shown in Figure 20. During testing, the specimen is placed in a zip-lock bag after measuring its dimensions and while setting up testing equipment. After the test is complete, the tested specimen and its broken fragments are vacuum sealed again. These preservation techniques are used to ensure both the specimen, and the cut pieces are all preserved and accounted for.



Figure 20 – Shale sealing and storage. Left: shale is stored in vacuum sealed bags to preserve in-situ water content. Right: cooler container for added protection. From Morgan (2015).

The specimen preparation techniques described above were used for all shale specimens tested throughout this study for consistency and to preserve the shale’s mechanical and chemical integrity.

3.2 Experimental Procedure

Previously, Morgan (2015) studied fracture initiation, -propagation, and -coalescence in Opalinus Shale specimens subjected to unconfined compression tests. The objective of these experiments is to observe crack initiation, -propagation and -coalescence patterns, and then associate the observed behavior with the stress-strain-time data. Testing Vaca Muerta Shale followed the same procedure for a consistent basis of comparison. The flaw pair specimens Morgan tested had a variety of flaw geometries as shown in Figure 21. Due to the scarcity of Vaca Muerta Shale samples, only three tests were run for this study.

Two 2a-30-30 (0) Vaca Muerta specimens (specimens labeled: VM1-2a-30-30 (0) and VM2-2a-30-30 (0)) were tested to compare stepped flaw crack behavior. One 2a-30-0 (0) Vaca Muerta specimen (specimen labeled: VM3-2a-30-0 (0)) was tested to compare the co-planar flaw crack behavior.

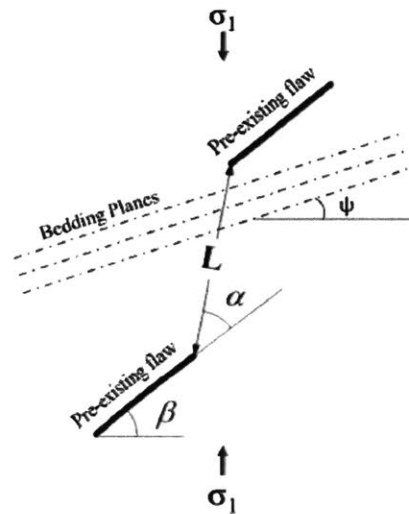


Figure 21 – Definition of flaw pair geometries. Flaw pair geometries are defined by ligament length (L), flaw inclination angle (β), bridging angle (α), and bedding plane angle (ψ). A geometry is reported in the format L - β - α (ψ).

3.2.1 Testing Setup

Morgan's Opalinus Shale test specimens were loaded uniaxially in a 60-KIP Baldwin™ hydraulic loading frame. Time, load and axial displacement was recorded for all tests, which were load-controlled at a constant rate of 1200 lbs/min. The tests were recorded with high resolution images taken every 2 seconds throughout the test, and high speed video (7,500 frames/second) capturing the last 1.6 seconds of the test. The high-speed camera was electronically connected to the data acquisition system and set to automatically trigger and save the data when the machine detects a significant drop in load during the test. Automatically triggering the high-speed camera makes it possible to synchronize time, load, and axial displacement with the high-speed video. Upon triggering, the camera is set to save 80% of the

1.6 seconds before the break detect, and 20% of the 1.6 seconds after the break detect. The test setup is shown in Figure 22 and a schematic is shown in Figure 23.

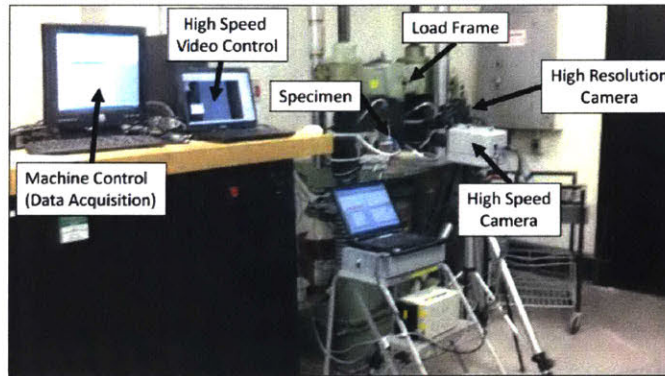


Figure 22 - Photograph of the test setup used for specimens with flaw pairs. From Morgan (2015).

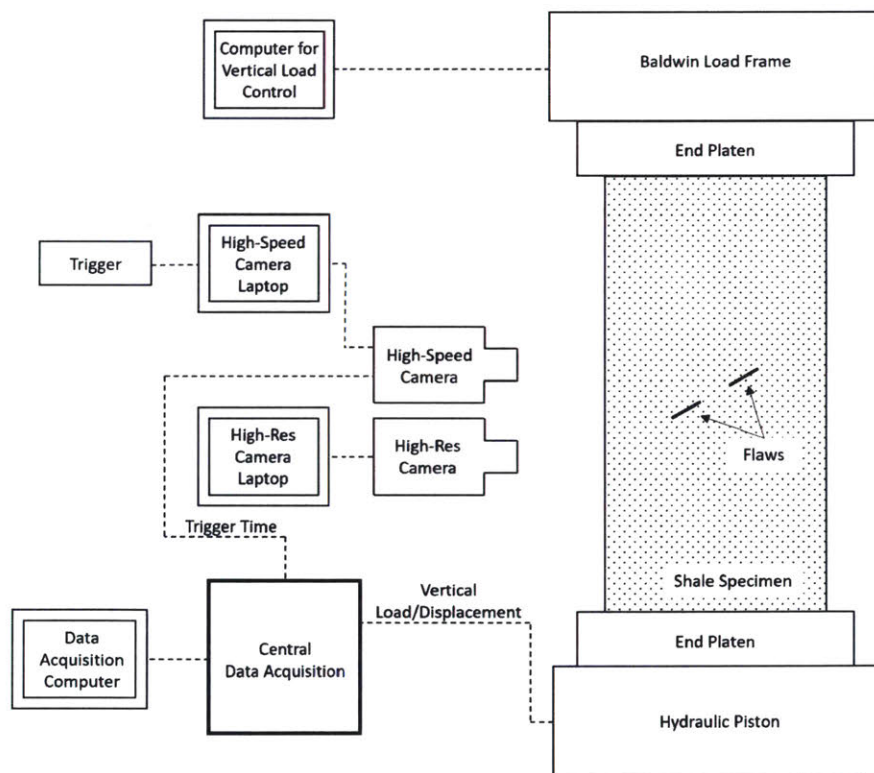


Figure 23 – Uniaxial compression on shale specimen with flaw pairs setup schematic. Central data acquisition saves vertical load and displacement data from load frame as well as high-speed camera trigger to relate observed crack events to stress-strain-time data.

VM1-2a-30-30 (0) was tested in the same 60-KIP Baldwin™, but VM2-2a-30-30 (0) and VM3-2a-30-0 (0) were tested in a 200-KIP Baldwin™ with the same procedure described above. The change in load frame was due to concerns that the 60-KIP load frame's crosshead might be slightly skewed due to bent metal plates.

Testing Imagery

As shown in the above photograph and schematic, crack events were recorded using a high-resolution camera taking a 2 second time-lapse throughout the test and a high-speed video capturing the final 1.6 seconds of the test at 7,500 frames/second.

The high-resolution camera used was a Nikon™ D90 with a 105-mm lens, shown in Figure 24. The role of this camera is to take a 2 second time-lapse from the beginning of loading until failure of the specimen.

This is done to capture key events that may occur in the specimen prior to failure such as crack initiation, spalling, crack closing, etc., which would otherwise be missed by the high-speed video. This camera was connected to its designated computer installed with DigiCam Control™, a third-party software used to adjust the camera settings for optimum focus on the specimen surface as well as control the time-lapse.



Figure 24 – Nikon™ D90 high-resolution camera with a 105-mm lens used to take a 2 second time-lapse from beginning of loading until catastrophic failure of specimen. Taken from Morgan (2015).

The high-speed video camera used was a Photron™ SA-5 with a 90 mm Tamron™ lens, shown in Figure 25. This camera has two primary objectives. First, it is used to capture the sudden failure of the specimen to allow one to distinguish a multitude of events that occur fractions of a second apart and determine the type of cracks and coalescence patterns as classified by Wong & Einstein (2009a, 2009b). The user can adjust settings such as frame rate, resolution, and trigger partition of recorded data. For this study, a frame rate of 7,000 frames per second (fps) and a resolution of 600x800 pixels was set which provided 1.6 seconds of recording time. The second objective is to provide a time synchronization point as this camera is connected to the central data acquisition system. This can allow one to relate what is observed to the stress-strain-time data. Details of data synchronization will be discussed below.

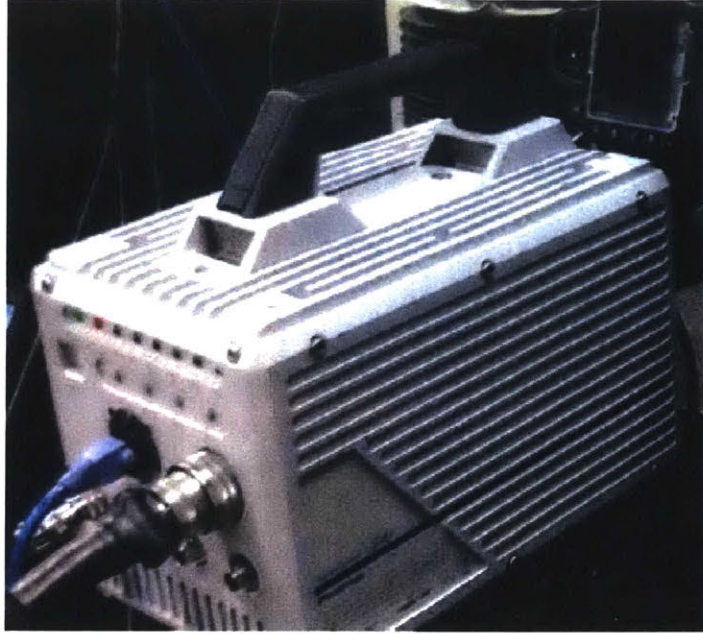


Figure 25 - Photron™ SA-5 high-speed camera which was used to capture high-speed cracking events. For this study, it was set to 7,000 fps and 600x800 pixel resolution to allow 1.6 seconds of recording time. Taken from Morgan (2015).

Two Dolan-Jenner Fiberlite™ units were used to provide optimum lighting for testing imagery, shown in Figure 26. Each unit is fitted with dual branch fibers providing a total of four spotlights evenly luminating the specimen surface during the test.

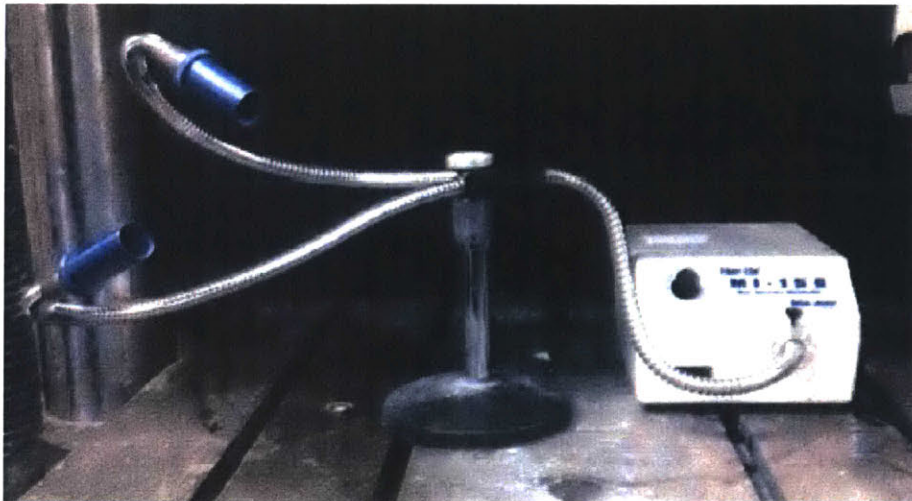


Figure 26 - Dolan-Jenner Fiberlite™ MI-150 fiber optic lighting. Two lighting units, each fitted with dual branch fibers, were used for optimum luminescence of specimen surface. Taken from Morgan (2015).

Data Synchronization

One of the objectives of this experiment is to relate key events that are observed to the stress-strain-time data. The load frame is connected to the central data acquisition system which records the vertical load and displacement data (Figure 23). The high-speed camera is also connected to the central data acquisition system which records the trigger time. The load frame is set to load-control and subjects the specimen to a constant loading rate. However, a break-detect is programmed where the load frame will stop applying more load when a significant drop in load is detected, i.e. when the specimen goes through sudden failure. At this point, the camera is manually triggered, and the trigger time is recorded. By having all instruments recording to the same data acquisition system, one can accurately determine where an image from the high-speed video lies relative to the load/displacement data. The high-resolution image synchronization will be discussed in section 3.2.2 below.

3.2.2 Analysis

After a test is completed, the specimen and its broken fragments are resealed and stored. The next step is an intricate analysis procedure to describe the crack behavior of the tested specimen. This analysis process is summarized in the workflow shown in Figure 27.

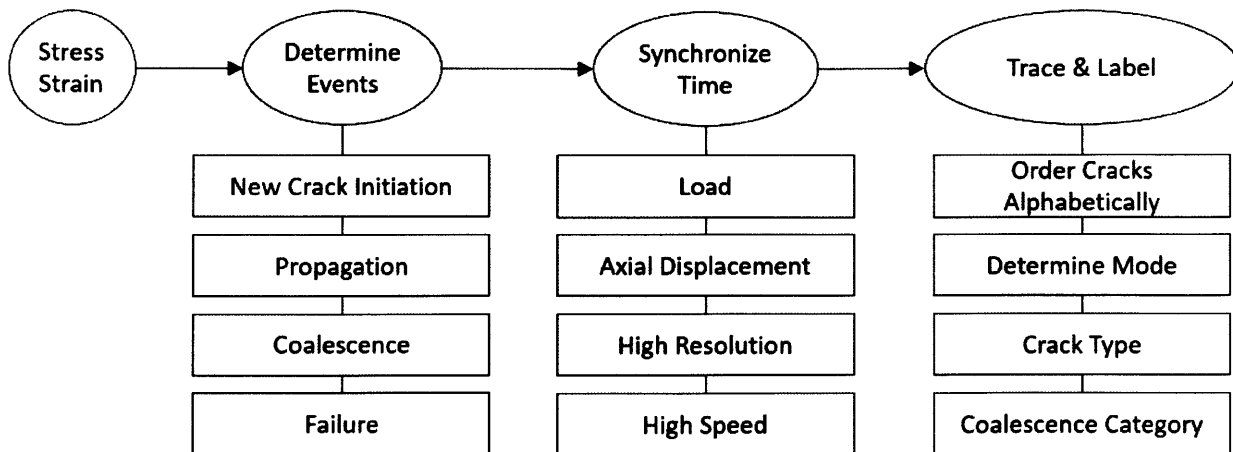


Figure 27 – Analysis workflow of uniaxial compression fracture experiments.

First, stress, strain, and deformability (modulus) are calculated from the recorded vertical load and displacement data using:

$$\sigma = \frac{F}{A} \dots\dots\dots(1),$$

$$\varepsilon = \frac{\Delta L}{L} \dots\dots\dots(2),$$

$$E_{50} = \frac{\partial \sigma}{\partial \varepsilon} \dots\dots\dots(3).$$

Young’s modulus is determined according to ASTM D7012-14, as the tangent modulus measured at a fixed percentage of ultimate strength (E_{50} is measured at 50% of the ultimate strength of the specimen).

Next, key events are determined from the high-resolution images and high-speed video. The high-speed video is analyzed, frame by frame, to identify crack initiation, -propagation, and -coalescence. Usually though, cracking in shale initiates prior to the high-speed video capture window, so the high-speed video analysis is supplemented with the high-resolution image analysis, as some cracks initiate as early as 30-50% of maximum applied load.

Next, time data synchronization is done to correlate the time, load, axial displacement data with the high-speed video and high resolution images in order to identify the key frames’ time of occurrence. As previously mentioned, the manual trigger time of the high-speed video is known and recorded on the central data acquisition system. So all high-speed frames are time synchronized with the stress-strain-time data. As for the high-resolution images, synchronizing them requires a careful, approximate comparison by eye with the known high-speed frames, where a high-resolution image is matched to a high-speed frame. After identifying the matching frame, the high-resolution images can be associated with the stress-strain-time data to within fractions of a second.

After analyzing all the imagery and synchronizing it with all other data, the key image frames that show crack initiation, crack propagation, and crack coalescence are identified and their respective times of occurrence are known. Each of these key event frames is put into a photo editing software to trace the events. Afterwards, cracks are labeled alphabetically based on order of occurrence. Crack modes (tensile or shear) are determined by reanalyzing the imagery. Also, crack types, as defined by Wong and Einstein (2009b) and Morgan (2015), shown in Figure 28 are determined.

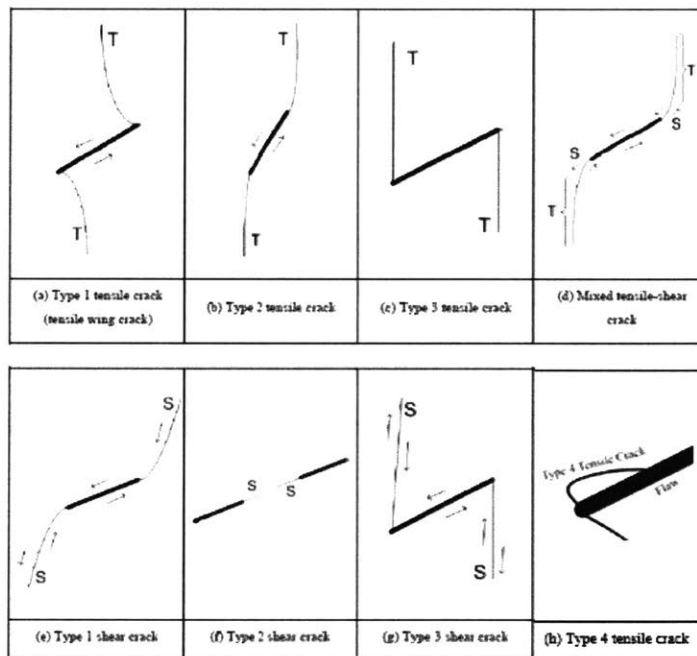


Figure 28 - Seven crack types proposed by Wong and Einstein (2009b) and an eighth crack proposed by Morgan (2015).

T=Tensile Cracks, S=Shear Cracks.

Then coalescence category describing the behavior of coalescence of the pre-cut flaw pair is determined as defined by Wong and Einstein (2009b) and shown in Figure 29. Finally, the traced cracks and their labels are collated and presented with stress-strain data. Analyses of tested specimens are shown in section 3.3 “Dry” Fracture Results.


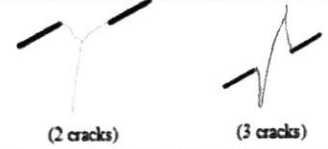
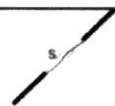
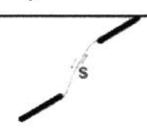
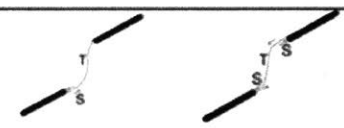

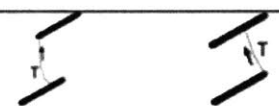

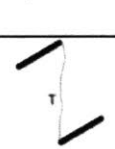
Category	Coalescence patterns	Crack types involved
1		No coalescence
2		Indirect coalescence by two or multiple cracks (crack types vary)
3		Type 2 S crack(s)
4		Type 1 S crack(s)
5		One or more type 2 S crack(s) and type 2 T crack segments between inner flaw tips
6		Type 2 T crack(s). There may be occasional short S segments present along the coalescence crack.
7		Type 1 T crack(s)
8		Flaw tips of the same side linked up by T crack(s) not displaying wing appearance (crack type not classified). There may be occasional short S segments present along the coalescence crack.
9		Type 3 T crack(s) linking right tip of the top flaw and left tip of the bottom flaw. There may be occasional short S segments present along the coalescence crack.

Figure 29 - Nine coalescence patterns proposed by Wong and Einstein (2009a). These observations were made on molded gypsum and Carrara Marble subjected to unconfined compression.

3.3 “Dry” Fracture Results

This section is titled “Dry” Fracture Results because the fractures are induced by the uniaxial load and are dry whereas in the next chapter, the fractures are induced by hydraulic pressure and are wet. A total of three Vaca Muerta shale flaw-pair specimens were prepared and tested. The first was uniaxially

loaded in a 60-KIP (270 kN) Baldwin™ hydraulic loading frame. The other two were uniaxially loaded in a 200-KIP (900 kN) Baldwin™ hydraulic loading frame. All specimens were load-controlled at a constant rate of 1,200 lbs/min (5.3 kN/min). Load, axial displacement, and time data were recorded at a rate of 100 samples per second from the transducers by ADMET's MTESTW software on the computer controlling the load-frame (refer to Figure 22 and Figure 23). Specimen dimensions were measured prior to testing for stress/strain calculations.

3.3.1 Flaw Pairs in Vaca Muerta Shale

The flaw geometries chosen were a coplanar flaw geometry 2a-30-0 (0) and a stepped flaw geometry 2a-30-30 (0) shown in Figure 30.

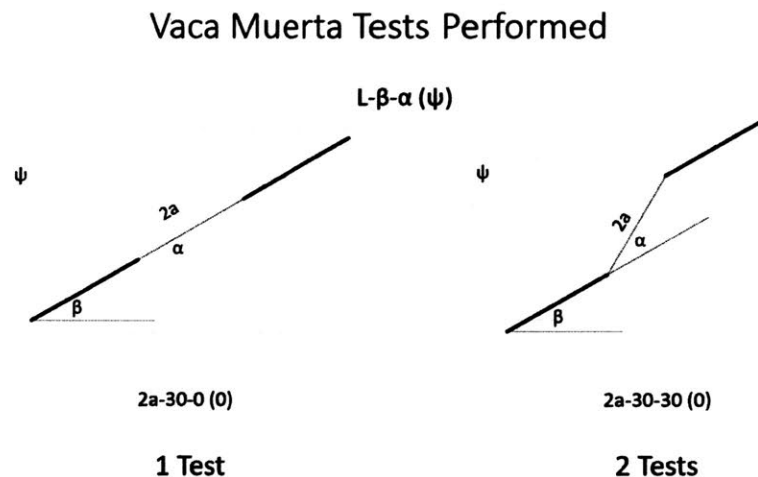


Figure 30 – Geometries of flaw pairs tested on Vaca Muerta Shale specimens. Left: coplanar flaw geometry with horizontal bedding planes 2a-30-0 (0). Right: Stepped flaw geometry with horizontal bedding planes 2a-30-30 (0).

Vaca Muerta shale specimens with the geometries shown in Figure 30 were subjected to uniaxial load at constant loading rate until failure. The chronological progression of cracking events is captured and described. Distinct cracking characteristics such as initial crack type and en echelon cracks will be presented. In the case of the highly heterogeneous Vaca Muerta shale, crack interaction with “beef”

layers will also be shown. Finally, the coalescence pattern type as well as the crack initiation and coalescence stress are identified and shown.

Similar to the study done by Morgan (2015), tensile cracks are characterized by an opening of the crack faces while shear cracks by a relative sliding along the crack faces. Combined tensile-shear cracking refers to cracks which initiate as one crack type, tensile or shear, and then propagate as the other crack type. An example of a crack label is shown in Figure 31.

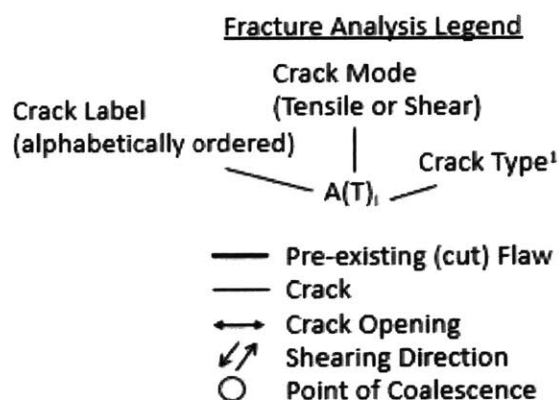


Figure 31 – Fracture analysis legend. Cracks are labeled alphabetically in chronological order of initiation. Crack mode is either tensile or shear. Crack type is defined based on Wong and Einstein (2009b) and Morgan (2015).

3.3.1.1 Coplanar Flaw Geometry

This section shows the result from the test conducted on Vaca Muerta shale with the coplanar flaw pairs shown in Figure 30 with horizontal bedding planes. Specifically, the geometry tested was 2a-30-30 (0).

The crack types and coalescence categories defined by Wong and Einstein (2009a), Wong and Einstein (2009b), and Morgan (2015), respectively, will be used extensively in this section (refer to Figure 28 and Figure 29).

The stress-strain data are presented in Figure 32 with selected events identified by symbols on the curve. Note, some of the crack labels were omitted due to lack of space on the figure, but are shown in the more detailed frame sketches shown next.

Figure 32 shows the classic initial non-linear trend indicative of seating effects as well as possible micro-cracks closing in the specimen. The specimen then quickly reaches the linear elastic region where E_{50} was calculated to be 1914 MPa. Note that first crack initiation $A(T)_I$ occurred at 7.43 MPa; at about 32% of maximum stress. The specimen then started yielding around 22.8 MPa indicated by sketch 3. This specimen reached a maximum stress of 23.2 MPa at which point had accumulated a strain of 1.29%. The two flaws coalesced after an additional 0.14% strain was achieved after 0.73 seconds followed by sudden failure.

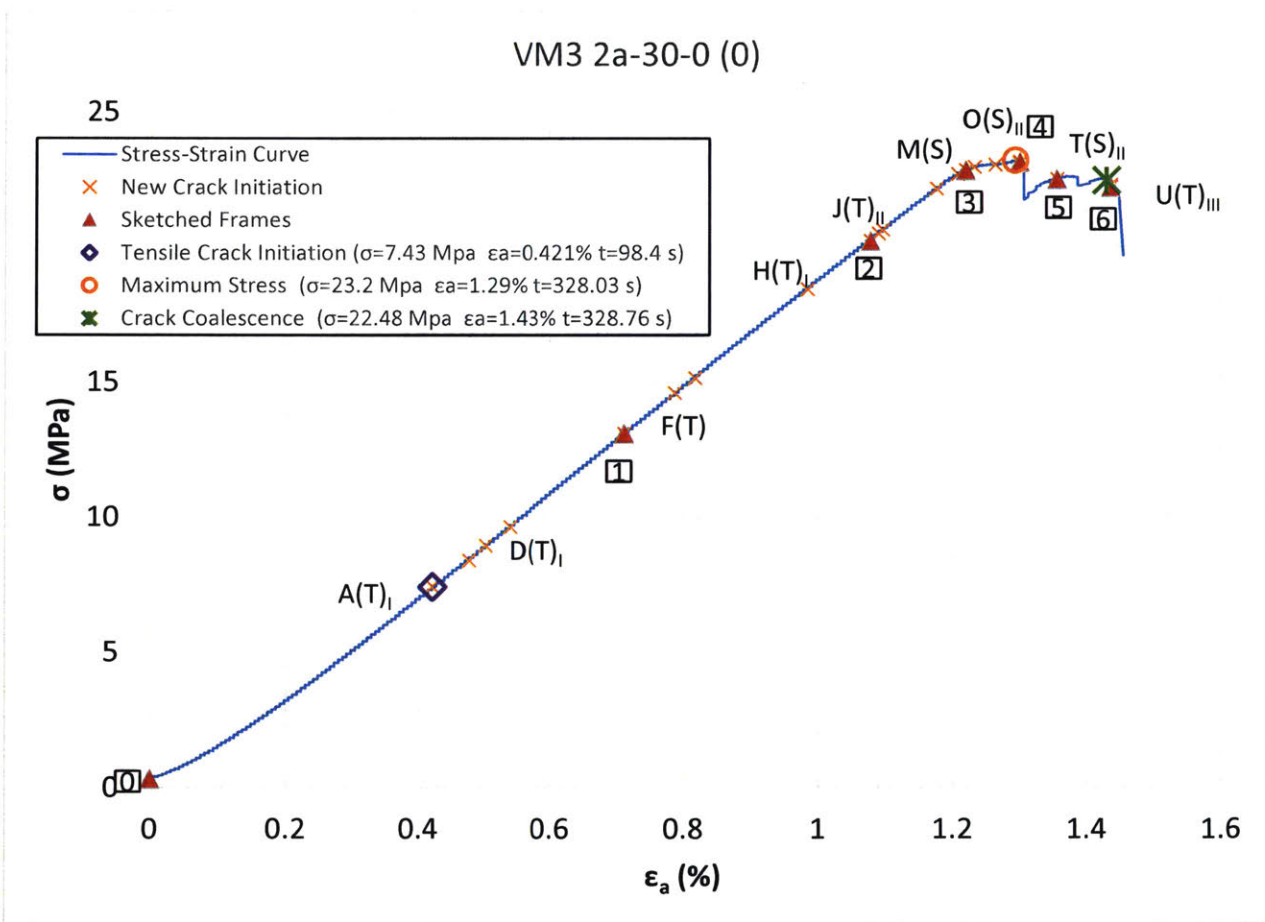


Figure 32 – Stress-Strain curve for Vaca Muerta shale with coplanar flaw pair subjected to uniaxial loading. Yellow “x” indicates crack initiation. A red triangle indicates a sketched frame while the boxed number indicates sketch number, where the detailed sketches are shown next from Figure 33 to Figure 39. Orange circle indicates maximum stress. Green “✱” indicates coalescence stress.

A total of six frames were sketched throughout this test and will be discussed in detail. Sketch 0 (refer to Figure 33) is taken at the beginning of the test to show the initial configuration of the specimen prior to loading, indicated by “0” in Figure 32. The photograph is taken from the high-resolution images. All cracks are labeled alphabetically based on their chronological initiation.

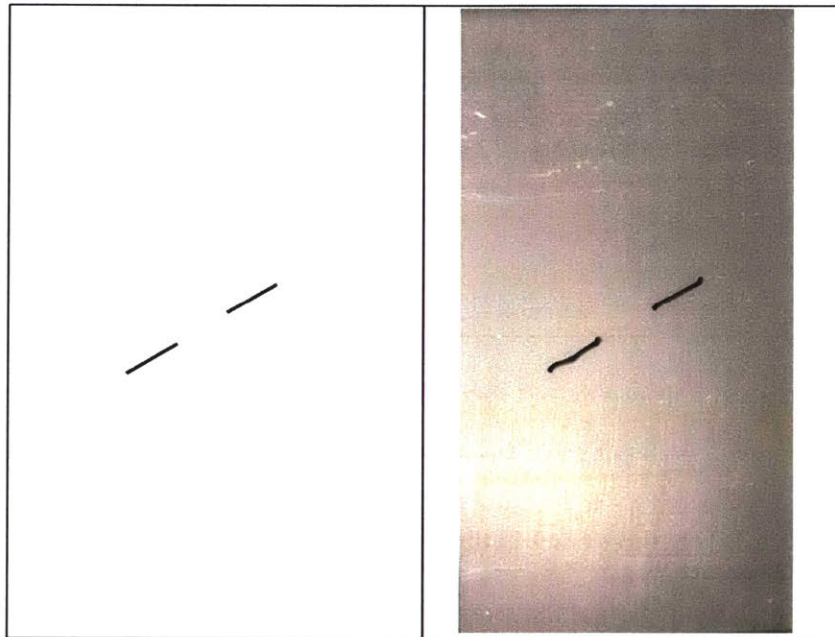


Figure 33 – Sketch 0 as referred to in Figure 32. Left: sketch of cracks. Right: photograph of the specimen at this point in the experiment. Right: frame-time-stress-strain data as well as observations.

Sketch 1 (refer to Figure 34) captures crack initiation. It is taken at 56% of maximum stress and is within the elastic region of the stress-strain curve in Figure 32. At this point of the test: $t = 180.4 \text{ seconds}$, $\sigma = 13.1 \text{ MPa}$, $\varepsilon = 0.712 \%$. Tensile wing crack $A(T)_I$ is the first crack to initiate on the inner tip of the left flaw, then tensile wing crack $B(T)_I$ initiates at the outer tip of the same flaw. Afterwards, tensile wing crack $C(T)_I$ initiates at the inner tip of the right flaw, followed by $D(T)_I$ initiating on the outer tip. Finally, $E(T)_{II}$ initiates near $B(T)_I$.

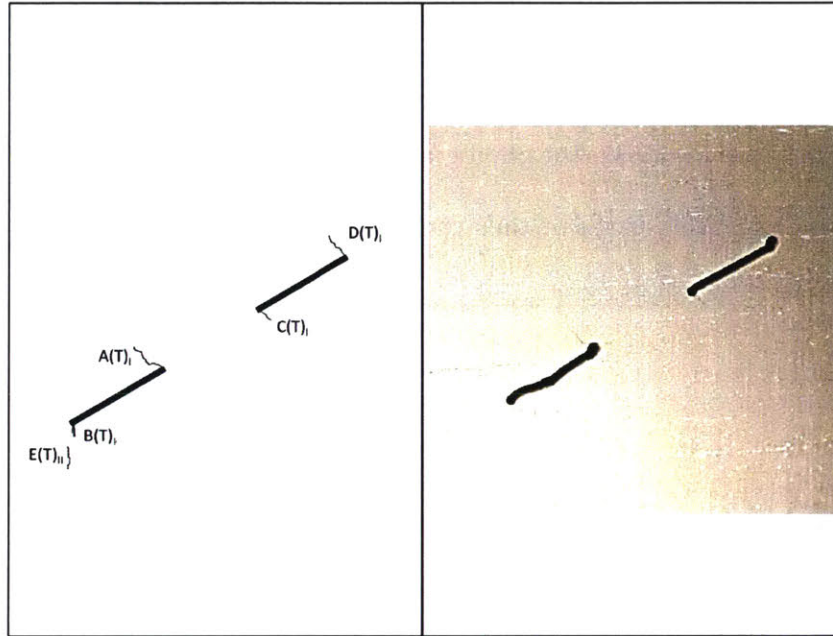


Figure 34 – Sketch 1 as referred to in Figure 32. Left: sketch of cracks. Center: photograph of the specimen at this point in the experiment. Right: frame-time-stress-strain data as well as observations.

Sketch 2 (refer to Figure 35) captures crack initiation and propagation. It is taken at 87% of maximum stress and is within the elastic region of the stress-strain curve in Figure 32. At this point of the test: $t = 284.4$ seconds, $\sigma = 20.2$ MPa, $\varepsilon = 1.08$ %. Tensile crack F(T) initiates between and above both flaws. Tensile crack G(T) initiates above the outer tip of the right flaw. Then tensile wing crack A(T)_i, D(T)_i, and E(T)_{ii} propagate and arrest. Afterwards, crack H(T)_i initiates. Finally, tensile crack I(T) initiates below the right flaw.

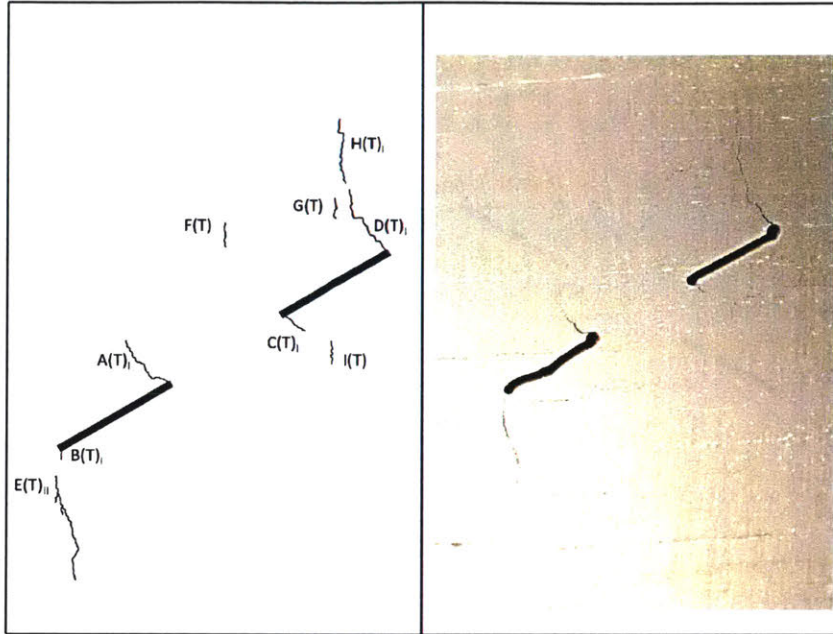


Figure 35 – Sketch 2 as referred to in Figure 32. Left: sketch of cracks. Right: photograph of the specimen at this point in the experiment. Right: frame-time-stress-strain data as well as observations.

Sketch 3 (refer to Figure 36) captures crack initiation and propagation. It is taken at 98% of maximum stress and is at the end of the elastic region of the stress-strain curve in Figure 32. At this point of the test: $t = 322.4$ seconds, $\sigma = 22.8$ MPa, $\varepsilon = 1.22$ %. Tensile crack $J(T)_{II}$ initiates far above the inner tip of the right flaw and propagates towards F(T). Then, $E(T)_{II}$ propagates further and coalesces with the outer tip of the left flaw. Afterwards, tensile crack $K(T)$ initiates right above the inner tip of the right flaw. Crack $H(T)_I$ propagates down and coalesces with $D(T)_I$. Then crack $L(T)$ initiates above $K(T)$ and they form an array of en echelon tensile cracks. After some time, en echelon shear cracks, denoted as $M(S)$, begin to initiate, followed by tensile crack $N(T)_{III}$ which initiates below $M(S)$.

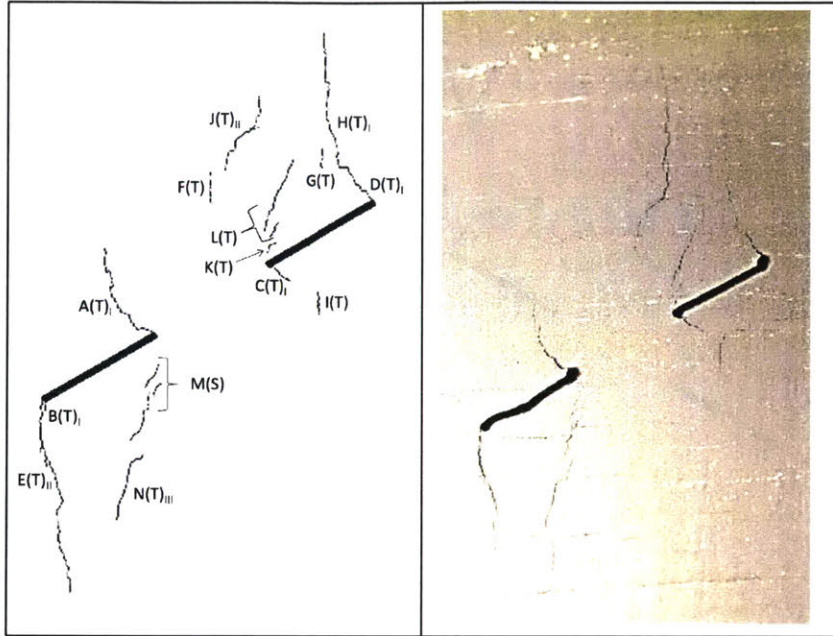


Figure 36 – Sketch 3 as referred to in Figure 32. Left: sketch of cracks. Right: photograph of the specimen at this point in the experiment. Right: frame-time-stress-strain data as well as observations.

Sketch 4 (refer to Figure 37) captures crack initiation and propagation. It is taken beyond the elastic region of the stress-strain curve in Figure 32. At this point of the test: $t = 328.2 \text{ seconds}$, $\sigma = 23.2 \text{ MPa}$, $\epsilon = 1.3 \%$. Crack $A(T)_I$ continues to propagate, followed by $L(T)$ and then $J(T)_{II}$. Then, shear crack $O(S)_{II}$ initiates below the inner tip of the left flaw and connects with the flaw tip followed by the propagation of $N(T)_{III}$. Next, tensile crack $P(T)_{III}$ initiates at the outer tip of the right flaw and propagates downwards. Afterwards, tensile crack $Q(T)$ initiates far above the outer tip of the left flaw.

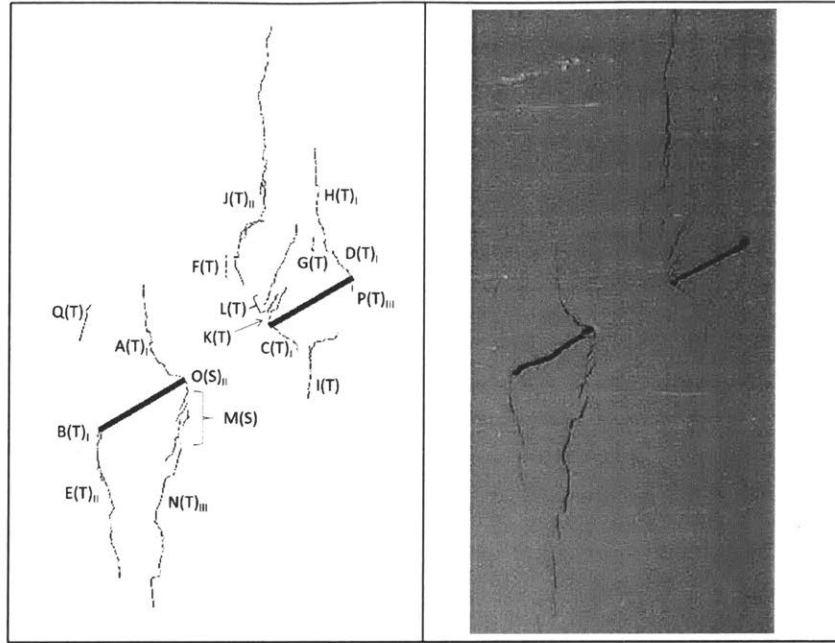


Figure 37 – Sketch 4 as referred to in Figure 32. Left: sketch of cracks. Right: photograph of the specimen at this point in the experiment. Right: frame-time-stress-strain data as well as observations.

Sketch 5 (refer to Figure 38) captures crack initiation and propagation, as well as major tensile opening. It is taken beyond the elastic region of the stress-strain curve in Figure 32. At this point of the test: $t = 328.4$ seconds, $\sigma = 22.5$ MPa, $\varepsilon = 1.36$ %. Tensile crack R(T)_{iii} branches downward from the top tip of Q(T), and then propagates upward, where another tensile crack S(T) branches off. Crack R(T)_{iii} coalesces with the outer tip of the left flaw. Then tensile crack J(T)_{ii} begins significantly opening in tension, followed by tensile crack N(T)_{iii}. Afterwards, shear crack T(S)_{ii} initiates in the zone above and in between the two flaws. More en echelon shear cracks develop at M(S).

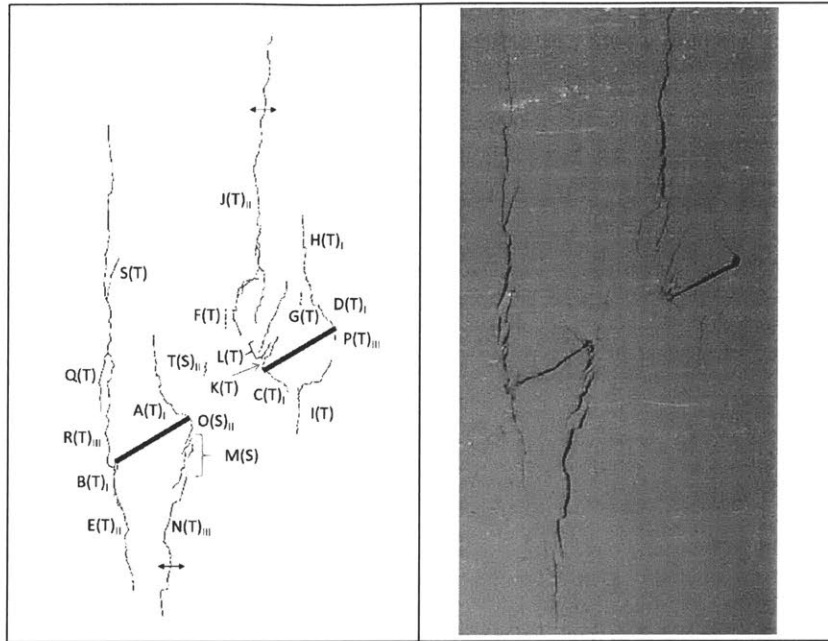


Figure 38 – Sketch 5 as referred to in Figure 32. Left: sketch of cracks. Right: photograph of the specimen at this point in the experiment. Right: frame-time-stress-strain data as well as observations.

Sketch 6 (refer to Figure 39) captures crack propagation, major tensile opening, and coalescence leading to the catastrophic failure of the specimen. It is taken beyond the elastic region of the stress-strain curve in Figure 32. At this point of the test: $t = 328.8 \text{ seconds}$, $\sigma = 22.2 \text{ MPa}$, $\varepsilon = 1.44 \%$. Shear crack $T(S)_{II}$ propagates down and coalesces with $O(S)_{II}$ at the inner tip of the right flaw. Shortly after, $J(T)_{II}$ begins opening in tension followed by the propagation of $T(S)_{II}$ until the point of coalescence at the tip of $J(T)_{II}$ (indicated by a circle on the sketch). Next, tensile crack $U(T)_{III}$ initiates below the outer tip of the right flaw and propagates up until coalescing with $P(T)_{III}$ and down until it opens in tension causing the sample to fail, sliding along $T(S)_{II}$.

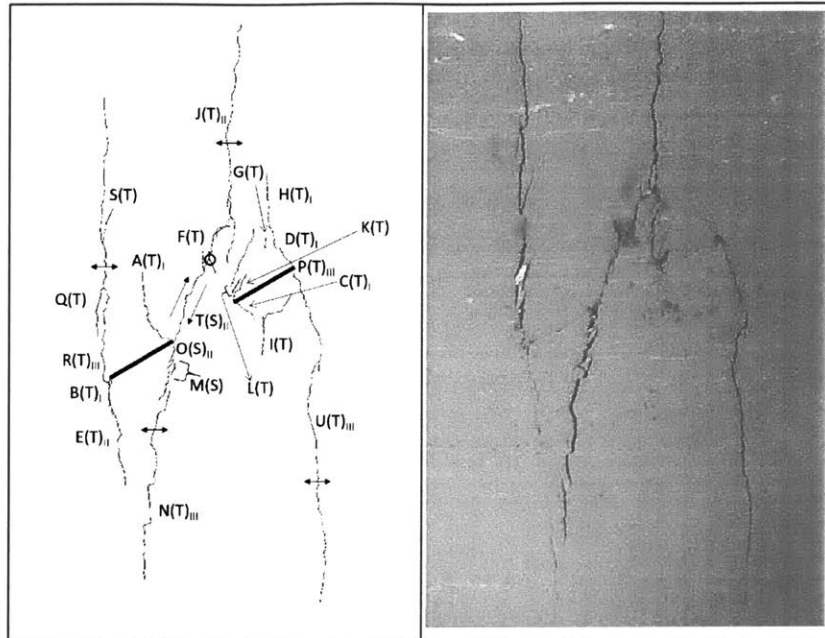


Figure 39 – Sketch 6 as referred to in Figure 32. Left: sketch of cracks. Right: photograph of the specimen at this point in the experiment. Right: frame-time-stress-strain data as well as observations.

This concludes the detailed analysis of the uniaxial compression test on Vaca Muerta shale with a coplanar flaw pair geometry of 2a-30-0 (0). The resulting coalescence was a Category 2: Indirect coalescence by multiple cracks (refer to Figure 29). Table 3 summarizes all key event information associating the tabulated events with the respective stress-strain-time data as well as sketch number.

Table 3 – Summary of all cracks, types, image origin, frame number, initiation time, initiation stress, initiation strain, and sketch.

Crack and Coalescence Type Summary							
Crack Name	Crack Type	HS/HR	Frame	Initiation Time (s)	Initiation Stress (MPa)	Initiation Strain (%)	Sketch
A(T) _I	Type 1 - Tensile	HR	3902	98.44	7.431	0.421	1
B(T) _I	Type 1 - Tensile	HR	3909	112.44	8.398	0.477	
C(T) _I	Type 1 - Tensile	HR	3913	120.44	8.950	0.501	
D(T) _I	Type 1 - Tensile	HR	3918	130.44	9.638	0.539	
E(T) _{II}	Type 2 - Tensile	HR	3943	180.44	13.092	0.712	
F(T)	No Type - Tensile	HR	3954	202.44	14.597	0.786	2
G(T)	No Type - Tensile	HR	3958	210.44	15.142	0.817	
H(T) _I	Type 1 - Tensile	HR	3982	258.44	18.438	0.984	
I(T)	No Type - Tensile	HR	3995	284.44	20.237	1.077	
J(T) _{II}	Type II - Tensile	HR	3997	288.44	20.509	1.089	3
K(T)	En Echelon - Tensile	HR	3998	290.44	20.652	1.096	
L(T)	En Echelon - Tensile	HR	4009	312.44	22.164	1.176	
M(S)	En Echelon - Shear	HR	4013	320.44	22.709	1.207	
N(T) _{III}	Type III - Tensile	HR	4014	322.44	22.845	1.219	
O(S) _{II}	Type II - Shear	HR	4015	324.44	22.967	1.232	4
P(T) _{III}	Type III - Tensile	HR	4016	326.44	23.053	1.263	
Q(T)	No Type - Tensile	HS	-4373	328.22	23.153	1.300	
R(T) _{III}	Type III - Tensile	HS	-4268	328.23	23.160	1.300	5
S(T)	No Type - Tensile	HS	-4023	328.26	23.110	1.300	
T(S) _{II}	Type II - Shear	HS	-2673	328.44	22.515	1.356	
Indirect Coalescence: Category 2		HS	-311	328.76	22.480	1.430	6
U(T) _{III}	Type III - Tensile	HS	-265	328.765	22.300	1.436	
Failure		HS	-174	328.777	22.222	1.436	

3.3.1.2 Stepped Flaw Geometry

This section shows the result from one out of two of the tests conducted on Vaca Muerta shale with stepped flaw pairs with horizontal bedding planes. The tested geometry is 2a-30-30 (0) as shown in Figure 30.

The stress-strain data is presented in Figure 40 with selected events identified by symbols onto the curve. Note, some of the crack labels were omitted due to lack of space on the figure, but are shown in the more detailed frame sketches shown next.

Figure 40 shows an initial non-linear trend indicative of seating effects as well as possible micro-cracks closing in the specimen. The specimen then quickly reaches the linear elastic region where E_{50} was calculated to be 3051 MPa. Note that first crack initiation $A(T)_i$ occurred at 8.55 MPa; at about 32% of maximum stress. The data does not show an obvious yield point prior to fracture. This specimen reached a maximum stress of 23.2 MPa at which point had accumulated a strain of 0.976%. The two flaws coalesced and the specimen failed in quick succession.

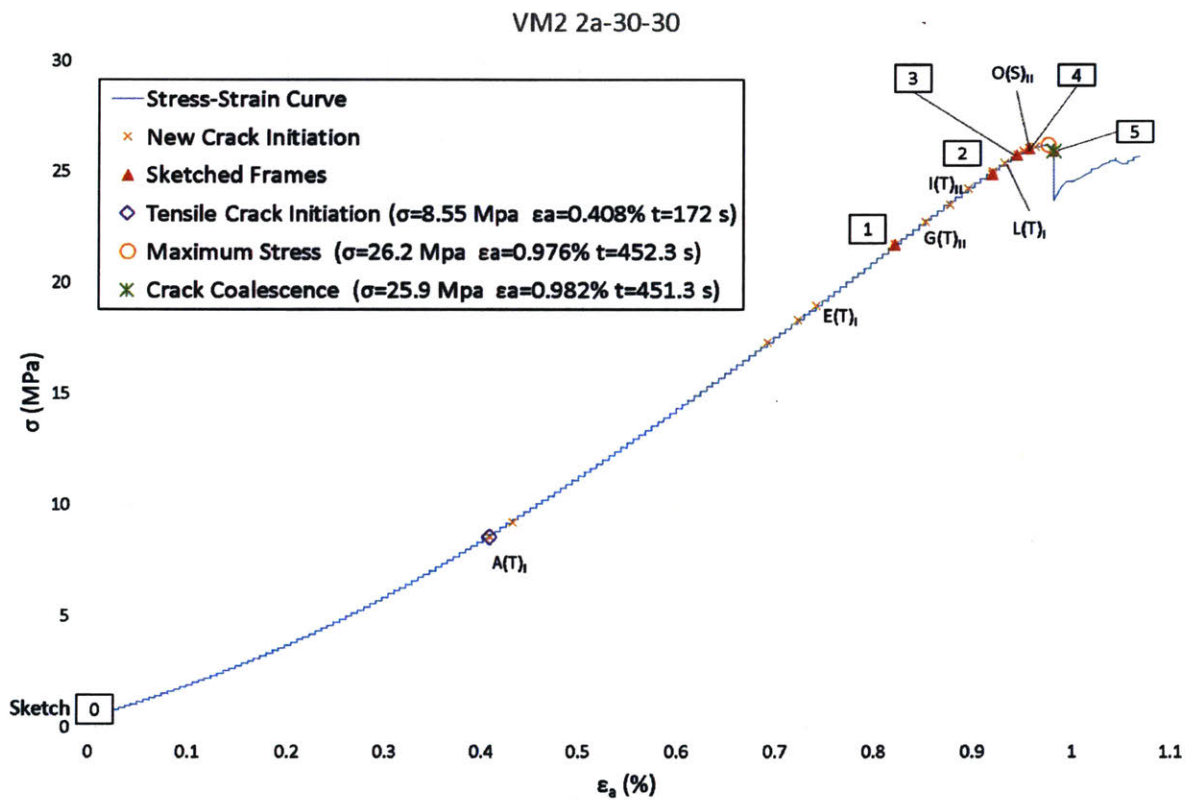


Figure 40– Stress-Strain curve for Vaca Muerta shale with stepped flaw pair subjected to uniaxial loading. Yellow “x” indicates crack initiation. A red triangle indicates a sketched frame while the boxed number indicates sketch number, where the detailed sketches are shown next from Figure 41 to Figure 46. Orange circle indicates maximum stress. Green “*” indicates coalescence stress.

A total of five frames were sketched throughout this test and will be discussed in detail. Sketch 0 (refer to Figure 41) is taken at the beginning of the test to show the initial configuration of the specimen prior

to loading indicated by “0” in Figure 40. The photograph is taken from the high-resolution images. All cracks are labeled alphabetically based on their chronological initiation order.

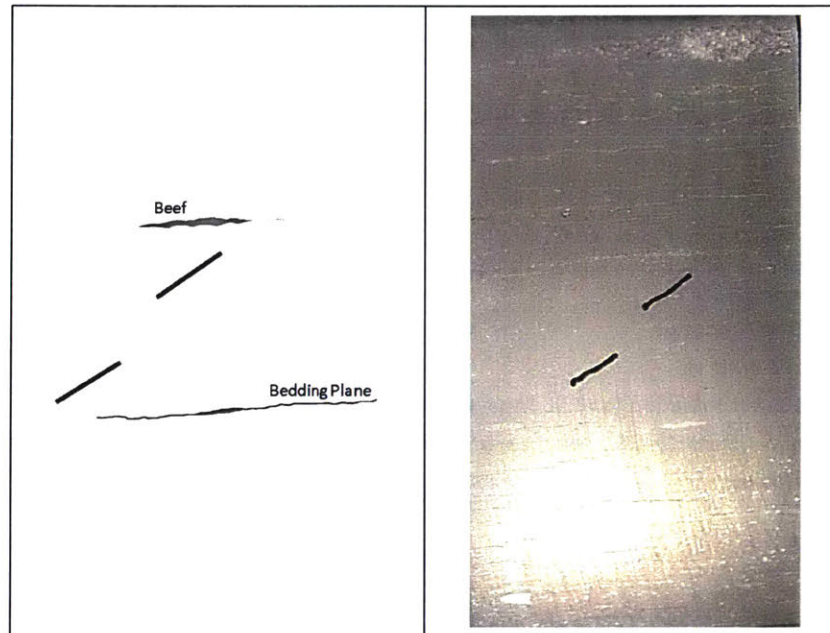


Figure 41 – Sketch 0 as referred to in Figure 40. Left: sketch of cracks. Right: photograph of the specimen at this point in the experiment. Right: frame-time-stress-strain data as well as observations.

Sketch 1 (refer to Figure 42) captures crack initiation. It is taken at 82% of maximum stress and is within the elastic region of the stress-strain curve in Figure 40. At this point of the test: $t = 380 \text{ seconds}$, $\sigma = 21.7 \text{ MPa}$, $\varepsilon = 0.821 \%$. Tensile wing crack A(T)₁ is the first crack to initiate on the inner tip of the left flaw. Next, tensile crack B(T) initiates above the bedding plane, propagating towards it until it arrests at the bedding plane. Then tensile wing crack C(T)₁ initiates at the inner tip of the right flaw, followed by D(T) in between the flaws, and tensile wing crack E(T)₁ on the outer tip of the right flaw. Afterwards, B(T) continues past the bedding plane. Finally, shear crack F(S) initiates in between the flaws.

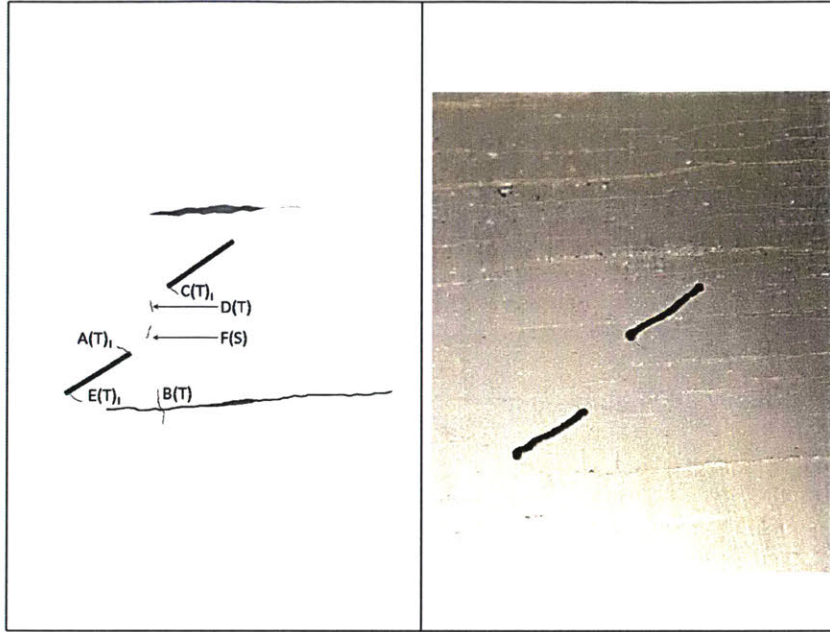


Figure 42 – Sketch 1 as referred to in Figure 40. Left: sketch of cracks. Right: photograph of the specimen at this point in the experiment. Right: frame-time-stress-strain data as well as observations.

Sketch 2 (refer to Figure 43) captures crack initiation and propagation. It is taken at 95% of maximum stress and is within the elastic region of the stress-strain curve in Figure 40. At this point of the test: $t = 430 \text{ seconds}$, $\sigma = 24.9 \text{ MPa}$, $\varepsilon = 0.92 \%$. Tensile crack $G(T)_{II}$ initiates above the outer tip of the left flaw and propagates downward. Then tensile crack $H(T)$ initiates between the flaws, eventually forming an array of an echelon cracks. Tensile crack $I(T)_{II}$ initiates at the bottom of the beef layer and propagates towards $G(T)_{II}$. Finally, tensile crack $J(T)_{II}$ initiates below the outer tip of the left flaw and propagates both up and down.

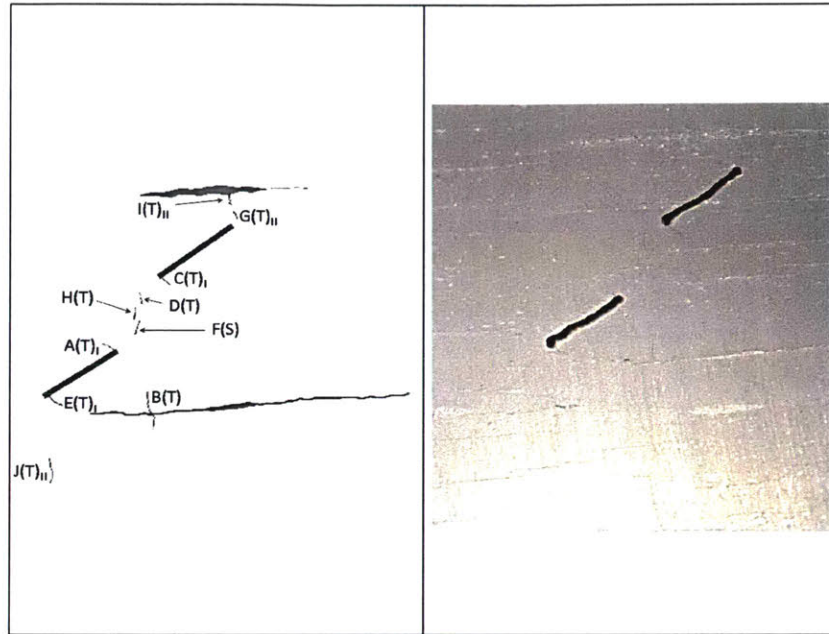


Figure 43 – Sketch 2 as referred to in Figure 40. Left: sketch of cracks. Right: photograph of the specimen at this point in the experiment. Right: frame-time-stress-strain data as well as observations.

Sketch 3 (refer to Figure 44) captures crack initiation and propagation. It is taken at 98% of maximum stress and is towards the end of the elastic region of the stress-strain curve in Figure 40. At this point of the test: $t = 444 \text{ seconds}$, $\sigma = 25.7 \text{ MPa}$, $\epsilon = 0.945 \%$. Tensile crack $K(T)_{II}$ initiates above the beef and propagates towards it. Then tensile crack $L(T)$ initiates below the left flaw's outer tip. Crack $J(T)_{II}$ slightly propagates up and down. Next, crack $I(T)_{II}$ coalesces with crack $G(T)_{II}$. Finally, crack $M(T)$ initiates below the outer tip of the right flaw.

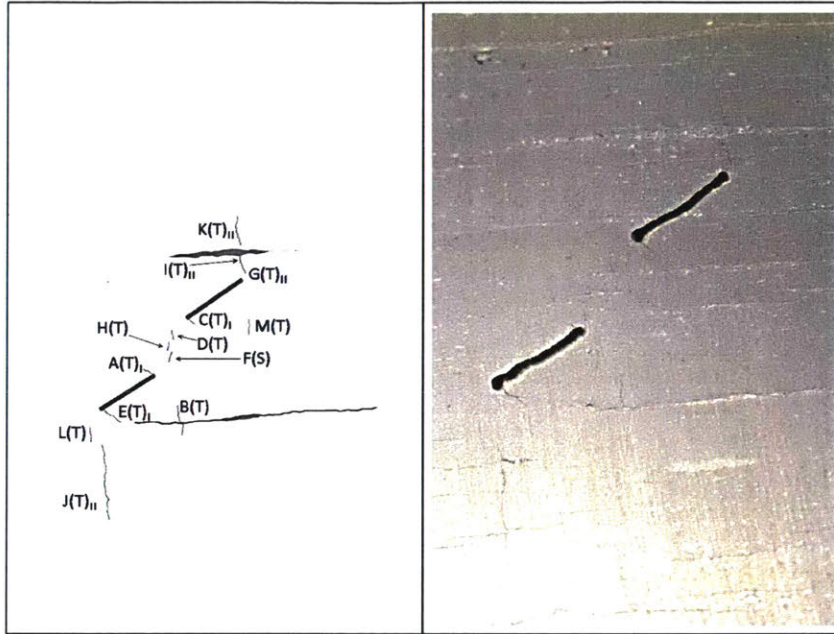


Figure 44 – Sketch 3 as referred to in Figure 40. Left: sketch of cracks. Right: photograph of the specimen at this point in the experiment. Right: frame-time-stress-strain data as well as observations.

Sketch 4 (refer to Figure 45) captures crack initiation and propagation. It is taken beyond the elastic region of the stress-strain curve in Figure 40. At this point of the test: $t = 448 \text{ seconds}$, $\sigma = 26.1 \text{ MPa}$, $\varepsilon = 0.957 \%$. Tensile crack $N(T)_{II}$ initiates near $K(T)_{II}$'s upper tip and propagates down arresting at the beef, also causing $K(T)_{II}$ to close. Next, tensile crack $D(T)$ propagates and coalesces with the inner tip of the right flaw. Then shear crack $O(S)_{II}$ initiates at the inner tip of the left flaw and propagates towards $F(S)$. Afterwards, cracks $J(T)_{II}$ and $N(T)_{II}$ propagate towards the specimen boundaries and the en echelon array $H(T)$ develops further.

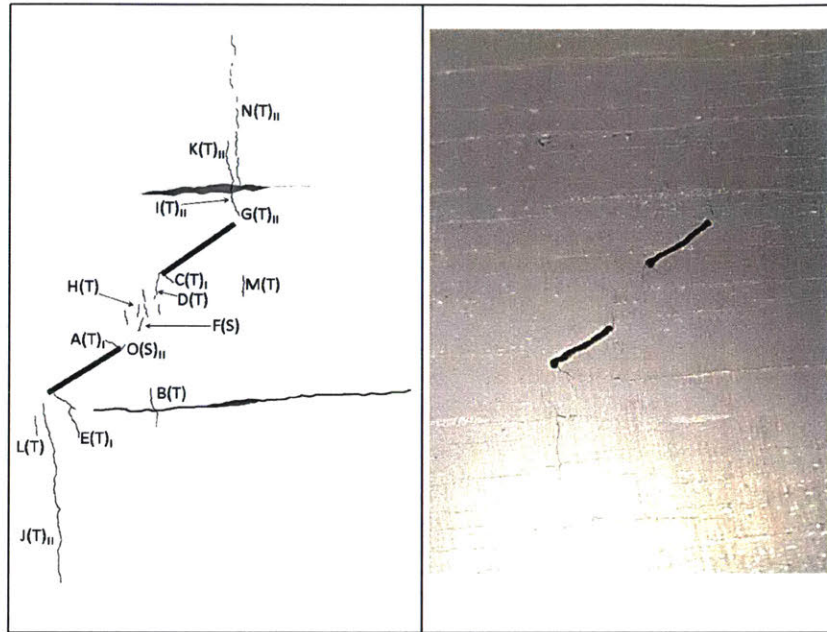


Figure 45 – Sketch 4 as referred to in Figure 40. Left: sketch of cracks. Right: photograph of the specimen at this point in the experiment. Right: frame-time-stress-strain data as well as observations.

Sketch 5 (refer to Figure 46) captures crack propagation, major tensile opening, and coalescence leading to the catastrophic failure of the specimen. It is taken beyond the elastic region of the stress-strain curve in Figure 40. At this point of the test: $t = 452 \text{ seconds}$, $\sigma = 25.92 \text{ MPa}$, $\epsilon = 0.982 \%$. Prior to failure, $O(S)_{II}$ coalesces with $F(S)$, which coalesces with $D(T)$. $D(T)$ became a mixed-mode tensile-shear crack, starting off as a tensile crack and is now on the shear crack plane of $O(S)_{II}$ and $F(S)$. Upon failure, cracks $J(T)_{II}$ and $N(T)_{II}$ open in tension and there is direct coalescence (Category 5) between the two flaws.

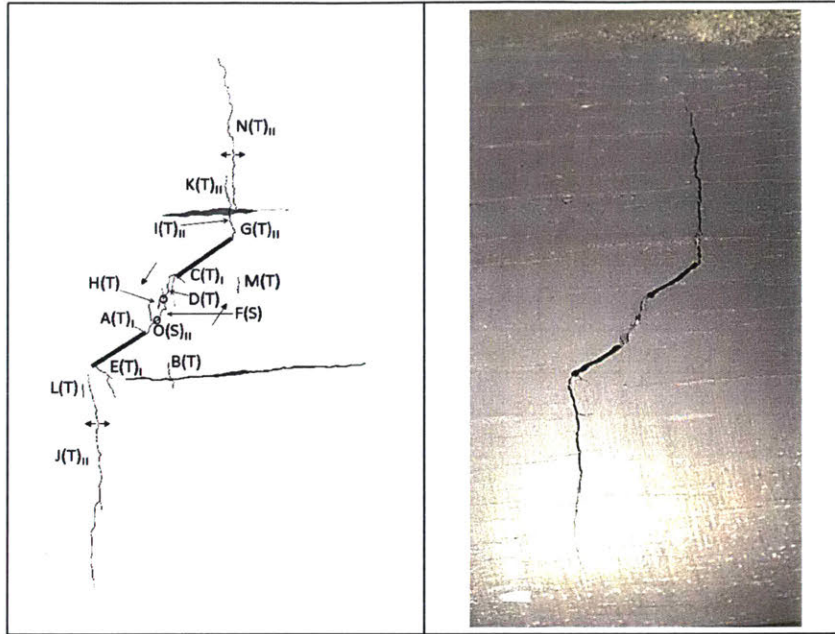


Figure 46 – Sketch 5 as referred to in Figure 40. Left: sketch of cracks. Right: photograph of the specimen at this point in the experiment. Right: frame-time-stress-strain data as well as observations.

This concludes the detailed analysis of the uniaxial compression test on Vaca Muerta shale with a stepped flaw pair geometry of 2a-30-30 (0). The resulting coalescence was a Category 5: one or more Type 2 S crack(s) and Type 2 T crack segments between inner flaw tips, as defined by Wong and Einstein (2009a). Table 4 summarizes all key event information associating the tabulated events with the respective stress-strain-time data as well as sketch number.

Table 4 – Summary of all cracks, types, image origin, frame number, initiation time, initiation stress, initiation strain, and sketch.

Crack and Coalescence Type Summary							
Crack Name	Crack Type	HS/HR	Frame	Initiation Time (s)	Initiation Stress (MPa)	Initiation Strain (%)	Sketch
A(T) _i	Type 1 - Tensile	HR	4114	172.00	8.550	0.408	1
B(T)	No Type - Tensile	HR	4119	182.00	9.179	0.432	
C(T) _i	Type 1 - Tensile	HR	4183	310.00	17.284	0.692	
D(T)	En Echelon - Tensile	HR	4191	326.00	18.287	0.723	
E(T) _i	Type 1 - Tensile	HR	4196	336.00	18.942	0.741	
F(S)	No Type Shear	HR	4218	380.00	21.694	0.821	
G(T) _{ii}	Type II - Tensile	HR	4226	396.00	22.716	0.852	2
H(T)	En Echelon	HR	4232	408.00	23.476	0.877	
I(T) _{ii}	Type II - Tensile	HR	4238	420.00	24.216	0.896	
J(T) _{ii}	Type II - Tensile	HR	4243	430.00	24.859	0.920	3
K(T) _{ii}	Type II - Tensile	HR	4244	432.00	24.976	0.920	
L(T)	No Type - Tensile	HR	4247	438.00	25.363	0.933	
M(T)	No Type - Tensile	HR	4250	444.00	25.743	0.945	4
N(T) _{ii}	Type II - Tensile	HR	4251	446.00	25.933	0.951	
O(S) _{ii}	Type II - Shear	HR	4252	448.00	26.058	0.957	5
Direct Coalescence: Category 5		HS	-9151	451.328	25.920	0.982	
Failure		HS	-9151	451.328	25.920	0.982	

3.3.2 Comparison

The objective of this study is to see how the Vaca Muerta Shale crack behavior compares to Opalinus Shale. Due to the scarcity of Vaca Muerta Shale samples, it would be ideal if a substitute can be used for future studies on a more abundant material, such as Opalinus Shale. In this section, the two materials are compared.

Table 5 provides a summary of the observed coalescence behavior observed in the Opalinus Shale specimens tested by Morgan (2015) and the Vaca Muerta Shale specimens tested in this study. Note the numbers in parenthesis are a ratio of how many specimens were of that specific category to the total

number of specimens with that geometry. For example: a total of four Opalinus Shale with the geometry 2a-30-30 (0) were tested, three of these resulted in a category 5 and one was a category 4 (Figure 29).

Table 5 – Summary of the crack coalescence behavior, as defined by Wong and Einstein (2009b), observed in Opalinus Shale and Vaca Muerta Shale with the flaw geometries described in the table.

Geometry	Opalinus Shale	Vaca Muerta Shale	Correspondence
2a-30-0 (0)	Indirect – 2 (3/3)	Indirect – 2 (1/1)	Corresponds well
2a-30-30 (0)	Direct – 5 (3/4)	Direct – 5 (1/2)	Corresponds well
	Direct – 4 (1/4)	Indirect – 2 (1/2)	

Starting with the 2a-30-0 (0) flaw geometry, all Opalinus Shale test specimens showed similar Category 2 - Indirect Coalescence. The VM3-2a-30-0 (0) also showed Category 2 – Indirect Coalescence, similar to that observed in the Opalinus Shale (refer to Figure 47). The conclusion is that the Vaca Muerta coalescence behavior corresponds well with what was observed in Opalinus Shale of the same flaw geometry.

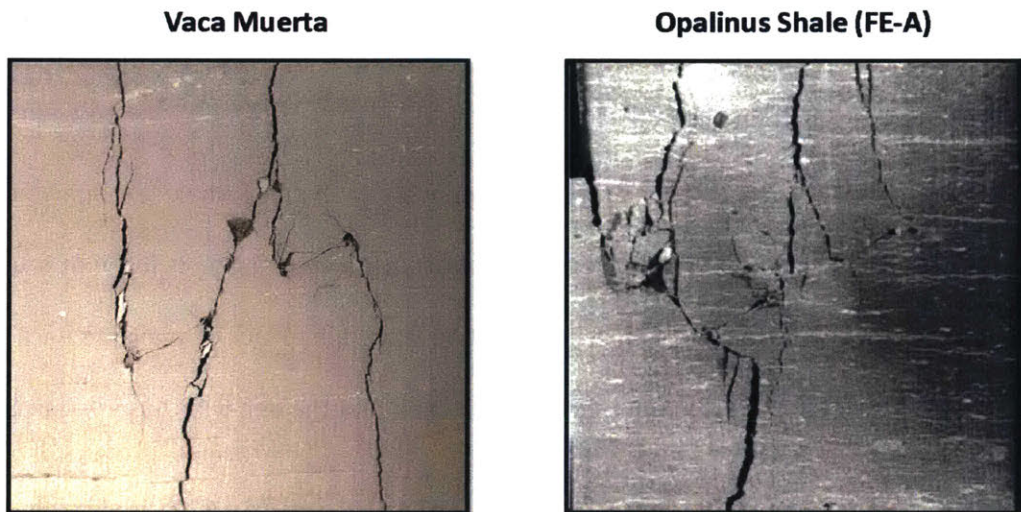


Figure 47 – Comparison of coalescence behavior observed in Vaca Muerta and Opalinus shales, both showing Category 2: indirect coalescence by multiple cracks.

Next, the 2a-30-30 (0) flaw geometry is compared. Three out of four Opalinus Shale test specimens showed Category 5 – Direct Coalescence behavior. VM1-2a-30-30 (0) showed Category 2 – Indirect Coalescence crack behavior (for analysis, see Appendix A1). As mentioned previously, it was suspected that the load frame testing this specimen was inducing shear rather than vertical uniaxial loading conditions. When VM2-2a-30-30 (0) was tested with the 200-KIP load frame, it showed coalescence behavior that corresponded with what was observed in Opalinus Shale test specimens of the same flaw geometry (refer to Figure 48).

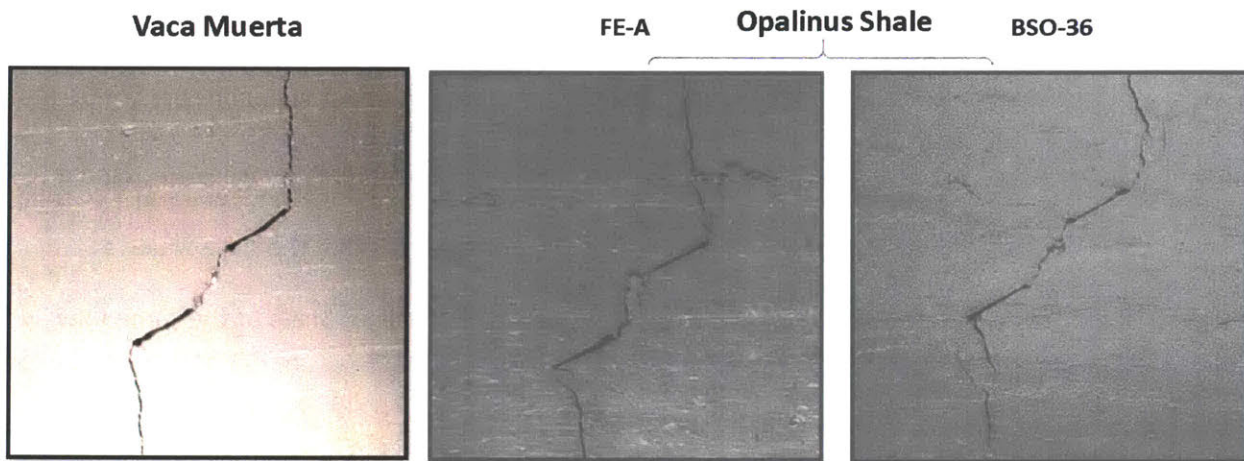


Figure 48 – Comparison of coalescence behavior observed in Vaca Muerta and Opalinus shales, both showing Category 5: one or more Type 2 S crack(s) and Type 2 T crack segments between inner flaw tips.

Of course, one Vaca Muerta Shale test specimen corresponding to Opalinus Shale test specimen’s crack coalescence behavior is not enough to conclude correspondence. Repeating tests three or four time, such as what Morgan did with Opalinus Shale, could not be done due to lack of available Vaca Muerta Shale core samples. However, it can be optimistically assumed that the behavior observed in Opalinus Shale may be extended to the Vaca Muerta Shale.

4. Hydraulic Fracture Experiments

In Chapter 3, the “dry” fracture process in Vaca Muerta shale corresponds well to that which was observed in Opalinus shale. This means that the fracture behavior observed in Opalinus shale can be extended to Vaca Muerta shale. From this point on, the material tested is Opalinus shale (BSO-36) where specimens are subjected to a constant uniaxial stress and an individual flaw is pressurized as shown in the center sketch of Figure 49. Through this loading scheme, the behavior of a pressurized flaw propagating a hydraulic fracture can be observed. The aim is to see what effect the presence of a second (non-pressurized) flaw will have on the propagating hydraulic fracture’s behavior at various flaw geometries. The following section will discuss the experimental setup, which was developed, as well as present testing results.

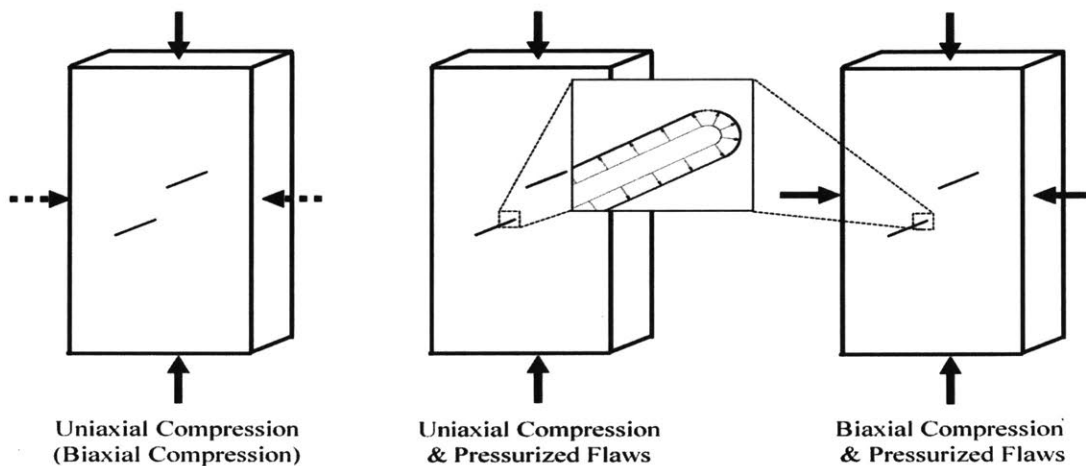


Figure 49 – Planned testing procedure for experimental results. (Gonçalves da Silva, 2016)

4.1 Experimental Procedure

The objective of this experiment is to observe crack-initiation and -propagation of a hydraulically induced fracture and its interaction with a pre-existing non-pressurized flaw, as well as associating the observed behavior with the pressure-time data. New equipment was developed to pressurize a single flaw.

4.1.1 Test Setup

Keeping the objective of visually capturing the fracture behavior in mind, the experimental setup becomes fairly complex. The shale specimen is prepared as mentioned before. The vertical load application is the same, as well as the high speed and high resolution cameras' setup. However, a setup for hydraulic pressurization of a single flaw in a way that can be captured visually had to be introduced. The entirety of the setup is shown in one schematic in Figure 50. The following section discusses the components involved in this experiment. The flaw pressurization device is modified from the design originally developed at MIT by Gonçalves da Silva (2016), which applies hydraulic pressure only in the flaw.

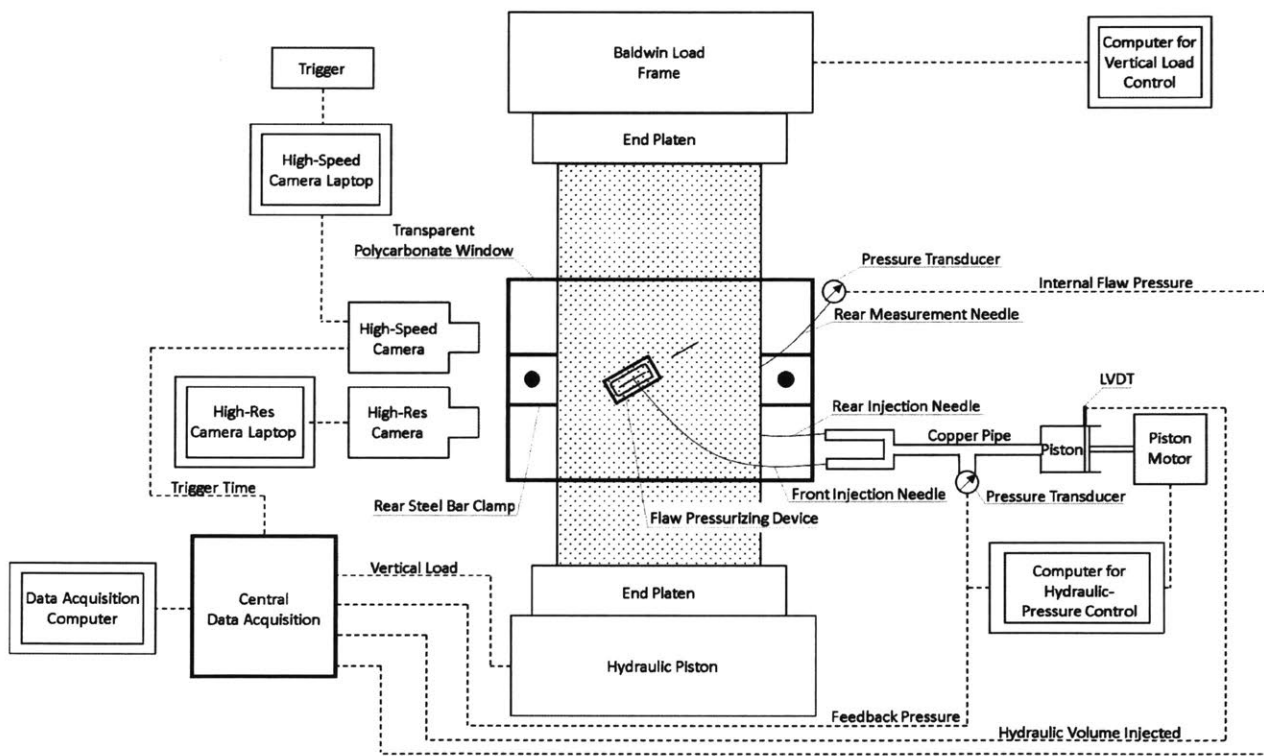


Figure 50 - Experimental setup for uniaxial compression tests with hydraulic fracturing on shale specimens. The shale specimen has the flaw pressurizing device clamped externally by polycarbonate window from the front and a steel bar from the rear. The central data acquisition system collects vertical load, feedback pressure, hydraulic volume injected, internal flaw pressure, and trigger time data.

4.1.1.1 Flaw Pressurizing Device Components

The flaw must be sealed from the front and rear of the specimen while being fully transparent from the front for observations. A three-dimensional rendering of the flaw pressurizing device is shown in Figure 51 (front view) and Figure 52 (rear view).

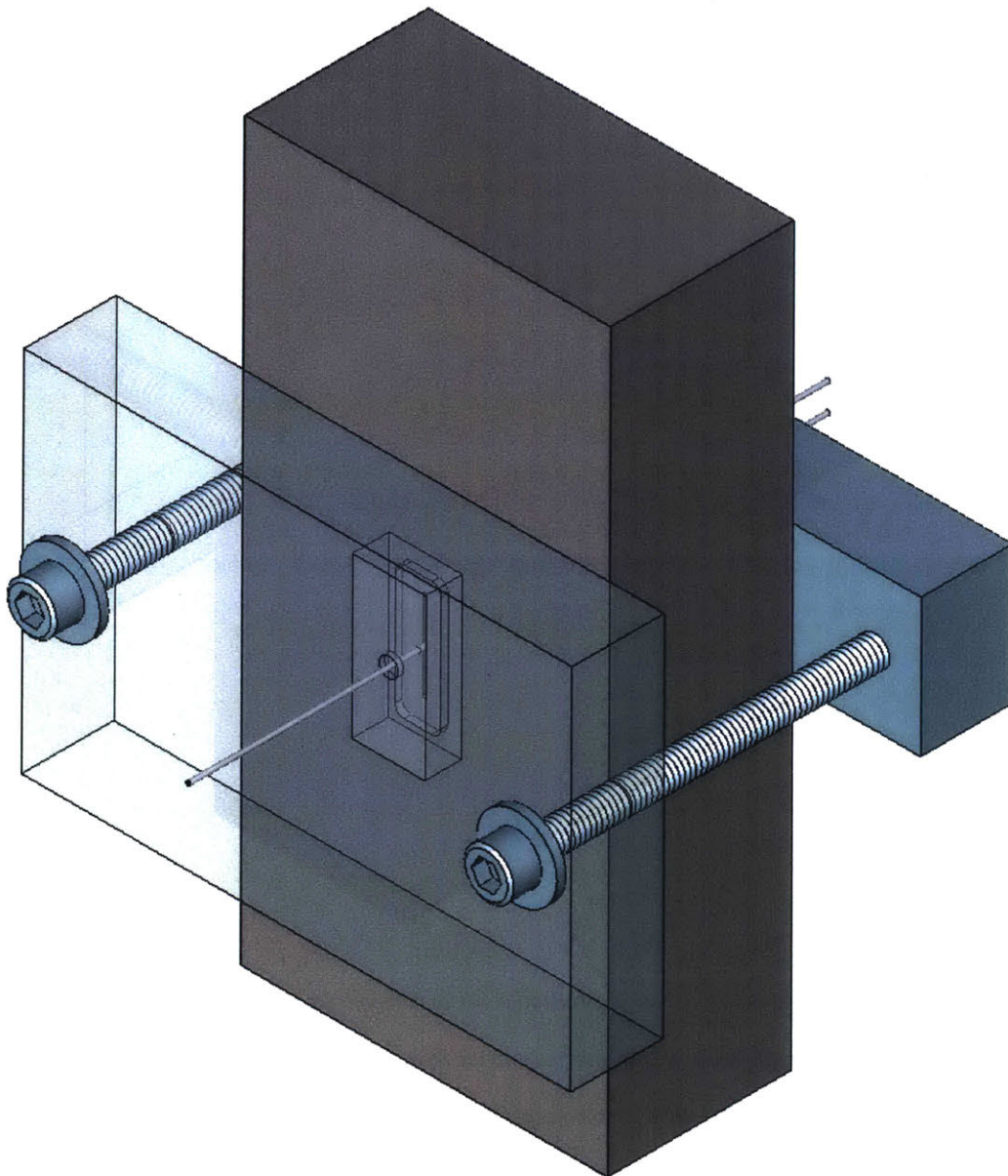


Figure 51 – Three-dimensional rendering of flaw pressurization device components (oblique front view) showing transparent polycarbonate window and flaw seal with front injection needle inserted into flaw. Note: example specimen in figure has a single vertical flaw. Other geometries possible by simply rotating flaw seal to same orientation of the pressurized flaw.

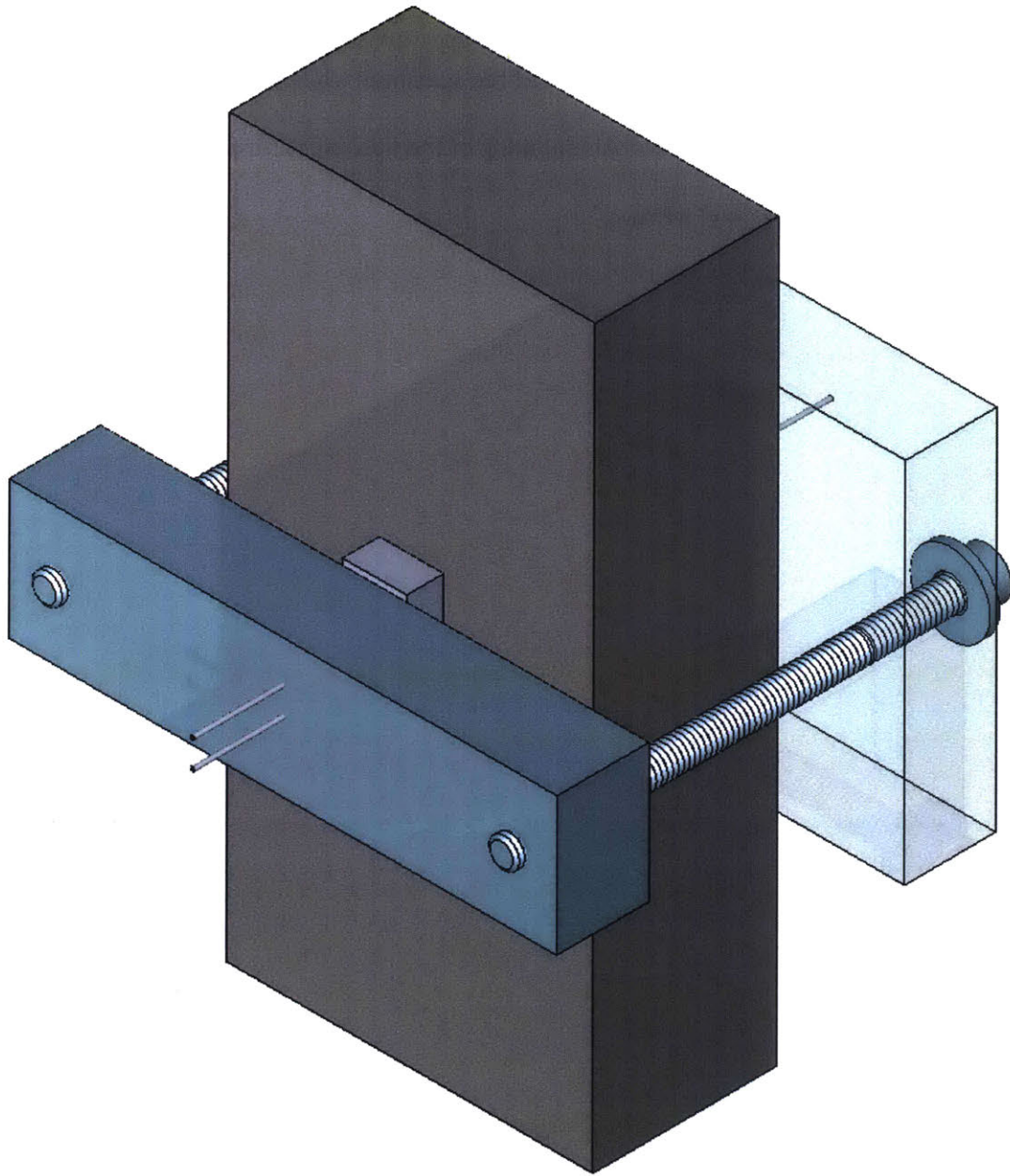


Figure 52 – Three-dimensional rendering of flaw pressurization device components (oblique rear view). Transparency is not a priority for the rear components. Both needles are inserted into the flaw. The bottom needle is the rear injection needle (runs through center of steel bar and flaw seal) while the top needle is the pressure measurement needle (0.15" away from injection needle). For other flaw orientations, the flaw seal is rotated and holes are drilled into the steel bar to accommodate the pressure measurement needle.

The following is a description of the individual components of the pressurizing device setup, starting on the specimen surface outward, and starting with the front side of the specimen:

1. Transparent Silicon Rubber Membranes:

Directly pressed against the flaw is a piece of 0.63" (1.6 mm) thick transparent silicon rubber sheet (Figure 53). This transparent sheet is laser-cut to the required dimensions to seal the flaw and fit in a housing. It also has a single laser-cut hole for the injection needle. This transparent silicon rubber membrane fits into the transparent polycarbonate housing and allows one to visually capture events that may occur behind it on the front face of the specimen.

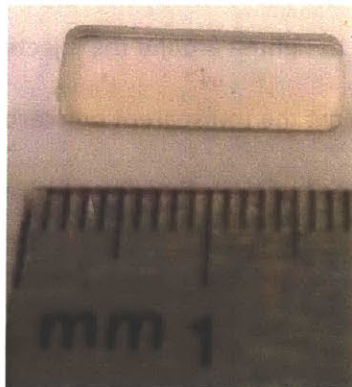


Figure 53 - Transparent silicon rubber membrane after laser-cutting from 1.6 mm thick sheet. This membrane is pressed against the specimen surface with the front injection needle passing through its center hole into the flaw. The membrane is optically transparent.

2. Transparent Polycarbonate Housing:

The front housing is machined out of transparent polycarbonate into a rectangular prismatic block (Figure 54). A hole is drilled into the middle of the block for the injection needle. On the specimen-facing side, a recess is machined into the block to house the transparent silicon rubber membrane. On the opposite side, a small circular recess is machined around the hole into the block as a housing for an O-ring seal. After machining, the housing is no longer transparent, so it is vapor polished to reduce its surface roughness and restore its clarity to an optical finish.

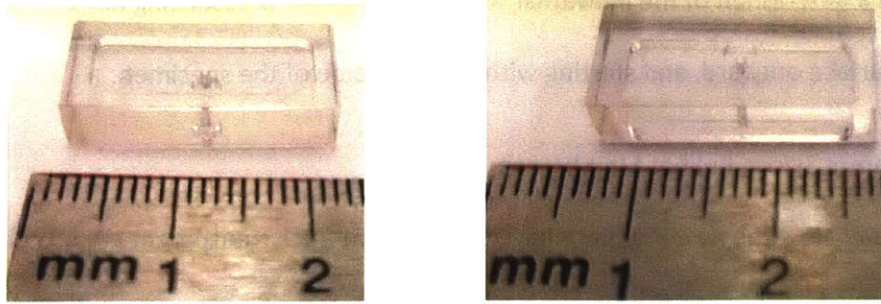


Figure 54 – Transparent polycarbonate housing after machining followed by vapor polish. Left: specimen-facing side (front) of housing where transparent membrane fits in recess. Right: outside-facing side (back) of housing where O-ring seal fits in recess.

3. O-ring Seal

An O-ring seal (Figure 55) is placed into the circular recess on the outside of the transparent polycarbonate housing. Its purpose is to tighten around the injection needle as the transparent polycarbonate window is pressed against the transparent polycarbonate housing. It prevents the injection needle from moving, as well as hydraulic fluid from leaking during pressurization.



Figure 55 - O-ring seal which sits in the circular recess on the back side of the housing. When pressure is applied, the O-ring seals around the injection needle, preventing needle movement or leakage.

4. Transparent Polycarbonate Window

The final component on the front of the specimen is the transparent polycarbonate window (Figure 56). It is a 1/2" thick sheet of polycarbonate, which is machined to have a width greater than the specimen width. An injection needle sized hole is drilled into the window to allow the injection needle to slide through the other components and into the flaw. Two screw sized holes are drilled near the side edges of the window for screws to slide through and screw into the rear steel clamping bar. The window serves as the front clamp, holding the housing down onto the specimen surface.

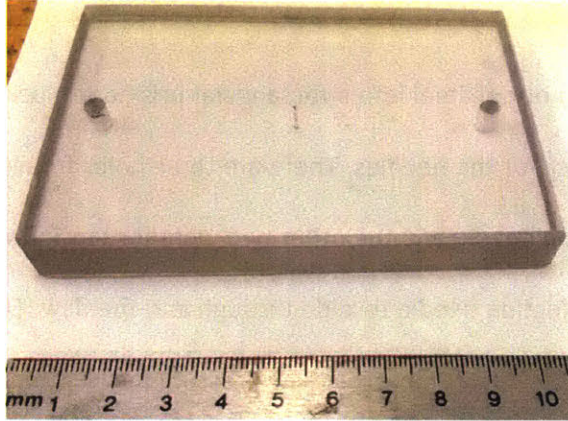


Figure 56 - Transparent polycarbonate window machined to be greater than the specimen width that allows one to see the specimen. It acts as the front external clamp and holds the membrane and housing against the specimen face.

Next are the components on the rear of the specimen, where transparency is not required:

5. Silicon Rubber Membrane:

Directly pressed against the flaw on the rear of the specimen is a 0.063" (1.6 mm) thick silicon rubber sheet (Figure 57). In the same manner as the front seal, it is laser cut to the same dimensions to seal the flaw and fit in a housing. A hole is laser-cut in the middle for the second injection needle. A second hole is laser-cut for a third needle. This silicon rubber membrane fits into the steel housing.

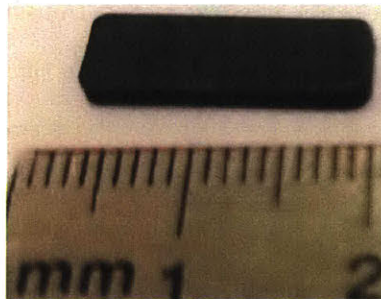


Figure 57 - Silicon rubber membrane after laser-cutting from 1.6 mm thick sheet. This membrane is pressed against the backside of the specimen. The central hole is for the rear injection needle and the offset hole is for the pressure measurement needle.

Transparency is not needed.

6. Steel Housing:

The rear housing is machined out of steel into a rectangular prismatic block (Figure 58). Three through-holes are drilled into the block for the needles. There are three holes from the original design, where the middle hole is for the injection needle and the other two were for tension wires. However, now the middle hole is for the rear injection needle to slide through into the flaw. The second hole is for a third needle to slide through into the flaw for internal flaw pressure measurements. The last hole is not currently in use, but may be an access point into the flaw if needed. On the specimen-facing side, a recess is machined into the block to house the silicon rubber membrane. On the opposite side, three small circular recesses are machined around each through-hole, into the block, as housings for O-ring seals for each needle.

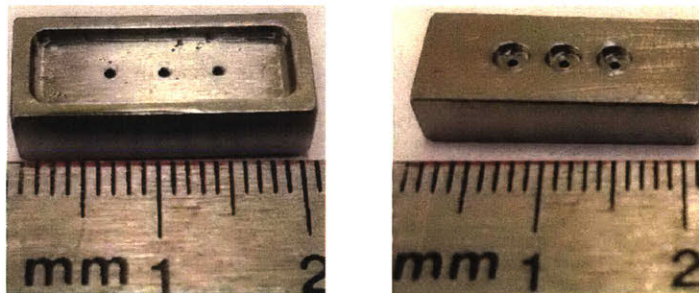


Figure 58 – Steel housing from original design by Gonçalves da Silva (2016) with three holes. Only two are used for this modified design. Left: specimen-facing side (front) of housing where membrane fits into recess. Right: outside-facing side (back) of housing where O-ring seals fit in recesses.

7. O-ring Seal(s):

O-ring seals (Figure 55) are placed into the circular recesses on the outside of the steel housing. Their purpose is to tighten around a needle as the steel block presses against the steel housing. They prevent their respective needles from moving, as well as hydraulic fluid from leaking throughout pressurization.

8. Steel Plate:

This component is from the original design. It is a rectangular prismatic block machined from steel with three holes (Figure 59). It serves the same function as the window on the front of the specimen: to push on the O-ring seals and have them tighten around the needles. In this application, only two of the three holes are used, but access to the third is available.

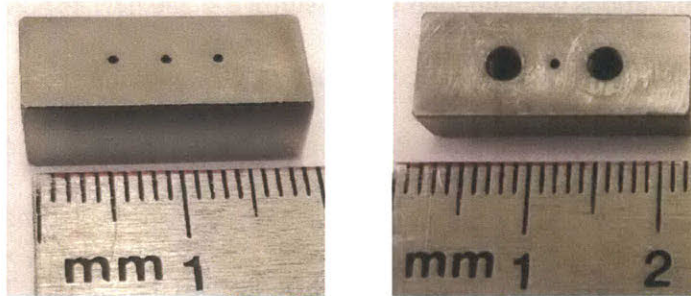


Figure 59 – Steel plates with three needle sized holes from original design by Gonçalves da Silva (2016). Only two holes are used for this modified design. Left: specimen-facing side (front) of plate where it presses against the O-ring and steel housing. Right: outside-facing side (back) of plate where it is supported by the rear steel bar clamp.

9. Steel Bar Clamp:

The rear steel bar clamp (Figure 60) is a steel bar machined with access holes for the needles to pass through for various flaw geometries. Threaded screw holes are also machined into it to tie the device together.

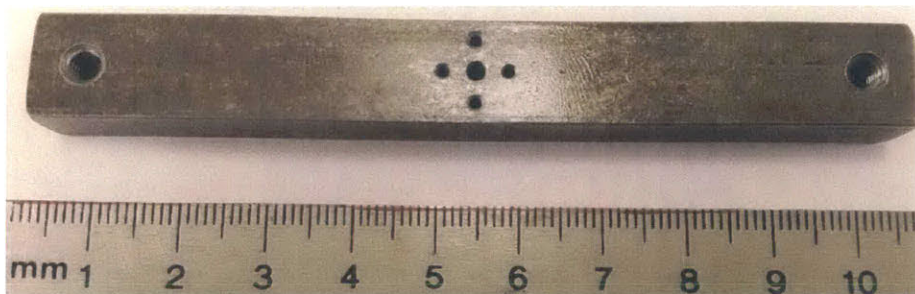


Figure 60 – Rear steel bar clamp machined to be greater than the specimen width and threaded holes to receive screws from front transparent polycarbonate window. It acts as the rear external clamp and holds the membrane and housing against the

specimen face. Various holes drilled around center hole to give the flow pressure measurement needle access to the other components and the flaw.

4.1.1.2 Hydraulic Pressure Apparatus Components

The apparatus used to apply hydraulic pressure to the specimen was developed by Gonçalves da Silva (2016) at MIT. It was originally designed to apply hydraulic pressure to a large pressure enclosure on granite specimens. Modifications were needed to pressurize a single flaw instead of the enclosure device used by Gonçalves da Silva (2016). A T-connection (see Figure 50) was prepared at the end of the copper pipe to distribute the flow of hydraulic fluid to two injection needles, one injecting from the front side of the specimen, and the other from the back of the specimen. Another modification done to the apparatus was tuning its PID (Proportional-Integral-Derivative) parameters. The components of the apparatus are described below.

1. Injection Needles

There are two injection needles (Figure 61). The front injection needle goes through the transparent polycarbonate window, O-ring seal, transparent polycarbonate housing, transparent silicon rubber membrane, and into the flaw. The rear injection needle goes through the steel bar clamp, steel plate, O-ring seal, steel housing, silicon rubber membrane, and into the flaw. The other end of each needle ties into the copper pipe T-connection (refer to Figure 50).

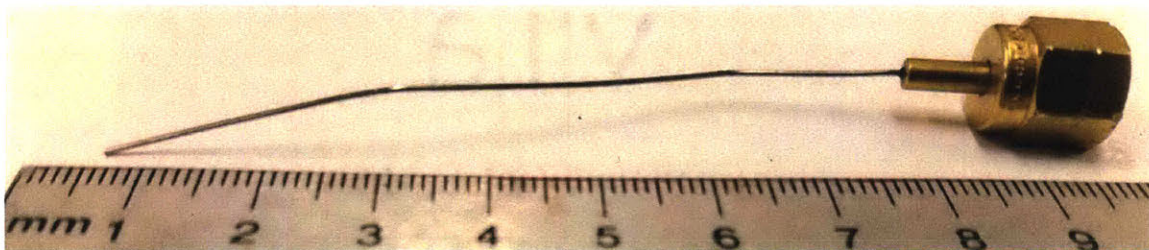


Figure 61 - Picture of injection needle. Needle tip passes through pressurization device components and into the flaw. Opposite end screws into copper pipe.

2. Copper Pipe

The copper pipe transmits hydraulic fluid from the piston to the injection needles into the flaw.

3. PVA Pressure Transducer (Feedback)

A pressure transducer is located at the end of the copper pipe. It measures the pressure at the piston outlet. This pressure measurement reading goes into the PID feedback control algorithm. This pressure transducer is also connected to the central data acquisition system (refer to Figure 50).

4. Pressure Volume Actuator (PVA)

The PVA contains the hydraulic fluid and is driven by a motor. Prior to a test, it is cycled to release any air trapped in the system. Pressure at the outlet of the PVA is used as the feedback for the PID control algorithm to pressure-control the experiments.

5. Linear Variable Differential Transformer (LVDT)

An LVDT is attached to the PVA measuring its displacement. With the piston's known dimensions, the volume associated with the movement of the piston is calculated. During a test, the movement of the piston is calculated as the volume injected into the flaw. This LVDT is connected to the central data acquisition system (refer to Figure 50).

6. Motor

The motor drives the piston. It receives an output signal from the PID control algorithm and injects fluid to achieve the desired pressure.

7. Computer for Hydraulic Pressure Control

This computer has a PID control algorithm coded for hydraulic pressure control. The measured PVA pressure goes into the PID control algorithm feedback loop which, in turn, produces an output signal that controls the displacement of the piston to produce the desired hydraulic pressure.

8. Measurement Needle

The third needle is inserted into the flaw from the rear-side of the specimen. Initially, it is open to atmospheric pressure serving as a bleed hole. The hydraulic fluid flows into the flaw from the two injection needles, and displaces air out of the bleed hole. Then the hydraulic fluid starts flowing out of the measurement needle, the only opening in the system. Once constant-pressure flow is established, it is assumed that the flaw is fully saturated with hydraulic fluid. Then the flaw pressure transducer is attached, closing the system. Special precautions have to be taken to minimize the possibility of air entering the system during the process of attaching the needle to the pressure transducer. The flaw pressure transducer is attached, the needle acts as a probe, allowing one to record internal pressure of the flaw throughout the pressurization process.

9. Flaw Pressure Transducer

This pressure transducer gives a more accurate measurement of hydraulic pressure inside the flaw than the feedback pressure transducer, especially during fracture initiation (breakdown pressure) and propagation. This pressure transducer is connected to the central data acquisition system (refer to Figure 50).

4.1.1.3 PID-Control Feedback Loop

The following section will discuss the PID control algorithm. First, a brief description of PID control theory is given and the PID parameters are introduced. Next, the major characteristics of PID algorithm response are described. Then parameter tuning guidelines are given, followed by the newly tuned PID parameters and their resulting pressure response.

PID-Control Theory

A proportional-integral-derivative (PID) controller algorithm is coded into the hydraulic pressure-control computer. The user sets the desired target pressure. The algorithm reads the current measured

pressure from the PVA pressure transducer (Feedback Pressure) located at the piston outlet and computes the error: $e = Target\ Pressure - Feedback\ Pressure$. After going through the PID controller algorithm, an output signal u is computed and sent to the motor. The motor drives the piston and a new feedback pressure is measured from the PVA pressure transducer. The loop is repeated as the PID controller algorithm reduces the error over time. The output signal is computed each time according to the following equation:

$$u(t) = k_p \cdot e(t) + k_i \cdot \int_0^t e(\tau) d\tau + k_d \cdot \frac{de(t)}{dt} \dots\dots\dots(4),$$

where k_p , k_i , and k_d are constants multiplied by the magnitude of the error, the summation of the errors, and the slope of the errors, respectively, at time t . This closed-loop feedback process is summarized in Figure 62.

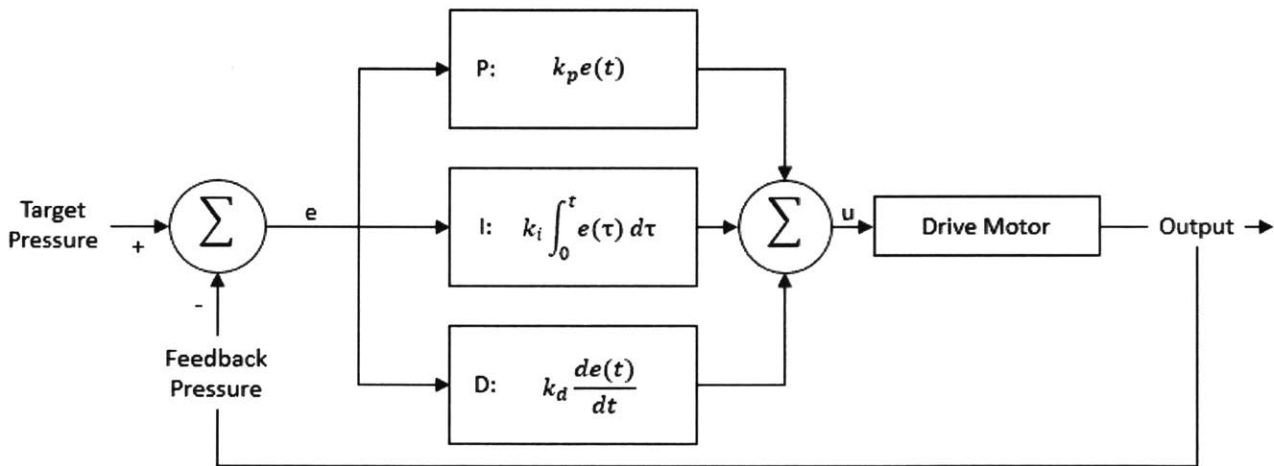


Figure 62 – Schematic of closed-loop feedback process of a PID controller.

The algorithm in Figure 62 was coded as:

$$u(t) = k_1 \cdot e_i + k_2 \cdot (e_i - e_{i-1}) + k_3 \cdot (\sum_{i=1}^n k_4^{n-i} \cdot e_i) \dots\dots\dots (5),$$

where k_1 corresponds to k_p , k_2 corresponds to k_d , k_3 & k_4 correspond to k_i , i is the iteration variable that represents time in the loop, and n is the maximum number of iterations until the present time. The PID parameters that were tuned are k_1 , k_2 , k_3 , and k_4 .

Characteristics and Effects

There are four major characteristics influenced by the PID algorithm and its parameters (Zhong, 2006).

1. Steady-state error (offset), which is the difference between the steady-state output and the desired output.
2. Overshoot, which is how much the peak output is higher than the steady-state output.
3. Rise time, which is the time it takes for the output to rise from 10% to 90% of its steady-state output.
4. Settling time, which is the time it takes for the system to converge to its steady-state output.

The following table summarizes the effects that increasing each PID parameter has on these characteristics:

Table 6 - Effects of increasing PID parameters (Zhong, 2006)

Response to increasing:	Steady-State Error	Overshoot	Rise Time	Settling Time
k_p	↓	↑	↓	No Effect
k_i	Eliminate	↑	↓	↑
k_d	No Effect	↓	No Effect	↓

PID Tuning Guidelines

Certain guidelines are set to efficiently tune the PID parameters depending on the desired output. This is usually done by starting with a P-controller (by tuning k_p and setting $k_i=k_d=0$). After tuning the P-

controller, k_i can be introduced in the equation to tune the PI-controller (by tuning k_p and k_i and setting $k_d=0$). After tuning the PI-controller, k_d can be introduced to tune the PID-controller (by tuning all parameters). This process is explained in further detail below.

For this research, the most important criterion is to minimize overshoot to avoid accidental fracture of the specimen. The PID parameters are adjusted by trial and error. The first step is to determine a value for k_1 (k_p) while keeping $k_2 = k_3 = k_4 = 0$ (starting with P-controller). The proportional term, k_1 , chosen will have a high overshoot and some steady-state error. The objective is to have a k_1 value that yields a ballpark estimate of the desired overshoot and steady-state error that will later be eliminated.

Then k_i is introduced by choosing values for k_3 and k_4 . The integral terms, k_3 and k_4 , aim to eliminate the steady-state error and reduce the overshoot.

Finally, k_d is introduced by choosing values for k_2 . The derivative term aims at reducing overshoot and settling time. Depending on the desired objective, one can manipulate the output signal using these guidelines to reduce, for instance, overshoot and/or steady-state error.

PID Manual Tuning

As mentioned previously, this hydraulic fracturing apparatus was used for the research done on hydraulic fracturing of granite using the enclosure device (Gonçalves da Silva, 2016). In that case, the entire front face of the specimen, the flaws, and the entire back face of the specimen were encased in the enclosure and subjected to hydraulic pressure. An example of the pressure response observed for that setup is seen in Figure 63. As seen in the figure, the pressure (red curve) is increased in 0.5 MPa increments and held for some time at each increment. The pressure converges to the target pressure with no overshoot and minimum offset.

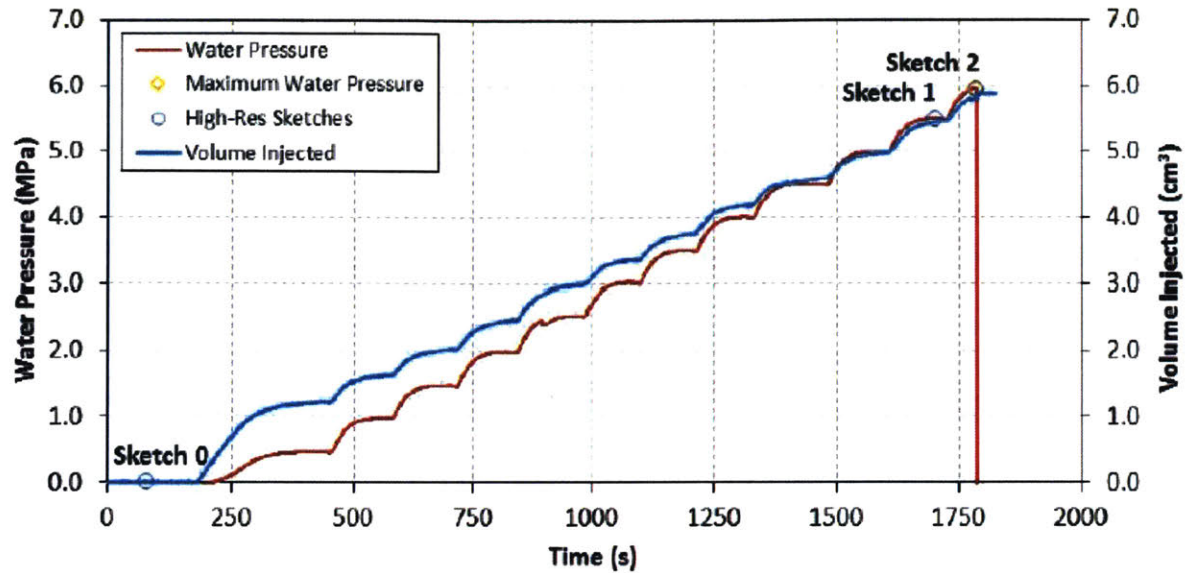


Figure 63 - An example of the pressure response (red curve) in a granite hydraulic fracture experiment using the enclosure device. The target pressure is increased at 0.5 MPa increments. Pressure converges to target pressure with no overshoot and minimum offset.

For this research, the pressurization apparatus was modified to pressurize only a single flaw. In other words, the volume that is being pressurized is greatly reduced, which affects the response of the system. The result of applying the same PID parameters used on the modified flaw pressurizing device is shown in Figure 64. The pressure response of the system shows overshoot, offset, and ringing, all of which seem to become more pronounced as the target pressure is increased.

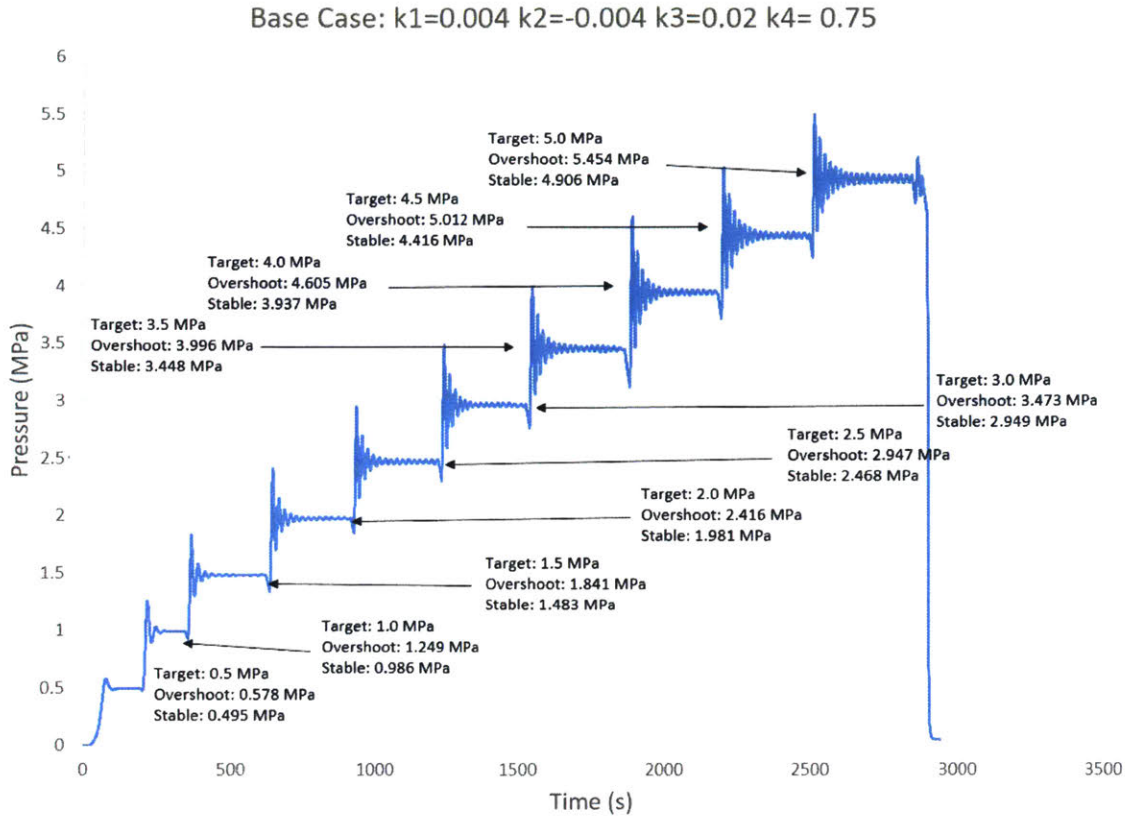


Figure 64 – Result of PID algorithm prior to any tuning. PID parameters are same as those used by Gonçalves da Silva (2016) in granite hydraulic fracture experiments using enclosure device. When applied to new pressurizing device on a single flaw only, overshoot, offset, and ringing is observed and is more pronounced as pressure is increased.

By following the previously mentioned guidelines, and after many iterations, a new set of PID parameters were determined for the modified apparatus. For convenience and availability, the tuning trials were done on a 3/8" thick acrylic specimen with a hairline crack laser-cut into it (Figure 65). The volume of this flaw is not equal to the volume of the flaw in a 1" thick shale specimen, but results in acceptable pressure responses. These pressure responses, seen in Figure 66, show minimized overshooting, offset, and ringing.

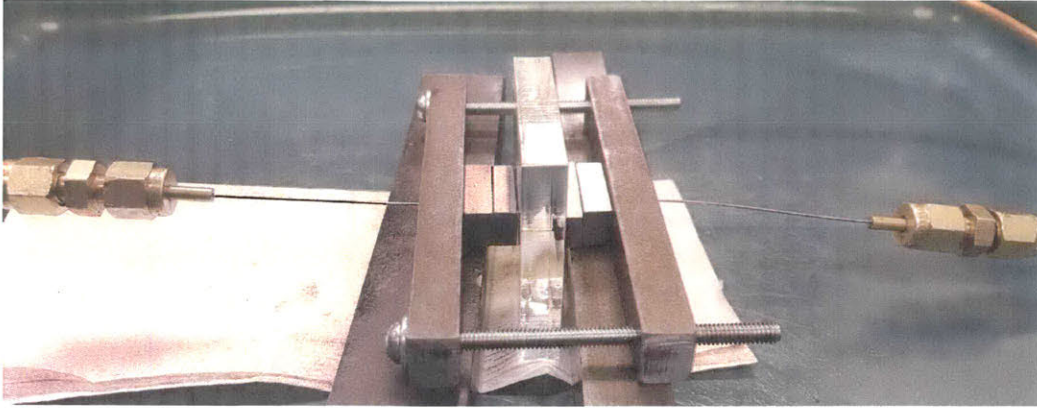


Figure 65 – 3/8" thick acrylic specimen with a hairline crack laser-cut through it used for PID tuning of hydraulic fracture apparatus.

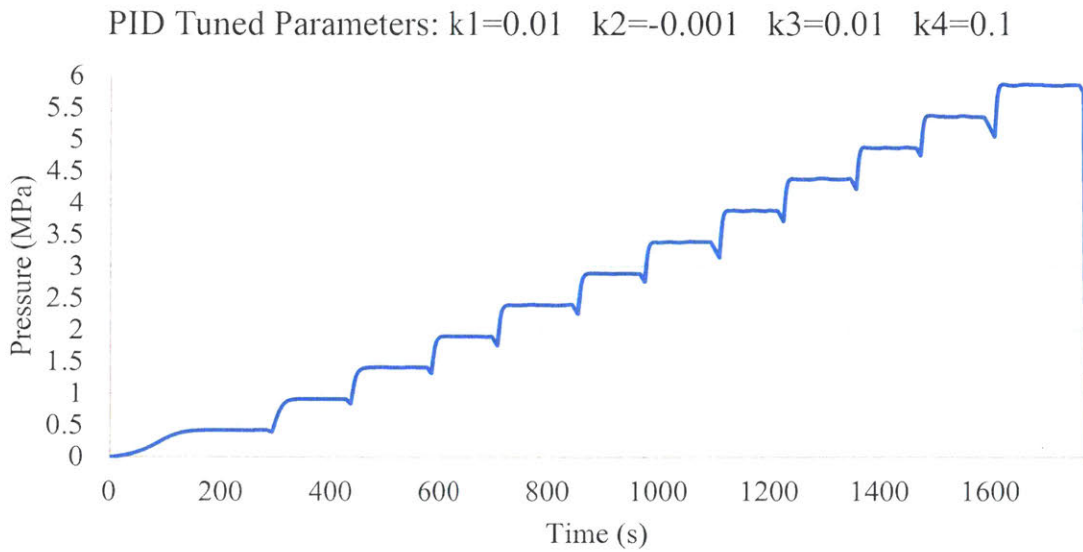


Figure 66 - Final PID parameters determined for modified pressurization device for single flaw pressurization in a 3/8" thick acrylic specimen. Pressure response shows minimized overshooting, offset, and ringing. Undershooting is a result of escaping the program to input a new target pressure command.

Finally, these PID parameters were tested on a shale specimen with a single vertical flaw oriented perpendicular to the bedding plane orientation. The pressure response of these PID parameters is shown in Figure 67. The offset is small in magnitude and consistent for each target pressure increment. There is no overshoot when converging to a target pressure, and pressure is stable after convergence.

Note the pressure drop before each incremental increase is due to inputting the command to increase pressure. A program was written to automate the pressurization process as will be shown in the results section for the flaw pair geometries tested.

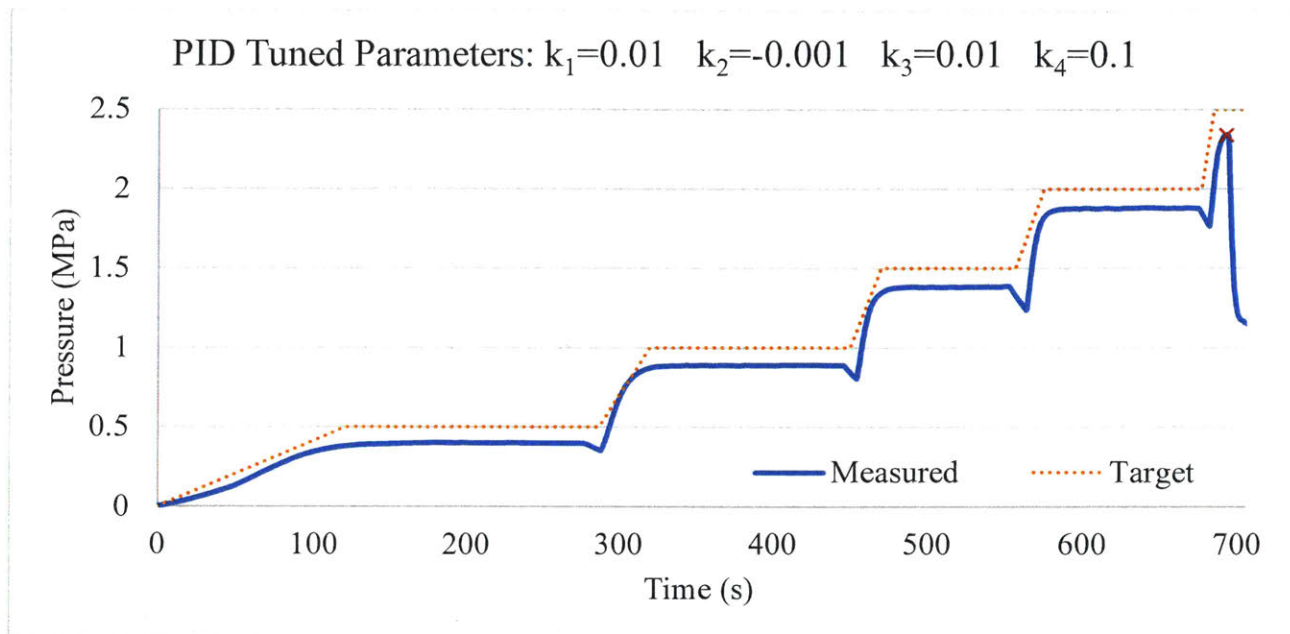


Figure 67 – Testing tuned PID Parameters on a shale specimen with a single vertical flaw oriented perpendicular to bedding planes. Offset is constant at each pressure increment. There is no overshooting. Pressure is stable after it converges. Note: red “x” is when specimen fractured.

To summarize, this section presented the equipment developed for the new pressurizing device that meets the objective of pressurizing a single flaw. The modifications on the hydraulic fracture apparatus were described. Finally, the steps involved in tuning the PID parameters to precisely pressure-control the pressurization process were shown along with results. All experimental design components required to successfully pressurize a single flaw were established in this section. The experimental procedure is described in the next section.

4.1.2 Test Procedure

The test being conducted is a uniaxial compression test on Opalinus shale with hydraulic fracturing as opposed to the uniaxial compression without hydraulic fracturing discussed in Chapter 3.

Many iterations with regard to testing components, as well as procedure, were required before reaching the current results. This section will discuss and describe some considerations. First, the reason and method of choosing a constant uniaxial stress is thoroughly described. Then the method behind saturating the flaw prior to pressurization is explained. Afterwards, flaw tangential stress calculations are introduced, discussing their advantages and disadvantages. Finally, the steps to run a single experiment are listed from specimen preparation till end of test.

4.1.2.1 *Constant Uniaxial Stress*

Gonçalves da Silva (2016) applied hydraulic pressure to a flaw in shale that resulted in hydraulic fluid to flow through bedding planes. No fracture was initiated, only flow through bedding planes. This is a mechanism, but the focus of the study is to observe fracture behavior. Also, applying a stress in one direction is closer to the real stress state in reality than not confining the specimen at all.

By applying enough uniaxial stress perpendicular to the bedding planes, pressurizing the flaw results in a fracture with little to no flow through bedding planes. It is important to note that the uniaxial stress applied should be high enough to keep the bedding planes closed, but not high enough to create a tensile crack at the flaw tips where there is a stress concentration.

“First Crack Initiation” stresses observed by Morgan (2015) were studied to determine an appropriate magnitude for the applied uniaxial stress. The tests chosen for this were various flaw geometries in reference with horizontal bedding planes (Figure 68). The lowest stress that induced a tensile crack was 6.8 MPa. The average of all first crack initiation stresses is 9.9 MPa. The constant uniaxial stress chosen

for the hydraulic fracture experiments was chosen to be 3.5 MPa, about half of the lowest first crack initiation stress and about one third of the average.

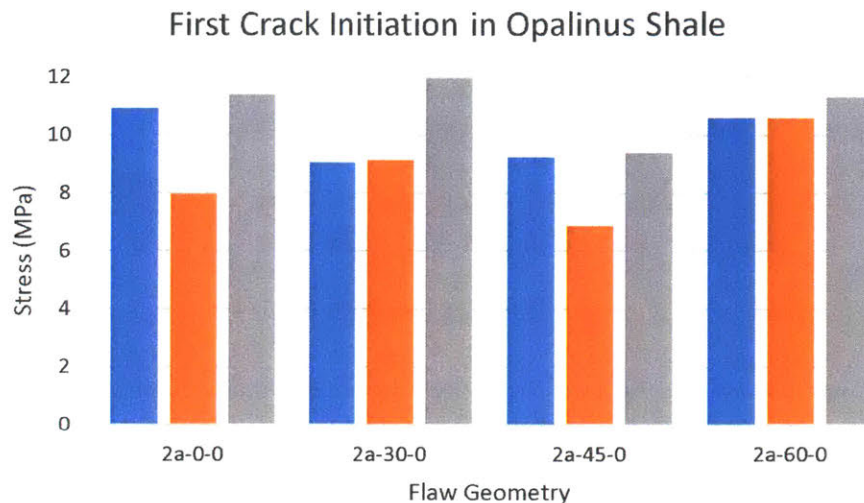


Figure 68 - First crack initiation stresses in Opalinus shale with horizontal bedding planes observed by Morgan (2015). Each bar refers to a first crack initiation stress in a specimen (each geometry was tested three times).

As shown in Figure 68, by applying 3.5 MPa, the specimen will not fracture due to stress concentration at the flaw tip from the applied vertical load, regardless of flaw orientation. Also, 3.5 MPa is high enough to keep the bedding planes closed and prevent the hydraulic fluid from flowing through during pressurization. Note that this chosen stress is only applicable to specimens with horizontal bedding plane orientation.

As shown in Figure 69, the first crack initiation stress dramatically changes for a given flaw geometry with variation in bedding plane orientation. The applied constant uniaxial stress must be modified according to any variation in bedding plane orientation in future experiments.

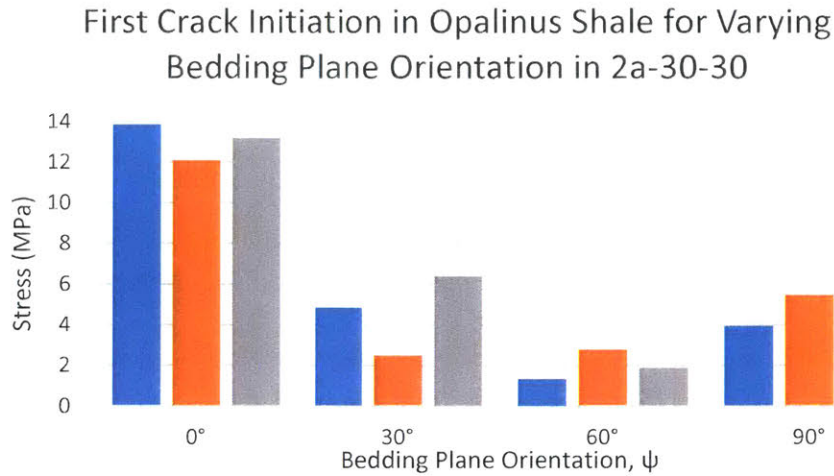


Figure 69 - Effect of varying bedding plane orientation on first crack initiation in Opalinus shale with 2a-30-30 geometry flaws.

4.1.2.2 Flaw Saturation

It is important to make sure there is no air in the system when pressurizing. The system can be cycled to remove air. However, the flaw is initially filled with air when sealing the specimen. The front and rear injection needles deliver the pumped hydraulic fluid into the flaw. The third needle is placed into the rear side of the specimen, where the needle tip is inside the flaw and the other end is open to atmospheric pressure (refer to Figure 51 and Figure 52). This third needle acts as a bleed hole, where the hydraulic fluid fills the flaw and pushes the air out through the third needle rather than compressing the air and having it dissolve in the fluid. After constant-pressure flow is established by monitoring the PVA pressure measurements, the flaw pressure transducer is attached to the flowing end of the third needle, closing the system and allowing pressurization. This process is illustrated in Figure 70.

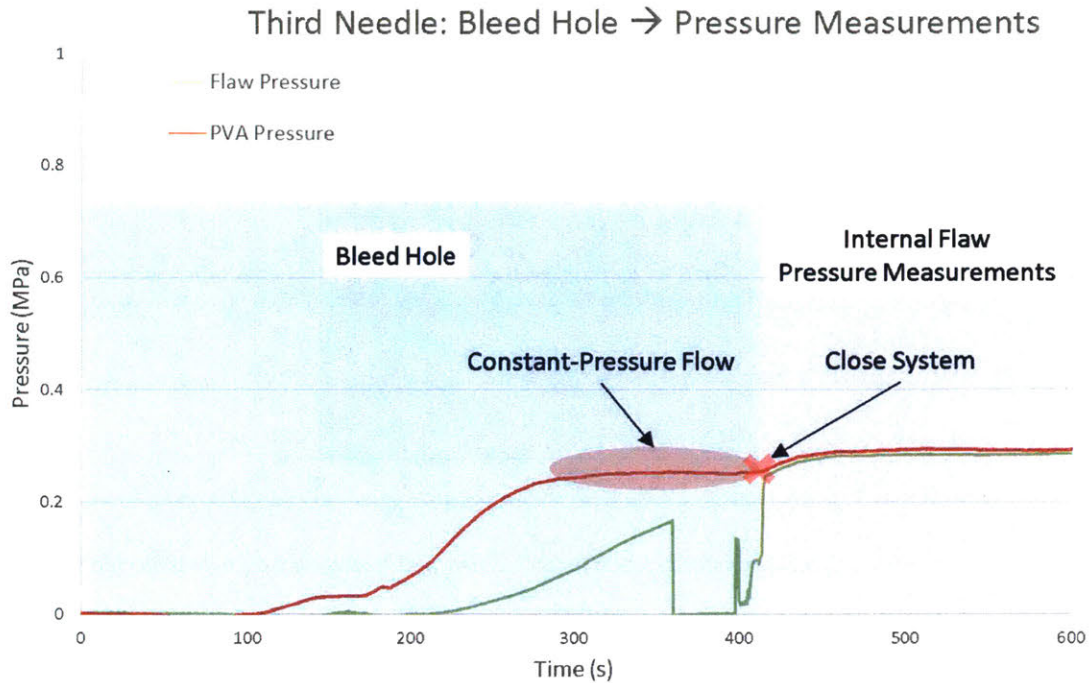


Figure 70 - Dual functionality of third needle which uses feedback pressure transducer initially, then internal flow pressure transducer after closing system.

4.1.2.3 Tangential Stress Distribution Calculations

The experiment may be modeled using the elastic solution for a pressurized elliptical crack (Pollard and Fletcher, 2005). The problem is modeled according to the loading conditions and geometry shown in Figure 71 and assumes that the material is isotropic and homogeneous.

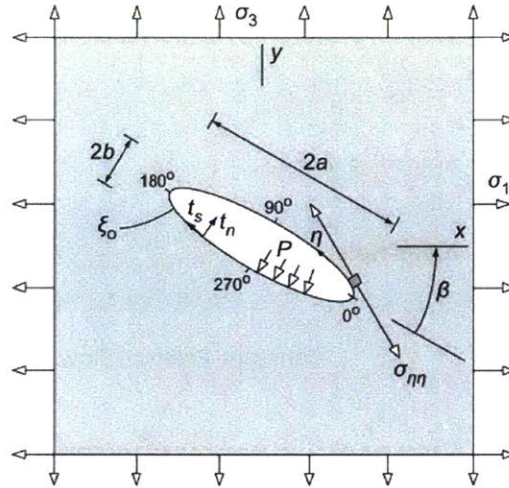


Figure 71 - Schematic of elastic boundary value problem for an inclined, pressurized elliptical hole subjected to biaxial applied stress (Pollard and Fletcher, 2005).

The tangential stress may be expressed as:

$$\sigma_t = -P + \frac{(\sigma_1 + \sigma_3 + 2P)2ab}{(a^2 + b^2) - (a^2 - b^2)\cos(2\eta)} - \frac{(\sigma_1 - \sigma_3)[(a + b)^2 \cos(2(\beta - \eta)) - (a^2 - b^2) \cos(2\beta)]}{(a^2 + b^2) - (a^2 - b^2)\cos(2\eta)}$$

Table 7 tabulates the input parameters that best represent the actual experiment for the above expression.

Table 7 - Input parameters that describe loading conditions and geometry of the experiment.

Lateral Stress	Vertical Stress	Internal Pressure	Inclination Angle	Radius of Curvature	Half Length	Half Width
σ_1 [MPa]	σ_3 [MPa]	P [MPa]	β [rad]	ρ [mm]	a [mm]	b [mm]
0	-3.5	0-3.5	$\pi/2$	0.35	4.23	1.22

The results of tangential stress for elliptical angles $\eta = -90^\circ$ to 90° are plotted in Figure 72, where $\eta = 0^\circ$ is at the flaw tip.

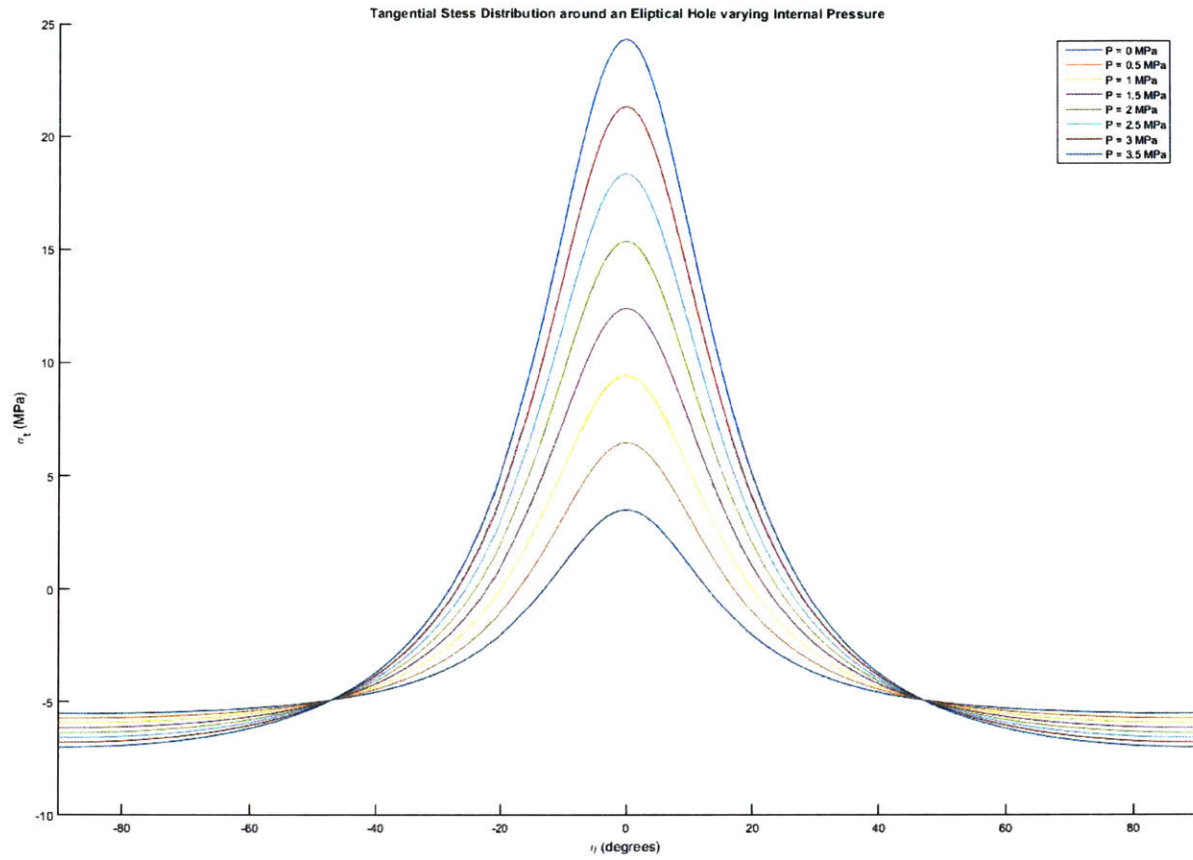


Figure 72 - Normal stress component, $\sigma_t = \sigma_{\eta\eta}(\xi = \xi_0)$, acting tangential to the hole boundary with varying internal pressures

for the case of: $\sigma_3 = -3.5 \text{ MPa}$, $\sigma_1 = 0 \text{ MPa}$, $\beta = \frac{\pi}{2}$, $\rho = 0.35$, $a = 4.23$, $b = \sqrt{\rho \cdot a} = 1.22$

It is clear that the maximum tangential stress throughout the test is located at $\eta = 0^\circ$, the flaw tip. The magnitude of the tangential stress at the flaw tip ranges from $\sigma_t(P=0 \text{ MPa})=3.5 \text{ MPa}$ to $\sigma_t(P=3.5 \text{ MPa})=24.34 \text{ MPa}$. This plot confirms that there is a large tensile stress concentrated at the flaw tip increasing with applied hydraulic pressure, allowing one to predict that the resulting fracture will initiate at $\eta = 0^\circ$. Using this elastic solution, one can vary any of the input parameters in Table 7 and predict where a fracture will initiate.

Discrepancies between the model and the experimental observations in stress magnitudes and fracture initiation location occur for a few reasons. First, the model assumes the material is homogenous and isotropic, which shale is not. Also, the model assumes the flaw is elliptical whereas they are closer to

rectangular slits with circular tips. Regardless of these differences, the model serves as a reasonable guide to estimate where and what stress concentrations are given the geometry and loading conditions.

4.1.2.4 Summary of Experimental Steps

The uniaxial compression test with hydraulic fracture experiment follows the following steps:

1. Prepare specimen with desired geometry as discussed in Section 3.1 with emphasis on the polishing of the specimen front and rear surfaces to prevent leaks. Ensure dimensions are recorded after this.
2. Setup flaw pressurizing device on specimen as shown in Figure 51 and Figure 52 without applying too much clamping force by only finger-tightening the clamping screw. Note that the needles are inserted into the flaw on one end and disconnected from the other end at this step. This is to allow the specimen to expand when applying uniaxial load without being constrained by the flaw pressurizing device.
3. Set the specimen between top and bottom load platens in the load frame. Ensure that specimen is centered relative to platens and that platens are centered relative to the load frame to minimize any induced shear.
4. Calculate cross sectional area perpendicular to loading direction, then calculate how much uniaxial force needs to be applied to induce 3.5 MPa (507 psi) of stress in the specimen (may vary depending on specimen dimensions). For exactly 2 in², force is calculated to be 1015 lbs. Apply 3.5 MPa (507 psi) under load-control settings and hold throughout the duration of the experiment.
5. After load is applied and held, the clamping screws on the pressuring device can be tightened, effectively sealing the flaw.
6. Connect the two injection needles to the copper pipe T-joint. This connects the specimen to the hydraulic fracture apparatus as shown in Figure 50 with the exception of the flaw pressure measurement transducer. The third needle is acting as a “bleed-hole” at this stage.

7. Setup both high-resolution and high-speed cameras. Apply even lighting on specimen surface and focus cameras. Start time-lapse with high-resolution camera and ensure the high-speed camera is recording and ready to capture.
8. Start hydraulic fracture apparatus and inject fluid through the front and rear injection needles into the sealed flaw by setting a small target pressure, such as 0.5 MPa (72 psi). Continue to inject fluid to completely saturate the flaw with fluid and expel all air from the third needle which is open to atmosphere (as shown in Figure 70).
9. As fluid is injected, the PVA pressure is monitored and is observed to increase until plateauing off (note this pressure will be far off from the target pressure since the system is open to atmosphere). At this stage, constant-pressure flow is established and the flaw is assumed to be saturated with fluid (Figure 70).
10. The internal flaw pressure measuring pressure transducer is then attached to the third needle, effectively sealing the system. At this point, the measured internal flaw pressure will equal the measured PVA pressure, and both will increase towards the target pressure of 0.5 MPa (since the system is now closed, flowing into the sealed flaw will increase the pressure).
11. Take note of the recorded pressure after establishing steady-state pressure and calculate the offset pressure (target pressure - measured steady-state pressure). An offset occurs due to the PID algorithm which was tuned to eliminate overshoot. Eliminating overshoot was prioritized over eliminating offset because overshoot may result in accidental over pressure of the specimen which may cause fracture. Offset is easily dealt with:

Example: for a target pressure = 0.5 MPa, and measured steady-state pressure = 0.42 MPa, the calculated offset pressure = $0.5 - 0.42 = 0.08$ MPa. So to actually achieve 0.5 MPa, input $0.5 + 0.08 = 0.58$ MPa as the target pressure, and to achieve 1 MPa, input 1.08 MPa as the target pressure, etc. Note, the offset pressure is constant for all pressure increments.

12. Add offset pressure to all target pressure increments to achieve actual target pressure.
13. At this point, the specimen is under constant uniaxial load. The flaw is sealed and saturated with fluid. The pressure increments (considering the offset pressure) are known. The test can effectively begin. The final step is to pressurize the flaw in increasing 0.5 MPa increments, holding each pressure step for 1-2 minutes until a hydraulic fracture initiates and propagates.
14. Capture high-speed video and save. Stop high-resolution time-lapse.

This summarizes the steps required to run a uniaxial compression with hydraulic fracture of an individual flaw experiment. The analysis process for these tests is identical to the “dry” fracture experiments except rather than relating events to stress-strain data, they are related to pressure-volume data. This will be shown in section 4.2 Results.

4.2 Results

A total of nine tests were conducted on Opalinus Shale prisms. First, three specimens with a single vertical flaw were tested as a proof of concept of the experiment. Then three specimens with flaw pairs with a geometry of 2a-30-30 were tested. After that, three more specimens with flaw pairs of geometry 2a-30-60 were tested. The objective of the flaw pair experiments is to capture the interaction of a hydraulic fracture with a pre-existing non-pressurized crack.

4.2.1 Single Vertical Flaw

Uniaxial tests with hydraulic fracture, in which flaw pressure is computer-controlled, were conducted on Opalinus shale prismatic specimens with a single vertical flaw cut into them. The single vertical flaw geometry was chosen for the proof of concept of the flaw pressurizing experimental setup. The results presented next are for one of three specimens tested. The full analysis for this specimen is shown below, starting with the test data plotted in Figure 73.

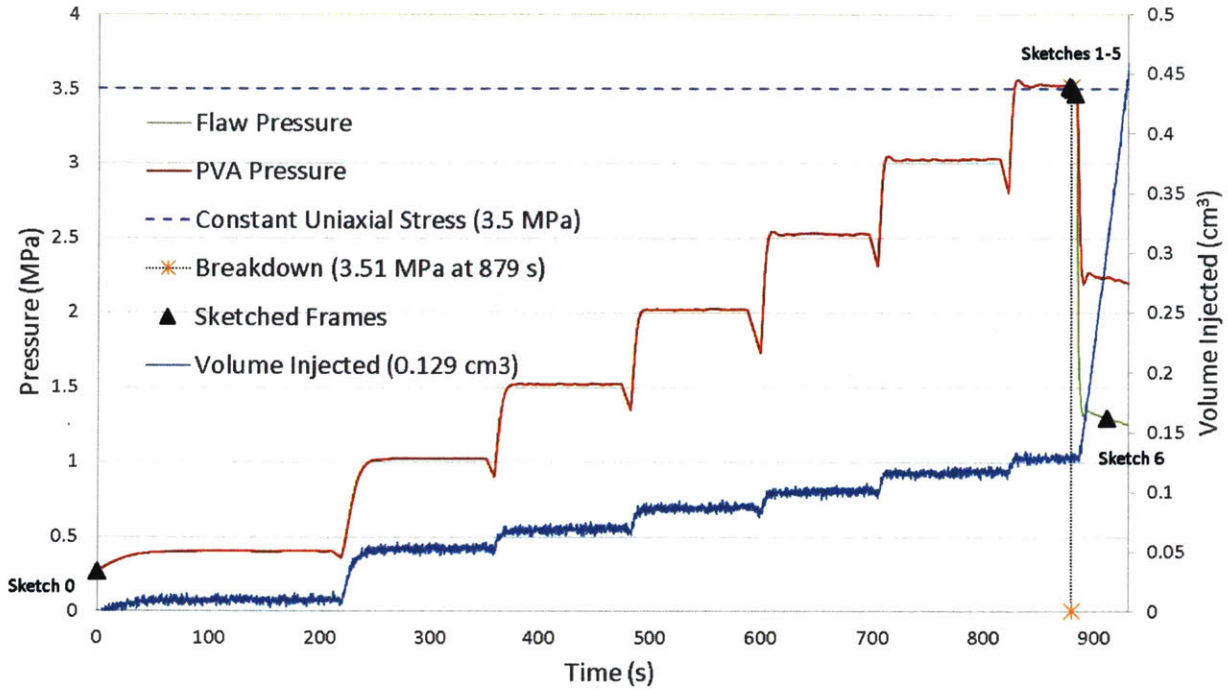


Figure 73 - Test data collected from PVA pressure transducer, feedback pressure transducer, and PVA LVDT on Opalinus shale prismatic specimen with a single vertical flaw. Test starts when system is closed by attaching flaw pressure transducer to third needle. Test ends after fracture stops propagation.

The example shown is for the test data on the specimen OP-HF-SF-90-A. After the flaw was pressurized to a target pressure of 3.5 MPa, the pressure was held for approximately 48 seconds before failing due to crack propagation. Table 8 tabulates the dimensions of the specimen tested, while Table 9 shows the test data.

Table 8 - Dimensions of specimen OP-HF-SF-90-A.

OP-HF-SF-90-A Dimensions			
Height (h)	Width (w)	Thickness (t)	Area (A=wxt)
[in]	[in]	[in]	[in ²]
3.1572	1.9812	1.0516	2.0834

Table 9 - Summary of test loads and volume.

OP-HF-SF-90-A Test Summary			
Vertical Applied Load	Vertical Applied Stress	Maximum Hydraulic Pressure	Volume Injected until Loss of Pressure
[kN]	[MPa]	[MPa]	[cm ³]
4.70	3.5	3.56	0.1288

Figure 74 is a zoomed version of Figure 73. It clearly shows the point at which the flaw pressure measurements diverge from the PVA pressure measurements. This happens because the flaw pressure transducer is directly reading the pressure inside the flaw whereas the feedback pressure transducer is at the PVA outlet (Figure 50). For this reason, the flaw pressure transducer is taken as the reference with regard to the pressure state inside the flaw. Figure 74 also shows a time lag when the volume increases to compensate for the pressure loss, as the apparatus is set up with pressure-control. The lag is simply due to the delay of the feedback control system since the volume injected is dependent on the feedback pressure transducer measurements. Finally, Figure 73 and Figure 74 show the times at which sketches were taken for the analysis of the fracture initiation and propagation shown next.

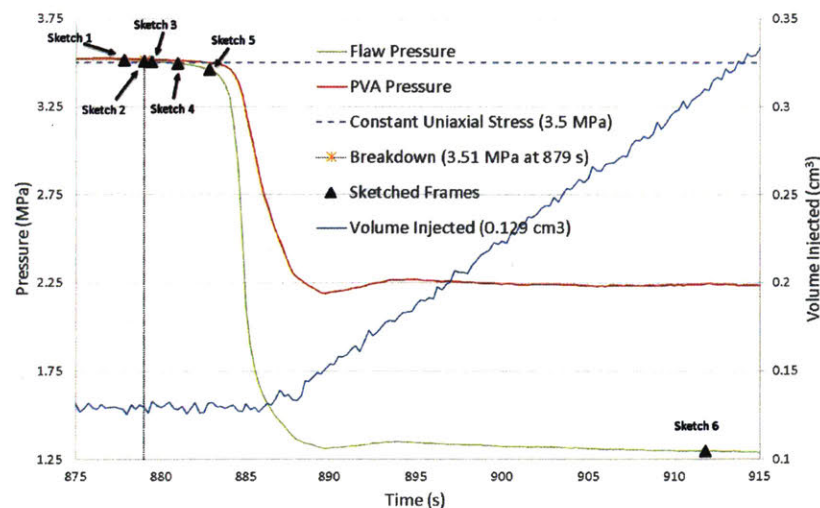


Figure 74 - Test data from Figure 73 zoomed in to time of specimen failure to clarify curve trend and show sketch data points.

Figure 75 shows Sketch 0 taken at the beginning of the test, as indicated in Figure 73. This is a prismatic 4"x2"x1" specimen with a single vertical flaw at its center and horizontal bedding planes. As shown, the flaw is fully saturated with hydraulic fluid at this stage and testing is ready to commence. There is initial pressure of 0.26 MPa in the flaw from the saturation process. Volume is referenced back to this point in the test, the point at which the system was closed. At this point in the test, $t = 0 \text{ seconds}$, $P = 0.267 \text{ MPa}$, $V = 0 \text{ cm}^3$. The pressure is then increased in 0.5 MPa increments until specimen failure.

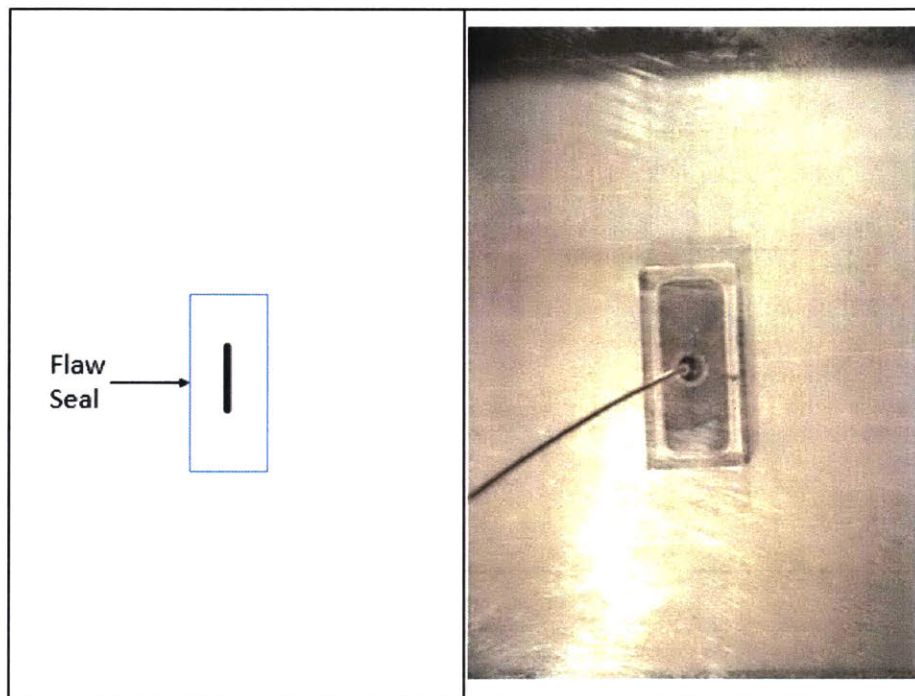


Figure 75 – Sketch 0: initial configuration of the specimen with saturated flaw.

Sketch 1 is taken moments before the fractures propagate past the flaw seal boundary (refer to Figure 74). At this point in the test, $t = 877.831 \text{ seconds}$, $P = 3.515 \text{ MPa}$, $V = 0.1287 \text{ cm}^3$. The fracture path from the flaw tips to the flaw seal boundary is back-interpreted from later frames as they are not clearly visible until the cracks have propagated.

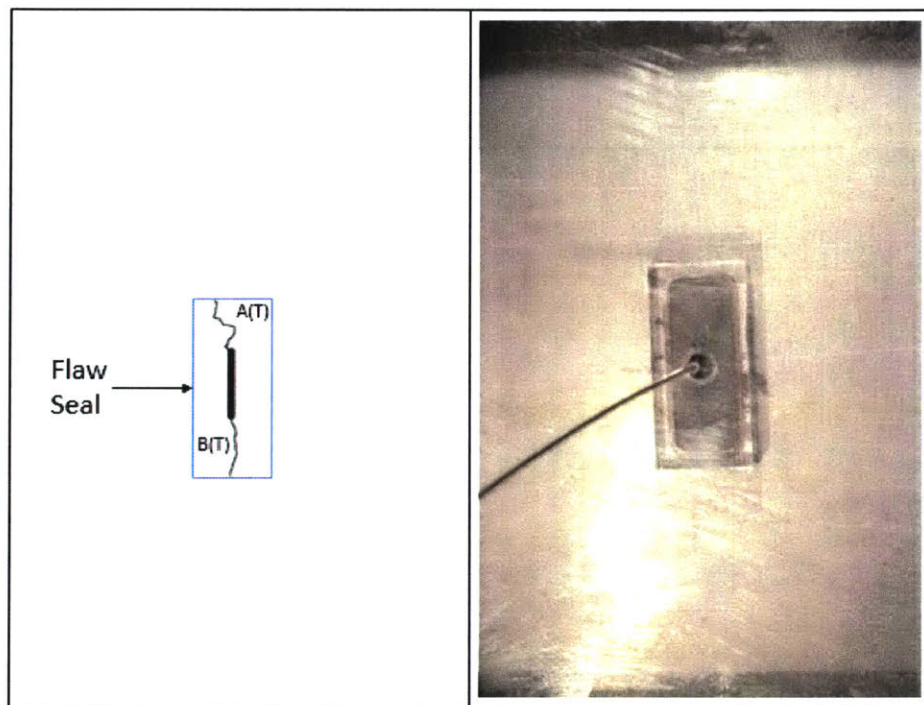


Figure 76 - Sketch 1: crack initiation within flaw seal boundaries.

Sketch 2 is taken at $P_{\text{breakdown}}$, the pressure at which the internal flaw pressure drops due to a fracture propagating past the flaw seal boundary (refer to Figure 74). At this point in the test, $t = 879$ seconds, $P = 3.507$ MPa, $V = 0.1296$ cm³. Tensile crack A(T) propagates past the top of the flaw seal boundary as shown in Figure 77. This will be referred to as the “breakdown” of the specimen, i.e., the test breakdown pressure $P_{\text{breakdown}}=3.516$ MPa at 879 seconds from the start of the test. It should be noted that the reported value of volume injected in Sketch 2 is less than that reported in Sketch 1. This is due to the noise in the data as shown in Figure 74, and the reported values lie within the noise band. The total volume injected into the flaw until breakdown is 0.1288 cm³.

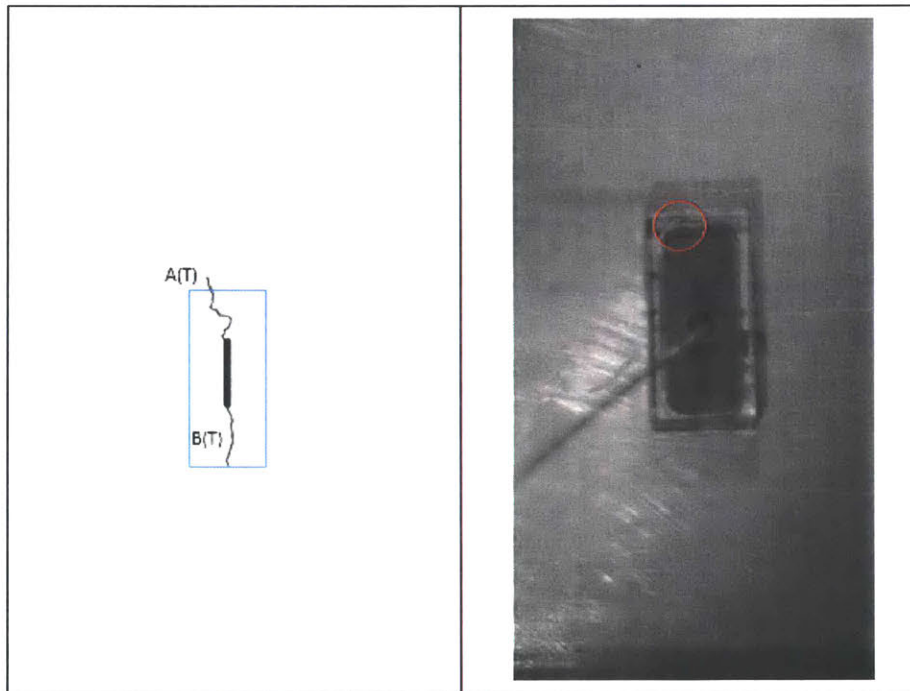


Figure 77 - Sketch 2: crack initiation, A(T) propagates past flaw seal.

Sketch 3 is taken after $P_{\text{breakdown}}$ (refer to Figure 74). At this point in the test, $t = 879.452 \text{ seconds}$, $P = 3.506 \text{ MPa}$, $V = 0.1262 \text{ cm}^3$. Tensile crack A(T) continues propagating. After 0.45 seconds of crack A(T)'s propagation, tensile crack B(T) propagates past the flaw seal (Figure 78).

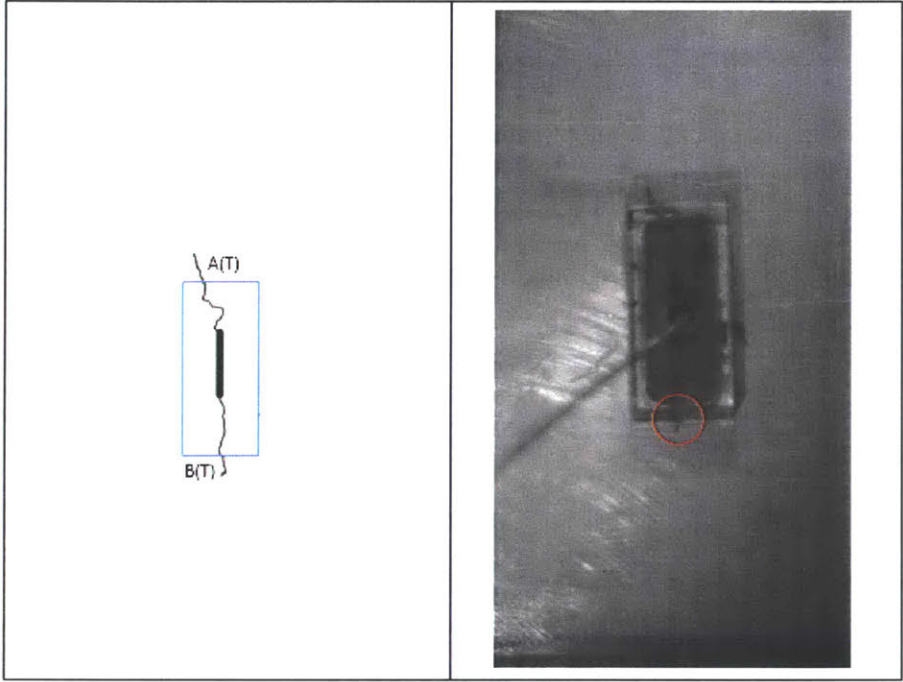


Figure 78 - Sketch 3: crack initiation, B(T) propagates past flaw seal boundary.

Sketch 4 is taken after $P_{\text{breakdown}}$ (refer to Figure 74). At this point in the test, $t = 880.992 \text{ seconds}$, $P = 3.497 \text{ MPa}$, $V = 0.1288 \text{ cm}^3$. This sketch shows tensile cracks A(T) and B(T) continue propagation (Figure 79). Throughout propagation, a lag was observed between the advancement of the crack and the hydraulic fluid leaking out of the propagating crack at the crack tip. This was apparent for A(T) where the crack tip was advancing upwards whereas B(T) was advancing in the same direction of the oil flowing out of both cracks, minimizing visibility.

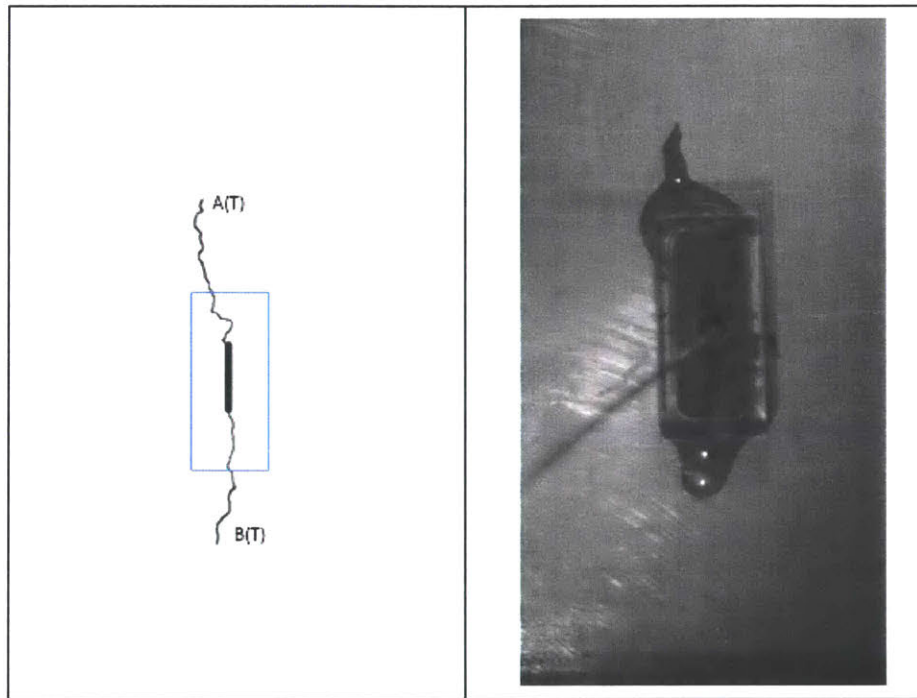


Figure 79 - Sketch 4: crack propagation, lag between crack tip and fluid front.

Sketch 5 is taken after $P_{\text{breakdown}}$ (refer to Figure 74). At this point in the test, $t = 882.831 \text{ seconds}$, $P = 3.462 \text{ MPa}$, $V = 0.1317 \text{ cm}^3$. This sketch shows tensile cracks A(T) and B(T) continue propagation (Figure 80). Tensile crack (B(T)) stops propagating at this point. Tensile crack B(T) propagated for 3.28 seconds since propagating past the flaw seal boundary.

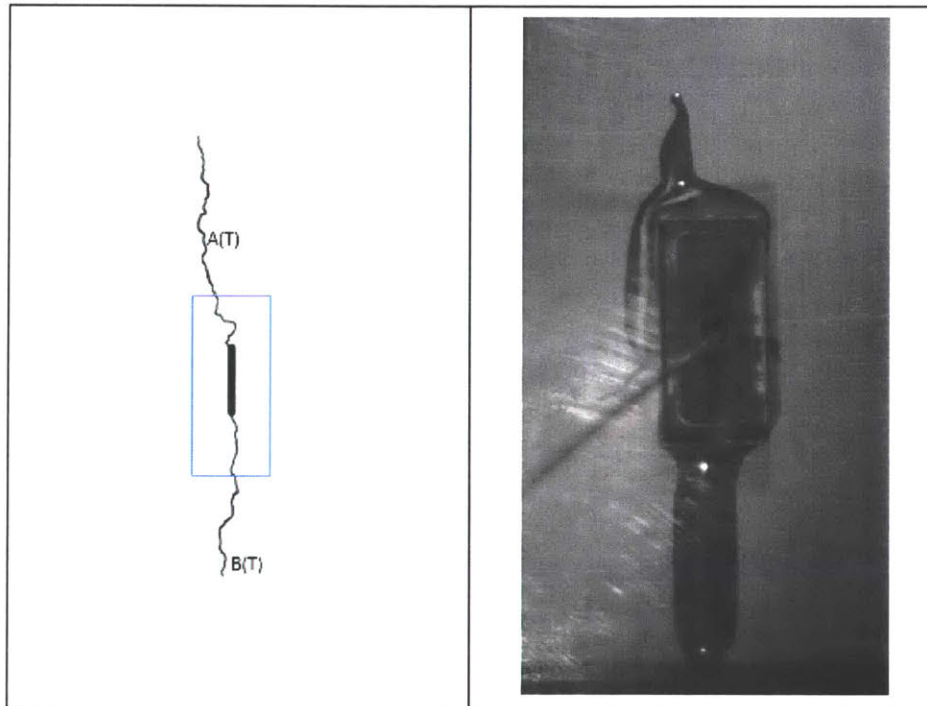


Figure 80 - Sketch 5: crack propagation, end of crack B(T) propagation.

Sketch 6 is taken towards the end of test (refer to Figure 74). At this point in the test, $t = 911.831$ seconds, $P = 1.297$ MPa, $V = 0.3103$ cm³. Tensile crack A(T) stops propagating at this point (Figure 81). Crack A(T) propagated for 32.83 s since propagating past the flaw seal boundary.

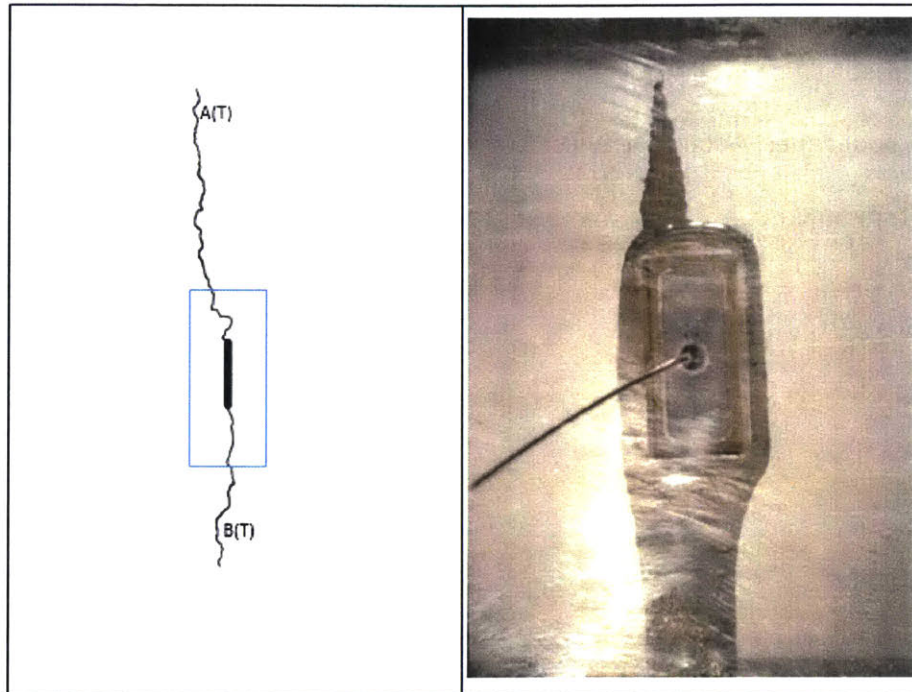


Figure 81 - Sketch 6: end of crack A(T) propagation.

As seen in the analysis of this specimen, the propagating hydraulic fracture is not a simple straight fracture. On a macro scale, the fracture apparently propagates away from the long axis of the flaw perpendicular to the loading direction. However, when closely following the fracture, kinks in fracture direction can be seen. These kinks seem to be related to the bedding planes, where the fracture repeatedly propagates and arrests at some bedding plane boundaries. Another aspect observed is the fluid lagging behind fracture propagation. The high-speed video captures, in slow motion, the fracture propagating as well as the fluid bleeding out of the propagating fracture. It was very clear when the fracture propagated ahead of the fluid. This lag is initially hypothesized to occur when an arrested fracture at a bedding plane continues propagating.

Two other specimens with a single vertical flaw were tested in the same manner and the detailed analyses can be seen in Appendix A2. Figure 82 shows a summary of all uniaxial compression tests with hydraulic fracturing run on Opalinus shale specimens with horizontal bedding planes and a single vertical flaw. All tests show similar fracture behaviors, where a fracture propagates in the direction of applied load. Fracture propagation in all specimens was observed to be a series of advancing and arresting at bedding plane boundaries. Also, lag between crack tip and fluid front during fracture propagation was observed in all specimens.

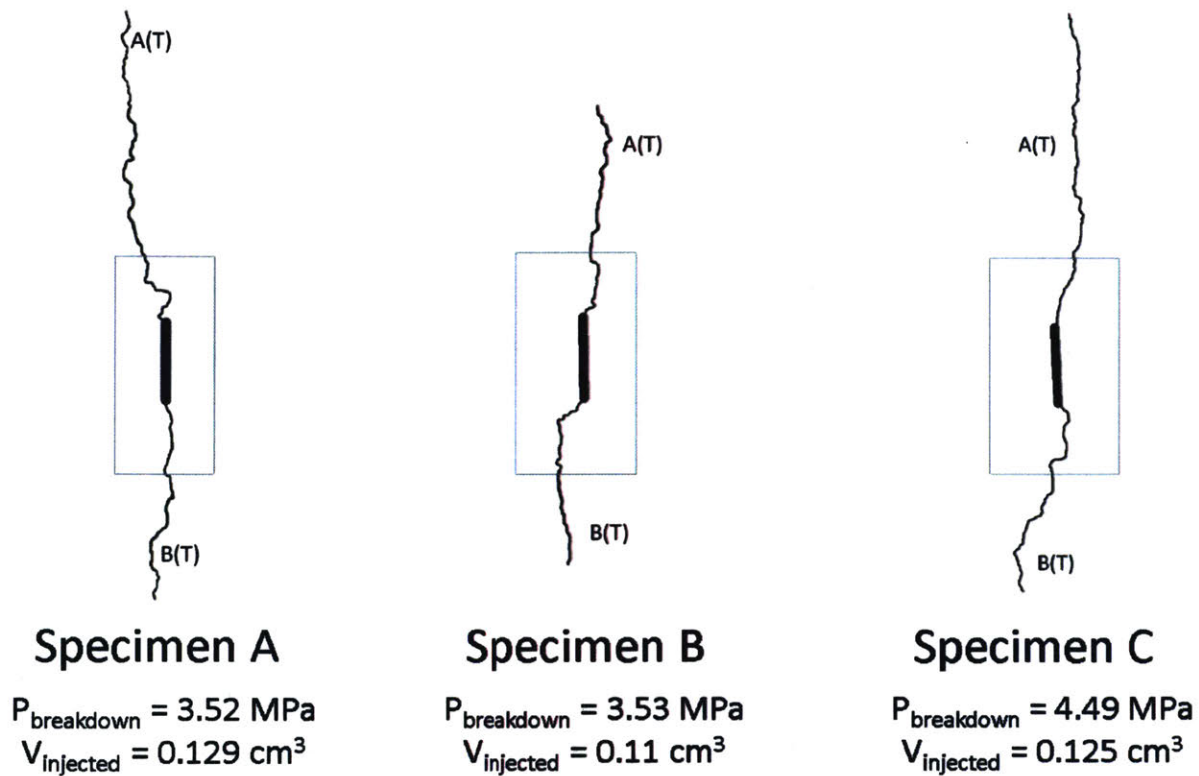


Figure 82 – Summary of all uniaxial compression with hydraulic fracture tests of a single vertical flaw showing observed fracture behavior, breakdown pressure, and total injected volume at breakdown.

4.2.2 2a-30-30

The previous section presented the results of uniaxial compression tests with pressurization of a pre-existing flaw in a specimen with a single vertical flaw. As stated previously, this geometry was chosen as

a proof of concept for this type of experiment. It was shown that with the experimental setup described in section 4.1.1, one can successfully induce hydraulic fractures from a pre-existing flaw in shale and visually capture their initiation and propagation as well as relate these events to the pressure-volume data.

To carry this one step further, specimens with flaw pairs were prepared and tested to visually capture the interaction of the induced hydraulic fracture with a pre-existing non-pressurized flaw. The first geometry tested was 2a-30-30 as shown in Figure 83. The bottom flaw was pressurized for all flaw geometries, in this case, it is the left flaw. The blue rectangle in Figure 83 indicates the rubber membrane that seals the oil inside the flaw throughout the pressurization process. The area inside the blue rectangle is subjected to a clamping force to seal the flaw, and the area outside of the blue rectangle is the free surface of the specimen. Once the hydraulic fracture propagates past the flaw seal boundary, oil starts flowing out of the induced hydraulic fracture. The bottom flaw is chosen for pressurization so that the oil flowing out of the hydraulic fracture does not obstruct the visual imagery, and key events can be accurately described.

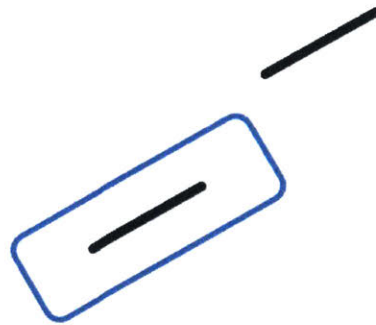


Figure 83 – 2a-30-30 geometry where the bottom flaw is pressurized and right flaw is not pressurized. The blue rectangle indicates the flaw seal boundary of the rubber membrane.

The results presented next are for one of three specimens tested and analyzed. The full analysis for this specimen is shown below, starting with the test data plotted in Figure 84.

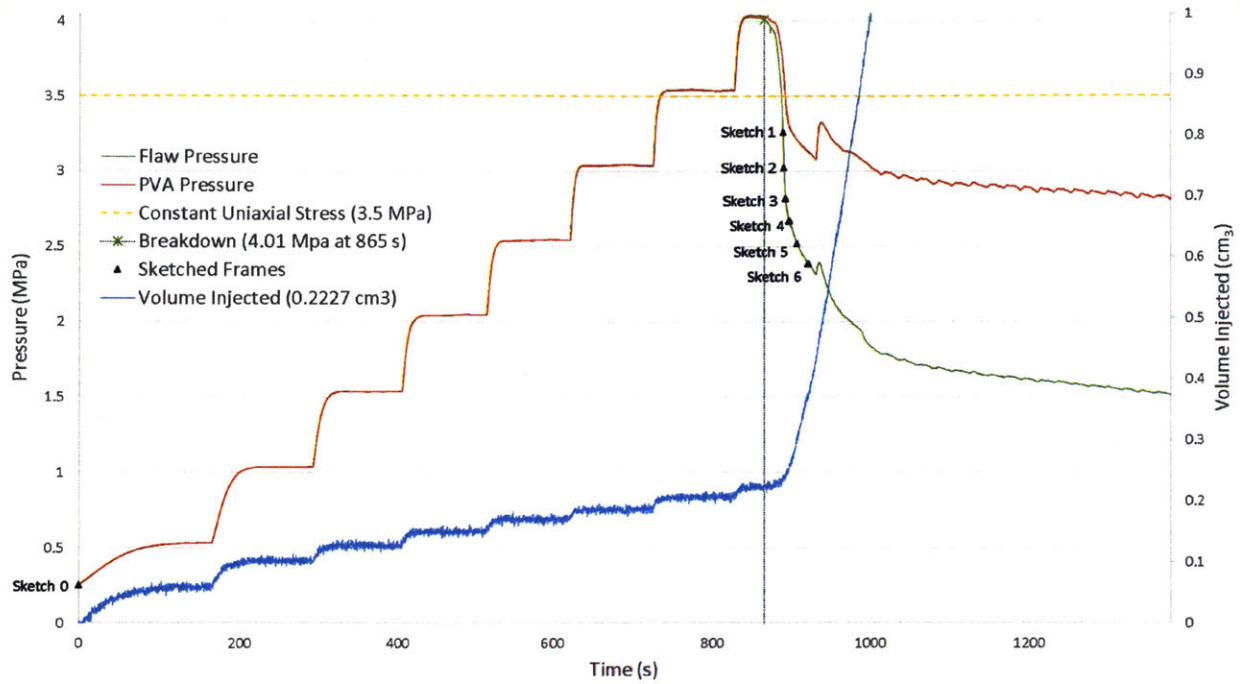


Figure 84 - Test data collected from PVA pressure transducer, feedback pressure transducer, and PVA LVDT on Opalinus shale prismatic specimen with flaw pair geometry 2a-30-30. Test starts when system is closed by attaching flaw pressure transducer to third needle. Test ends after fracture stops propagation.

The example shown is for test data on specimen OP-HF-2a-30-30-D. After the flaw was pressurized to a target pressure of 4.0 MPa, the pressure was held shortly before dropping due to crack propagation.

Table 10 tabulates the dimensions of the specimen tested, while Table 11 shows the test data.

Table 10 – Dimensions of specimen OP-HF-2a-30-30-D.

OP-HF-2a-30-30-D Dimensions			
Height (h)	Width (w)	Thickness (t)	Area (A=wxt)
[in]	[in]	[in]	[in ²]
3.962	1.843	0.928	1.710

Table 11 - Summary of test loads and injected volume for OP-HF-2a-30-30-D.

OP-HF-2a-30-30-D Test Summary			
Vertical Applied Load	Vertical Applied Stress	Maximum Hydraulic Pressure	Volume Injected until Loss of Pressure
[kN]	[MPa]	[MPa]	[cm ³]
3.86	3.5	4.03	0.2227

For convenience, Figure 85 is a zoomed version of Figure 84. It clearly shows the point at which the flaw pressure measurements diverge from the PVA pressure measurements and when the flaw pressure begins to drop. From Figure 85, it was determined that the breakdown pressure is 4.01 MPa which occurred at 865 seconds from the beginning of the test.

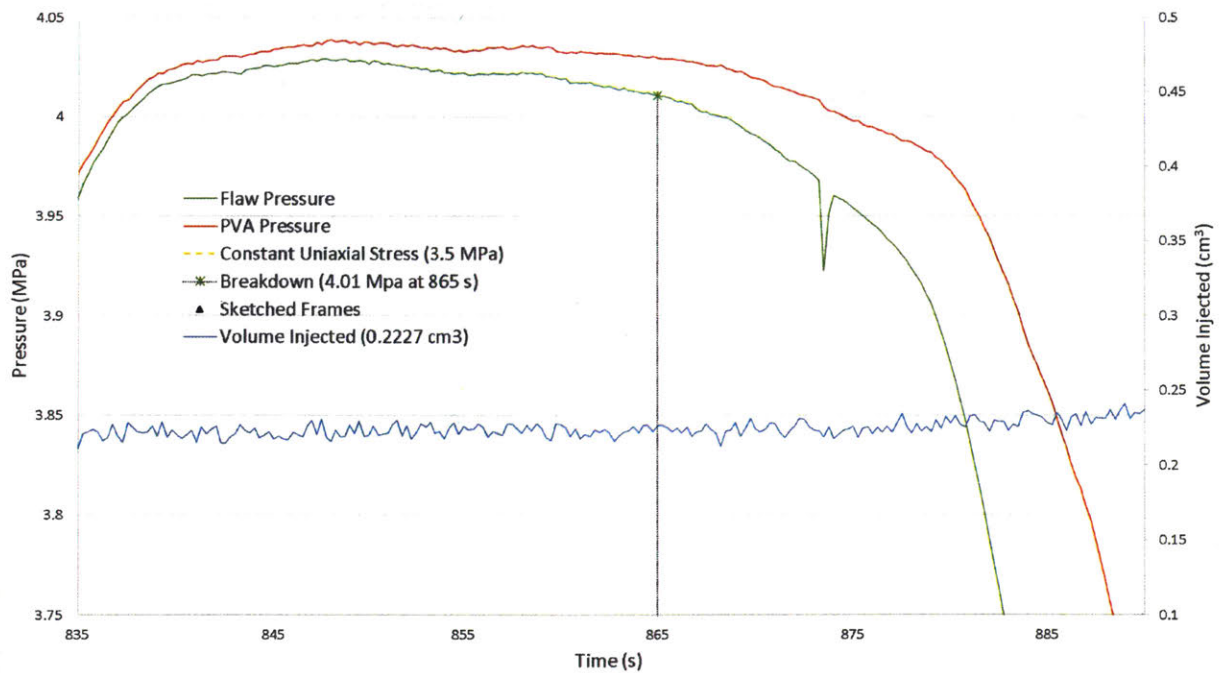


Figure 85 – Close-up (range from $t=835 - 890$ seconds and $P=3.75 - 4.05$ s) of pressure drop from test data shown in Figure 84 - Test data collected from PVA pressure transducer, feedback pressure transducer, and PVA LVDT on Opalinus shale prismatic specimen with flaw pair geometry 2a-30-30. Test starts when system is closed by attaching flaw pressure transducer to third needle. Test ends after fracture stops propagation.

Figure 86 shows Sketch 0 taken at the beginning of the test, as indicated in Figure 84. This is a prismatic 4"x2"x1" specimen with a flaw pair geometry of 2a-30-30 and horizontal bedding planes. As shown, the left flaw is fully saturated with hydraulic fluid at this stage and testing is ready to commence. There is an initial pressure of 0.271 MPa in the flaw from the saturation process. Volume injection is referenced back to this point in the test, the point at which the system was closed. At this point in the test, $t = 0 \text{ seconds}$, $P = 0.271 \text{ MPa}$, $V = 0 \text{ cm}^3$. The pressure is then increased in 0.5 MPa increments until specimen failure.

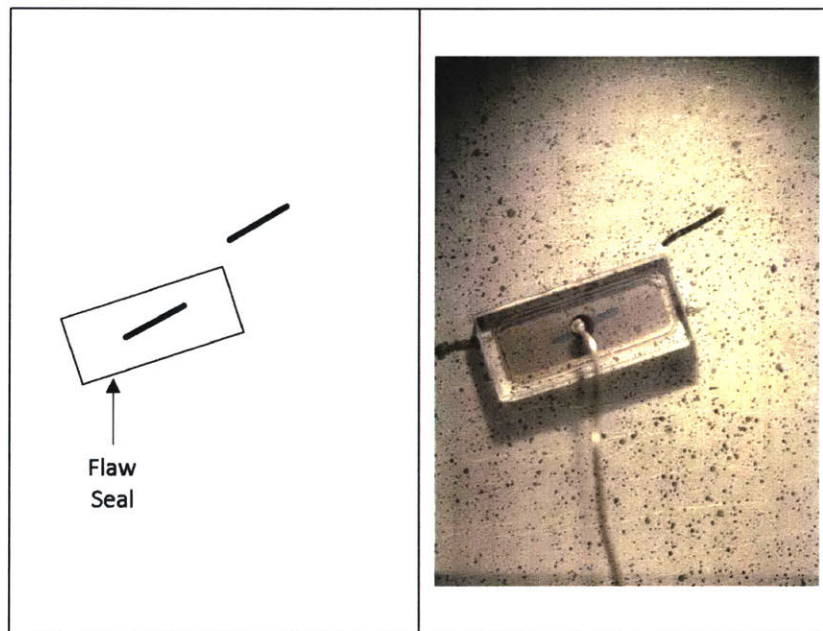


Figure 86 – Sketch 0: initial configuration of the specimen OP-HF-2a-30-30-D after flaw saturation.

Sketch 1 shows the first key events, the initiation of A(T) and B(T), which occurred after breakdown (refer to Figure 84). At this point in the test, $t = 889.37 \text{ seconds}$, $P = 3.262 \text{ MPa}$, $V = 0.2329 \text{ cm}^3$. Both tensile cracks A(T) and B(T) appeared during the same frame and were not visible before. A(T) was labelled first because it is the first crack to propagate past the flaw seal boundary. The close-up images were adjusted to show the visible cracks A(T) and B(T) more clearly. Pressure dropped 0.738 MPa from the target pressure with no crack propagation past the flaw seal boundary.

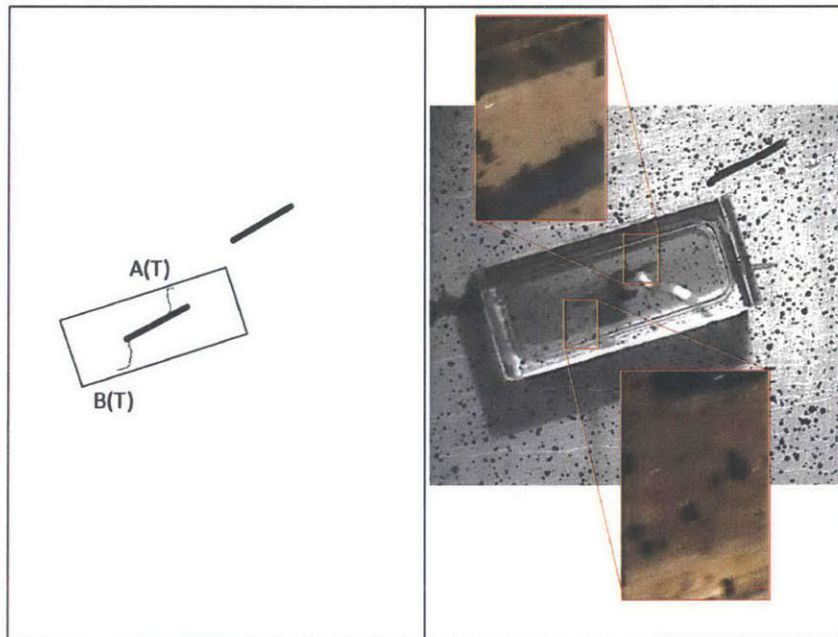


Figure 87 - Sketch 1: crack initiation within flaw seal boundaries.

Sketch 2 is taken during a steep pressure drop gradient (refer to Figure 84). At this point in the test, $t = 890.81 \text{ seconds}$, $P = 3.028 \text{ MPa}$, $V = 0.2378 \text{ cm}^3$. Tensile crack A(T) propagated past the flaw seal boundary. This first crack propagation past the flaw seal boundary occurred after pressure dropped 0.972 MPa from target pressure. Note that breakdown pressure did not correspond to immediate cracking events and that pressure had to drop significantly prior to any visible crack initiation or propagation.

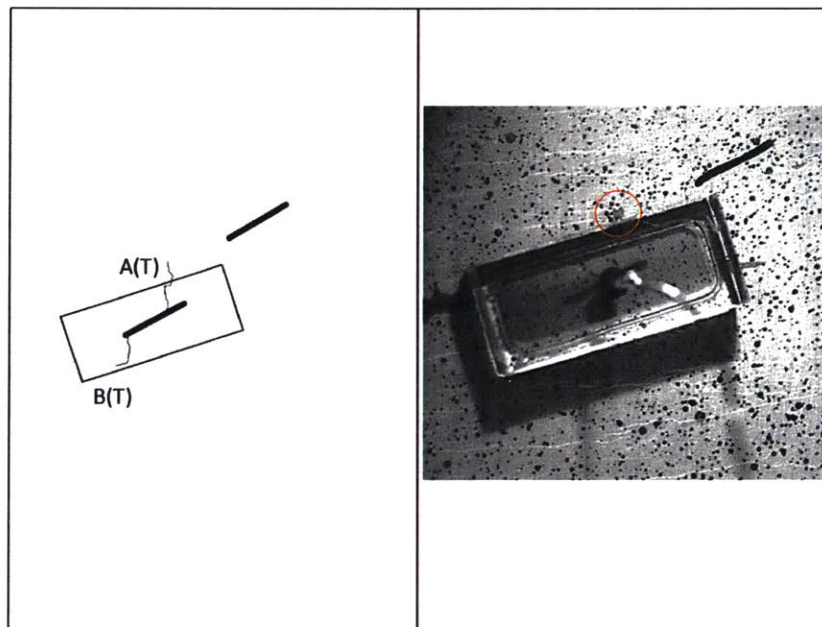


Figure 88 - Sketch 2: crack initiation, A(T) propagates past flaw seal.

Sketch 3 is taken during the previously mentioned steep pressure drop gradient (refer to Figure 84). At this point in the test, $t = 892.81 \text{ seconds}$, $P = 2.823 \text{ MPa}$, $V = 0.2414 \text{ cm}^3$. Tensile crack B(T) propagated past the flaw seal boundary. Tensile crack A(T) also continued propagating.

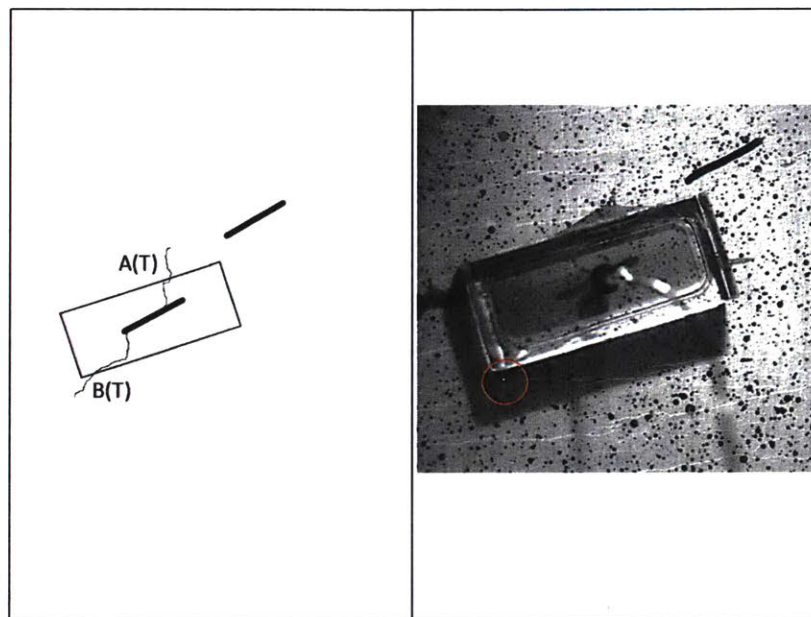


Figure 89 - Sketch 3: crack initiation, B(T) propagates past flaw seal boundary.

Sketch 4 is also taken during the previously mentioned steep pressure drop gradient (refer to Figure 84). At this point in the test, $t = 892.81 \text{ seconds}$, $P = 2.823 \text{ MPa}$, $V = 0.2414 \text{ cm}^3$. This sketch shows tensile cracks A(T) and B(T) continue propagation (Figure 90). Throughout propagation, a lag was observed between the advancement of the crack and the hydraulic fluid leaking out of the propagating crack behind the crack tip. Also, the way the cracks propagated was a repetition of the pressurized crack propagating in tension across bedding planes, then through a bedding plane, then across bedding planes again.

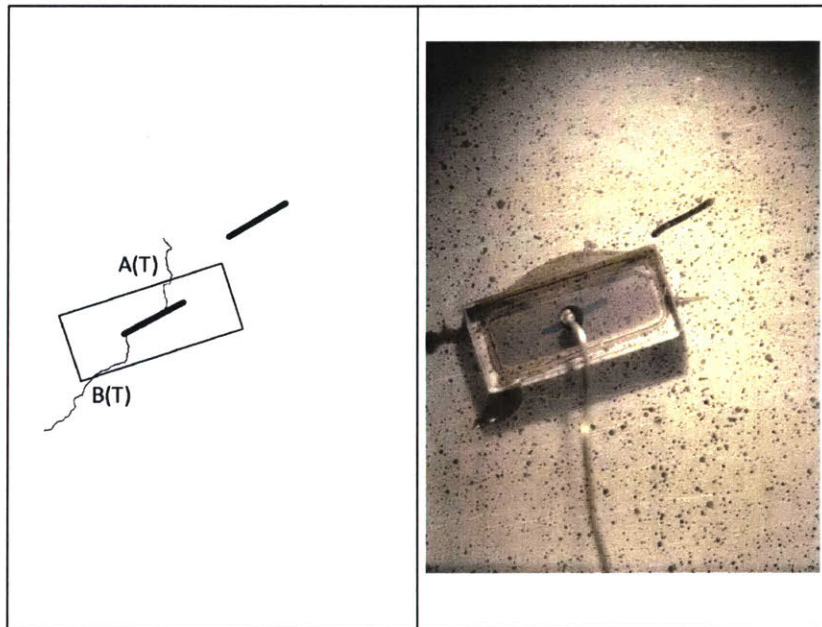


Figure 90 - Sketch 4: crack propagation, lag between crack tip and fluid front.

Sketch 5 is taken when the pressure drop gradient begins to stabilize (refer to Figure 84). At this point in the test, $t = 906.81 \text{ seconds}$, $P = 2.522 \text{ MPa}$, $V = 0.3039 \text{ cm}^3$. In the time between Sketch 4 and Sketch 5, tensile cracks A(T) and B(T) had continued propagation (Figure 91). However, tensile crack B(T) stopped propagating from this sketch onwards. Tensile crack B(T) propagated for 14 seconds since propagating past the flaw seal boundary.

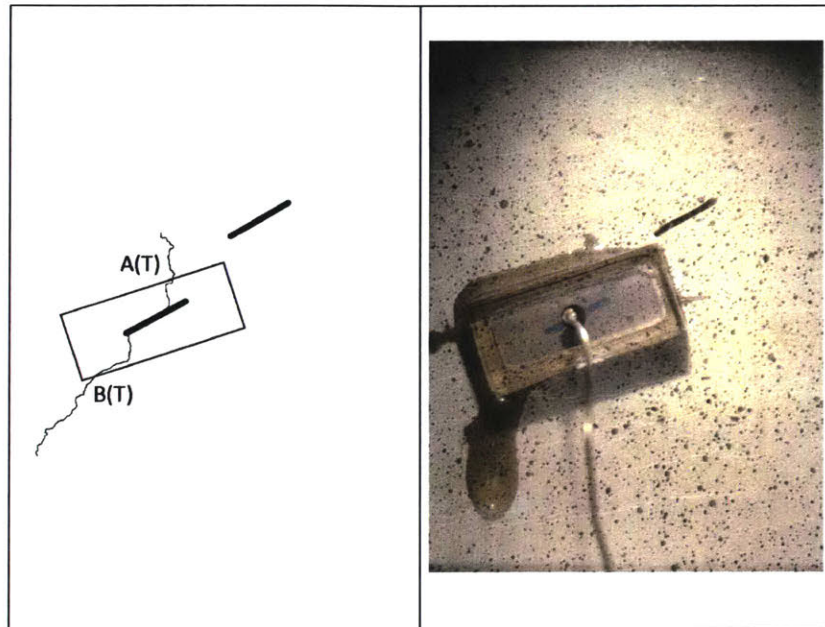


Figure 91 - Sketch 5: crack propagation, end of crack B(T) propagation.

Sketch 6 is taken at the end of the test (refer to Figure 84), determined by the lack of events afterwards. At this point in the test, $t = 920.81 \text{ seconds}$, $P = 2.389 \text{ MPa}$, $V = 0.3751 \text{ cm}^3$. In the time between Sketch 5 and Sketch 6, tensile crack A(T) slightly propagated and then stopped (Figure 92). Crack A(T) propagated for 30 seconds since propagating past the flaw seal boundary. After this point in the test, propagation of current cracks ceased, and no new cracks initiated. This geometry and loading condition resulted in category 1: no coalescence (refer to Figure 29).

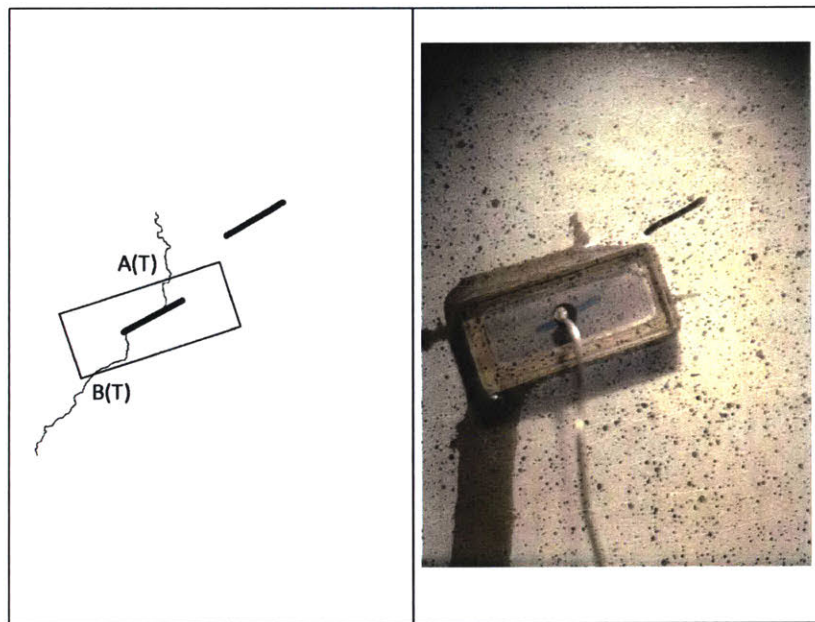


Figure 92 - Sketch 6: end of crack A(T) propagation.

There are a few key take-aways from the analysis of this test. The minute kinks in the fracture path observed in the single vertical flaw specimens were also observed throughout the fracture propagation in the 2a-30-30 specimen. Also, the lag between crack tip advancement and fluid front was observed, especially when a crack that has temporarily arrested continues propagating across bedding planes. Finally, a key result is the interaction of the pressurized hydraulic fracture with the non-pressurized flaw, or lack of it for this geometry.

Three other specimens with the same flaw geometry of 2a-30-30 were tested in the same manner and the detailed analyses can be seen in Appendix A2. Figure 93 shows a summary of all uniaxial compression with hydraulic fracture tests run on Opalinus shale specimens with horizontal bedding planes and a flaw pair geometry of 2a-30-30.

As can be seen, there is quite a bit of variability in the detailed fracture propagation path. However, the most consistent conclusion is that the 2a-30-30 flaw pair geometry results in no coalescence. For all tests, the hydraulic fractures propagate in the direction of uniaxial loading. Also, the mechanism of propagation is similar for all specimens: the induced hydraulic fracture propagates across bedding planes, arrests at a prominent bedding plane, pressurized oil fills the prominent bedding plane, then propagation across bedding planes continues.

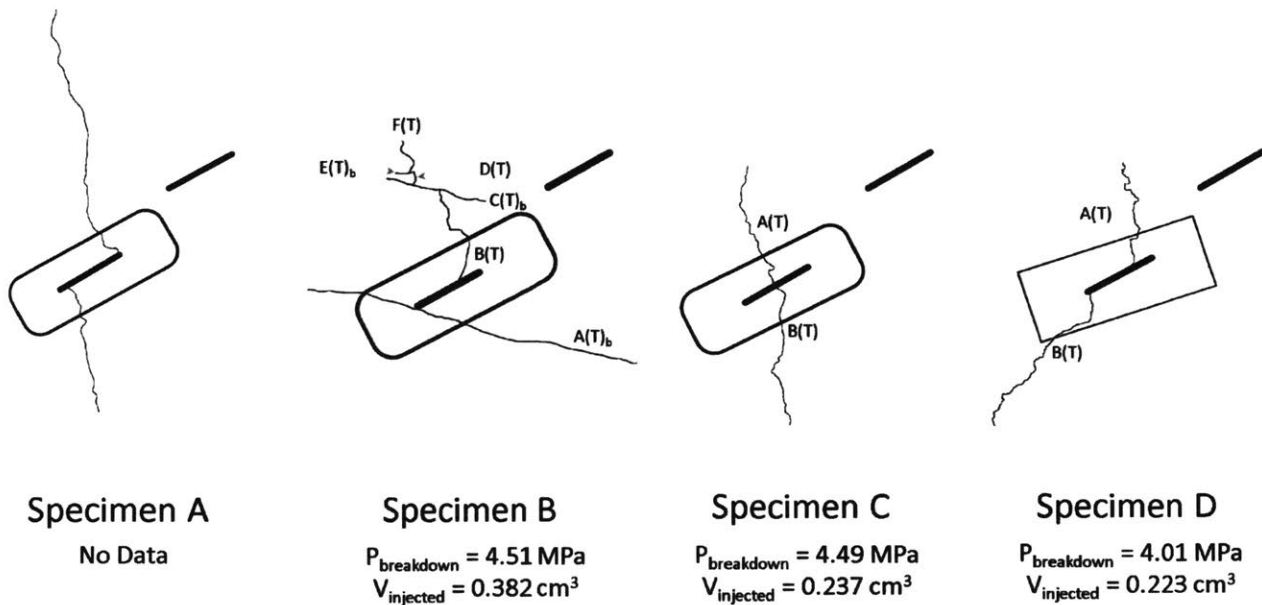


Figure 93 – Summary of all uniaxial compression with hydraulic fracture tests on flaw pair geometry 2a-30-30 showing observed fracture behavior, breakdown pressure, and total injected volume at breakdown.

What varies between the specimens is the degree of time/extent of bedding plane filling versus propagating across bedding. For example, in Specimen B, crack A(T)_b propagated along the bedding plane by filling it rather than propagate any crack vertically across bedding planes. However, tensile

crack B(T) propagated across bedding until it arrested at bedding plane C(T)_b, and propagated along C(T)_b significantly before D(T) propagated vertically. In the case of the hydraulic fractures in Specimen C and Specimen D, the time/extent a bedding plane was being filled was far less than that seen in Specimen B.

While looking at the propagation in detail, it was realized that the hydraulic fractures in Specimen C and Specimen D still did arrest at bedding planes and filled them throughout propagation, but the time propagating across bedding was faster than filling bedding. This is likely an indication of the condition of weakness planes (bedding planes) which in turn indicate the existence of possible flow paths between the two faces of a bedding plane. Crack A(T)_b in Specimen B likely had paths that the oil could flow through with less resistance all the way across the width of the specimen than to propagate a new crack. As for crack C(T)_b, the oil could only flow through the lateral extent shown with little resistance, and then D(T) could propagate after enough pressure in the bedding plane C(T)_b was established.

It was noted that Specimen B came from a core that had very weak bedding planes to the extent that the core could be easily pulled apart by hand. Specimen B was much more challenging to prepare than Specimen C and Specimen D. The fact that Specimen C and Specimen D were more “intact” than Specimen B explains why the pressurized oil may not have filled any bedding planes significantly throughout the propagation process.

4.2.3 2a-30-60

This next and final experimental series ran the same experiments as before on specimens with a flaw pair geometry of 2a-30-60, as shown in Figure 94. As stated previously, the bottom flaw is chosen for pressurization so that the oil flowing out of the hydraulic fracture does not obstruct the visual imagery, and key events can be accurately described.

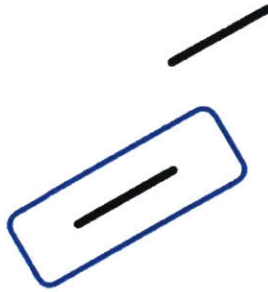


Figure 94 – 2a-30-60 geometry where the bottom flaw is pressurized and right flaw is not pressurized. The blue rectangle indicates the flaw seal boundary of the rubber membrane.

The results presented next are for one of three specimens tested. The full analysis for this specimen is shown below, starting with the test data plotted in Figure 95.

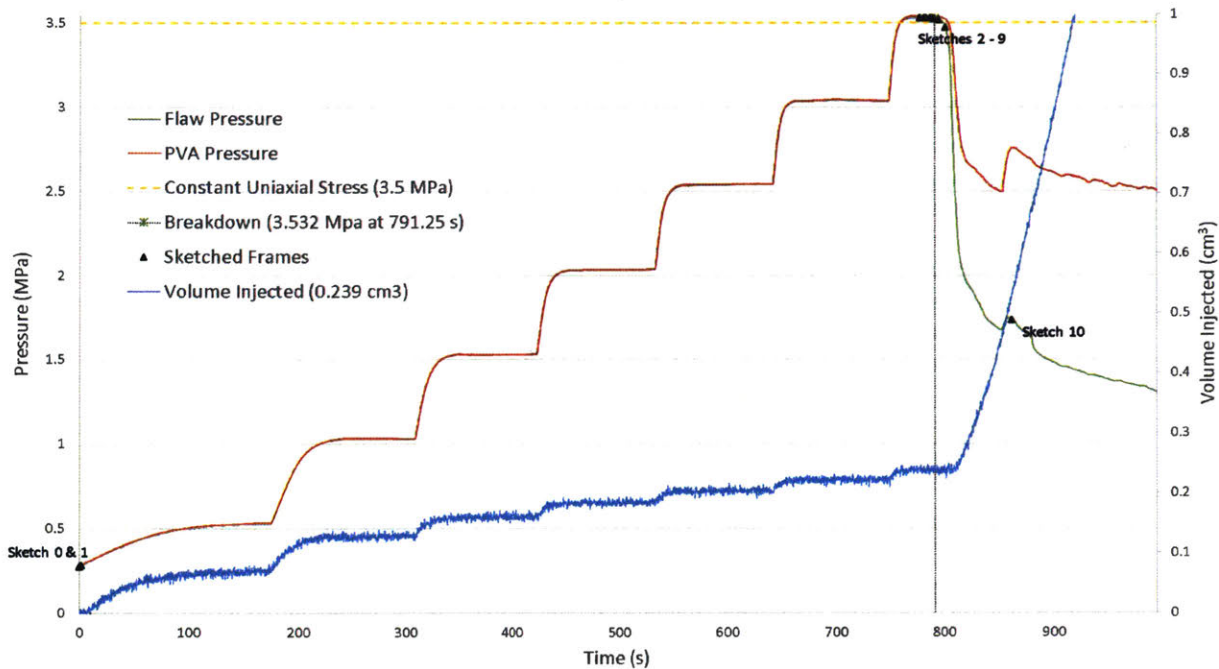


Figure 95 - Test data collected from PVA pressure transducer, feedback pressure transducer, and PVA LVDT on Opalinus shale prismatic specimen with flaw pair geometry 2a-30-60. Test starts when system is closed by attaching flaw pressure transducer to third needle. Test ends after fracture stops propagation.

The example shown is for the test OP-HF-2a-30-60-C. After the flaw was pressurized to a target pressure of 3.5 MPa, the pressure was held shortly before dropping due to crack propagation. Table 12 tabulates the dimensions of the specimen tested, while Table 13 shows the test data.

Table 12 – Dimensions of specimen OP-HF-2a-30-60-C.

OP-HF-2a-30-60-C Dimensions			
Height (h)	Width (w)	Thickness (t)	Area (A=wxt)
[in]	[in]	[in]	[in ²]
4.073	2.185	1.026	2.24

Table 13 - Summary of test loads and injected volume for OP-HF-2a-30-30-D.

OP-HF-2a-30-30-D Test Summary			
Vertical Applied Load	Vertical Applied Stress	Maximum Hydraulic Pressure	Volume Injected until Loss of Pressure
[kN]	[MPa]	[MPa]	[cm ³]
5.06	3.5	3.53	0.239

For convenience, Figure 96 is a zoomed version of Figure 95. It shows the point at which the flaw pressure begins to drop. From Figure 96, it was determined that the breakdown pressure is 3.53 MPa which occurred at 791.25 seconds from the beginning of the test.

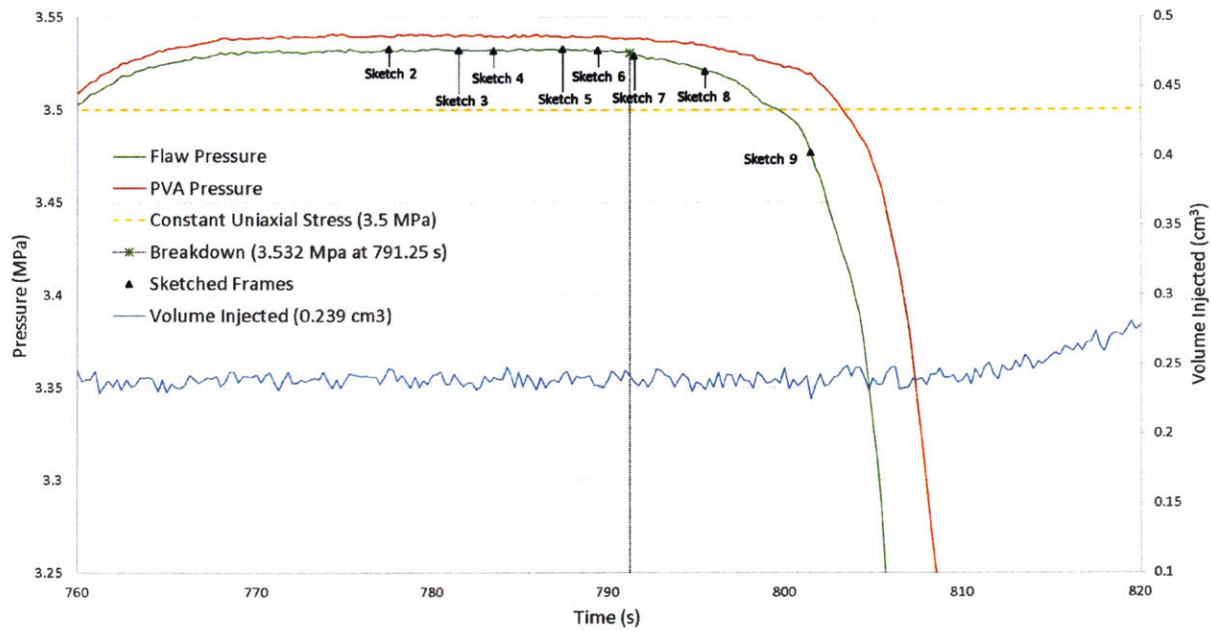


Figure 96 – Close-up of pressure drop from test data shown in Figure 95 used to determine specimen breakdown.

Figure 97 shows Sketch 0 taken at the beginning of the test, as indicated in Figure 95. This is a prismatic 4"x2"x1" specimen with a flaw pair geometry of 2a-30-60 and horizontal bedding planes. As shown in Figure 97, the left flaw is fully saturated with hydraulic fluid at this stage and testing is ready to commence. The initial pressure from the saturation phase is 0.277 MPa. Volume injection is referenced back to this point in the test, the point of which the system was closed. At this point in the test, $t = 0$ seconds, $P = 0.277$ MPa, $V = 0$ cm³. The pressure is then increased in 0.5 MPa increments until specimen failure. Note that some bedding planes intersecting the pressurized flaw were filled with oil during the saturation phase.

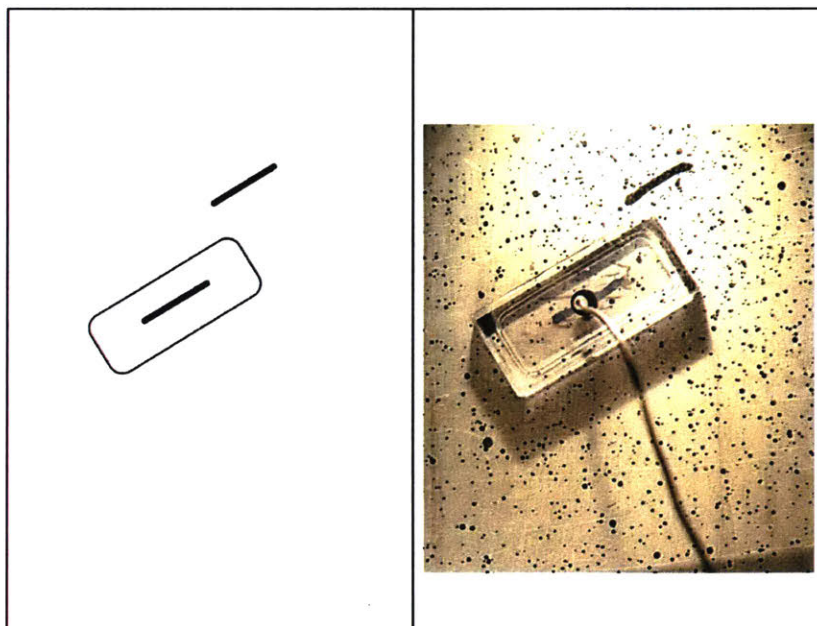


Figure 97 – Sketch 0: initial configuration of the specimen OP-HF-2a-30-60-C after flaw saturation.

Sketch 1 is taken moments after Sketch 0 (refer to Figure 95). At this point in the test, $t = 1.052 \text{ seconds}$, $P = 0.282 \text{ MPa}$, $V = 0.0013 \text{ cm}^3$. Tensile crack A(T)_i initiated during the saturation phase prior to pressurization. The outer tip of the left flaw coincided with a bedding plane at the initiation point of A(T)_i, which developed into a crack upon filling with oil. Tensile crack B(T)_i initiated at this time in the test; i.e. the beginning of the pressurization phase. The inner tip of the left flaw also coincides with a bedding plane at the initiation point of B(T)_i (Figure 98).

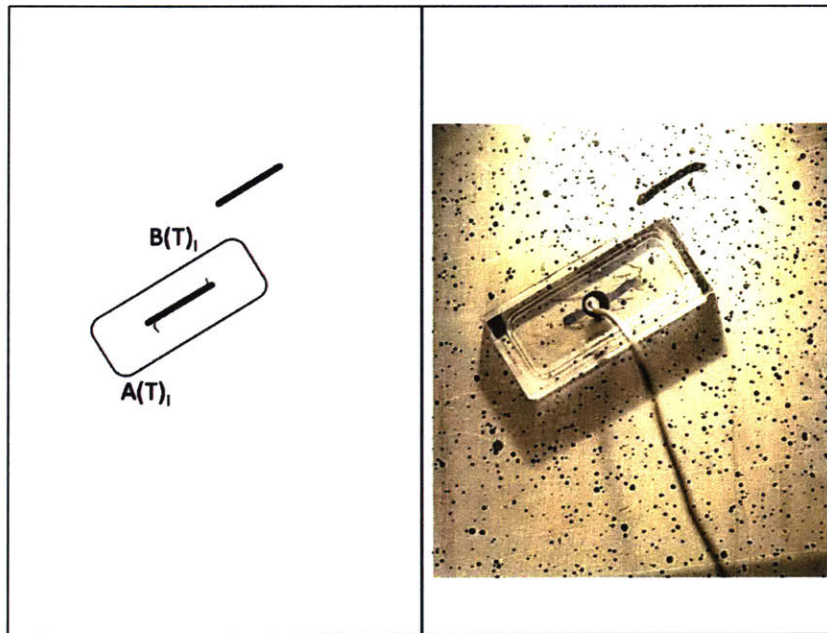


Figure 98 - Sketch 1: crack initiation within flaw seal boundaries.

Sketch 2 is taken prior to the determined breakdown pressure (refer to Figure 95). At this point in the test, $t = 777.502 \text{ seconds}$, $P = 3.533 \text{ MPa}$, $V = 0.2471 \text{ cm}^3$. First, $A(T)_i$ propagated slightly within the flaw seal boundary and then arrested at a bedding plane. Afterwards, $B(T)_i$ propagated and arrested at a bedding plane as well. However, as the pressure increased, $B(T)_i$ propagated horizontally through the bedding plane it was arrested at, and then vertically upwards across bedding planes to the flaw seal boundary (this frame, Figure 99). Upon reaching the flaw seal boundary, a very small droplet of oil was observed to form at this point. However, pressure remained stable.

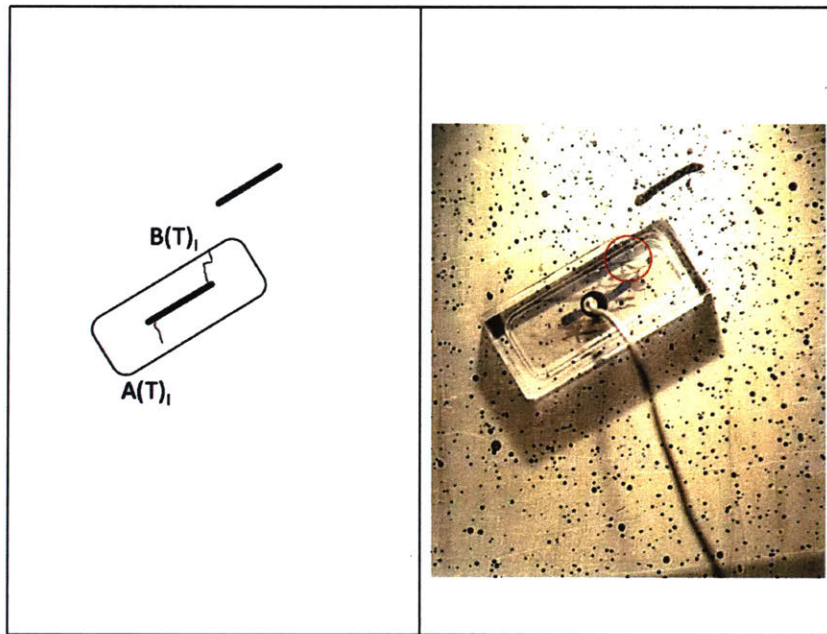


Figure 99 - Sketch 2: crack propagation within flaw seal boundary, $B(T)_i$ arrests at boundary.

Sketch 3 is taken prior to the determined breakdown pressure (refer to Figure 95). At this point in the test, $t = 781.502 \text{ seconds}$, $P = 3.532 \text{ MPa}$, $V = 0.2380 \text{ cm}^3$. Tensile crack B(T)_i remained arrested at the flaw seal boundary. Tensile crack A(T)_i continued propagating and arrested at the flaw seal boundary as well (Figure 100).

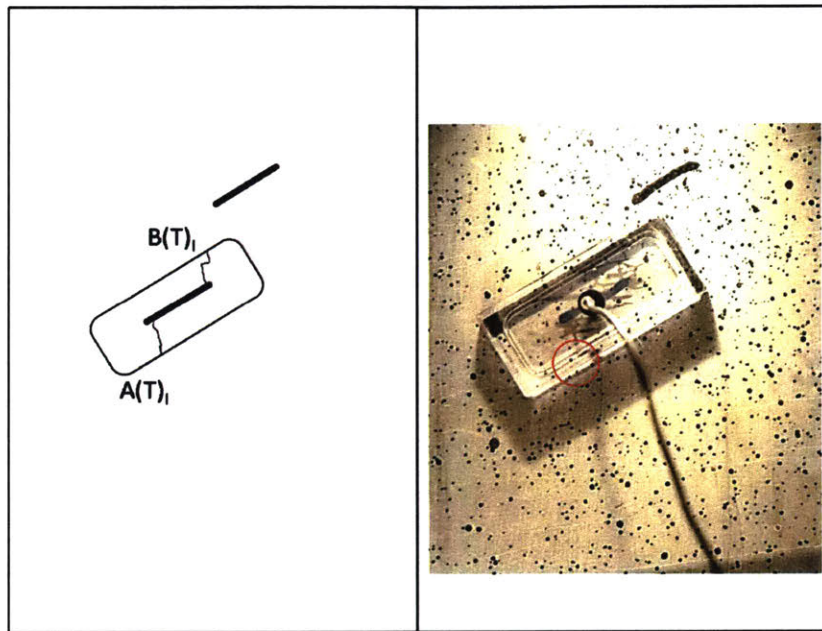


Figure 100 - Sketch 3: crack propagation with flaw seal boundary, A(T)_i arrests at flaw seal boundary.

Sketch 4 is taken prior to the determined breakdown pressure (refer to Figure 95). At this point in the test, $t = 783.502 \text{ seconds}$, $P = 3.532 \text{ MPa}$, $V = 0.2409 \text{ cm}^3$. The pressure remains constant at this point. As pressure was held, tensile crack $A(T)_1$ began propagating past the flaw seal boundary (Figure 101). (Despite $B(T)_1$ reaching the flaw seal boundary first, $A(T)_1$ propagated past the boundary first.)

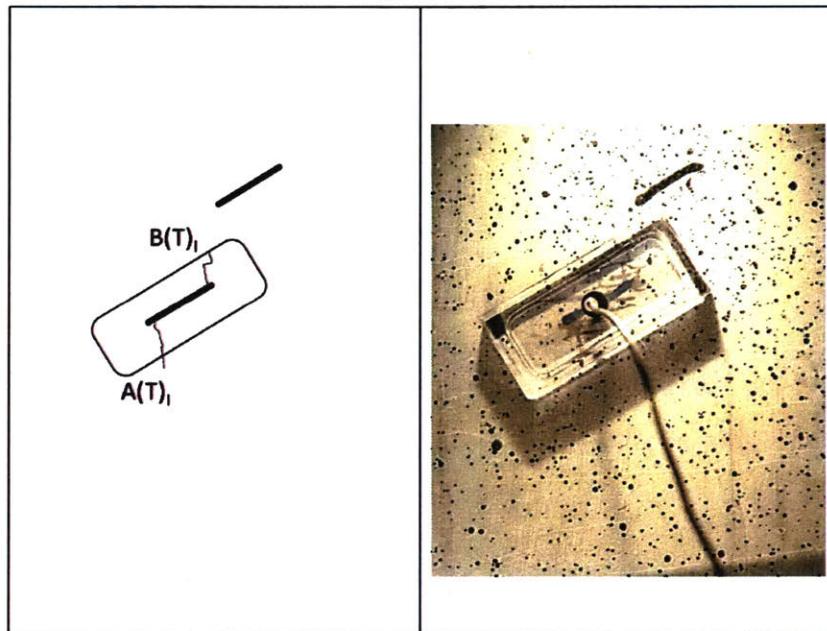


Figure 101 - Sketch 4: crack propagation past flaw seal boundary, $A(T)_1$.

Sketch 5 is taken prior to the determined breakdown pressure (refer to Figure 95). At this point in the test, $t = 787.502 \text{ seconds}$, $P = 3.533 \text{ MPa}$, $V = 0.2429 \text{ cm}^3$. Tensile crack A(T)₁ continued to propagate in a series of advancements and arrests at bedding plane boundaries, displaying a jagged propagation path. B(T)₁ propagated past the flaw seal boundary towards an angular-shaped fossil embedded in the shale matrix (indicated by the red arrow and circle in Figure 102).

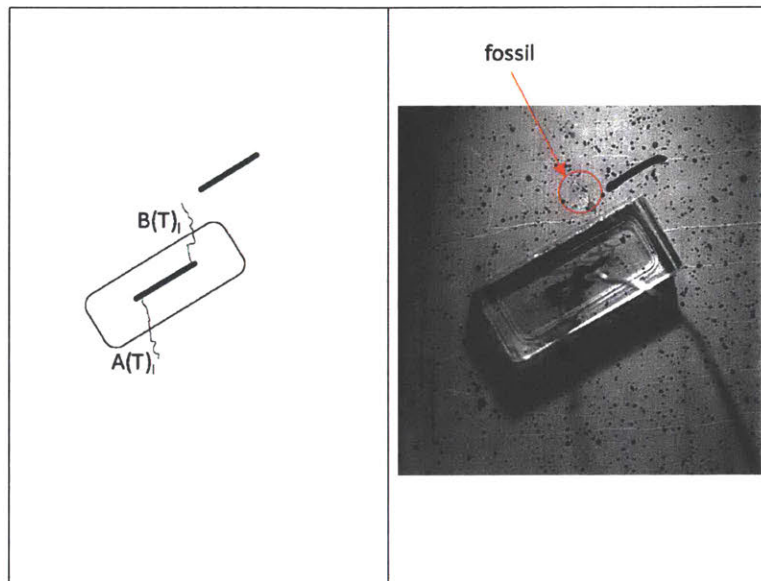


Figure 102 - Sketch 5: crack propagation past flaw seal boundary, B(T)₁.

Sketch 6 is taken moments prior to the determined breakdown pressure (refer to Figure 95). At this point in the test, $t = 789.502 \text{ seconds}$, $P = 3.532 \text{ MPa}$, $V = 0.2349 \text{ cm}^3$. Rather than propagate through the fossil, $B(T)_i$ propagated around the fossil boundary (Figure 103). $A(T)_i$ continued propagating in the same jagged manner stated for Sketch 5.

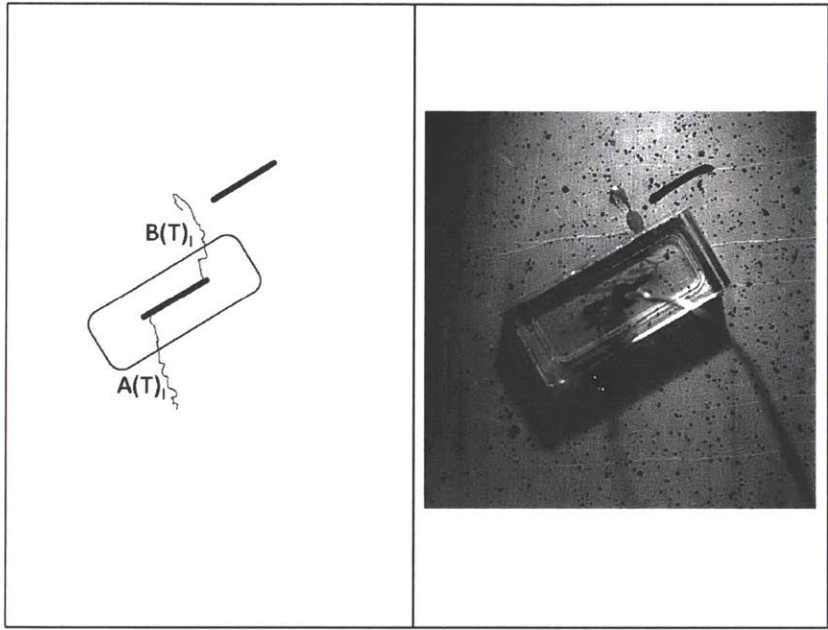


Figure 103 - Sketch 6: crack propagation.

Sketch 7 is taken moments after the determined breakdown pressure (refer to Figure 95). At this point in the test, $t = 791.502 \text{ seconds}$, $P = 3.530 \text{ MPa}$, $V = 0.2372 \text{ cm}^3$. After $B(T)_i$ completed propagation around the perimeter of the fossil, it continued propagating upwards past the fossil (Figure 104). This fossil is seen on the specimen surface and does not penetrate through the entire thickness of the specimen, whereas $B(T)_i$ does (observed after the experiment). It is likely that $B(T)_i$ did not propagate around the perimeter of the fossil, rather it propagated behind the fossil, and the oil flowed out around the fossil perimeter. $B(T)_i$ arrested at this point. Crack $A(T)_i$ continued propagating.

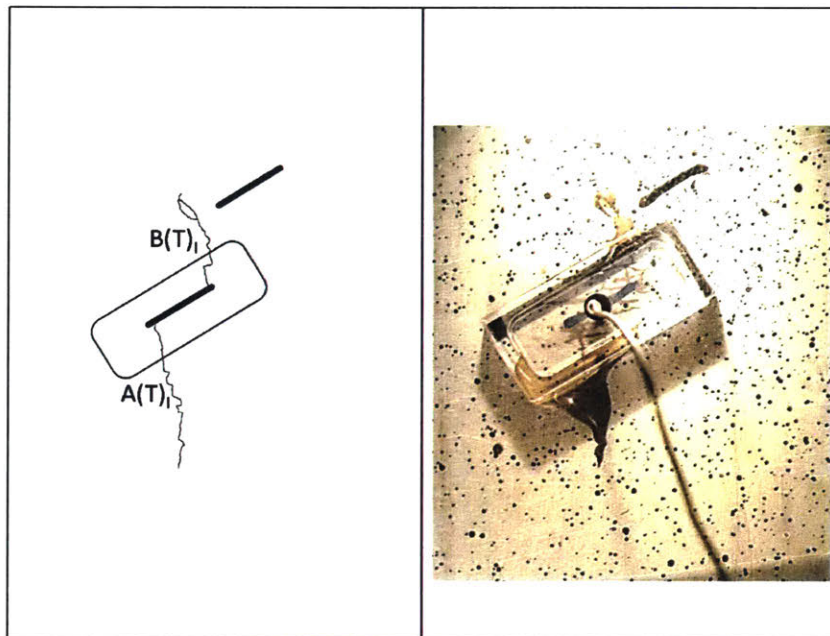


Figure 104 - Sketch 7: crack propagation, $B(T)_i$ arrests.

Sketch 8 is taken after the determined breakdown pressure (refer to Figure 95). At this point in the test, $t = 795.502 \text{ seconds}$, $P = 3.521 \text{ MPa}$, $V = 0.2314 \text{ cm}^3$. Although $B(T)_i$ stopped propagating, a new tensile crack, $C(T)_i$, branched off $B(T)_i$ at a bedding plane (Figure 105). $C(T)_i$ propagated along the bedding plane towards the right flaw.

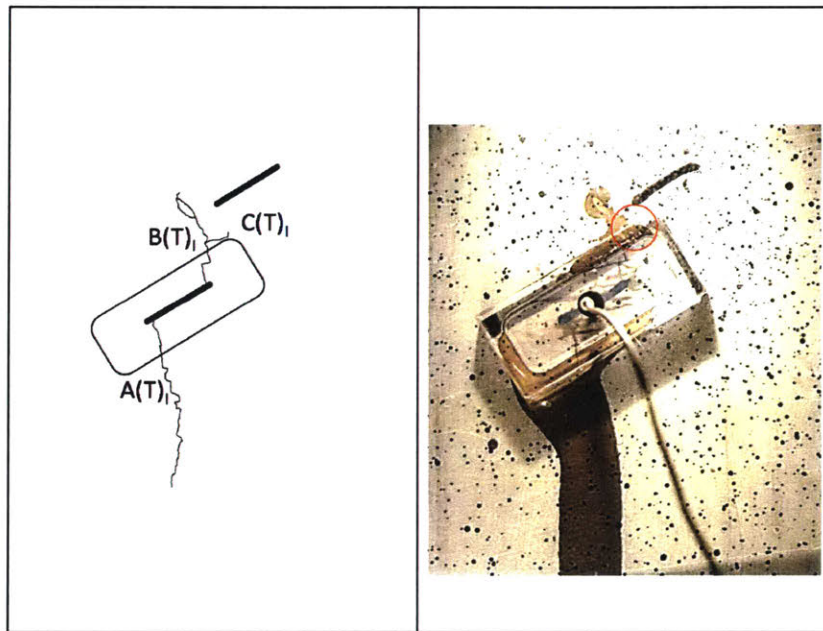


Figure 105 - Sketch 8: crack propagation, $C(T)_i$ branches off $B(T)_i$.

Sketch 9 is taken after the determined breakdown pressure (refer to Figure 95). At this point in the test, $t = 801.502 \text{ seconds}$, $P = 3.477 \text{ MPa}$, $V = 0.2246 \text{ cm}^3$. Once $C(T)_i$ reached a point below the inner tip of the right flaw, its propagation mechanism changed from propagating through a bedding plane to propagating across bedding planes upwards towards the inner tip of the right flaw (Figure 106). $A(T)_i$ continued propagating and arrested at this point.

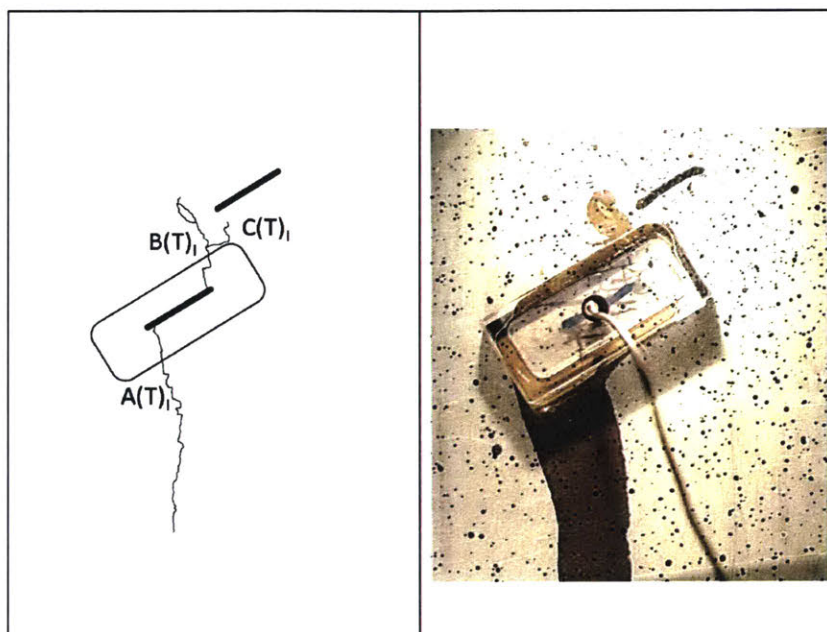


Figure 106 - Sketch 9: crack propagation, $A(T)_i$ arrests.

Sketch 10 is taken towards the end of the test after significant pressure dropped (refer to Figure 95). At this point in the test, $t = 861.502 \text{ seconds}$, $P = 1.737 \text{ MPa}$, $V = 0.5328 \text{ cm}^3$. $B(T)_i$ and $A(T)_i$ remained arrested throughout the duration between Sketch 9 and Sketch 10. $C(T)_i$ continued propagating slowly across bedding planes in a jagged series of advancements and arrests towards the inner tip of the right flaw until coalescing (Figure 107). This geometry and loading condition lead to a category 2: indirect coalescence by two cracks.

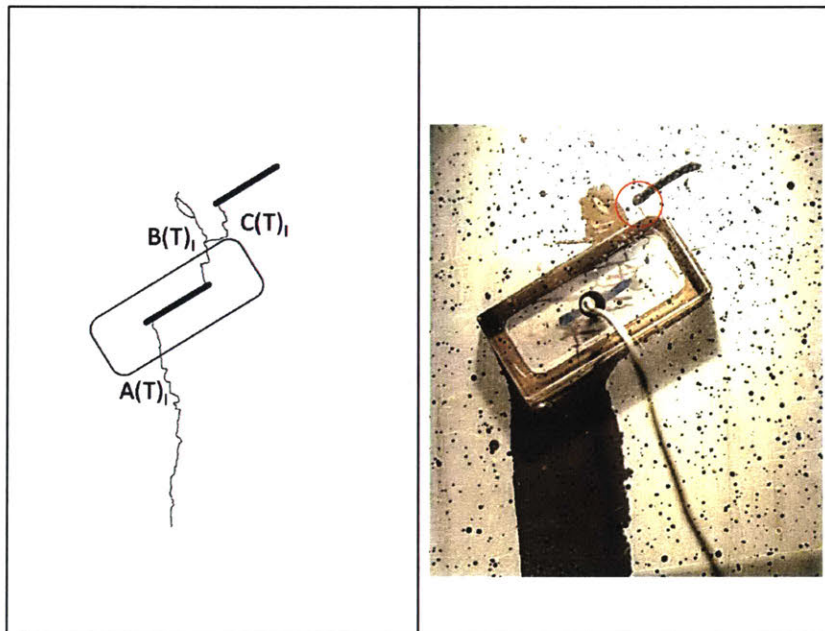


Figure 107 - Sketch 10: coalescence.

The hydraulic fractures produced in this specimen behaved similar to the other geometries tested in two aspects. First, all shale specimens showed that hydraulic fractures propagate in a jagged manner of propagating across some bedding planes, and along others. Also, the lag between crack tip and fluid front was observed. The difference observed in the 2a-30-60 geometry relative to the 2a-30-30 was the interaction between the pressurized hydraulic fracture with the non-pressurized flaw (see below).

Two other specimens with the same flaw geometry of 2a-30-60 were tested in the same manner and the detailed analyses can be seen in Appendix A2. Figure 108 shows a summary of all uniaxial compression tests with hydraulic fracturing on Opalinus shale specimens with horizontal bedding planes and a flaw pair geometry of 2a-30-60.

Again, there is quite a bit of variability in the detailed fracture propagation path. Also again, the most consistent conclusion is that the 2a-30-60 flaw pair geometry results in indirect coalescence.

For all tests, the hydraulic fractures propagating across bedding planes propagate in the direction of uniaxial loading.

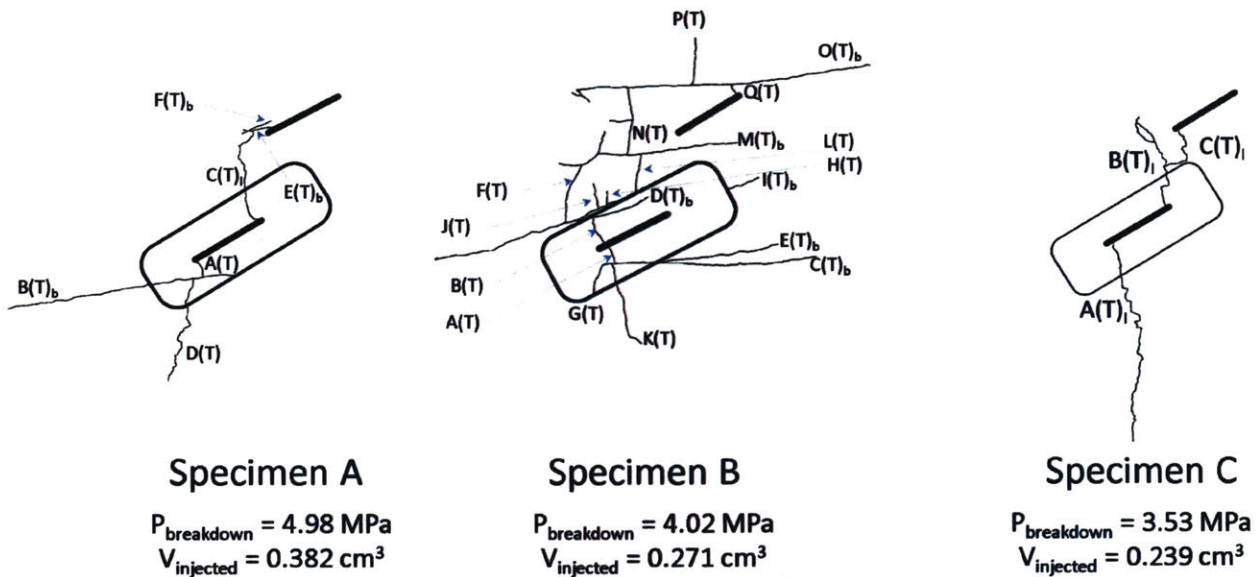


Figure 108 – Summary of all uniaxial compression with hydraulic fracture tests on flaw pair geometry 2a-30-60 showing observed fracture behavior, breakdown pressure, and total injected volume at breakdown.

Like the previous geometry, what varies between the specimens is the degree of time/extent of bedding plane filling versus propagating across bedding. For example, Specimen B was very weak along many bedding planes whereas Specimen C was the most “intact” specimen. Specimen A had a significant bedding plane, B(T)_b, that allowed oil to flow through. There is a strong relation between how well a specimen’s bedding planes are held together and the extent of bedding plane flow observed.

While the hydraulic fracture propagation paths observed in all three specimens were different, all specimens resulted in coalescence between the two flaws. Although the coalescence points on the non-pressurized flaw differed for each specimen, the pressurized hydraulic fractures propagated and coalesced at the non-pressurized flaw tips. This may be due to a tensile stress concentration induced by the uniaxial load on the specimen.

This concludes section 4.2 Results.

4.3 Discussion

This section will discuss the major finding of the experiments shown in section 4.2.

4.3.1 Lag Between Crack Tip and Liquid Front

One of the major questions that puzzled researchers and industry engineers was the nature of the propagating hydraulic fracture in the field. One possibility is that the fluid front is constantly moving along with the advancing crack tip. Another is that the fluid front was lagging behind the crack tip. One of the advantages of the hydraulic fracture laboratory experiment described in section 4.1 is the ability to visually capture such phenomena.

Figure 109 shows two examples of the lag between the propagating hydraulic fracture and the driving pressurized liquid. The left image was obtained from the high-speed video of one of the tests done on a specimen with a single vertical flaw. Throughout the hydraulic fracture propagation, there were instances that clearly showed the crack temporarily stopping at a bedding plane, propping open the next segment of the fracture in tension, and only afterwards would the fluid fill the vacated space. The right image was obtained from the high-resolution images of one of the tests done on a specimen with a flaw pair geometry of 2a-30-60. The liquid can be seen here at about one third of the distance between the flaw seal boundary and the inner tip of the right flaw. This pressurized liquid propped open the crack which coalesced with the right flaw while the fluid lagged behind. The propagation of the crack was

faster than the advancement of the fluid, and as such, the liquid was slowly flowing into the void it created. Both images have been marked with a “1”, indicating the location of the liquid front, and a “2”, indicating the location of the crack tip.

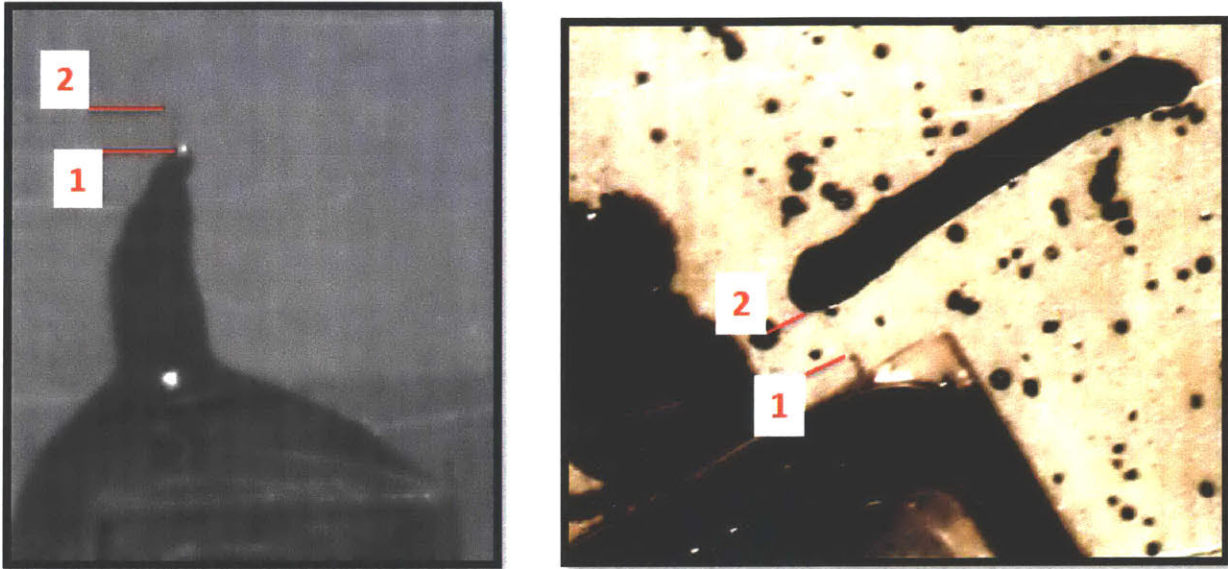


Figure 109 – examples of crack tip propagating ahead of driving pressurized liquid. Left: hydraulic fracture propagating from pressurized single vertical flow. Right: hydraulic fracture propagating from pressurized flaw interacting with non-pressurized flaw in 2a-30-60 geometry. 1: location of fluid front. 2: location of crack tip.

These are only two examples experimentally showing the lag between the propagating hydraulic fracture tip and the driving liquid. This “lag” was observed at least once for all specimens tested.

4.3.2 Propagation Process of a Hydraulic Fracture

The fluid lag discussed above leads to the discussion of the mechanism of propagation of a hydraulic fracture. Figure 110 shows a schematic of the different possible propagation paths a hydraulic fracture may take in a layered medium such as shale.

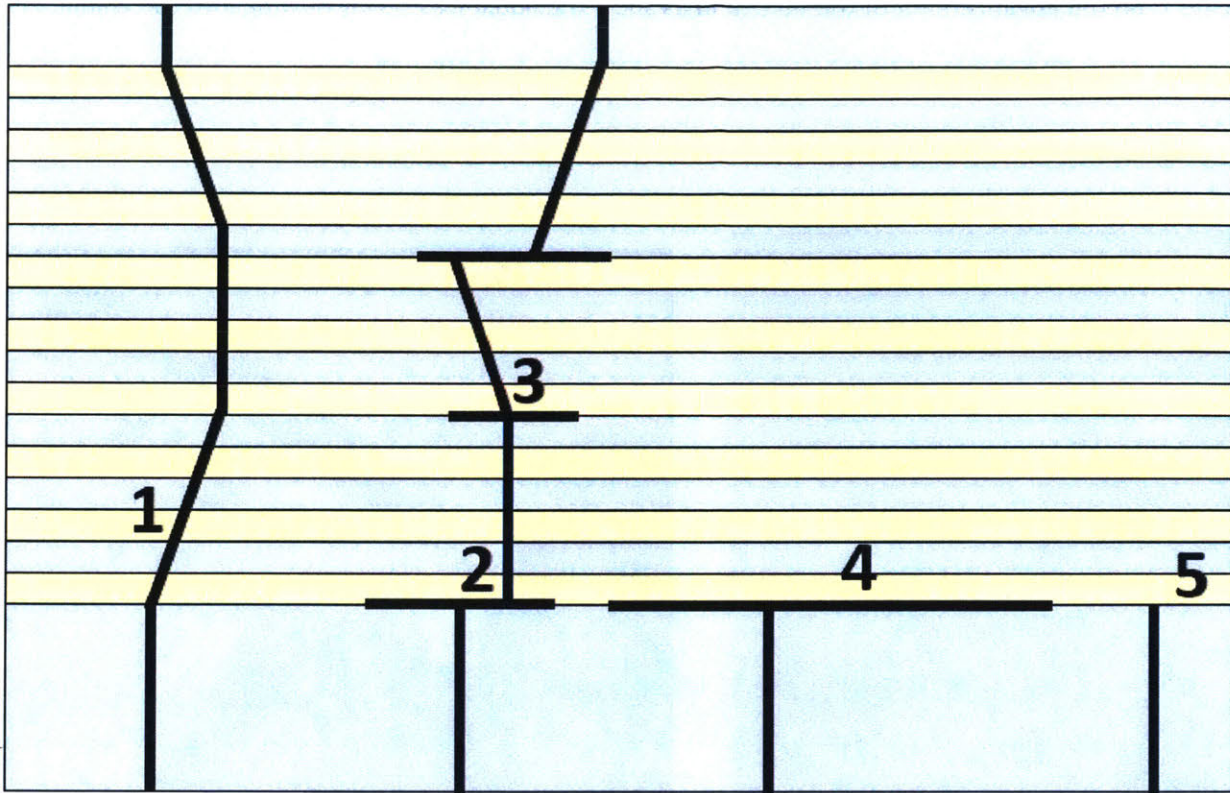


Figure 110 – Schematic of fracture propagation schemes in a horizontally layered material subjected to vertical uniaxial load.

Modified from Fisher and Warpinski (2012).

Such behaviors were observed for multiple tests that were presented in section 4.2. The hydraulic fracture in shale was observed to propagate in the following way:

- hydraulic pressure builds up and a hydraulic fracture initiates in tension then propagates in the direction of maximum applied stress (lag between advancing crack tip and fluid front may occur).
- When encountering a bedding plane, the hydraulic fracture:
 - either continues to propagate across the bedding plane without arresting (Figure 110 scheme: 1),
 - or temporarily arrests at the bedding plane and propagates along it until sufficient pressure builds up to allow the hydraulic fracture to continue propagating across, either at the original arrest point (Figure 110 scheme: 3) or elsewhere along the pressurized bedding plane (Figure 110 scheme: 2),

- or temporarily arrests at the bedding plane and propagates along it (Figure 110 scheme: 4) where there is not sufficient pressure build-up to allow the hydraulic fracture to continue propagating across bedding planes,
- or permanently arrests (Figure 110 scheme: 5) where there is not sufficient pressure build-up for further propagation.

Hydraulic fracture propagation is essentially a continuous incremental cycle of the above bullet points until the pressure is no longer high enough to drive the crack. The shale specimen OP-HF-2a-30-60-B (detailed analysis in Appendix A2) is taken as an example to illustrate some of the above-mentioned fracture propagation schemes (Figure 111). These observations hold for all shale specimens tested regardless of flaw geometry.

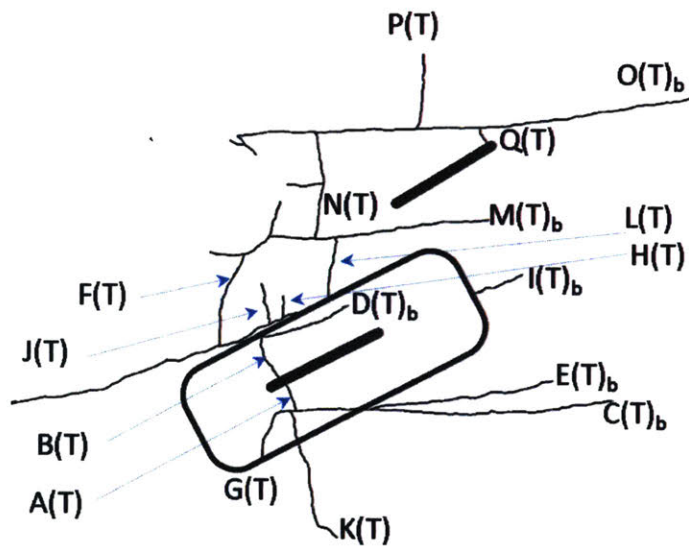


Figure 111 - Final sketch of specimen OP-HF-2a-30-60-B

5. Conclusions

The primary aim of this research was to gain a fundamental understanding of the mechanisms underlying the “dry” fracture process of different shales and to compare it with the hydraulic fracture process in shale.

Characterization

Two different shales were investigated: Vaca Muerta shale and Opalinus shale. The Vaca Muerta shale cores were extracted from a deep petroleum reservoir in the Neuquén Basin, Argentina whereas the Opalinus shale cores were extracted from a shallow clay-rich facies in Mont Terri.

Each shale’s mineralogy was found through XRPD. Vaca Muerta shale showed strong heterogeneity with data points scattered throughout the mineral ternary plot. Opalinus shale was far less heterogeneous as various samples gathered around the clay corner of the mineral ternary plot varying slightly in quartz and carbonate contents.

Mechanical properties of both shales were determined through uniaxial tests on intact prismatic specimens. Vaca Muerta shale had an ultimate strength of 29.4 MPa versus 17.3 MPa for Opalinus shale. It is also stiffer than the Opalinus shale with Young’s Modulus of 1.49 GPa versus 1.33 GPa.

Specimen Preparation

Specimen preparation techniques were developed for harder shales such as Vaca Muerta shale and shales that are high in quartz content. It was important to develop techniques that could successfully dry cut (given the water sensitivity of shale) and produce the desired specimen dimensions.

These harder shales were successfully cut using a diamond impregnated blade combined with a mist-spraying lubrication system using anhydrous oil as a lubricant to cool the blade. Holes were drilled using diamond coated drill bits combined with a sensitive hand-feeding chuck for drilling sub-millimeter sized

holes. The holes were drilled with the peck drilling technique, which helps remove drilled material as well as cooling the bit. Finally, a rigid steel wire coated with diamond was used to cut the flaws. After a specimen is cut, it is polished with sandpaper then vacuum sealed to preserve its natural water content.

“Dry” Fracture Experiments

Specimens were subjected to uniaxial load which induced fractures from pre-existing flaws. These “dry” fracture experiments were done on Vaca Muerta shale to compare them to Opalinus shale (Morgan, 2015).

The coalescence pattern between two flaws of the geometry 2a-30-0 resulted in indirect coalescence in Vaca Muerta as well as in Opalinus shales, while direct coalescence was observed for the 2a-30-30 geometry in both the Vaca Muerta and Opalinus shales.

Overall, Vaca Muerta shale displayed fracture initiation, -propagation, and –coalescence behavior that corresponded well to the one which was observed in Opalinus. The conclusion drawn from this is that the results from fracture tests on Opalinus shale can be extended to other shales.

Hydraulic Fracture Experiments

A test setup capable of pressurizing an individual flaw in prismatic shale specimens subjected to a constant uniaxial load and producing hydraulic fractures was developed. This setup also allows one to monitor internal flaw pressure throughout the pressurization process, as well as visually capture the processes that occur when the shale is hydraulically fractured.

Opalinus shale was tested using the developed setup mentioned above. First, three specimens with a single vertical flaw were tested and successfully hydraulically fractured. The hydraulic fracturing was visually captured and related to the internal flaw pressure. These tests were used for the proof of concept of the test setup, but also gave insight into the nature of a propagating hydraulic fracture. Of

particular interest are the observed lag between the crack tip and the liquid front as well as the way the hydraulic fracture propagates across and along to bedding planes.

Next, seven Opalinus shale specimens with flaw pairs were tested to capture the interaction of a hydraulic fractures produced from a pressurized flaw with a non-pressurized flaw. Four of these specimens had the geometry 2a-30-30, and three specimens had the geometry 2a-30-60.

All 2a-30-30 specimens showed no coalescence between the flaws while all 2a-30-60 specimens resulted in indirect coalescence. In all tests, a lag was visually captured between the crack tip and the liquid front.

Hydraulic fracture propagation in shale is complex because of the bedding planes. The hydraulic fractures normally propagate in the direction of the applied uniaxial load. However, when encountering a bedding plane, the hydraulic fracture either:

- either continues to propagate across the bedding plane without arrest,
- or temporarily arrests at the bedding plane and propagates along it until sufficient pressure builds up to allow the hydraulic fracture to continue propagating across (either at the original arrest point or elsewhere along the pressurized bedding plane),
- or temporarily arrests at the bedding plane and propagates along it (no sufficient pressure build-up to allow hydraulic fracture to continue propagating across bedding planes),
- or permanently arrests.

Flaw Interaction in Hydraulic Fracture versus “Dry” Fracture

Table 14 summarizes the results of the “dry” fracture experiments done by Morgan (2015) and the results of the hydraulic fracture experiments presented in section 4.2, showing that the coalescence patterns in the “dry” fracture experiments differ from those in the hydraulic fracture experiments.

Table 14 – Comparison of coalescence category observed in “dry” fracture experiment (uniaxial loading to failure) with hydraulic fracture experiment (pressurize an individual flaw to failure in an Opalinus shale specimen subjected to a constant uniaxial load) for two flaw pair geometries.

Flaw Pair Geometry	Coalescence Category	
	“Dry” Fracture	Hydraulic Fracture
2a-30-30	5: Direct	1: No Coalescence
2a-30-60	6: Direct	2: Indirect

Despite Opalinus shale specimens having the same geometries, the coalescence patterns observed differ due to the change in loading conditions. This systematic difference needs further investigation.

Summary

The major contributions of this thesis are:

- Development of a specimen preparation procedure that allows one to obtain specimens with different flaw geometries for a variety of shales.
- Development of a hydraulic fracture experiment that allows one to pressurize an individual flaw and monitor the pressure in the flaw while simultaneously allowing one to observe produced cracks in detail.
- Observation of the hydraulic fracture propagation mechanism as well as a lag between crack tip and liquid front during propagation.
- Distinguish the crack interaction behavior for “dry” and hydraulic fracture experiments for various flaw geometries.

Bibliography

- Alberta Energy Regulator (AER) (2017). What is Unconventional Oil and Gas?. <https://www.aer.ca/about-aer/spotlight-on/unconventional-regulatory-framework/what-is-unconventional-oil-and-gas>
- Askenazi, A., Biscayart, P., Cáneva, M., Montenegro, S., Moreno, M., & SA, Y. (2013). Analogía entre la Formación Vaca Muerta y Shale Gas/Oil Plays de EEUU.
- Bobet, A. (1997). Fracture coalescence in rock materials: experimental observations and numerical predictions (Doctoral dissertation, Massachusetts Institute of Technology).
- Boggs, S. (2006). Principles of sedimentology and stratigraphy. Pearson Prentice Hall.
- Blatt, H., Middleton, G. V., & Murray, R. C. (1980), Origin of Sedimentary Rocks, 2nd Edition, Prentice-Hall, Inc. Englewood Cliffs
- Campbell, C. V. (1967). Lamina, laminaset, bed and bedset. *Sedimentology*, 8(1), 7-26.
- Cook, T., & Perrin, J. (2016, March 15). U.S. Energy Information Administration - EIA - Independent Statistics and Analysis. Retrieved January 3, 2017, from <http://www.eia.gov/todayinenergy/detail.php?id=25372>
- Energy4me. (2015). History of Hydraulic Fracturing | energy4me. Retrieved August 17, 2016, from <http://energy4me.org/hydraulic-fracturing/history-of-hydraulic-fracturing/>
- Fisher, M. K., & Warpinski, N. R. (2012, February 1). Hydraulic-Fracture-Height Growth: Real Data. Society of Petroleum Engineers. doi:10.2118/145949-PA
- Fri, R. W. (2006). From Energy Wish Lists to Technological Realities. *Issues in Science and Technology*, 23(1), 63-68.
- Germaine, J. T., & Germaine, A. V. (2009). Geotechnical laboratory measurements for engineers. Hoboken, NJ: John Wiley.
- Gonçalves da Silva, B. M. (2009). Modeling of crack initiation, propagation and coalescence in rocks (Master's thesis, Massachusetts Institute of Technology).
- Gonçalves da Silva, B. M. (2016). Fracturing processes and induced seismicity due to the hydraulic fracturing of rocks. (Doctoral dissertation, Massachusetts Institute of Technology).
- Hagenmana, E. (2014, October 20). Petroleum System and its Elements. Lecture presented at GEO 301 in American University of Nigeria, Yola. Retrieved January 3, 2017, from <http://www.slideshare.net/ykb778/element-of-petroleum-system>
- Magoon, L. and Beaumont, E. (2003). "Petroleum Systems". AAPG Search and Discover, Article # 40068
- Miller, J. T. (2008). Crack coalescence in granite (master's thesis, Massachusetts Institute of Technology).
- Montgomery, C. T., & Smith, M. B. (2010, December 1). Hydraulic Fracturing: History of An Enduring Technology. Society of Petroleum Engineers. doi:10.2118/1210-0026-JPT

- Morgan, S. P. (2015). An experimental and numerical study on the fracturing processes in Opalinus shale (Doctoral dissertation, Massachusetts Institute of Technology).
- National Energy Technology Laboratory (NETL). (2011, March). Shale Gas: Applying Technology to Solve America's Energy Challenges. Retrieved March 12, 2016, from <http://www.netl.doe.gov/technologies/oil-gas/publications/brochures/>
- National Research Council. 2001. Energy Research at DOE: Was It Worth It? Energy Efficiency and Fossil Energy Research 1978 to 2000. Washington, DC: The National Academies Press. doi: 10.17226/10165.
- Pollard, D. D., & Fletcher, R. C. (2005). Fundamentals of structural geology. Cambridge University Press.
- Potter, P. E., Maynard, J., & Pryor, W. A. (1980). Sedimentology of shale: study guide and reference source. Springer Science & Business Media.
- Reyes, O. M. L. (1991). Experimental study and analytical modelling of compressive fracture in brittle materials (Doctoral dissertation, Massachusetts Institute of Technology).
- Sagasti, G., Ortiz, A., Hryb, D., Foster, M., & Lazzari, V. (2014, August 25). Understanding Geological Heterogeneity to Customize Field Development: An Example from the Vaca Muerta Unconventional Play, Argentina. Unconventional Resources Technology Conference. doi:10.15530/URTEC-2014-1923357
- Saldungaray, P. M., & Palisch, T. T. (2012, January 1). Hydraulic Fracture Optimization in Unconventional Reservoirs. Society of Petroleum Engineers. doi:10.2118/151128-MS
- Selley, R. C. (1985). Elements of petroleum geology. New York: W.H. Freeman and Co.
- Singer, A., & Müller, G. (1979). Diagenesis in argillaceous sediments. *Developments in Sedimentology*, 25, 115-212.
- Tourtelot, H. A. (1960). Origin and use of the word "shale". *American Journal of Science*, 258, 335-343.
- Trembath, Alex, Jesse Jenkins, Ted Norhaus, and Michael Shellenberger. Where the Shale Gas Revolution Came From. Rep. N.p.: Breakthrough Institute, 2012. Print.
- US National Energy Technology Laboratory (NETL). (2011). Shale Gas: Apply Technology to Solve America's Energy Challenges [Brochure]. Author. Retrieved January 19, 2017, from <http://www.netl.doe.gov>
- Wells, B., & Wells, K. (2016, April 25). Shooters - A "Fracking" History. American Oil & Gas Historical Society (AOGHS) - Petroleum Age, 4. Retrieved January 3, 2017, from <http://aoghs.org/technology/hydraulic-fracturing/>
- Wong, L. N. Y. (2008) Crack coalescence in molded gypsum and Carrara marble (Doctoral Dissertation, Massachusetts Institute of Technology).
- Wong, L. N. Y., & Einstein, H. H. (2009a). Crack coalescence in molded gypsum and Carrara marble: part 1. Macroscopic observations and interpretation. *Rock Mechanics and Rock Engineering*, 42(3), 475-511.
- Wong, L. N. Y., & Einstein, H. H. (2009b). Crack coalescence in molded gypsum and Carrara marble: part 2—microscopic observations and interpretation. *Rock Mechanics and Rock Engineering*, 42(3), 513-545.

Yost, A. (1988). Eastern Gas Shales Research (Rep.). Morgantown, WV: Morgantown Energy Technology Center. doi:http://www.fischerhtropsch.org/DOE/_conf_proc/MISC/Confh89_6103/doe_metch89_6103h2A.pdf

Zhong, J. (2006) PID Controller Tuning: A Short Tutorial. ME475. Lecture. Purdue University.

Zou, C. (2013). Unconventional petroleum geology. Waltham, MA: Elsevier.
<http://dx.doi.org/10.1016/B978-0-12-397162-3.05001-5>

Appendix A – Analysis of Shale Fracture Experiments

Appendix A1 – Analysis of “Dry” Fracture Experiments on Vaca Muerta Shale

Specimens tested:

- VM1-2a-30-30
- VM2-2a-30-30
- VM3-2a-30-0

Appendix A2 – Analysis of Hydraulic Fracture Experiments on Opalinus Shale

Specimens Tested:

- OP-HF-SF-90-A
- OP-HF-SF-90-B
- OP-HF-SF-90-C
- OP-HF-2a-30-30-A
- OP-HF-2a-30-30-B
- OP-HF-2a-30-30-C
- OP-HF-2a-30-30-D
- OP-HF-2a-30-60-A
- OP-HF-2a-30-60-B
- OP-HF-2a-30-60-C

Appendix A1 – Analysis of “Dry” Fracture Experiments on Vaca Muerta Shale
VM1-2a-30-30 (0)

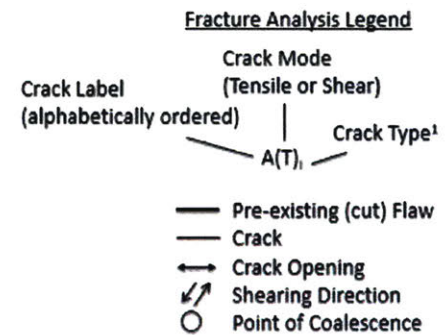
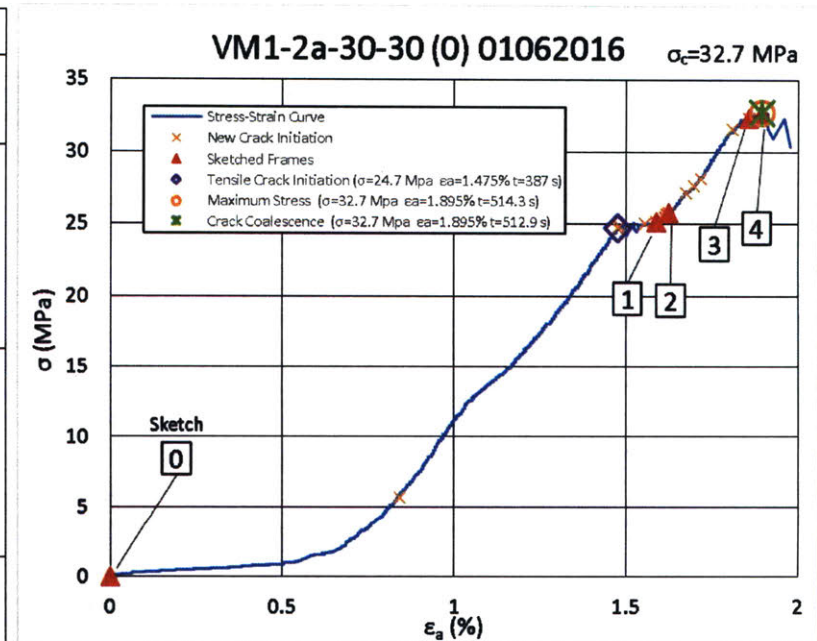
VM1-2a-30-30 (0)
01-06-2016


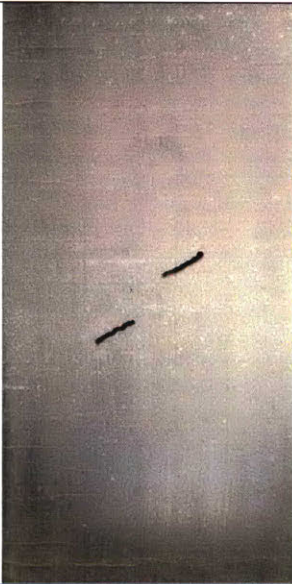
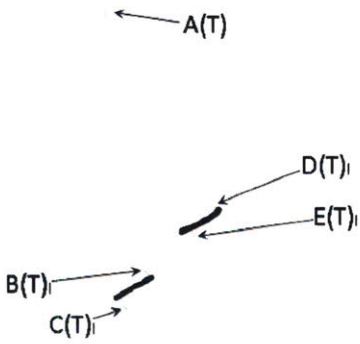
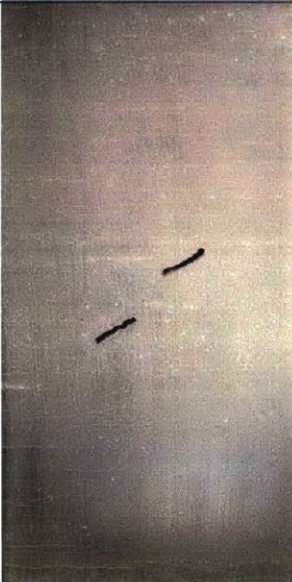
**Uniaxial Compression Test
on Vaca Muerta Shale**

*There were concerns in this test that the load frame had a skewed crosshead which may have induced shear in the specimen.

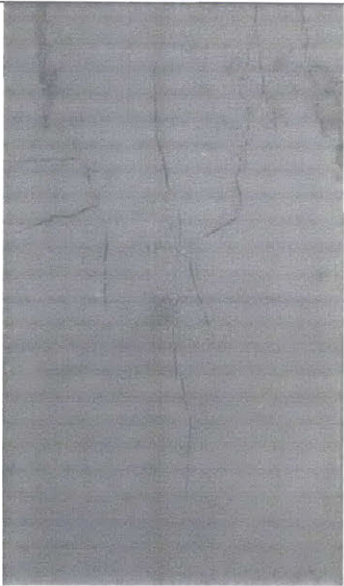
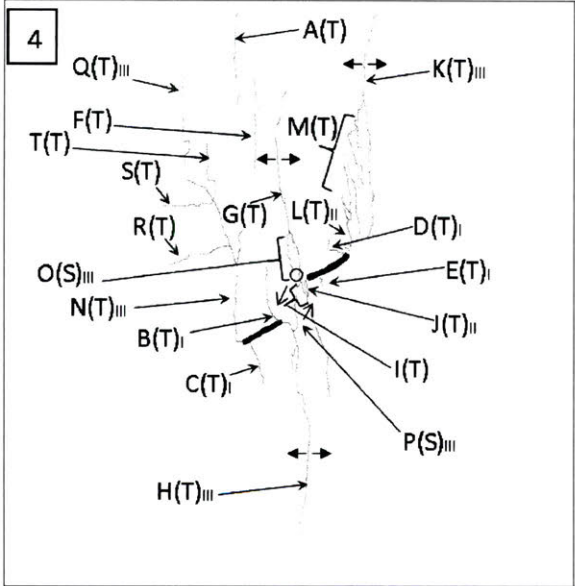
Crack and Coalescence Type ¹ Summary							
Crack Name	Crack Type	HS HR	Frame	Initiation Time (s)	Initiation Stress (MPa)	Initiation Strain (%)	Sketch
A(T)	No Type - Tensile	HR	1189	85.000	5.678	0.840	1
B(T) _i	Type 1 - Tensile	HR	1340	387.000	24.737	1.475	
C(T) _i	Type 1 - Tensile	HR	1341	389.000	24.862	1.482	
D(T) _i	Type 1 - Tensile	HR	1342	391.000	24.960	1.556	
E(T) _i	Type 1 - Tensile	HR	1343	393.000	25.115	1.586	
F(T)	No Type - Tensile	HR	1346	399.000	25.505	1.611	2
G(T)	No Type - Tensile	HR	1346	399.000	25.505	1.611	
H(T) _{iii}	Type 3 - Tensile	HR	1347	401.000	25.630	1.617	
I(T)	No Type - Tensile	HR	1347	401.000	25.630	1.617	
J(T) _{ii}	Type 1 - Tensile	HR	1348	403.000	25.763	1.623	
K(T) _{iii}	Type 3 - Tensile	HR	1359	425.000	27.156	1.673	3
L(T) _{ii}	Type 2 - Tensile	HR	1363	433.000	27.655	1.698	
M(T)	En Echelon	HR	1367	441.000	28.155	1.716	
N(T) _{iii}	Type 3 - Tensile	HR	1394	495.000	31.577	1.809	4
O(S) _{iii}	Type 3 - Shear	HR	1400	507.000	32.326	1.858	
P(S) _{iii}	Type 3 - Shear	HS	-295	512.961	32.716	1.895	
Q(T) _{iii}	Type 3 - Tensile	HS	-240	512.968	32.716	1.895	
R(T)	No Type - Tensile	HS	-239	512.968	32.716	1.895	
S(T)	No Type - Tensile	HS	-239	512.968	32.716	1.895	4
T(T)	No Type - Tensile	HS	-239	512.968	32.716	1.895	
Coalescence: Category 2		HS	-238	512.968	32.716	1.895	
Failure		HS	0	513.000	32.728	1.895	

1: Crack coalescence type based on Wong and Einstein (2009)



<div data-bbox="205 180 247 240" style="border: 1px solid black; padding: 2px; width: 20px; height: 20px; display: flex; align-items: center; justify-content: center;">0</div> 		<p>Frame: HR 1147 – Initial Time: 0 seconds σ: 0 MPa ϵ: 0 %</p> <p><i>Initial Configuration</i></p> <p>Prismatic Specimen: 4"x2"x1" Flaw Pairs: $2a = 3/8$" Ligament Spacing (L): $2a$ Flaw Angle (β): 30° Bridging Angle (α): 30° Bedding Orientation (ψ): 0°</p> <p>All cracks are labeled based on their initiation order.</p>
<div data-bbox="205 760 247 820" style="border: 1px solid black; padding: 2px; width: 20px; height: 20px; display: flex; align-items: center; justify-content: center;">1</div> 		<p>Frame: HR 1343 Time: 393 seconds</p> <p><i>Primary Tensile Wing Crack Initiation</i></p> <p>Tensile crack A(T) initiated first far from the coalescence zone due to edge effects in the early stages of the test. Later on, tensile cracks B(T), C(T), D(T), and E(T), all initiated sequentially within seconds of each other. These cracks eventually only propagate a little.</p>

<p>2</p>		<p>Frame: HR 1348 Time: 403 seconds</p> <p><i>Opening of Tensile Central Cracks</i></p> <p>Cracks F(T), G(T), and H(T)_{III} are tensile cracks opening in the middle of the sample from top to bottom. Tensile crack I(T) initiates near the inner tip of the right flaw. Afterwards, crack J(T)_{II} initiates at the inner tip of the right flaw and propagates downwards. Crack I(T) then propagates and connects G(T) to J(T)_{II}. Cracks G(T) and H(T)_{III} eventually dominate in tensile opening relative to other cracks.</p>
<p>3</p>		<p>Frame: HR 1400 Time: 507 seconds</p> <p><i>Development of Anti-Wing Cracks</i></p> <p>At this stage, anti-wing cracks begin to develop, starting with the initiation of crack K(T)_{III} on the upper right part of the sample. Crack L(T)_{II} then initiates on the outer tip of the right flaw propagating upwards. Then a series of en echelon cracks, M(T), initiate between K(T)_{III} and L(T)_{II}. Crack N(T)_{III} initiates from the outer tip of the left flaw and propagates upwards. Meanwhile, wing cracks B(T)_I, C(T)_I, and D(T)_I have propagated to their final extents. Crack H(T)_{III} coalesces with the inner tip of the inner flaw.</p>



Frame: HS -238
Time: 512.968 seconds

Shear Cracks, Indirect Coalescence, & Failure
 Shear crack $O(S)_{III}$ initiates off of $G(T)$ above the flaws and propagates near the inner tip of the right flaw, while shear crack $P(S)_{III}$ initiates off of $H(T)_{III}$ below the flaws and propagates towards $O(S)_{III}$. Then tensile crack $Q(T)_{III}$ initiates far from the coalescence zone on the top left of the sample and propagates down, eventually coalescing with anti-wing crack $N(T)_{III}$. Then $O(S)_{III}$ and $P(S)_{III}$ coalesce resulting in indirect coalescence of the flaws. Upon failure, tensile cracks $R(T)$, $S(T)$, and $T(T)$ branch off of $Q(T)_{III}$. The anti-wing cracks $G(T)$, $K(T)_{III}$, $H(T)_{III}$, and $N(T)_{III}$ open violently causing catastrophic failure.

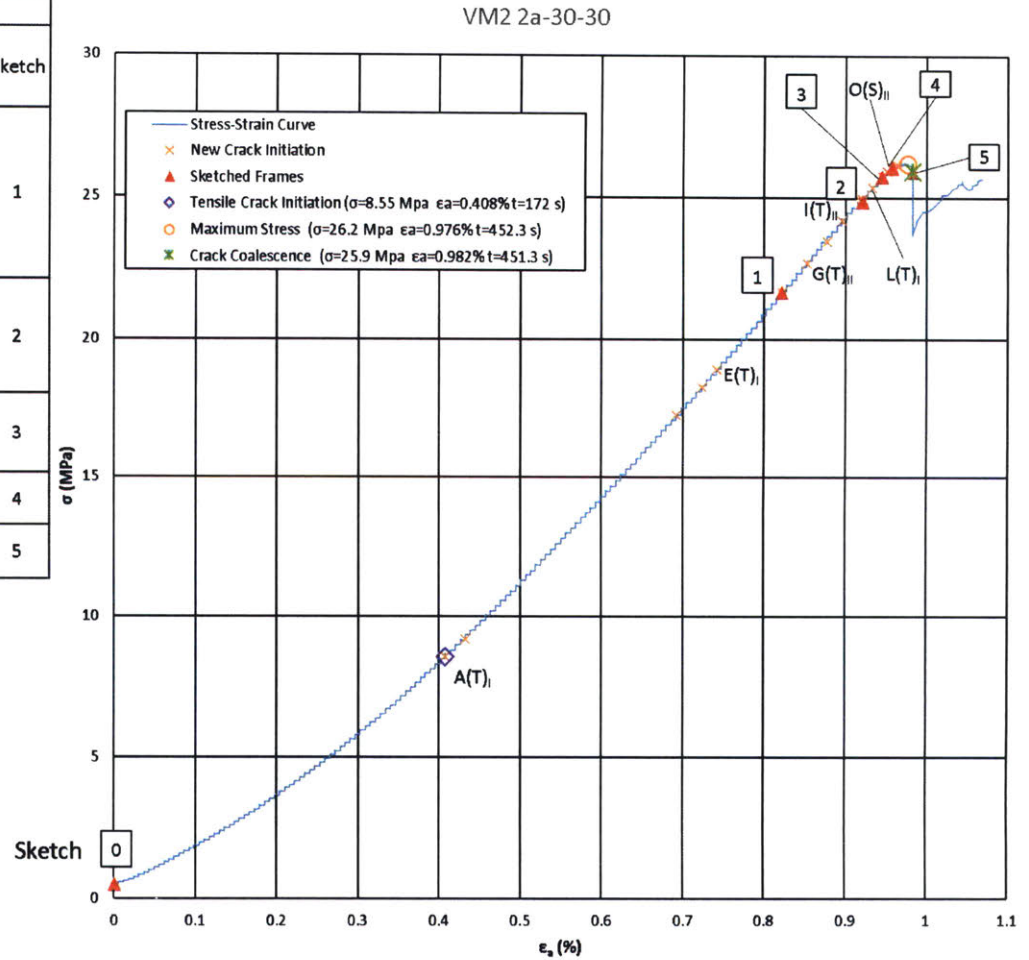
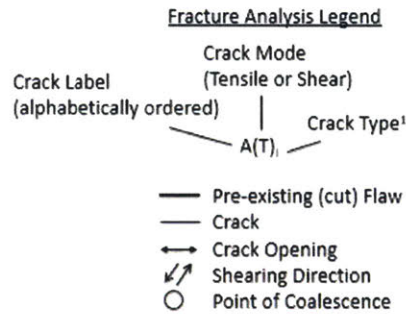
VM2-2a-30-30 (0)

VM2-2a-30-30 (0) 03-30-2016

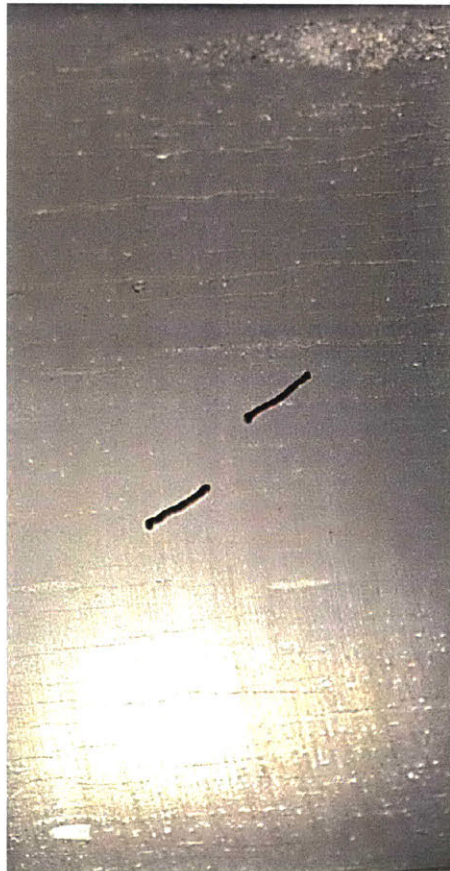
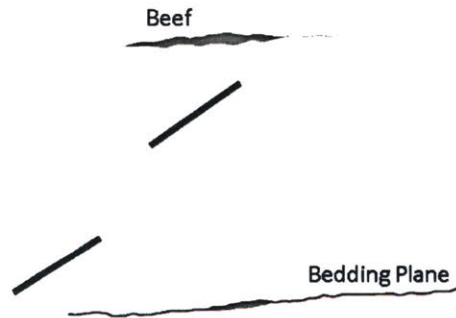
Uniaxial Compression Test
On Vaca Muerta Shale

Crack and Coalescence Type ¹ Summary							
Crack Name	Crack Type	HS/HR	Frame	Initiation Time (s)	Initiation Stress (MPa)	Initiation Strain (%)	Sketch
A(T)	Type 1 - Tensile	HR	4114	172.00	8.550	0.408	1
B(T)	No Type - Tensile	HR	4119	182.00	9.179	0.432	
C(T)I	Type 1 - Tensile	HR	4183	310.00	17.284	0.692	
D(T)	En Echelon - Tensile	HR	4191	326.00	18.287	0.723	
E(T)I	Type 1 - Tensile	HR	4196	336.00	18.942	0.741	
F(S)	No Type Shear	HR	4218	380.00	21.694	0.821	2
G(T)II	Type II - Tensile	HR	4226	396.00	22.716	0.852	
H(T)	En Echelon	HR	4232	408.00	23.476	0.877	
I(T)II	Type II - Tensile	HR	4238	420.00	24.216	0.896	3
J(T)II	Type II - Tensile	HR	4243	430.00	24.859	0.920	
K(T)II	Type II - Tensile	HR	4244	432.00	24.976	0.920	4
L(T)	No Type - Tensile	HR	4247	438.00	25.363	0.933	
M(T)	No Type - Tensile	HR	4250	444.00	25.743	0.945	5
N(T)II	Type II - Tensile	HR	4251	446.00	25.933	0.951	
O(S)II	Type II - Shear	HR	4252	448.00	26.058	0.957	
Coalescence	Category 5	HS	-9151	451.328	25.920	0.982	
failure		HS	-9151	451.328	25.920	0.982	

¹: Crack coalescence type based on Wong and Einstein (2009)



Sketch 0



Frame: HR 4028 – Initial

Time: 0 seconds

σ : 0 MPa

ϵ : 0 %

Initial Configuration

Prismatic Specimen: 4"x2"x1"

Flaw Pairs: 2a = 3/8"

Ligament Spacing (L): 2a

Flaw Angle (β): 30°

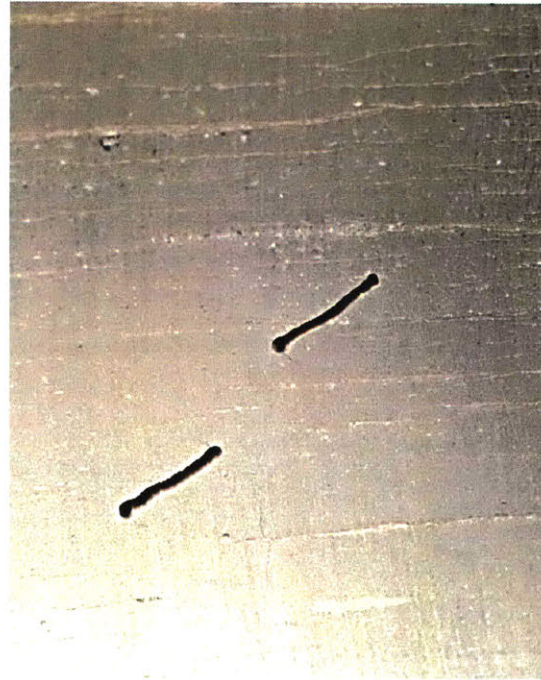
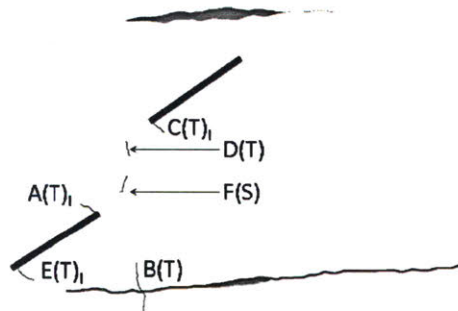
Bridging Angle (α): 30°

Bedding Orientation (ψ): 0°

All cracks are labeled based on their initiation order.

Above the double flaws is a "beef" inclusion and below them is a bedding plane with traces of beef, both of which act as a fracture propagation barrier.

Sketch 1

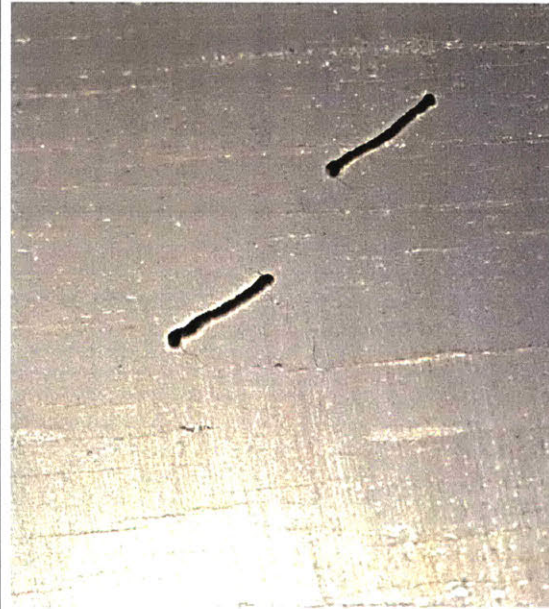
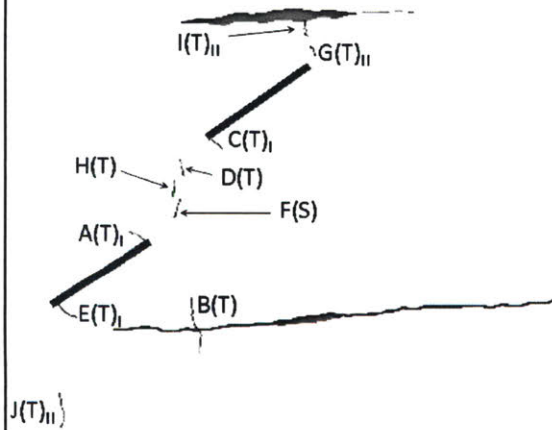


Frame: HR 4218
Time: 380 seconds
 σ : 21.7 MPa
 ϵ : 0.821 %

Crack Initiation

Tensile wing crack $A(T)_1$ is the first crack to initiate on the inner tip of the left flaw. Next, tensile crack $B(T)$ initiates above the bedding plane, propagating towards it until it arrests at the bedding plane. Then tensile wing crack $C(T)_1$ initiates at the inner tip of the right flaw, followed by $D(T)$ in between the flaws, and then tensile wing crack $E(T)_1$ on the outer tip of the left flaw. Afterwards, $B(T)$ continues past the bedding plane. Finally, shear crack $F(S)$ initiates in between the flaws.

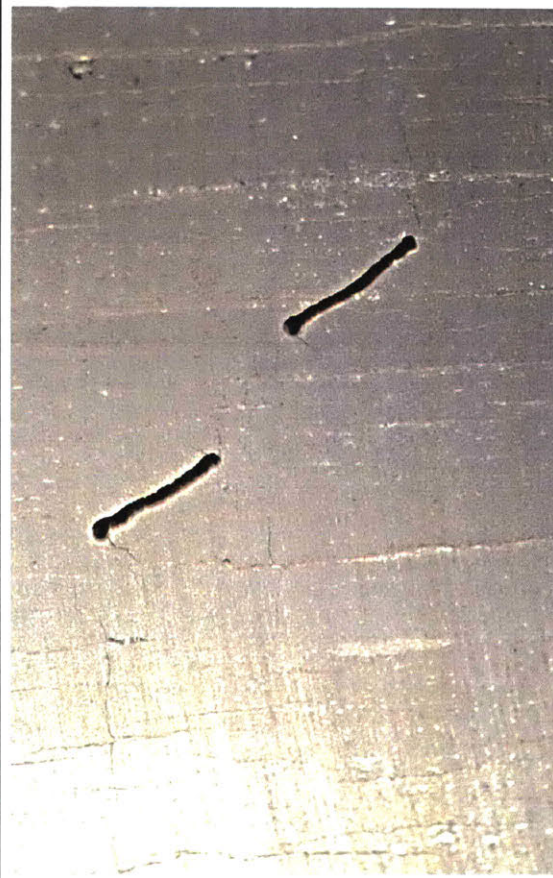
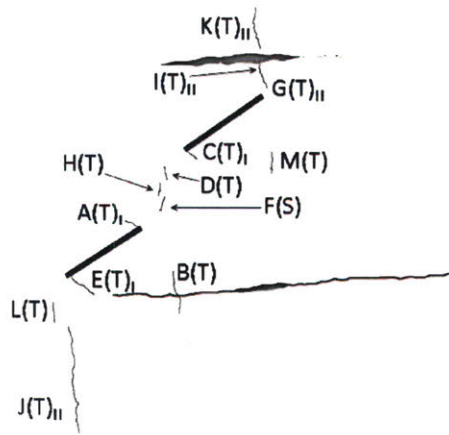
Sketch 2



Frame: HR 4243
Time: 430 seconds
 σ : 24.9 MPa
 ϵ : 0.920 %

Tensile crack $G(T)_{II}$ initiates above the outer tip of the left flaw and propagates downward. Then tensile crack $H(T)$ initiates between the flaws, eventually becoming an array of an echelon cracks. Tensile crack $I(T)_{II}$ initiates at the bottom of the beef layer and propagates towards $G(T)_{II}$. Finally, tensile crack $J(T)_{II}$ initiates below the outer tip of the left flaw and propagates both up and down.

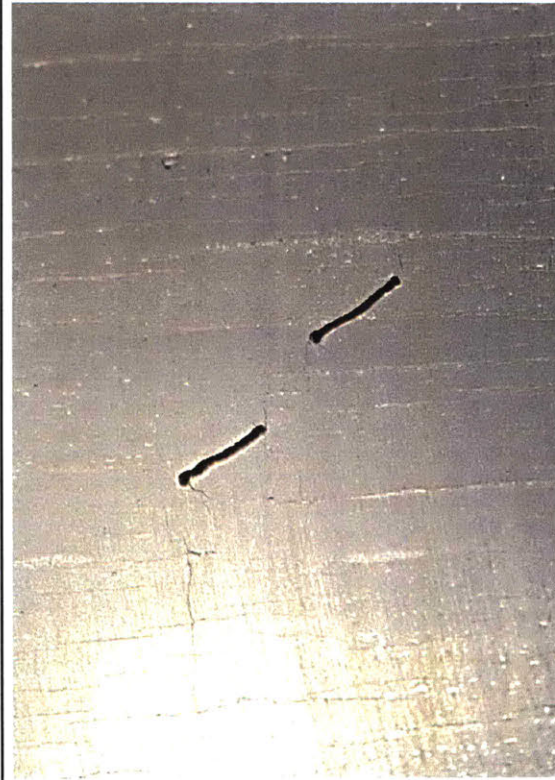
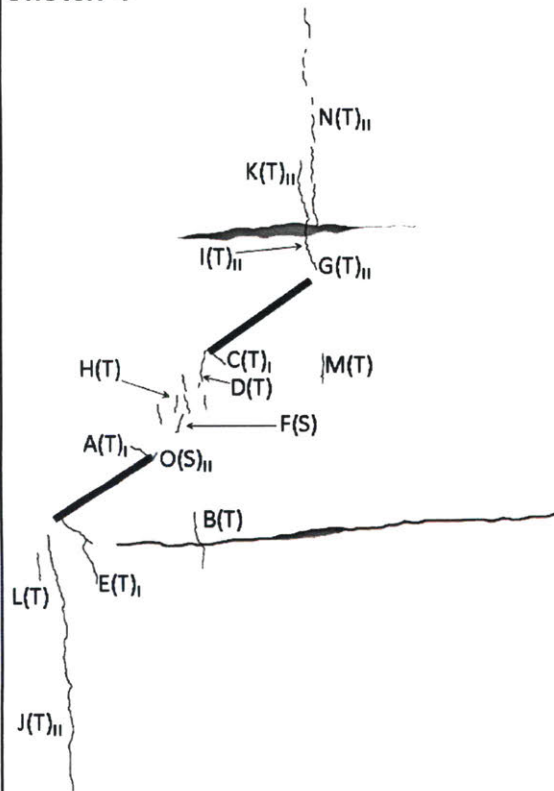
Sketch 3



Frame: HR 4250
Time: 444 seconds
 σ : 25.7 MPa
 ϵ : 0.945 %

Tensile crack $K(T)_{II}$ initiates above the beef and propagates towards it. Then tensile crack $L(T)$ initiates below the left flaw outer tip. Crack $J(T)_{II}$ slightly propagates up and down. Next, crack $I(T)_{II}$ coalesces with crack $G(T)_{II}$. Finally, crack $M(T)$ initiates below the outer tip of the right flaw.

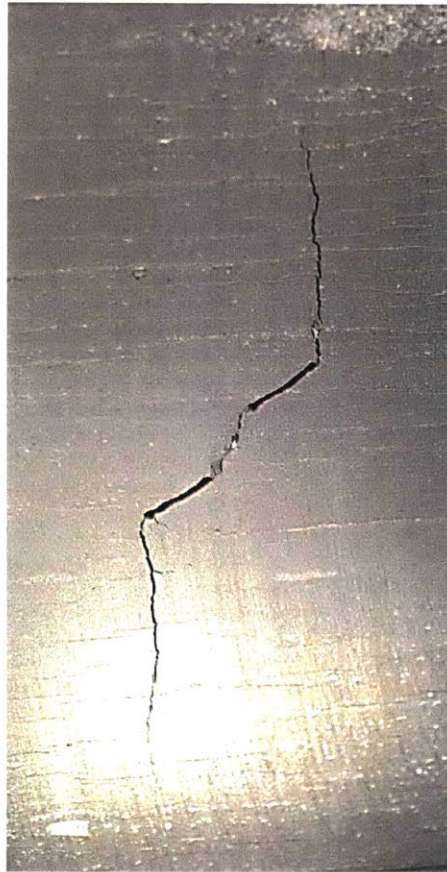
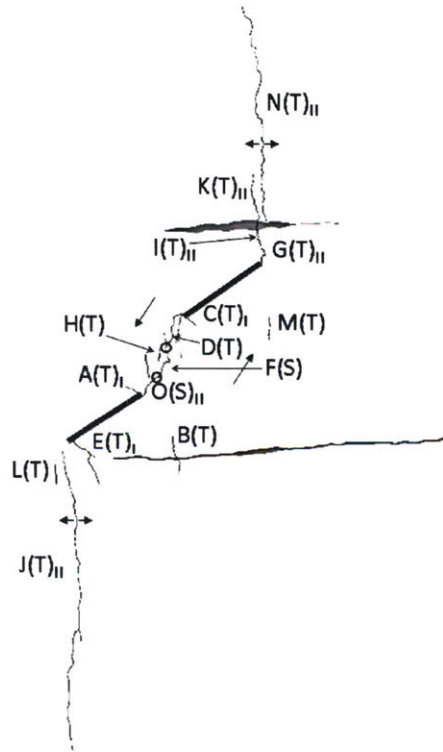
Sketch 4



Frame: HR 4252
 Time: 448 seconds
 σ : 26.1 MPa
 ϵ : 0.957 %

Tensile crack $N(T)_{II}$ initiates near $K(T)_{II}$'s upper tip and propagates down arresting at the beef, also causing $K(T)_{II}$ to close. Next, tensile crack $D(T)$ propagates and coalesces with the inner tip of the right flaw. Then shear crack $O(S)_{II}$ initiates at the inner tip of the left flaw and propagates towards $F(S)$. Afterwards, cracks $J(T)_{II}$ and $N(T)_{II}$ propagate towards the sample boundaries and the en echelon array $H(T)$ develops.

Sketch 5



Frame: HR 4253
Time: 452 seconds
 σ : 25.92 MPa
 ϵ : 0.982 %

Coalescence and Failure

Prior to failure, $O(S)_{II}$ coalesces with $F(S)$, which coalesces with $D(T)$. $D(T)$ became a mixed mode tensile-shear starting off as a tensile crack and now is on the shear crack plane of $O(S)_{II}$ and $F(S)$. Upon failure, cracks $J(T)_{II}$ and $N(T)_{II}$ open in tension and there is direct coalescence (Category 5) between the two flaws.

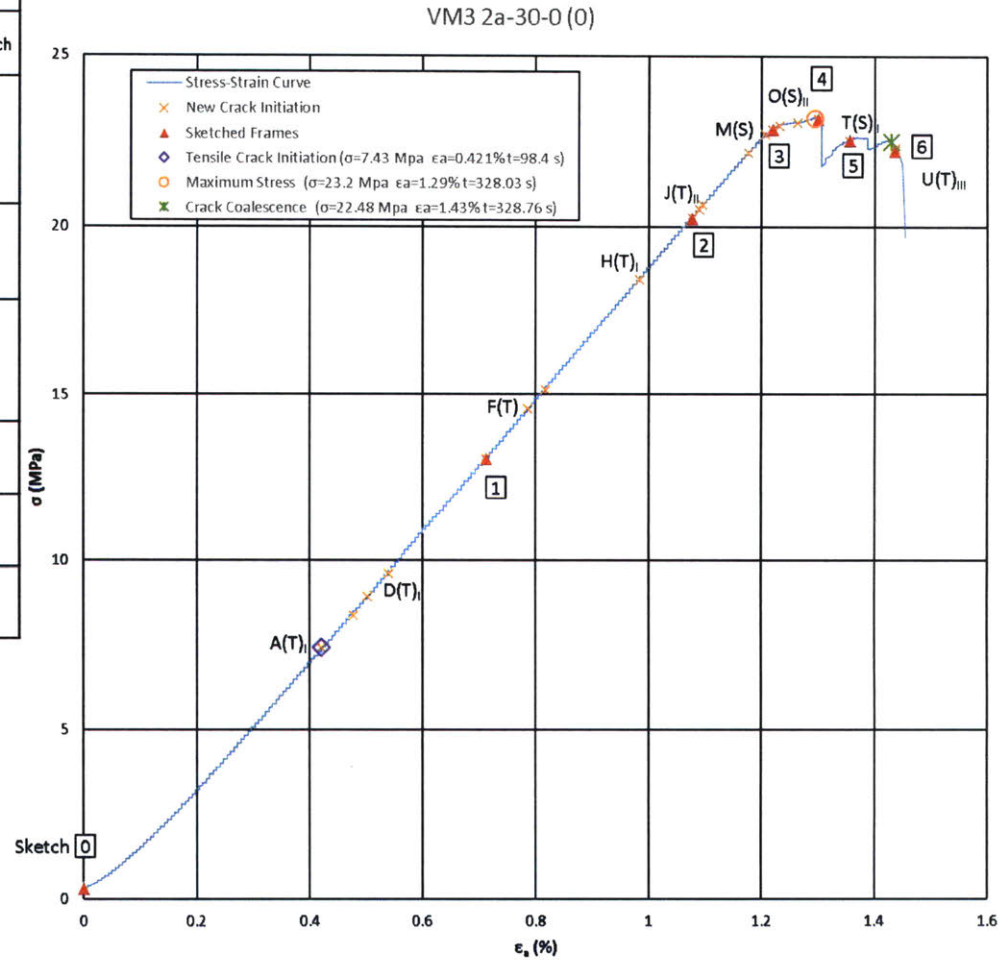
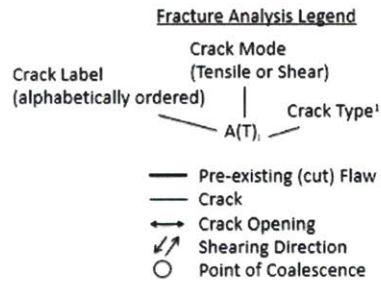
VM3-2a-30-0 (0)

VM3-2a-30-0 (0)
03-30-2016

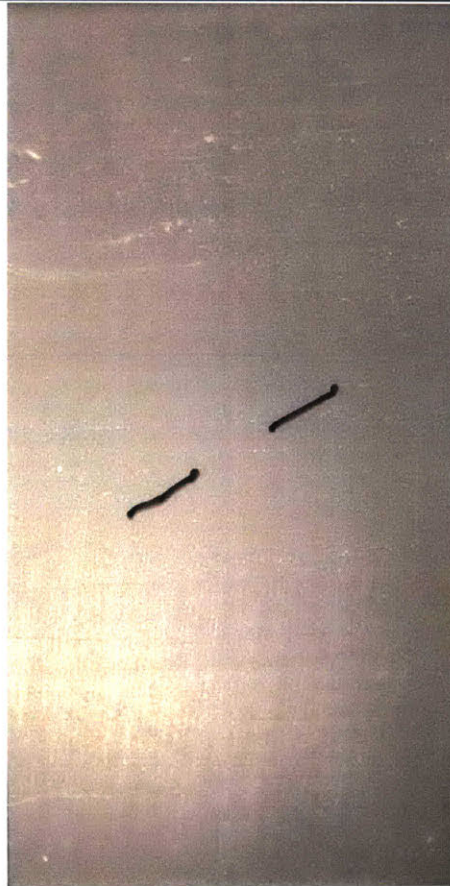
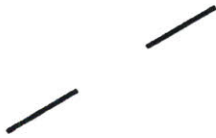
**Uniaxial Compression Test
on Vaca Muerta Shale**

Crack and Coalescence Type ¹ Summary							Sketch
Crack Name	Crack Type	HS/HR	Frame	Initiation Time (s)	Initiation Stress (MPa)	Initiation Strain (%)	
A(T) _I	Type 1 - Tensile	HR	3902	98.44	7.431	0.421	1
B(T) _I	Type 1 - Tensile	HR	3909	112.44	8.398	0.477	
C(T) _I	Type 1 - Tensile	HR	3913	120.44	8.950	0.501	
D(T) _I	Type 1 - Tensile	HR	3918	130.44	9.638	0.539	
E(T) _{II}	Type 2 - Tensile	HR	3943	180.44	13.092	0.712	2
F(T) _I	No Type - Tensile	HR	3954	202.44	14.597	0.786	
G(T) _I	No Type - Tensile	HR	3958	210.44	15.142	0.817	3
H(T) _I	Type 1 - Tensile	HR	3982	258.44	18.438	0.984	
I(T) _I	No Type - Tensile	HR	3995	284.44	20.237	1.077	
J(T) _{II}	Type II - Tensile	HR	3997	288.44	20.509	1.089	4
K(T) _I	En Echelon - Tensile	HR	3998	290.44	20.652	1.096	
L(T) _I	En Echelon - Tensile	HR	4009	312.44	22.164	1.176	5
M(S) _I	En Echelon - Shear	HR	4013	320.44	22.709	1.207	
N(T) _{III}	Type III - Tensile	HR	4014	322.44	22.845	1.219	6
O(S) _{II}	Type II - Shear	HR	4015	324.44	22.967	1.232	
P(T) _{III}	Type III - Tensile	HR	4016	326.44	23.053	1.263	
Q(T) _I	No Type - Tensile	HS	-4373	328.22	23.153	1.300	
R(T) _{III}	Type III - Tensile	HS	-4268	328.23	23.160	1.300	
S(T) _I	No Type - Tensile	HS	-4023	328.26	23.110	1.300	
T(S) _{II}	Type II - Shear	HS	-2673	328.44	22.515	1.356	
Indirect Coalescence: Category 2		HS	-311	328.76	22.480	1.430	
U(T) _{III}	Type III - Tensile	HS	-265	328.765	22.300	1.436	
Failure		HS	-174	328.777	22.222	1.436	

¹: Crack coalescence type based on Wong and Einstein (2009a)



Sketch 0



Frame: HR 3828 – Initial

Time: 0 seconds

σ : 0 MPa

ϵ : 0 %

Initial Configuration

Prismatic Specimen: 4"x2"x1"

Flaw Pairs: 2a = 3/8"

Ligament Spacing (L): 2a

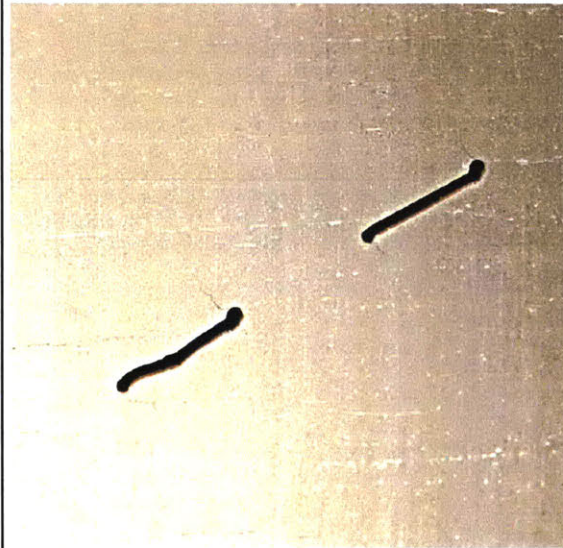
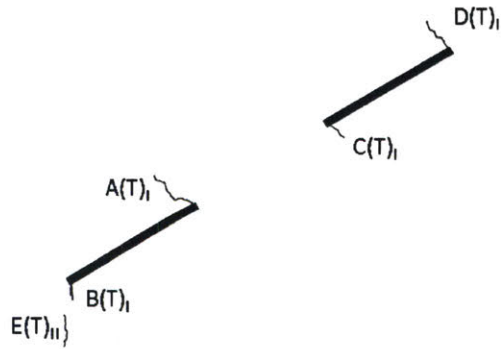
Flaw Angle (β): 30°

Bridging Angle (α): 0°

Bedding Orientation (ψ): 0°

All cracks are labeled based on their initiation order.

Sketch 1

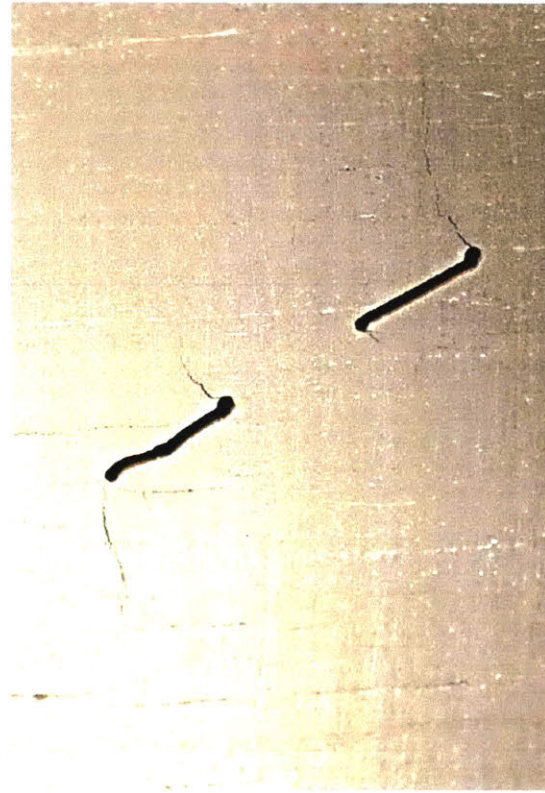
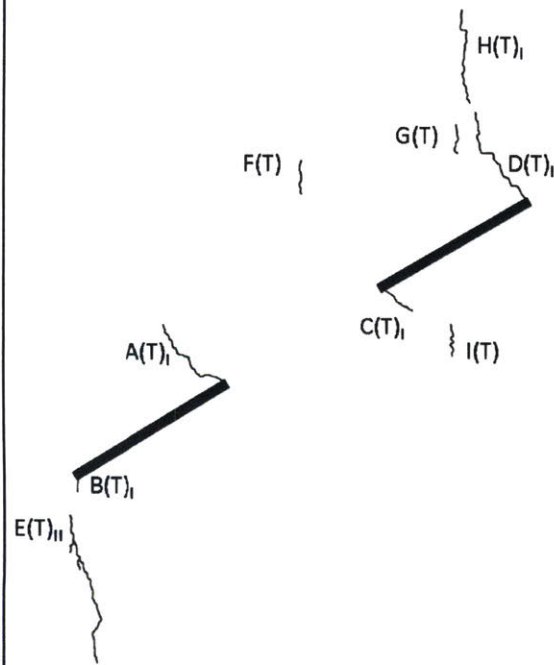


Frame: HR 3943
Time: 180.4 seconds
 σ : 13.1 MPa
 ϵ : 0.712 %

Crack Initiation

Tensile wing crack $A(T)_I$ is the first crack to initiate on the inner tip of the left flaw, then tensile wing crack $B(T)_I$ initiates at the outer tip of the same flaw. Afterwards, tensile wing crack $C(T)_I$ initiates at the inner tip of the right flaw, followed by $D(T)_I$ initiating on the outer tip. Finally, $E(T)_{II}$ initiates near $B(T)_I$.

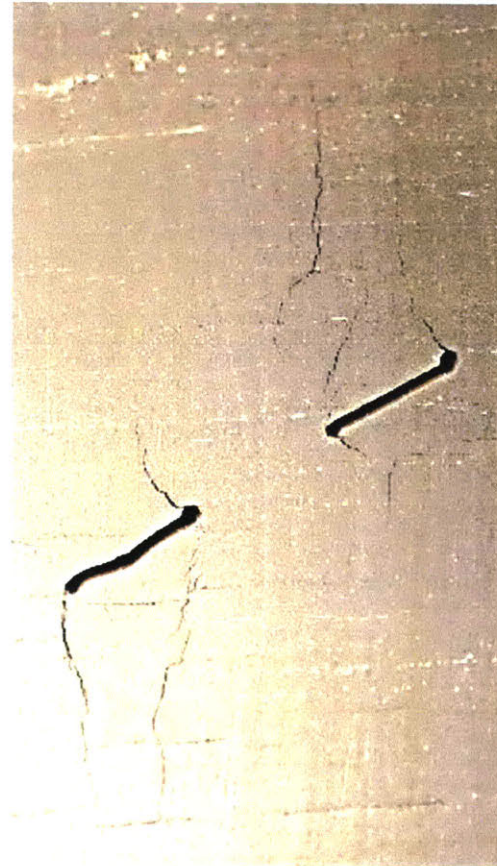
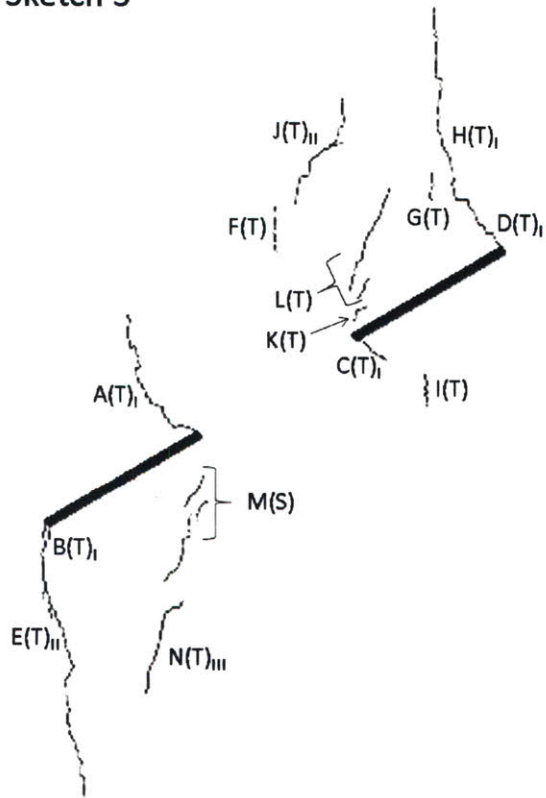
Sketch 2



Frame: HR 3995
Time: 284.4 seconds
 σ : 20.2 MPa
 ϵ : 1.08 %

Tensile crack F(T) initiates in between and above both flaws. Tensile crack G(T) initiates above the outer tip of the right flaw. Then tensile wing crack A(T)_I, D(T)_I, and E(T)_{II} propagate and stop. Afterwards crack H(T)_I initiates. Finally, tensile crack I(T) initiates below the right flaw.

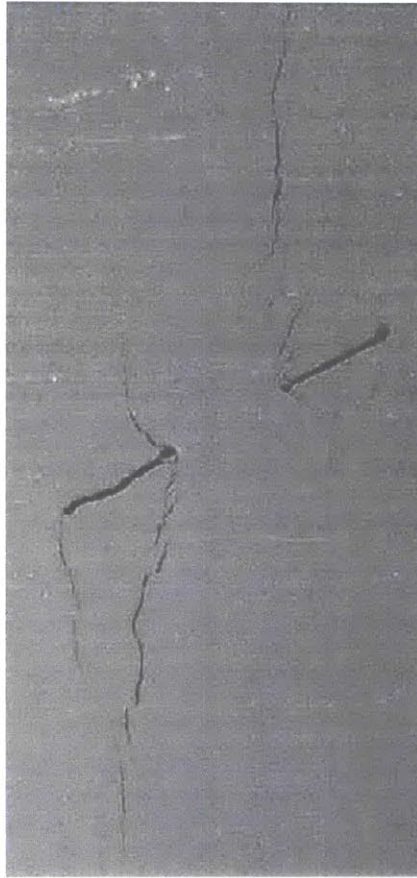
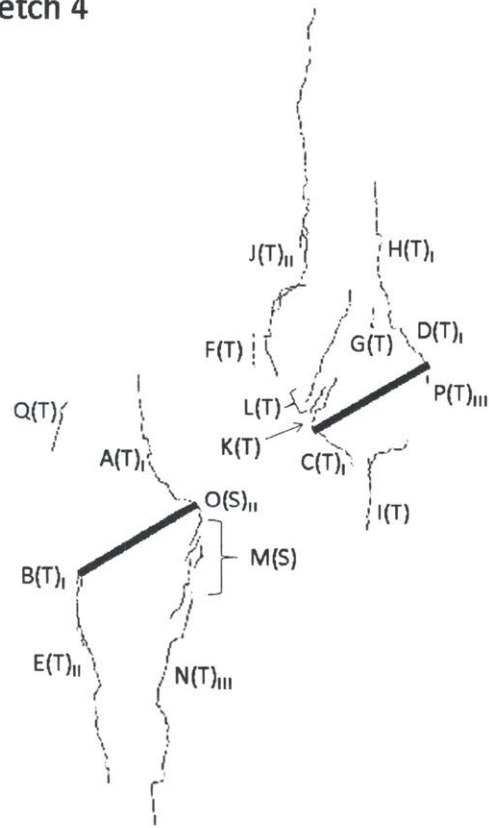
Sketch 3



Frame: HR 4014
Time: 322.4 seconds
 σ : 22.8 MPa
 ϵ : 1.22 %

Tensile crack $J(T)_{II}$ initiates far above the inner tip of the right flaw and propagates towards $F(T)$. Then, crack $E(T)_{II}$ propagates further and coalesces with the outer tip of the left flaw. Afterwards, tensile crack $K(T)$ initiates right above the inner tip of the right flaw. Crack $H(T)_I$ propagates down and coalesces with $D(T)_I$. Then crack $L(T)$ initiates above $K(T)$ and they form an array of an echelon tensile cracks. After some time, an echelon shear cracks $M(S)$ begin to initiate, followed by tensile crack $N(T)_{III}$ which initiates below $M(S)$.

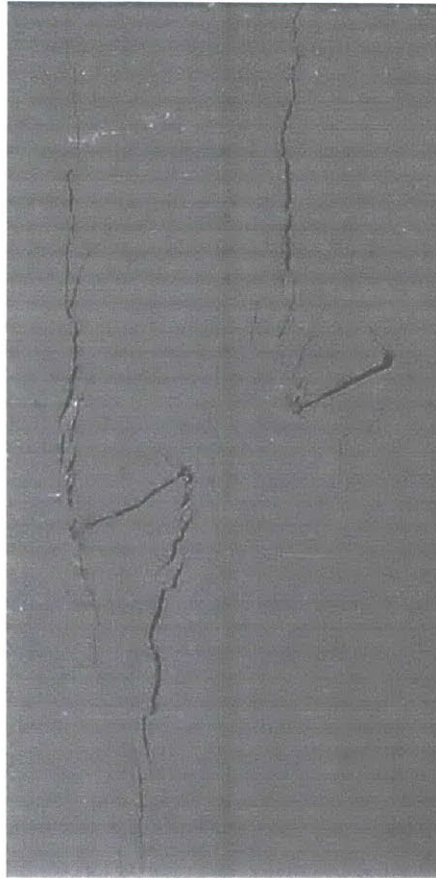
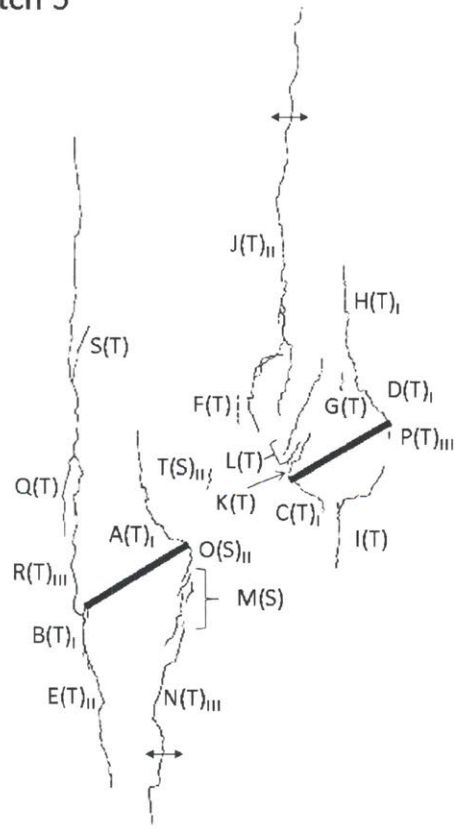
Sketch 4



Frame: HS -4373
Time: 328.2 seconds
 σ : 23.2 MPa
 ϵ : 1.30 %

Crack $A(T)_I$ continues to propagate, followed by $L(T)$, then $J(T)_{II}$. Then, shear crack $O(S)_{II}$ initiates below the inner tip of the left flaw and connects with the flaw tip followed by the propagation of $N(T)_{III}$. Next, tensile crack $P(T)_{III}$ initiates at the outer tip of the right flaw and propagates downwards. Afterwards, tensile crack $Q(T)_I$ initiates far above the outer tip of the left flaw.

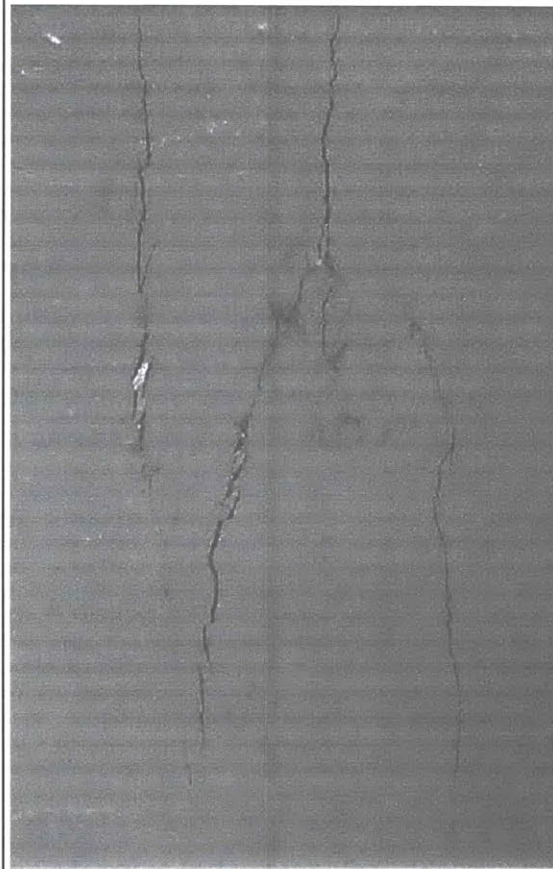
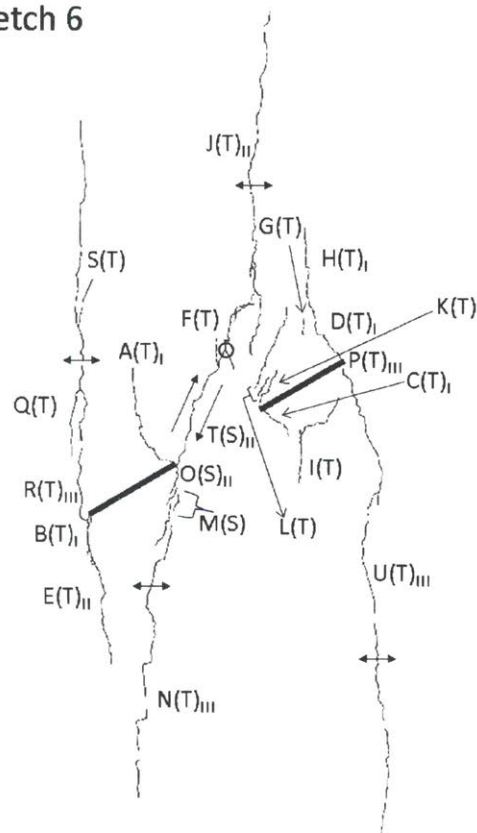
Sketch 5



Frame: HS -2673
Time: 328.4 seconds
 σ : 22.5 MPa
 ϵ : 1.36 %

Tensile crack $R(T)_{III}$ branches downward from the top tip of $Q(T)$, and then propagates upward, where another tensile crack $S(T)$ branches off. Crack $R(T)_{III}$ coalesces with the outer tip of the left flaw. Then tensile crack $J(T)_{II}$ begins opening in tension, followed by tensile crack $N(T)_{III}$. Afterwards, shear crack $T(S)_{II}$ initiates in the zone above and in between the two flaws. More en echelon shear crack develop at $M(S)$.

Sketch 6



Frame: HS -174
Time: 328.8 seconds
 σ : 22.2 MPa
 ϵ : 1.44 %

Shear crack $T(S)_{II}$ propagates down and coalesces with $O(S)_{II}$ at the inner tip of the right flaw. Shortly after, $J(T)_{II}$ begins opening in tension followed by the propagation of $T(S)_{II}$ until the point of coalescence at the tip of $J(T)_{II}$. Next, tensile crack $U(T)_{III}$ initiates below the outer tip of the right flaw and propagates up until coalescing with $P(T)_{III}$ and down until it opens up in tension causing the sample to fail, sliding along $T(S)_{II}$.

OP-HF-SF-90-A

07-26-2016

Uniaxial Compression with Hydraulic Fracture of

Opalinus Shale

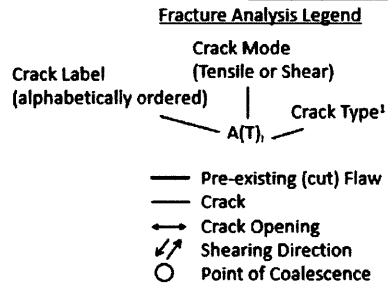
Experimental Procedure Notes:

- Flaw saturation phase fills flaw with oil that flows out of bleed hole to expel air from the system. This results in initial pressure build up in flaw shown at time = 0 seconds.
- After flaw saturation, system is closed by attaching pressure transducer to bleed hole.
- Pressurization of flaw is achieved using a PID pressure-control algorithm, where user-defined target pressures (P_{Target}) are defined and PVA injects oil to achieve P_{Target} .
- While holding a constant uniaxial compressive stress, flaw is pressurized in 0.5 MPa increments until specimen failure. Pressure step is held for 1-2 minutes before moving up to the next increment.

OP-HF-SF-90-A Dimensions			
Height (h)	Width (w)	Thickness (t)	Area (A=wxt)
in	in	in	in ²
3.1572	1.9812	1.0516	2.0834

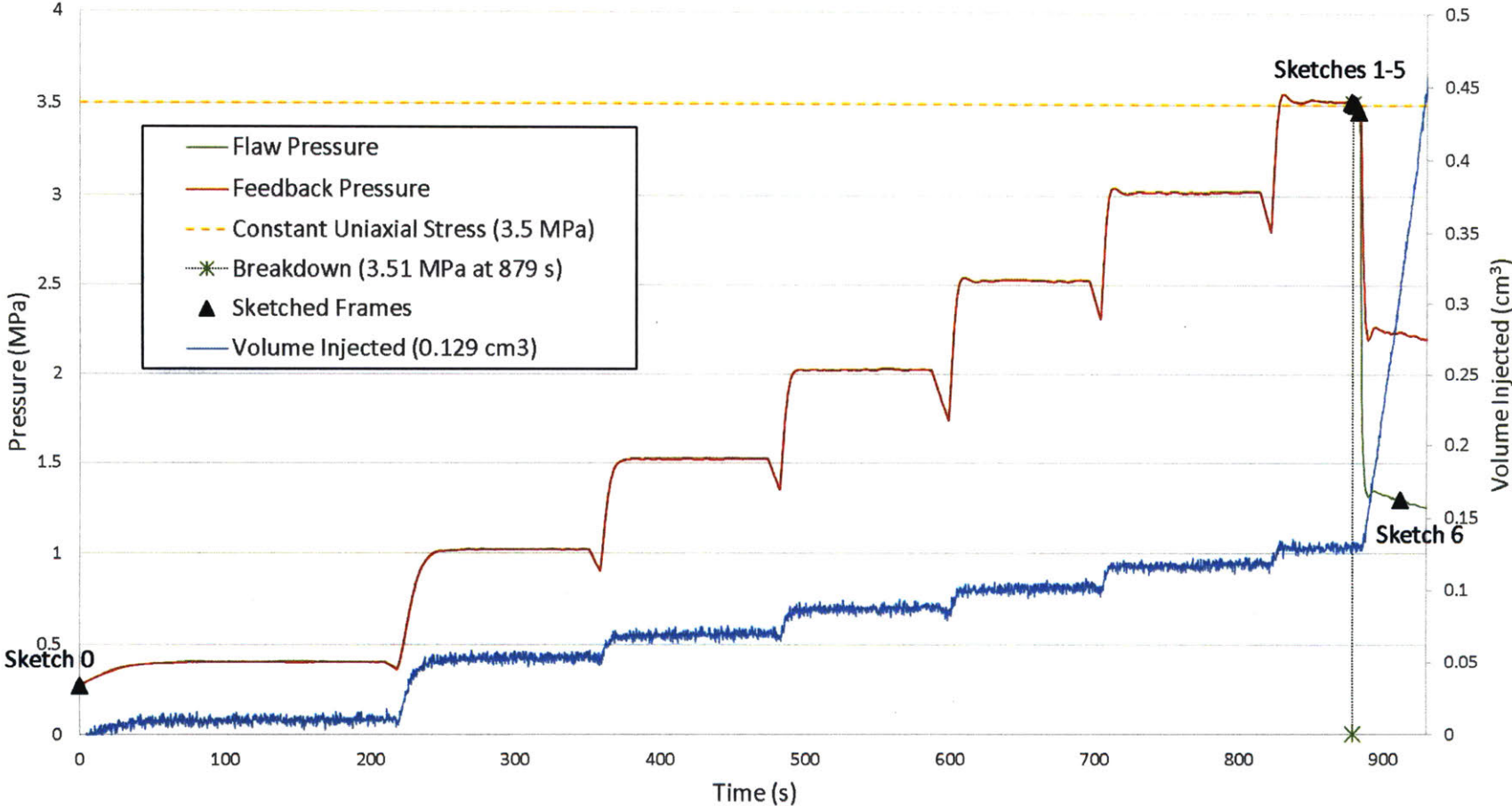
OP-HF-SF-90-A Test Summary			
Vertical Load Applied	Vertical Stress Applied	Maximum Hydraulic Pressure	Volume Injected until Loss of Pressure
kN	MPa	MPa	cm ³
4.70	3.5	3.56	0.1288

OP-HF-SF-90-A Sketch Summary						
Sketch Number	Type of Frame	Frame Number	Time from beginning of closing system	Hydraulic Pressure	Normalized Hydraulic Pressure	Volume Injected
			s	MPa		cm ³
0	High Resolution	9741	0	0.267	0.0750	0
1	High Resolution	9909	877.831	3.515	0.9874	0.128694
2	High Speed	-2492	879	3.507	0.9852	0.129553
3	High Speed	-2040	879.452	3.506	0.9849	0.126236
4	High Speed	-500	880.992	3.497	0.9823	0.128791
5	High Speed	1339	882.831	3.462	0.9725	0.131729
6	High Resolution	9916	911.831	1.297	0.3644	0.310342

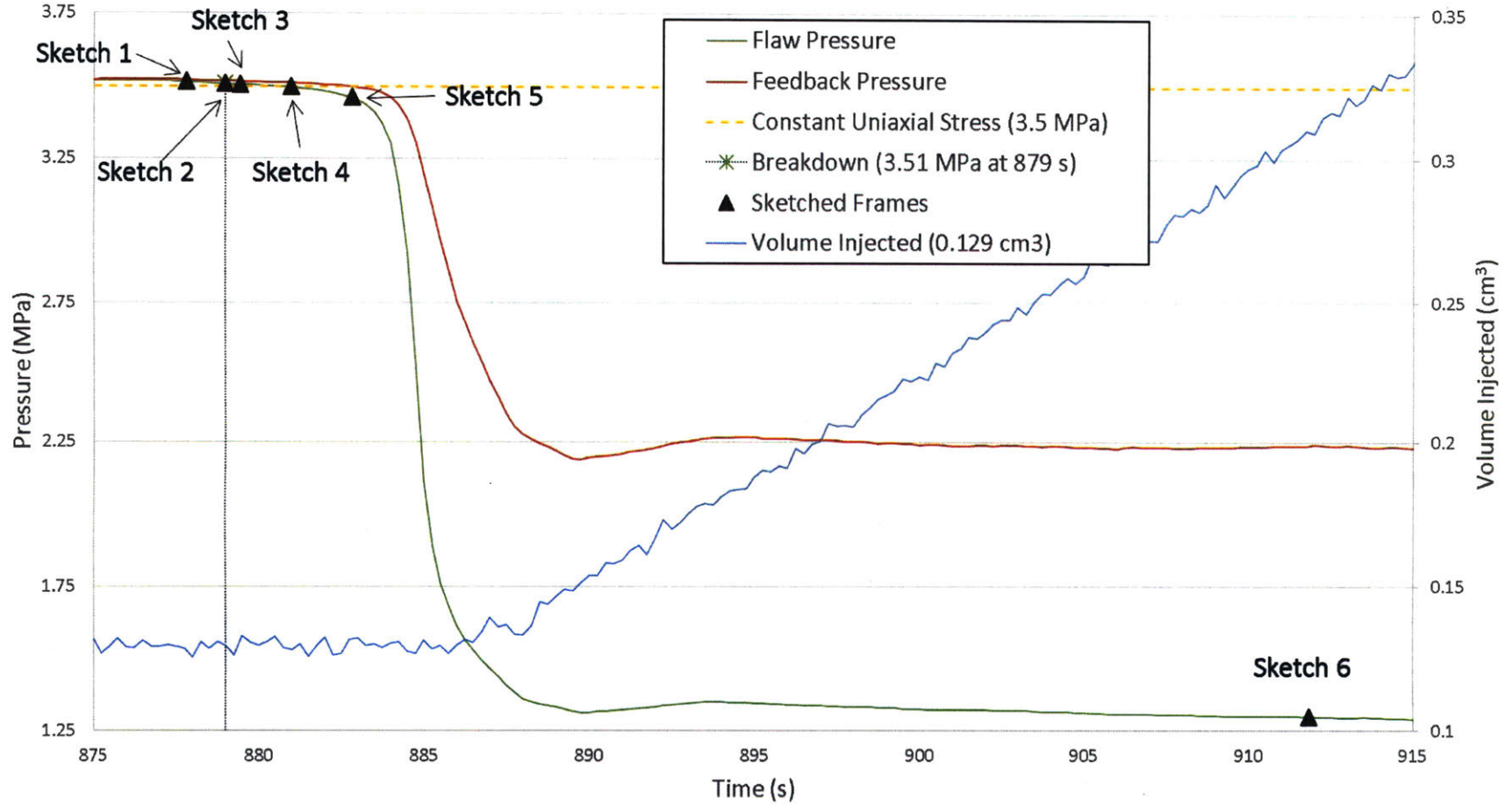


OP-HF-SF-A Fractures Summary				
Crack ID	Crack Type	Hydraulic Pressure at Crack Initiation	Hydraulic Pressure Normalized to the Maximum Hydraulic Pressure	Sketch
		Mpa	Pressure	
A(T)	no type	3.5072	0.985	2
B(T)	no type	3.5059	0.985	3

OP-HF-SF-90-A Test Data

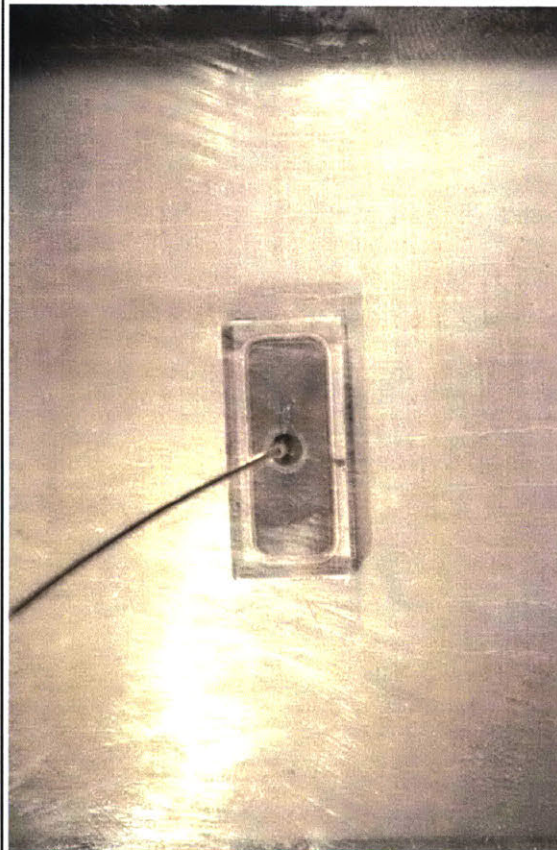


OP-HF-SF-90-A Test Data Close-Up



Sketch 0

Flaw
Seal



Frame: HR 9741 – Initial

Time: 0 seconds

σ : 3.5 MPa

P_{Target} : 0.5 MPa

P: 0.267 MPa

V: 0 cm³

Initial Configuration

Prismatic Specimen: 4"x2"x1"

Flaw: 2a = 3/8"

Ligament Spacing (L): N/A

Flaw Angle (β): 90°

Bridging Angle (α): N/A

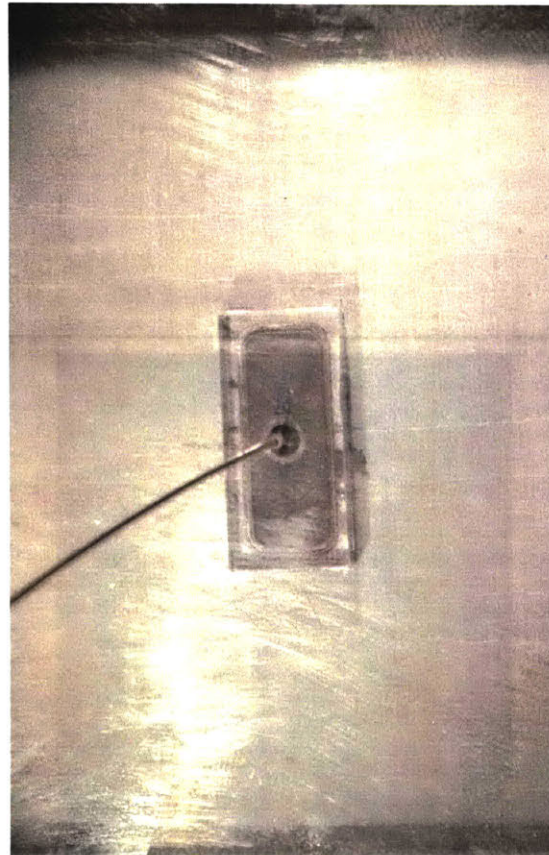
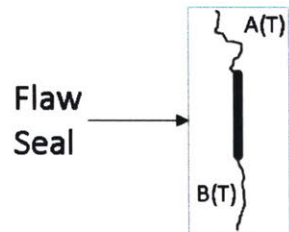
Bedding Orientation (ψ): 0°

Pressure Increments: 0.5 MPa

Pressure Hold Time: ~1 min

All cracks are labeled based on their initiation order.

Sketch 1



Frame: HR 9909
Time: 877.831 seconds
 σ : 3.5 MPa
 P_{Target} : 3.5 MPa
P: 3.515 MPa
V: 0.1287 cm³

Crack Initiation within Seal

The fracture path from flaw tips to seal boundaries is back-interpreted from later frames (HR 9910) as they are not visible until cracks have propagated.

Note: Cracks are labeled alphabetically in chronological order of crack initiation. If the order cannot be determined, then they are labeled chronologically by initiation past flaw seal.

Sketch 2



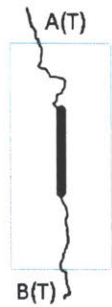
Frame: HS -2492
Time: 879 seconds
 σ : 3.5 MPa
 P_{Target} : 3.5 MPa
P: 3.507 MPa
V: 0.1296 cm³

Crack Initiation – Seal Break

Tensile crack A(T) propagates past top of flaw seal. At this point, the internal flaw pressure begins to drop.

This will be referred to as “Breakdown” of the specimen; i.e., the breakdown pressure $P_{\text{Breakdown}}=3.516$ MPa at 866 s from the beginning of the test. The average volume injected into the flaw until breakdown is 0.1288 cm³.

Sketch 3



Frame: HS -2040
Time: 879.452 seconds
 σ : 3.5 MPa
 P_{Target} : 3.5 MPa
 P : 3.506 MPa
 V : 0.1262 cm³

Crack Initiation – Seal Break

Tensile crack A(T) continues propagating.

After 0.45 s of crack A(T)'s propagation, tensile crack B(T) propagates past flaw seal.

Sketch 4



Frame: HS -500
Time: 880.992 seconds
 σ : 3.5 MPa
 P_{Target} : 3.5 MPa
 P : 3.497 MPa
 V : 0.1288 cm³

Crack Propagation

Tensile cracks A(T) and B(T) continue propagation.

Throughout propagation, a time lag was observed between the advancement of the crack and oil leaking out of the propagating crack at the crack tip.

Sketch 5



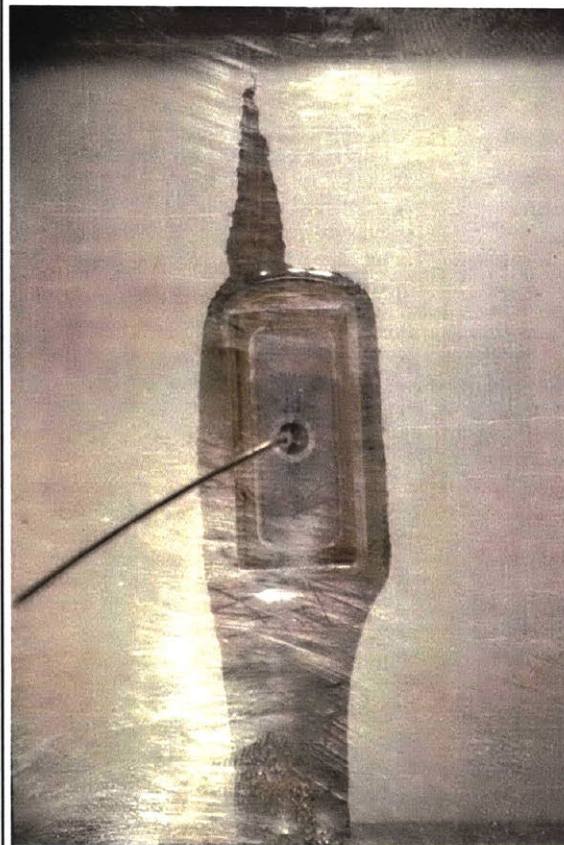
Frame: HS 1339
Time: 882.831 seconds
 σ : 3.5 MPa
 P_{Target} : 3.5 MPa
 P : 3.462 MPa
 V : 0.1317 cm³

Crack Propagation

Tensile crack A(T) continues to propagate.

Tensile crack B(T) stops propagating at this point. Crack B(T) propagated for 3.38 s since passing the flaw boundary.

Sketch 6



Frame: HR - 9916
Time: 911.831 seconds
 σ : 3.5 MPa
 P_{Target} : 3.5 MPa
P: 1.297 MPa
V: 0.3103 cm³

End of Crack Propagation

Tensile crack A(T) stops propagating at this point. Crack A(T) propagated for 32.83 s since passing the flaw boundary.

OP-HF-SF-90-B

07-26-2016

Uniaxial Compression With Hydraulic Fracture of Opalinus Shale

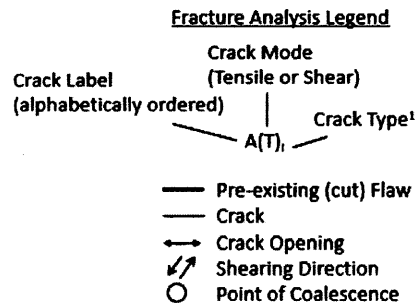
Experimental Procedure Notes:

- Flaw saturation phase fills flaw with oil that flows out of bleed hole to expel air from the system. This results in initial pressure build up in flaw shown at time = 0 seconds.
- After flaw saturation, system is closed by attaching pressure transducer to bleed hole.
- Pressurization of flaw is achieved using a PID pressure-control algorithm, where user-defined target pressures (P_{Target}) are defined and PVA injects oil to achieve P_{Target} .
- While holding a constant uniaxial compressive stress, flaw is pressurized in 0.5 MPa increments until specimen failure. Pressure step is held for 1-2 minutes before moving up to the next increment.

Specimen B Dimensions			
Height (h)	Width (w)	Thickness (t)	Area (A=wxt)
in	in	in	in ²
3.0627	2.0407	1.0408	2.1238

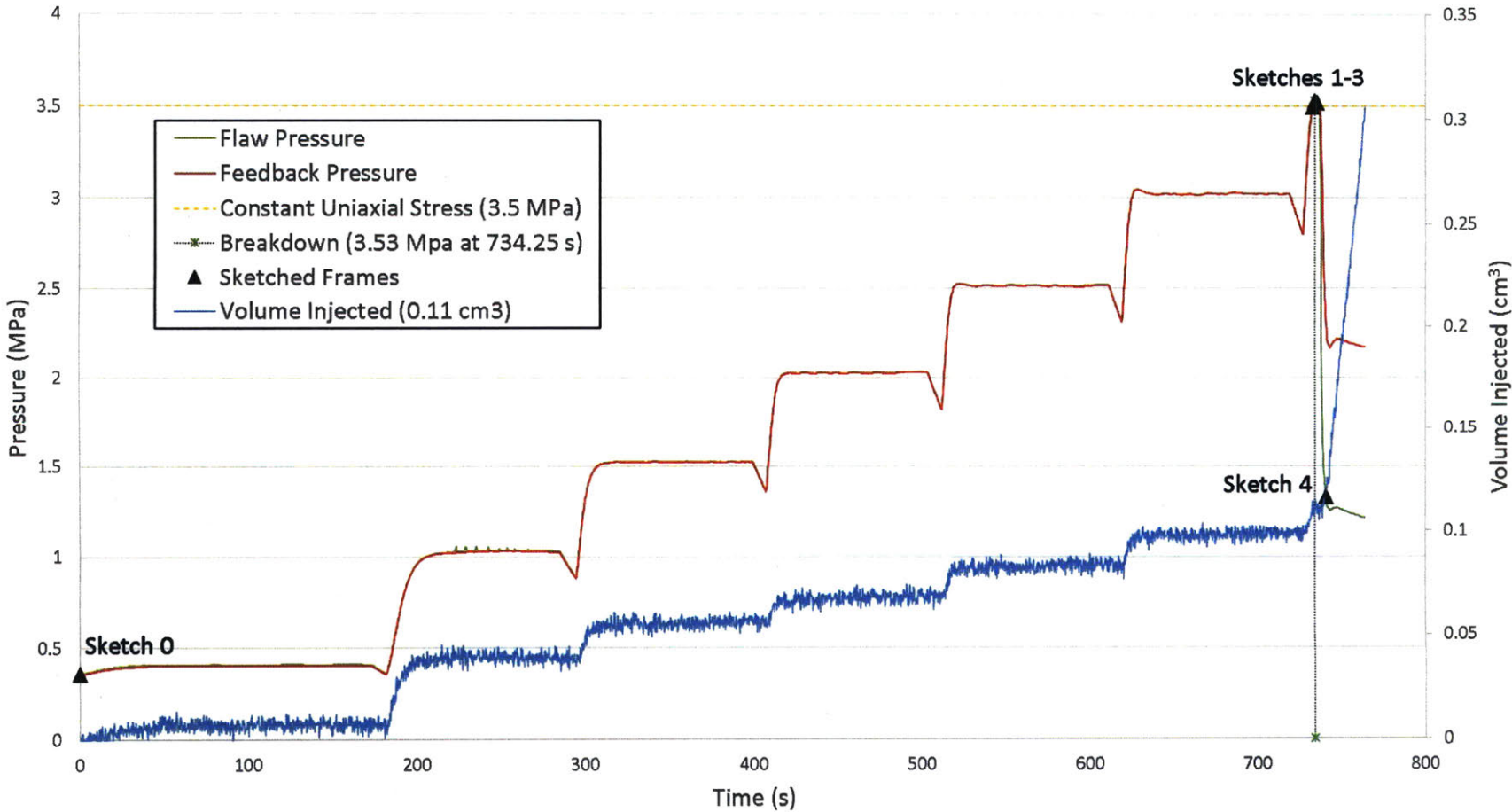
Test Summary			
Vertical Load Applied	Vertical Stress Applied	Maximum Hydraulic Pressure	Volume Injected until Loss of Pressure
kN	MPa	MPa	cm ³
4.80	3.5	3.53	0.11

Sketch Summary						
Sketch Number	Type of Frame	Frame Number	Time from beginning of Hydraulic closing system	Hydraulic Pressure	Normalized Hydraulic Pressure	Volume Injected
			s	MPa	Pressure	cm ³
0	High Resolution	9938	0	0.355	0.1006	0
1	High Resolution	0062	732.743	3.495	0.9901	0.1097
2	High Speed	-3333	734.25	3.53	1.0000	0.1108
3	High Speed	-2278	735.305	3.522	0.9977	0.1082
4	High Resolution	0066	740.743	1.328	0.3762	0.1187

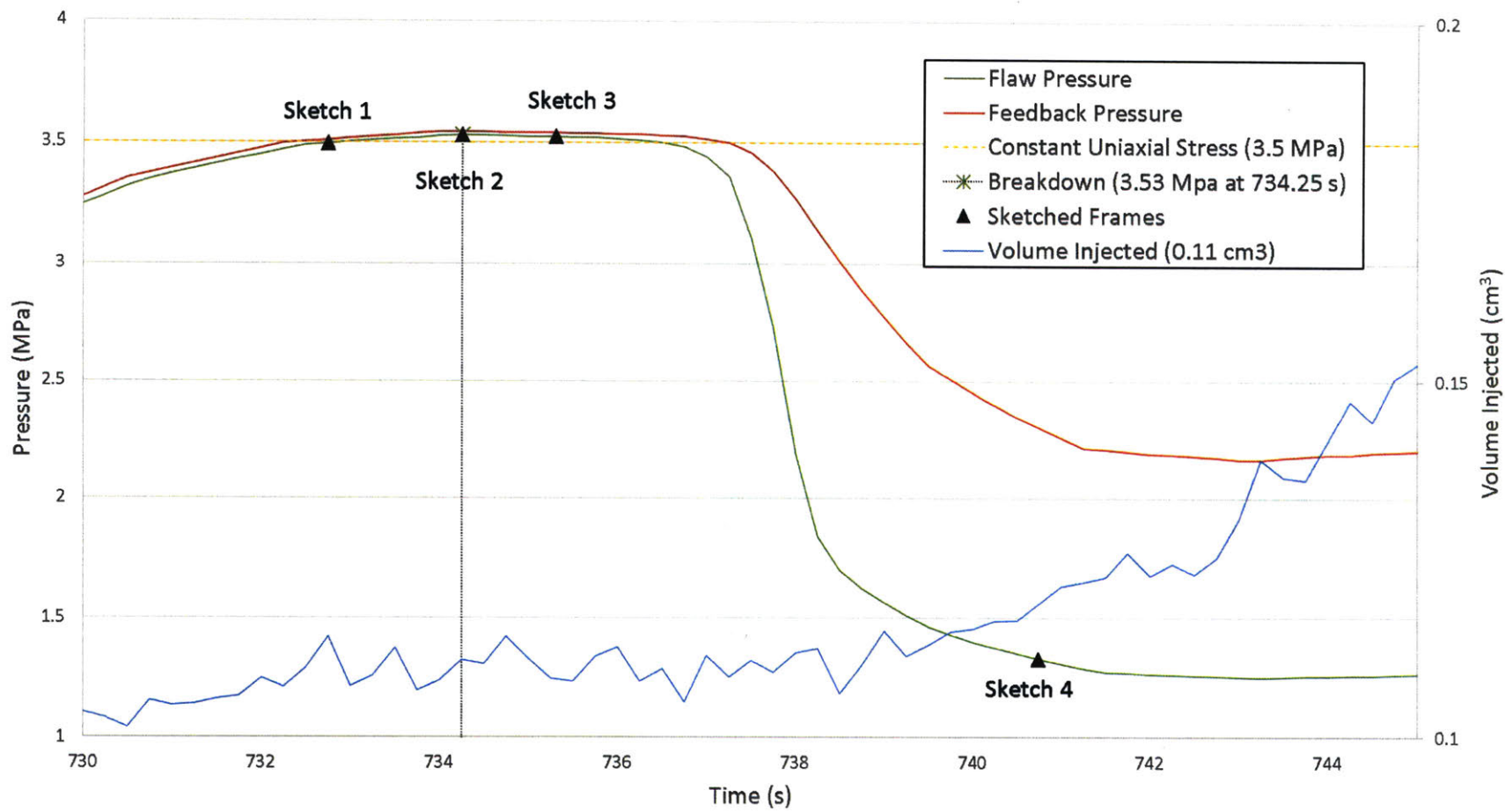


Cracks Summary				
Crack ID	Crack Type	Hydraulic Pressure at Crack Initiation	Hydraulic Pressure Normalized to the Maximum Hydraulic Pressure	Sketch
		Mpa	Pressure	
A(T)	no type	3.53	1.000	2
B(T)	no type	3.522	0.998	3

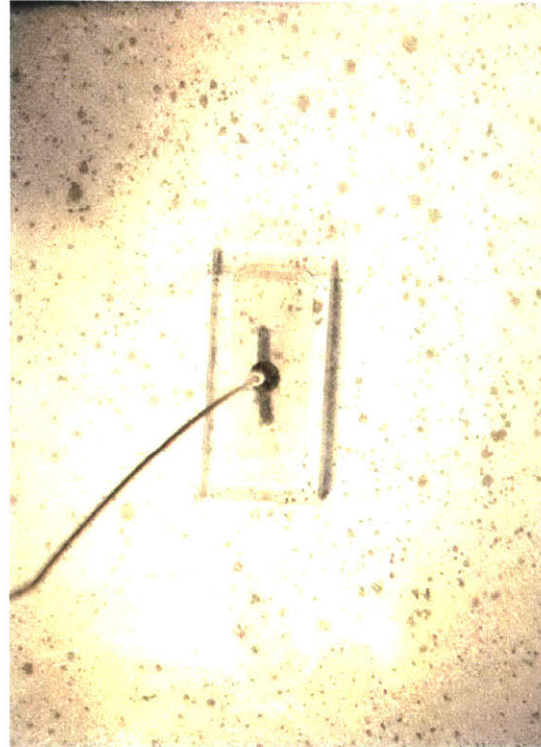
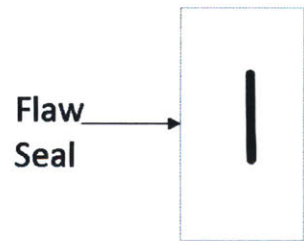
OP-HF-SF-90-B Test Data



OP-HF-SF-90-B Test Data Close-Up



Sketch 0



Frame: HR 9938 – Initial
Time: 0 seconds
 σ : 3.5 Mpa
 P_{Target} : 0.5 MPa
 P : 0.355 MPa
 V : 0 cm³

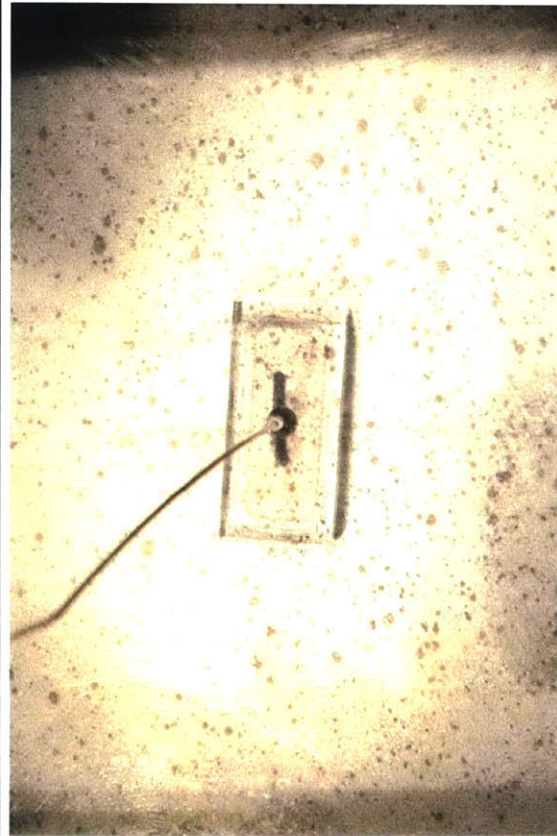
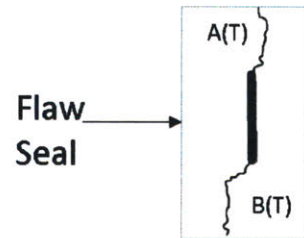
Initial Configuration

Prismatic Specimen: 4"x2"x1"
Flaw: 2a = 3/8"
Ligament Spacing (L): N/A
Flaw Angle (β): 90°
Bridging Angle (α): N/A
Bedding Orientation (ψ): 0°

Pressure Increments: 0.5 MPa
Pressure Hold Time: ~1 min

All cracks are labeled based on their initiation order.

Sketch 1



Frame: HR 0062
Time: 732.743 seconds
 σ : 3.5 MPa
 P_{Target} : 3.5 MPa
P: 3.495 MPa
V: 0.1097 cm³

Crack Initiation within Seal

The fracture path from flaw tips to seal boundaries is back-interpreted from later frames (HR 0066) as they are not visible until cracks have propagated.

Note: Cracks are labeled alphabetically in chronological order of crack initiation. If the order cannot be determined, then they are labeled chronologically by initiation past flaw seal.

Sketch 2



Frame: HS -3333
Time: 734.25 seconds
 σ : 3.5 Mpa
 P_{Target} : 3.5 MPa
P: 3.53 MPa
V: 0.1108 cm³

Crack Initiation – Seal Break

Tensile crack A(T) propagates past top of flaw seal. At this point, the internal flaw pressure begins to drop.

This will be referred to as “Breakdown” of the specimen; i.e., the breakdown pressure $P_{\text{Breakdown}}=3.53$ MPa at 734.25 s from the beginning of the test. The average volume injected into the flaw until breakdown is 0.11 cm³.

Sketch 3



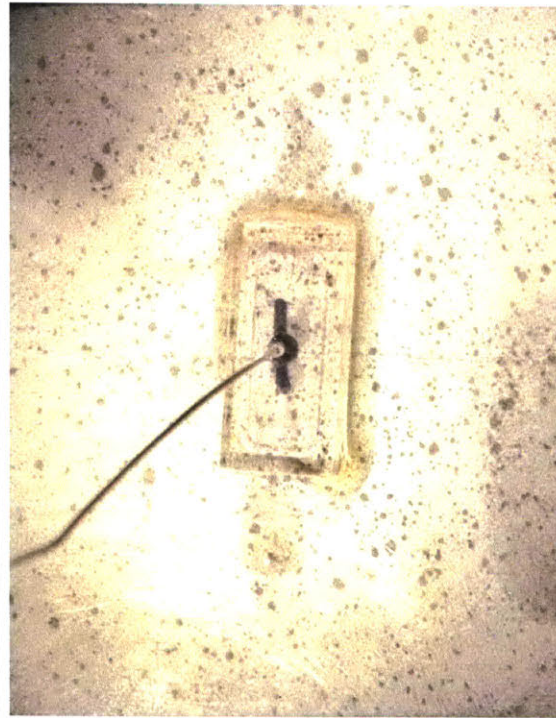
Frame: HS - 2278
Time: 735.305 seconds
 σ : 3.5 Mpa
 P_{Target} : 3.5 MPa
P: 3.522 MPa
V: 0.1082 cm³

Crack Initiation – Seal Break

Tensile crack A(T) continues propagating.

After 1.055 s of crack A(T)'s propagation, tensile crack B(T) propagates past flaw seal.

Sketch 4



Frame: HR 0066
Time: 740.743 seconds
 σ : 3.5 Mpa
 P_{Target} : 3.5 MPa
P: 1.328 MPa
V: 0.1187 cm³

End of Crack Propagation

Tensile cracks A(T) and B(T) stop propagating at this point. Total propagation time was 6.493 s since passing the flaw boundary.

Throughout propagation, a time lag was observed between the advancement of the crack and oil leaking out of the propagating crack at the crack tip.

OP-HF-SF-90-C

07-26-2016

Uniaxial Compression with Hydraulic Fracture of Opalinus Shale

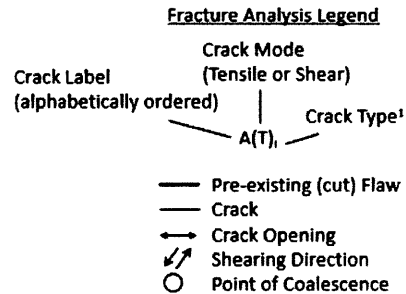
Experimental Procedure Notes:

- Flaw saturation phase fills flaw with oil that flows out of bleed hole to expel air from the system. This results in initial pressure build up in flaw shown at time = 0 seconds.
- After flaw saturation, system is closed by attaching pressure transducer to bleed hole.
- Pressurization of flaw is achieved using a PID pressure-control algorithm, where user-defined target pressures (P_{Target}) are defined and PVA injects oil to achieve P_{Target} .
- While holding a constant uniaxial compressive stress, flaw is pressurized in 0.5 MPa increments until specimen failure. Pressure step is held for 1-2 minutes before moving up to the next increment.

Specimen C Dimensions			
Height (h)	Width (w)	Thickness (t)	Area (A=wxt)
in	in	in	in ²
3.3652	1.9713	1.0064	1.9840

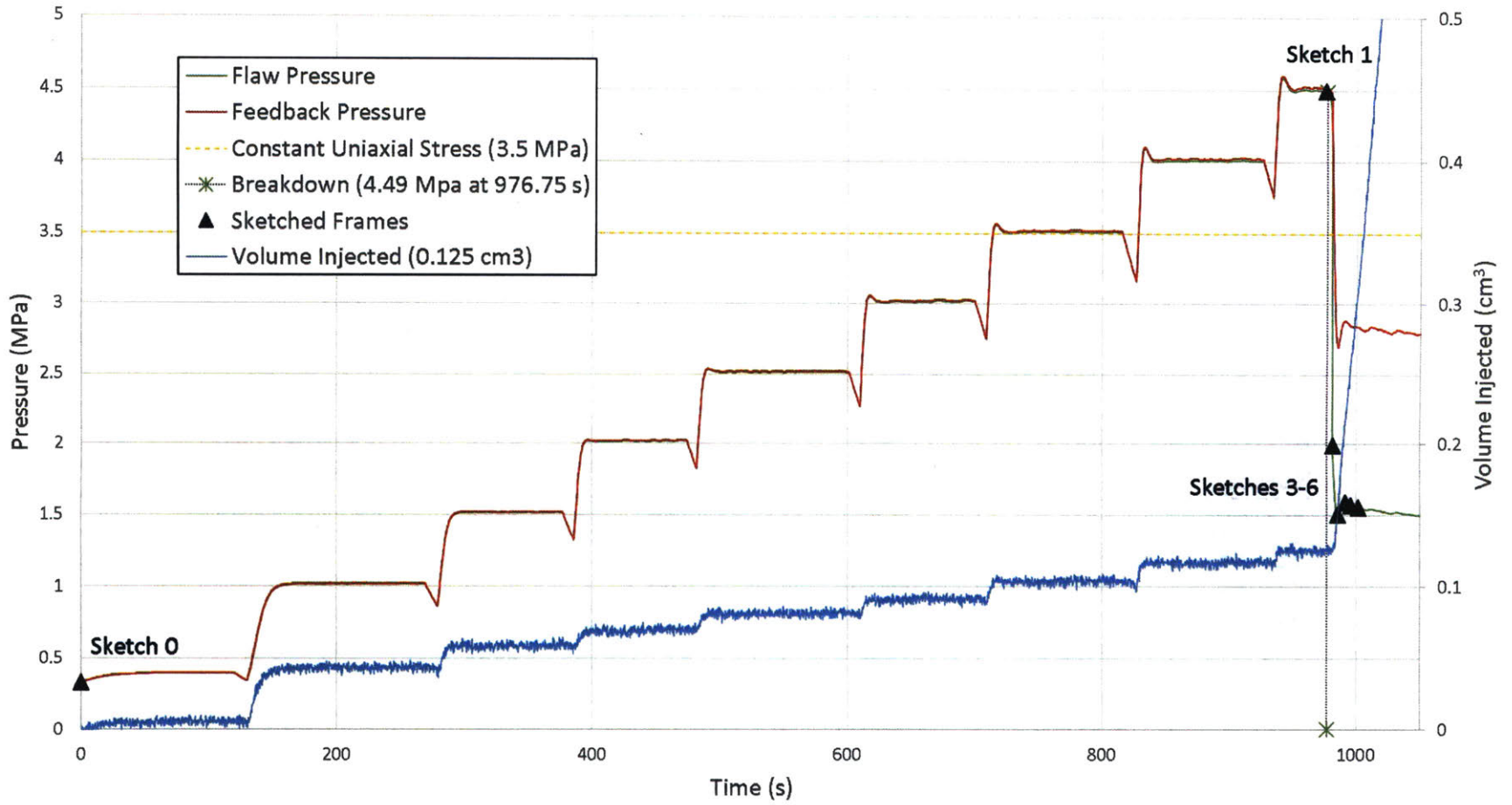
Test Summary			
Vertical Load Applied	Vertical Stress Applied	Maximum Hydraulic Pressure	Volume Injected until Loss of Pressure
kN	MPa	MPa	cm ³
4.48	3.5	4.58	0.125

Sketch Summary						
Sketch Number	Type of Frame	Frame Number	Time from beginning of closing system	Hydraulic Pressure	Normalized Hydraulic Pressure	Volume Injected
			s	MPa		cm ³
0	High Resolution	9533	0	0.32668	0.0713	0
1	High Resolution	9724	975.75	4.494149	0.9804	0.125563
2	High Resolution	9725	981.75	1.984692	0.4329	0.124639
3	High Resolution	9726	985.75	1.502671	0.3278	0.152751
4	High Resolution	9727	991.75	1.58827	0.3465	0.216232
5	High Resolution	9728	995.75	1.56542	0.3415	0.259565
6	High Resolution	9729	1001.75	1.554135	0.3390	0.317946

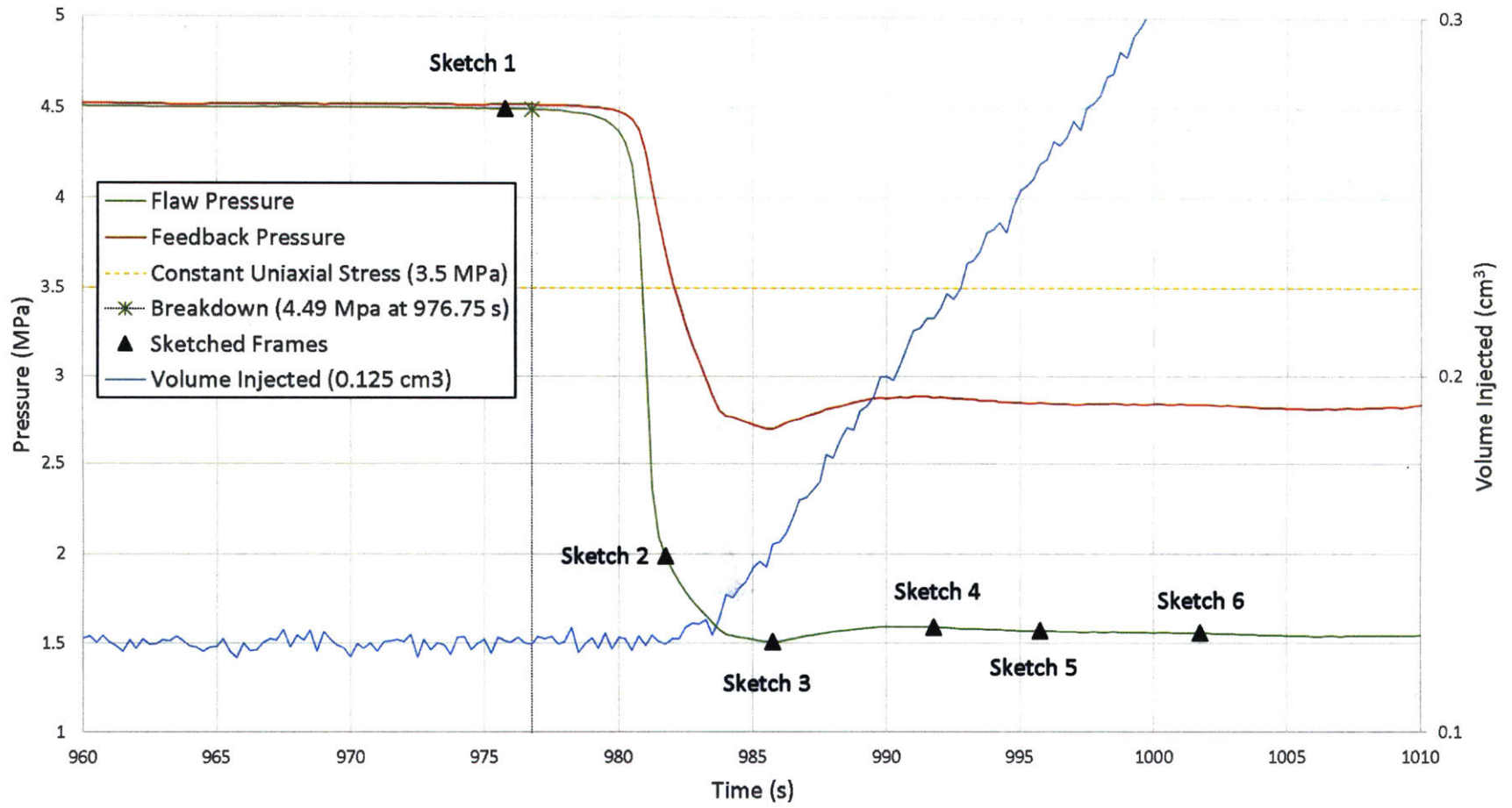


OP-HF-SF-B Fractures Summary				
Crack ID	Crack Type	Hydraulic Pressure at Crack Initiation	Hydraulic Pressure Normalized to the Maximum Hydraulic Pressure	Sketch
		Mpa		
A(T)	no type	4.49	0.98	2
B(T)	no type	4.49	0.98	2

OP-HF-SF-90-C Test Data

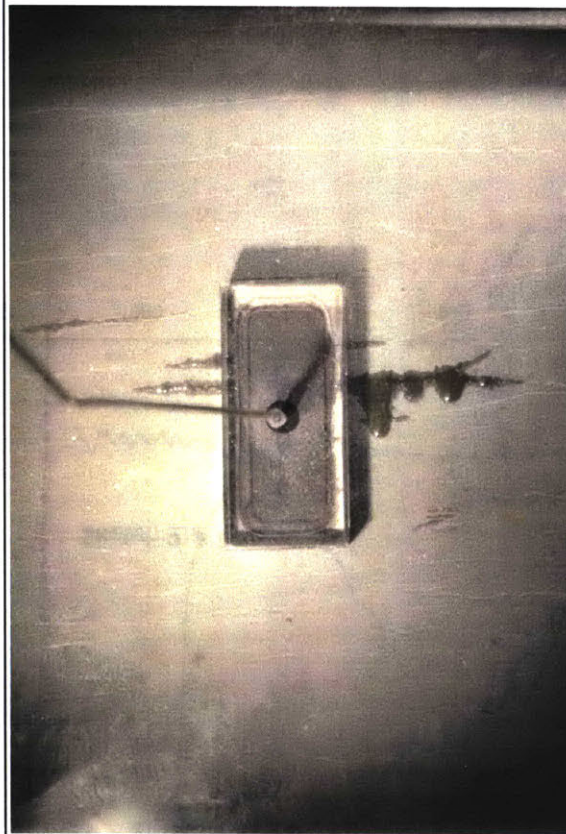


OP-HF-SF-90-C Test Data Close-Up



Sketch 0

Flaw
Seal →



Frame: HR 9533 – Initial
Time: 0 seconds
 σ : 3.5 Mpa
 P_{Target} : 0.5 MPa
P: 0.327 MPa
V: 0 cm³

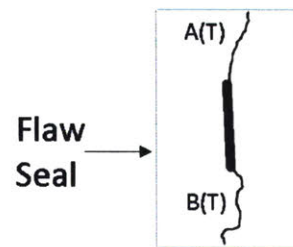
Initial Configuration

Prismatic Specimen: 4"x2"x1"
Flaw: 2a = 3/8"
Ligament Spacing (L): N/A
Flaw Angle (β): 90°
Bridging Angle (α): N/A
Bedding Orientation (ψ): 0°

Pressure Increments: 0.5 MPa
Pressure Hold Time: ~1 min

All cracks are labeled based on their initiation order.

Sketch 1



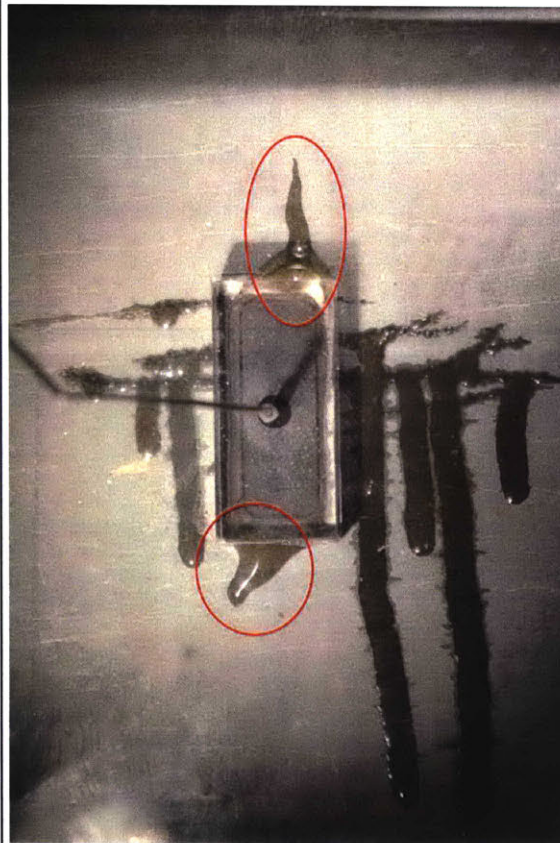
Frame: HR 9724
Time: 975.75 seconds
 σ : 3.5 Mpa
 P_{Target} : 4.5 MPa
P: 4.494 MPa
V: 0.1256 cm³

Crack Initiation within Seal

The fracture paths from flaw tips to seal boundaries is back-interpreted from later frames (HR 9729) as they are not visible until cracks have propagated.

Note: It was observed from the High Resolution images that after the flaw was oil saturated in Sketch 0, oil leaked through the bedding planes as pressure was increased. The leaking through the bedding planes did not reduce the hydraulic pressure or prevent it from holding during the incremental pressure increase or hold.

Sketch 2



Frame: HR 9725
Time: 981.75 seconds
 σ : 3.5 MPa
 P_{Target} : 4.5 MPa
 P : 1.985 MPa
 V : 0.1246 cm³

Crack Initiation – Seal Break

Cracks A(T) and B(T) propagated past the flaw seal causing the pressure drop observed in the Pressure/Time curve. Some oil leaks out of cracks as they propagate.

This will be referred to as “Breakdown” of the specimen; i.e., the breakdown pressure $P_{\text{Breakdown}}=4.49$ MPa at 976.75 s from the beginning of the test. The average volume injected into the flaw until breakdown is 0.125 cm³.

Note: High Speed video was not captured for this test. Time synchronization of High Resolution images was estimated by assuming this image (HR 9725) was taken 5 seconds after breakdown (observed at $t=976.75$).

Sketch 3



Frame: HR 9726
Time: 985.75 seconds
 σ : 3.5 Mpa
 P_{Target} : 4.5 MPa
P: 1.503 MPa
V: 0.1528 cm³

Crack Propagation

Cracks A(T) and B(T) continue to propagate.

At this stage in the test, the motor starts injecting more oil to compensate for the pressure loss (target is still 4.5 Mpa). Significant more oil leaks through cracks.

Sketch 4

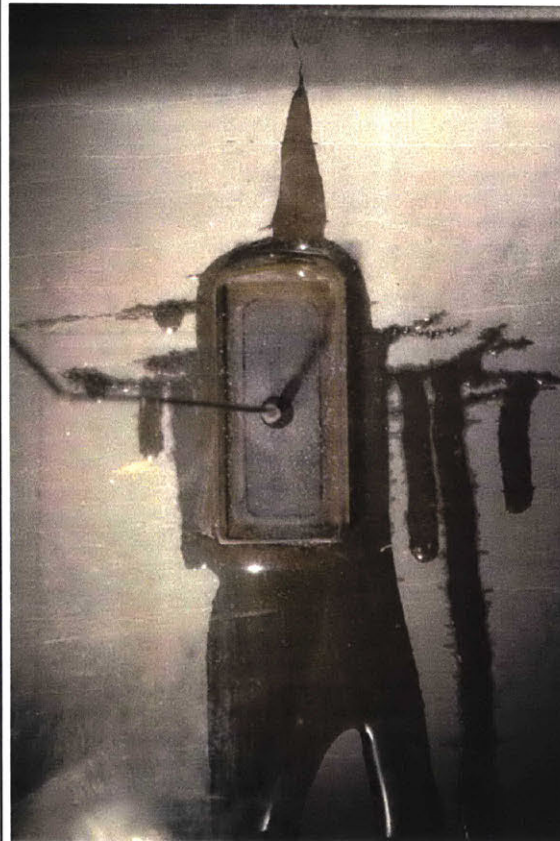
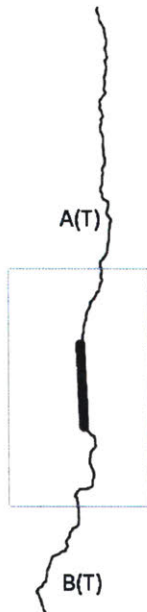


Frame: HR 9727
Time: 991.75 seconds
 σ : 3.5 Mpa
 P_{Target} : 4.5 MPa
P: 1.588 MPa
V: 0.2162 cm³

Crack Propagation

Crack A(T) continues to propagate. Significant more oil leaks through cracks.

Sketch 5

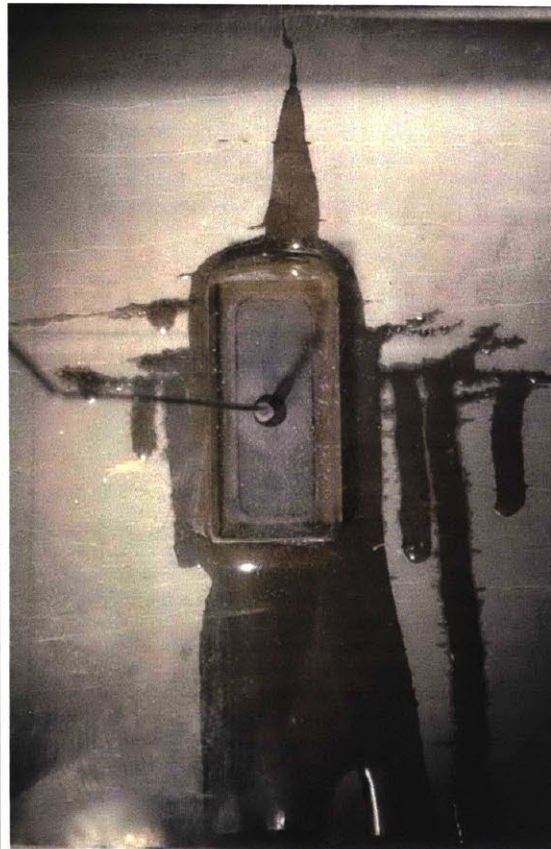


Frame: HR 9728
Time: 995.75 seconds
 σ : 3.5 Mpa
 P_{Target} : 4.5 MPa
P: 1.565 MPa
V: 0.2596 cm³

Crack Propagation

Crack A(T) continues to propagate. Significant more oil leaks through cracks.

Sketch 6



Frame: HR 9729
Time: 1001.75 seconds
 σ : 3.5 Mpa
 P_{Target} : 4.5 MPa
P: 1.554 MPa
V: 0.3179 cm³

End of Crack Propagation

Crack A(T) continues to propagate.
Crack B(T) also propagated after it was arrested for 20 seconds. Significant more oil leaks through cracks.
Total propagation time was 25 seconds.

OP-HF-2a-30-30-A

10-19-2016

Uniaxial Compression with Hydraulic Fracture of Opalinus Shale

Experimental Procedure Notes:

- Flaw saturation phase fills flaw with oil that flows out of bleed hole to expel air from the system. This results in initial pressure build up in flaw shown at time = 0 seconds.
- After flaw saturation, system is closed by attaching pressure transducer to bleed hole.
- Pressurization of flaw is achieved using a PID pressure-control algorithm, where user-defined target pressures (P_{Target}) are defined and PVA injects oil to achieve P_{Target} .
- While holding a constant uniaxial compressive stress, flaw is pressurized in 0.5 MPa increments until specimen failure. Pressure step is held for 1-2 minutes before moving up to the next increment.

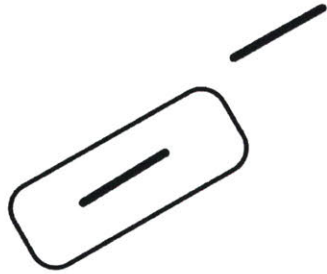
OP-HF-2a-30-30-A Dimensions			
Height (h)	Width (w)	Thickness (t)	Area (A=w x t)
[in]	[in]	[in]	[in ²]
3.942	2.086	0.930	1.940

OP-HF-2a-30-30-A Test Summary			
Vertical Load Applied	Vertical Stress Applied	Maximum Hydraulic Pressure	Volume Injected until Loss of Pressure
[kN]	[MPa]	[MPa]	[cm ³]
4.38	3.5	-	-

Note:

Specimen OP-HF-2a-30-30-A was loaded with uniaxial compression to 3.5 MPa and flaw was saturated. Upon starting the pressurization phase, the pump started injecting oil uncontrollably due to equipment malfunction. No data was collected for this test. Analysis only shows one image prior to testing and one image after uncontrolled pressurization.

Sketch 0



Frame:

Time: 0 seconds

σ : 3.5 MPa

P_{Target} :

P:

V: 0 cm³

Initial Configuration

Prismatic Specimen: 4"x2"x1"

Flaw: 2a = 3/8"

Ligament Spacing (L): 2a

Flaw Angle (β): 30°

Bridging Angle (α): 30°

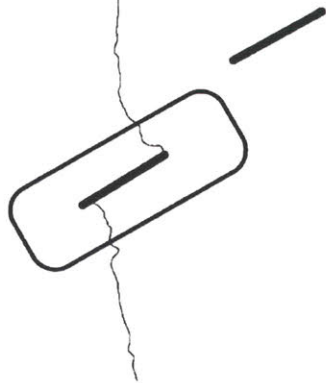
Bedding Orientation (ψ): 0°

Pressure Increments: 0.5 MPa

Pressure Hold Time: ~1 min

Sketch 1

Pressurized bedding plane that eventually allowed HF to propagate.



Crack Summary

Although no data was collected, the final image of the specimen after uncontrolled pressurization is shown.

What is clear in the image is that the hydraulic fracture propagated from the pressurized flaw in the direction of uniaxial loading.

Also, it was witnessed that the hydraulic fracture propagated across bedding planes, arrested at a prominent bedding plane and filled it, then continued propagating across. This behavior is seen four times as indicated by the arrows, and is also seen in the other tests.

This geometry and loading condition lead to a Category 1: No Coalescence.

OP-HF-2a-30-30-B

10-19-2016

Uniaxial Compression with Hydraulic Fracture of Opalinus Shale

Experimental Procedure Notes:

- Flaw saturation phase fills flaw with oil that flows out of bleed hole to expel air from the system. This results in initial pressure build up in flaw shown at time = 0 seconds.
- After flaw saturation, system is closed by attaching pressure transducer to bleed hole.
- Pressurization of flaw is achieved using a PID pressure-control algorithm, where user-defined target pressures (P_{Target}) are defined and PVA injects oil to achieve P_{Target} .
- While holding a constant uniaxial compressive stress, flaw is pressurized in 0.5 MPa increments until specimen failure. Pressure step is held for 1-2 minutes before moving up to the next increment.

OP-HF-2a-30-30-B Dimensions			
Height (h)	Width (w)	Thickness (t)	Area (A=w x t)
[in]	[in]	[in]	[in ²]
3.986	1.990	0.919	1.829

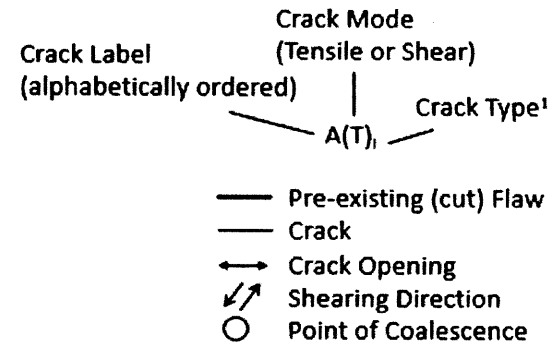
OP-HF-2a-30-30-B Test Summary			
Vertical Load Applied	Vertical Stress Applied	Maximum Hydraulic Pressure	Volume Injected until Loss of Pressure
[kN]	[MPa]	[MPa]	[cm ³]
4.13	3.5	4.51	0.3817

OP-HF-2a-30-30-B Sketch Summary						
Sketch Number	Type of Frame	Frame Number	Time from beginning of closing system	Hydraulic Pressure	Normalized Hydraulic Pressure (Pmax = 4.51 MPa)	Volume Injected
			[s]	[MPa]		[cm ³]
0	High Resolution	9715	0	0.3341	0.0741	0.0000
1	High Resolution	410	1442	3.5328	0.7840	0.3016
2	High Resolution	610	1844	4.4945	0.9974	0.3445
3	High Resolution	660	1944	4.1217	0.9147	0.4029
4	High Resolution	670	1964	4.0765	0.9046	0.4264
5	High Resolution	671	1966	4.0719	0.9036	0.4315
6	High Resolution	676	1976	4.0424	0.8971	0.4413
7	High Resolution	682	1988	4.0027	0.8882	0.4642
8	High Resolution	689	2002	4.0098	0.8898	0.4884

Notes:

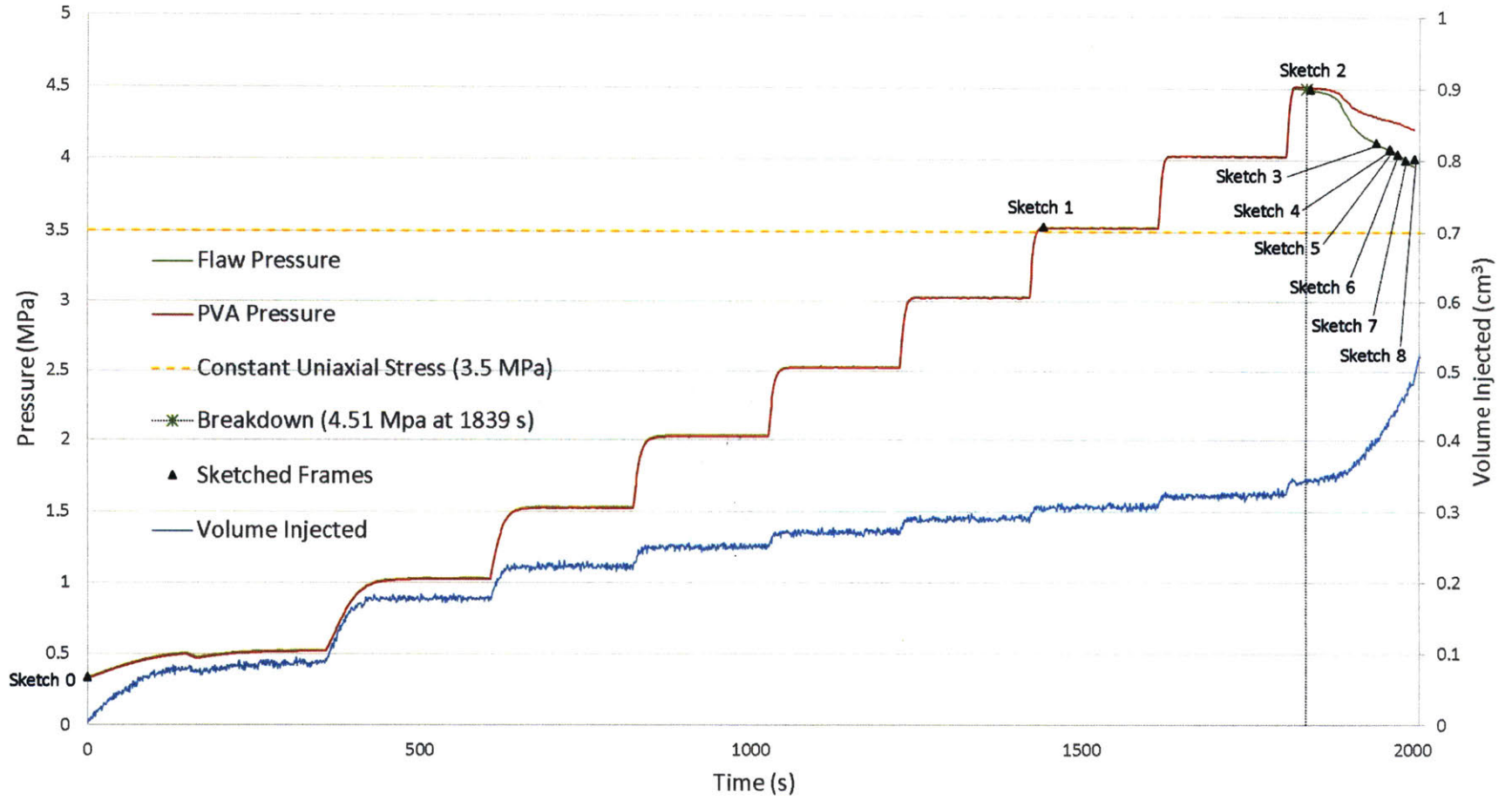
- Flow through bedding planes is denoted by a subscript “_b”.
- High-Speed video was not captured for this test.
- Table shows estimated crack initiation.
- Coalescence Category 1: no coalescence

Fracture Analysis Legend

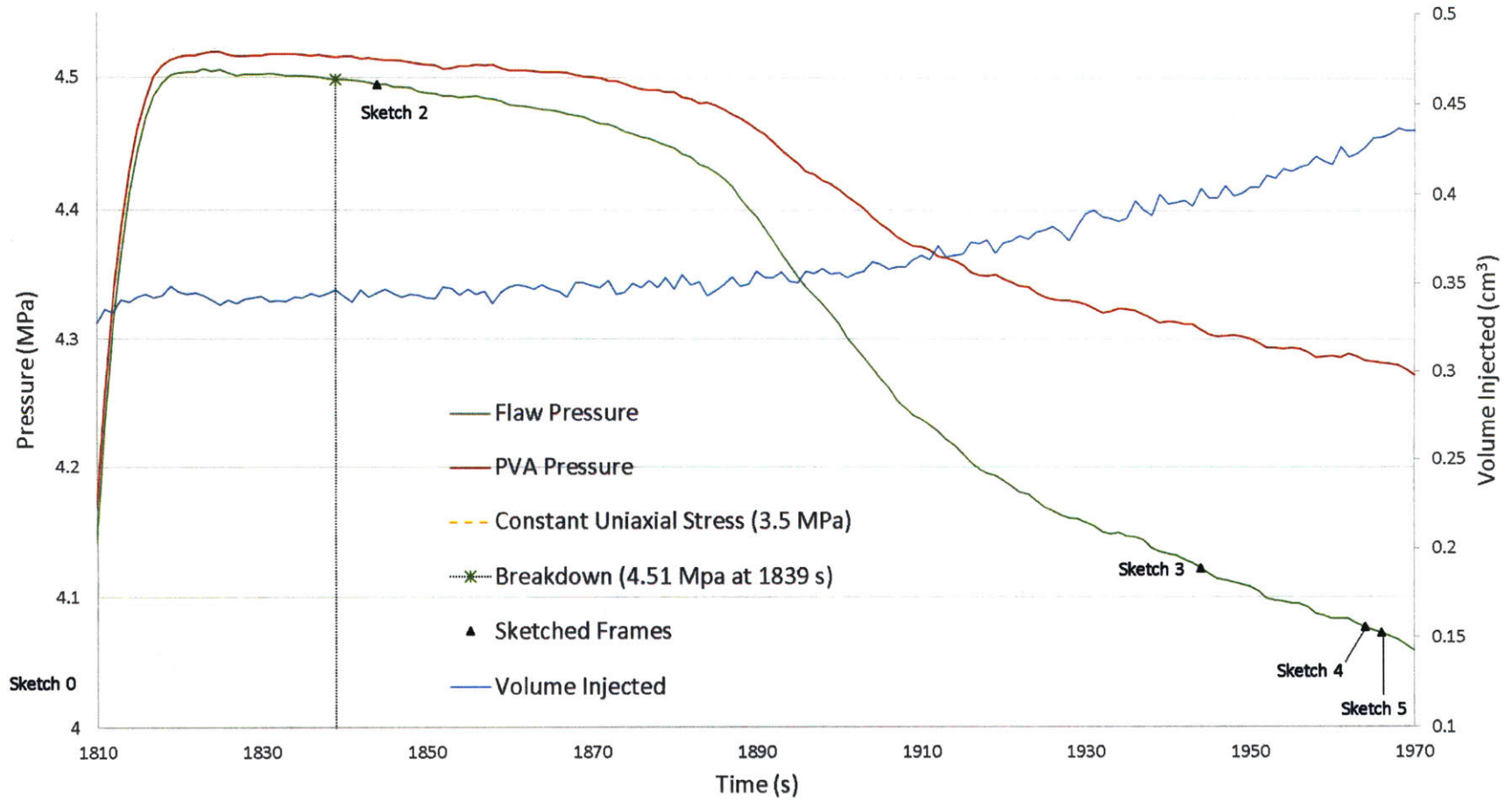


OP-HF-2a-30-30-B Fractures Summary							
Crack Label	Crack Type	Type of Frame	Frame Number	Time from beginning of closing system	Hydraulic Pressure	Normalized Hydraulic Pressure (P _{max} = 4.51 MPa)	Volume Injected
				[s]	[MPa]		[cm ³]
A(T) _b	Tensile – Bedding Flow	High Resolution	9715	0	0.3341	0.0741	0
B(T)	Tensile – No Type	High Resolution	607	1838	4.4989	0.9984	0.3439
C(T) _b	Tensile – Bedding Flow	High Resolution	668	1960	4.0830	0.9061	0.4164
D(T)	Tensile – No Type	High Resolution	671	1966	4.0719	0.9036	0.4315
E(T) _b	Tensile – Bedding Flow	High Speed	672	1968	4.0670	0.9025	0.4363
F(T)	Tensile – No Type	High Resolution	681	1986	4.0111	0.8901	0.4612
Coalescence Category 1: No Coalescence		High Resolution	-	-	-	-	-

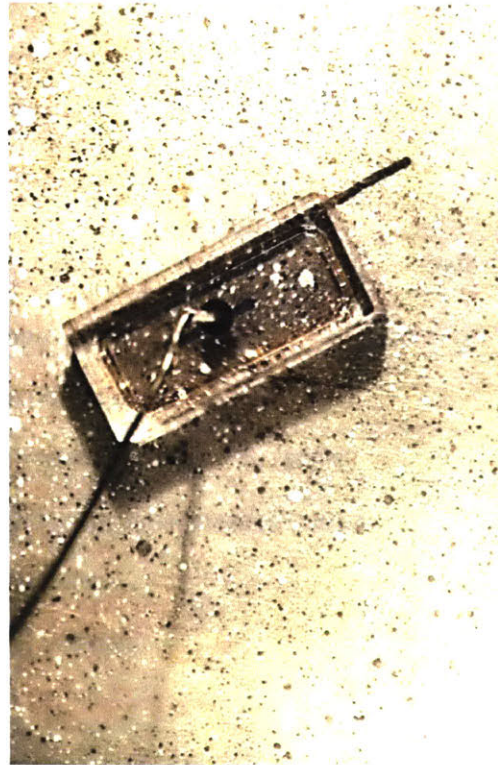
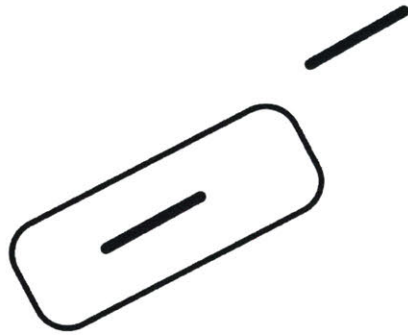
OP-HF-2a-30-30-B Test Data



OP-HF-2a-30-30-B Test Data Close-Up



Sketch 0



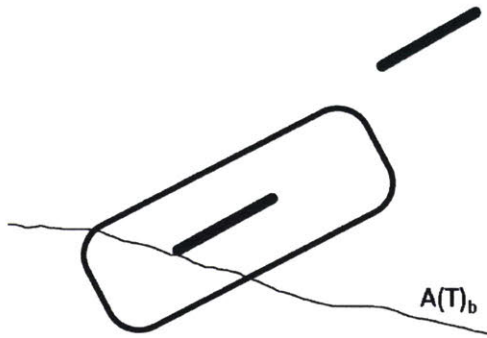
Frame: HR 9715 – Initial
Time: 0 seconds
 σ : 3.5 MPa
 P_{Target} : 0.5 MPa
 P : 0.334 MPa
 V : 0 cm³

Initial Configuration

Prismatic Specimen: 4"x2"x1"
Flaw: 2a = 3/8"
Ligament Spacing (L): 2a
Flaw Angle (β): 30°
Bridging Angle (α): 30°
Bedding Orientation (ψ): 0°

Pressure Increments: 0.5 MPa
Pressure Hold Time: ~1 min

Sketch 1



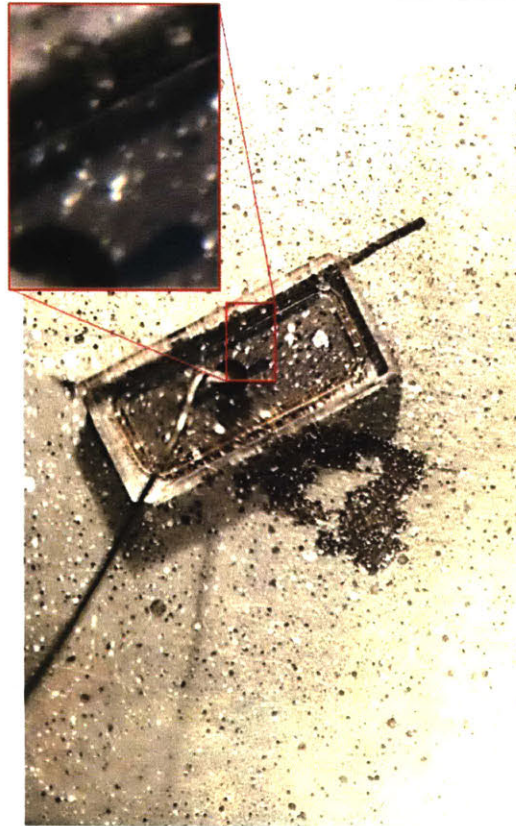
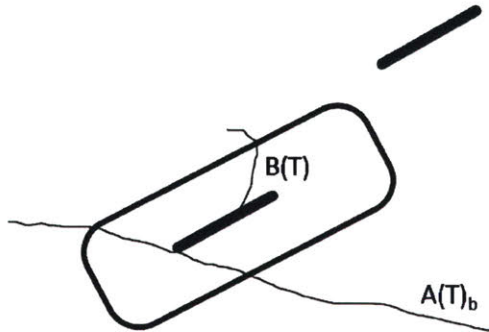
Frame: HR 410
Time: 1442 seconds
 σ : 3.5 MPa
 P_{Target} : 3.5 MPa
 P : 3.533 MPa
 V : 0.3016 cm³

Crack Initiation prior to Pressurization

This shale specimen had a bedding plane, $A(T)_b$, coinciding with the outer tip of the left flaw. $A(T)_b$ immediately started filling with oil from the saturation phase, and this is shown in Sketch 0. However, the oil was contained within close vicinity to the flaw seal boundary. Upon pressurizing to 3.5 MPa, pressurized oil advanced through $A(T)_b$ and started slowly flowing out onto the specimen surface, as shown in Sketch 1.

Note: Cracks are labeled alphabetically in chronological order of crack initiation. If the order cannot be determined, then they are labeled chronologically by initiation past flaw seal.

Sketch 2

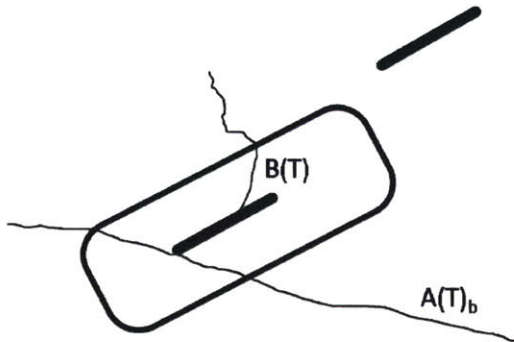


Frame: HR 610
Time: 1844 seconds
 σ : 3.5 MPa
 P_{Target} : 4.5 MPa
 P : 4.495 MPa
 V : 0.3445 cm³

Crack Initiation & Propagation

B(T) was the first crack to initiate and propagate. It initiated at the center of the left flaw and propagated up. After passing the flaw seal boundary, B(T) started propagating through bedding planes.

Sketch 3

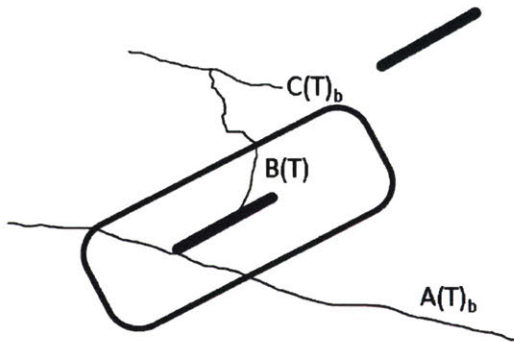


Frame: HR 660
Time: 1944 seconds
 σ : 3.5 MPa
 P_{Target} : 4.5 MPa
 P : 4.122 MPa
 V : 0.4029 cm³

Crack Propagation & Arrest

B(T) continues propagating, alternating between through bedding planes and across bedding planes as shown. Eventually, B(T) arrests at a bedding plane.

Sketch 4

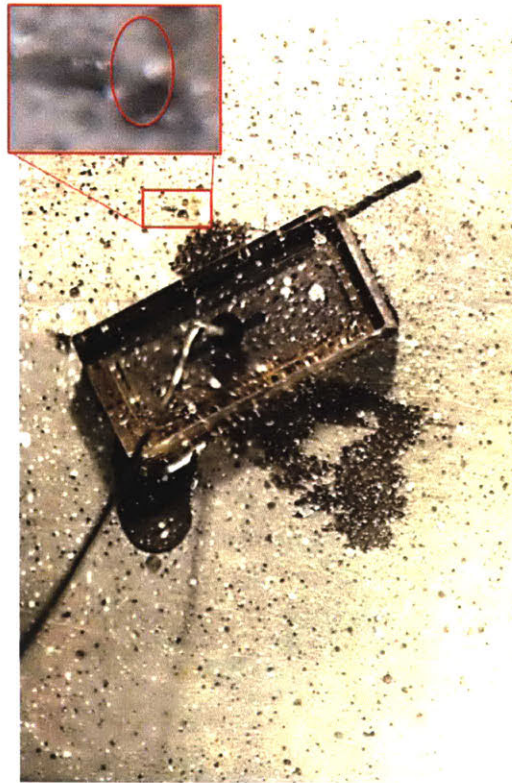
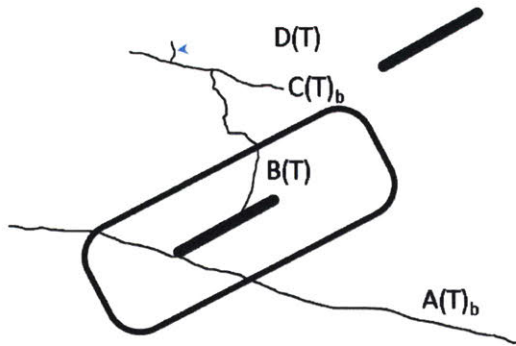


Frame: HR 670
Time: 1964 seconds
 σ : 3.5 MPa
 P_{Target} : 4.5 MPa
 P : 4.077 MPa
 V : 0.4264 cm³

Bedding Plane Flow

Pressurized oil from B(T) started flowing through bedding C(T)_b.

Sketch 5

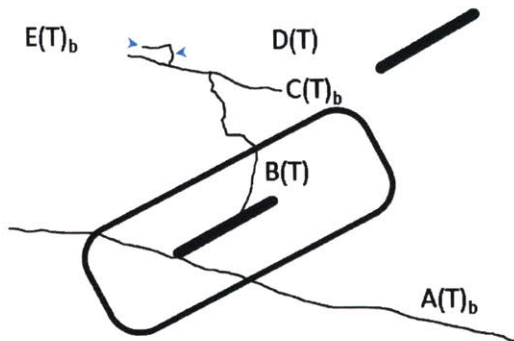


Frame: HR 671
Time: 1966 seconds
 σ : 3.5 MPa
 P_{Target} : 4.5 MPa
 P : 4.072 MPa
 V : 0.4315 cm³

Crack Initiation & Propagation

Tensile crack D(T) initiates from the pressurized bedding plane C(T)_b and slightly propagates upwards.

Sketch 6

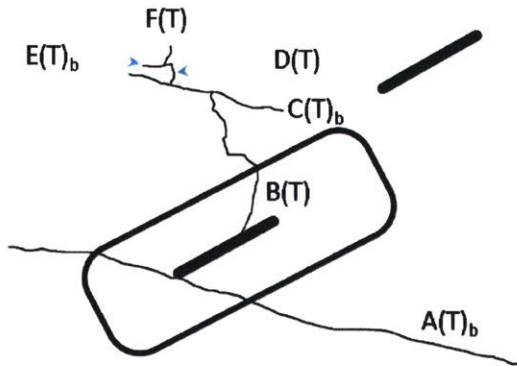


Frame: HR 676
Time: 1976 seconds
 σ : 3.5 MPa
 P_{Target} : 4.5 MPa
P: 4.042 MPa
V: 0.4413 cm³

Bedding Plane Flow

D(T) arrests at bedding plane E(T)_b. The pressurized oil then fills E(T)_b.

Sketch 7

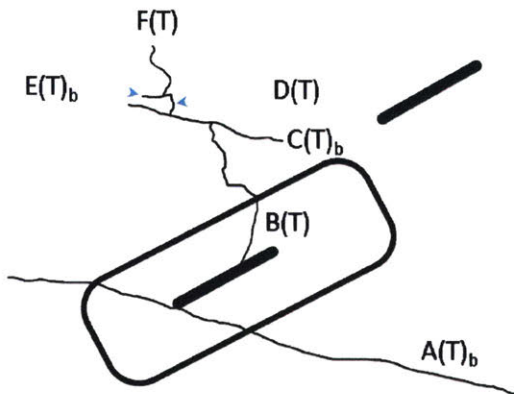


Frame: HR 682
Time: 1988 seconds
 σ : 3.5 MPa
 P_{Target} : 4.5 MPa
 P : 4.003 MPa
 V : 0.4642 cm³

Crack Initiation & Propagation

Tensile crack $F(T)$ initiates from the pressurized bedding plane $E(T)_b$ and slightly propagates upwards.

Sketch 8



Frame: HR 689
Time: 2002 seconds
 σ : 3.5 MPa
 P_{Target} : 4.5 MPa
P: 4.010 MPa
V: 0.4884 cm³

End of test

F(T) continued propagating slightly upwards and then arrested.

This geometry and loading condition lead to a Category 1: No Coalescence.

OP-HF-2a-30-30-C

10-19-2016

Uniaxial Compression with Hydraulic Fracture of Opalinus Shale

Experimental Procedure Notes:

- Flaw saturation phase fills flaw with oil that flows out of bleed hole to expel air from the system. This results in initial pressure build up in flaw shown at time = 0 seconds.
- After flaw saturation, system is closed by attaching pressure transducer to bleed hole.
- Pressurization of flaw is achieved using a PID pressure-control algorithm, where user-defined target pressures (P_{Target}) are defined and PVA injects oil to achieve P_{Target} .
- While holding a constant uniaxial compressive stress, flaw is pressurized in 0.5 MPa increments until specimen failure. Pressure step is held for 1-2 minutes before moving up to the next increment.

OP-HF-2a-30-30-C Dimensions			
Height (h)	Width (w)	Thickness (t)	Area (A=w x t)
[in]	[in]	[in]	[in ²]
3.859	1.933	0.930	1.797

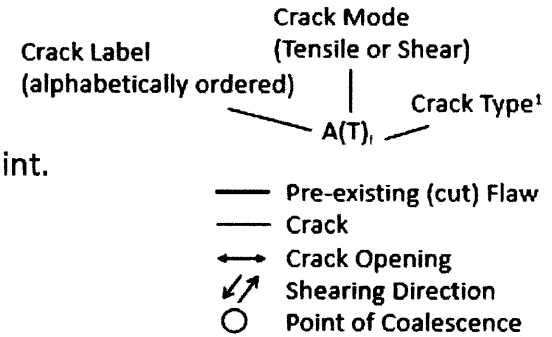
OP-HF-2a-30-30-C Test Summary			
Vertical Load Applied	Vertical Stress Applied	Maximum Hydraulic Pressure	Volume Injected until Loss of Pressure
[kN]	[MPa]	[MPa]	[cm ³]
4.06	3.5	4.49	0.2365

OP-HF-2a-30-30-C Sketch Summary						
Sketch Number	Type of Frame	Frame Number	Time from beginning of closing system	Hydraulic Pressure	Normalized Hydraulic Pressure (Pmax = 4.49 MPa)	Volume Injected
			[s]	[MPa]		[cm ³]
0	High Resolution	770	0	0.3564	0.0794	0.0000
1	High Resolution	771	2	0.3614	0.0805	0.0020
2	High Resolution	1391	1570	4.0305	0.8973	0.2211
3	High Resolution	1401	1590	4.0232	0.8957	0.2230
4	High Resolution	1462	1712	3.7974	0.8454	0.2915
5	High Resolution	1468	1724	3.7419	0.8331	0.3169

Notes:

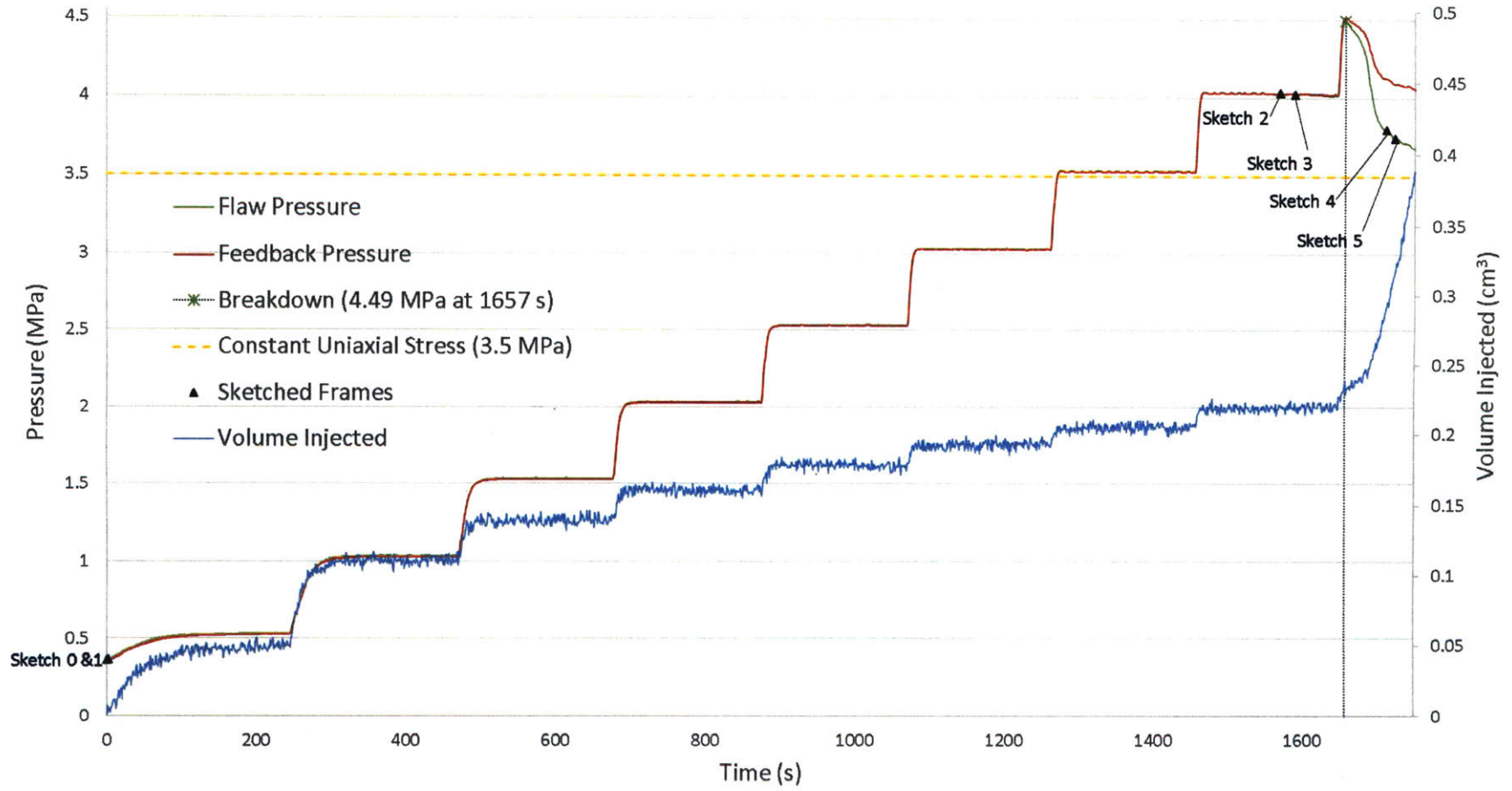
- Flow through bedding planes is denoted by a subscript “_b”.
- Bedding plane flow was difficult to see in this test due to the white paint.
- High-Speed video was not captured for this test.
- Table shows estimated crack initiation.
- Coalescence Category 1: no coalescence

Fracture Analysis Legend

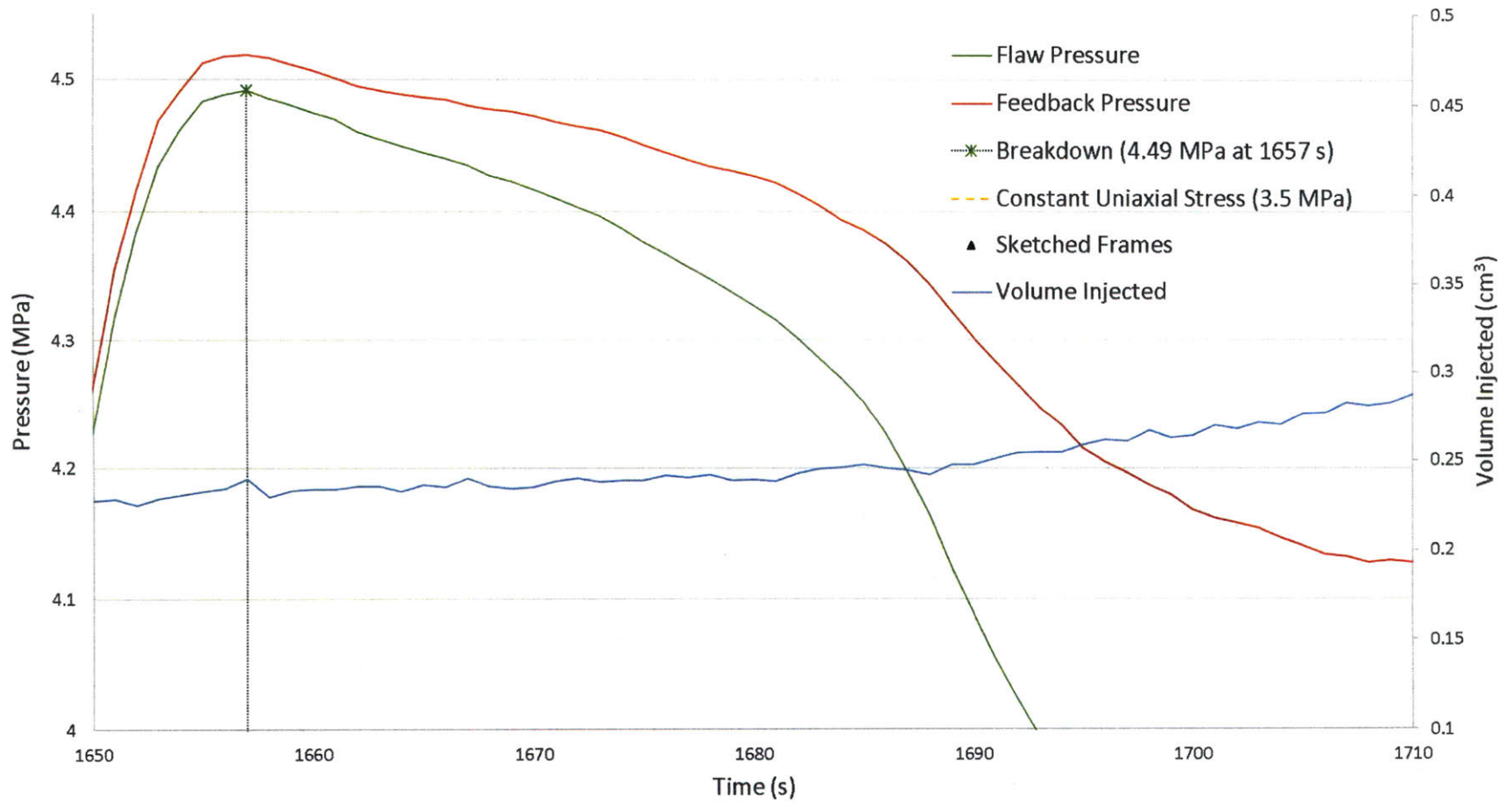


OP-HF-2a-30-30-C Fractures Summary							
Crack Label	Crack Type	Type of Frame	Frame Number	Time from beginning of closing system	Hydraulic Pressure	Normalized Hydraulic Pressure (P _{max} = 4.51 MPa)	Volume Injected
				[s]	[MPa]		[cm ³]
A(T)	Tensile – No Type	High Resolution	1391	1570	4.031	0.897	0.2211
B(T)	Tensile – No Type	High Resolution	1401	1590	4.023	0.896	0.2230
Coalescence Category 1: No Coalescence		High Resolution	-	-	-	-	-

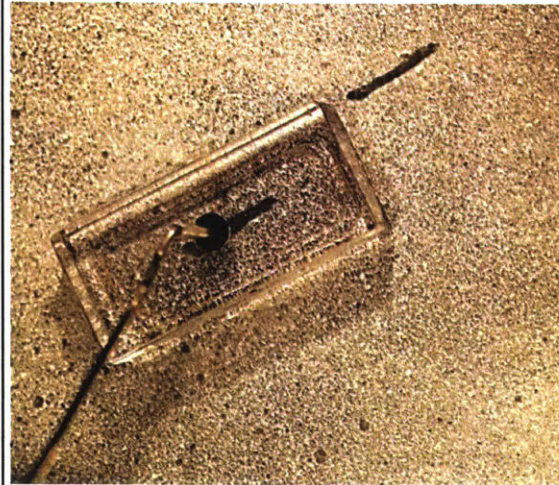
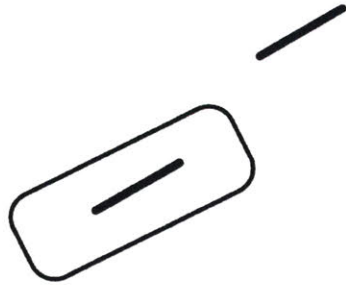
OP-HF-2a-30-30-C Test Data



OP-HF-2a-30-30-C Test Data Close-Up



Sketch 0



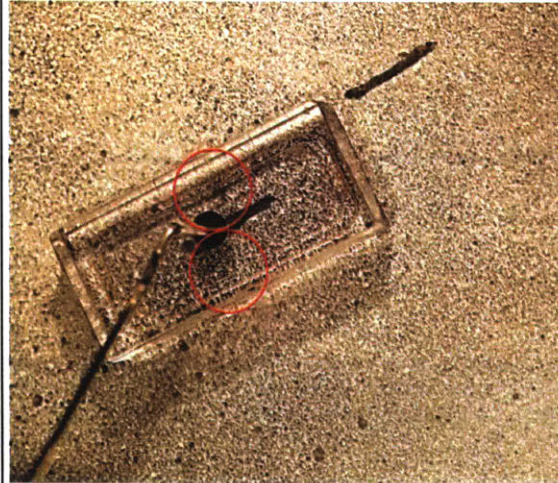
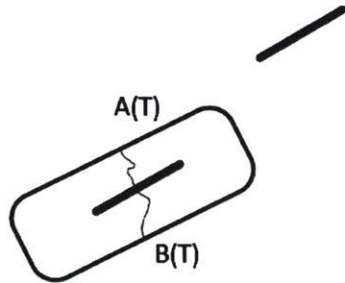
Frame: HR 770 – Initial
Time: 0 seconds
 σ : 3.5 MPa
 P_{Target} : 0.5 MPa
P: 0.356 MPa
V: 0 cm³

Initial Configuration

Prismatic Specimen: 4"x2"x1"
Flaw: 2a = 3/8"
Ligament Spacing (L): 2a
Flaw Angle (β): 30°
Bridging Angle (α): 30°
Bedding Orientation (ψ): 0°

Pressure Increments: 0.5 MPa
Pressure Hold Time: ~1 min

Sketch 1



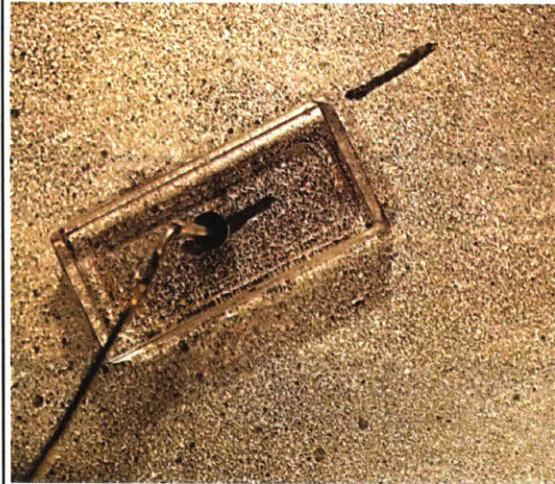
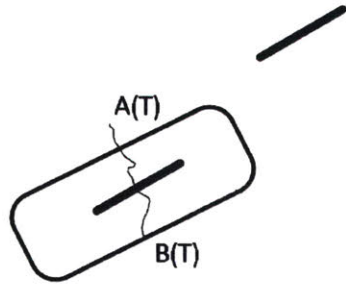
Frame: HR 771
Time: 2 seconds
 σ : 3.5 MPa
 P_{Target} : 0.5 MPa
P: 0.361 MPa
V: 0.0020 cm³

Crack Initiation prior to Pressurization

It is likely that this shale specimen had a pre-existing natural fracture intersecting the middle of the left flaw. This natural fracture was filled with oil during the saturation phase. The fracture on top of the flaw is labeled A(T) because it is the first to propagate past the flaw seal boundary later on. B(T) propagated past the flaw seal boundary afterwards.

Note: Cracks are labeled alphabetically in chronological order of crack initiation. If the order cannot be determined, then they are labeled chronologically by initiation past flaw seal.

Sketch 2

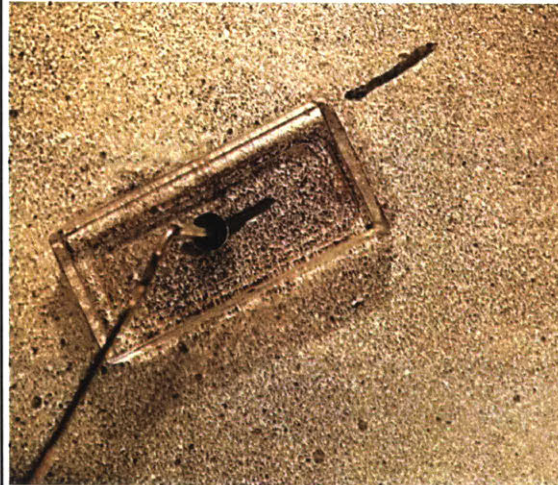
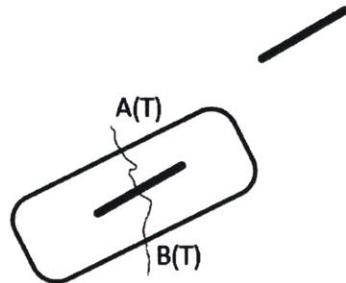


Frame: HR 1391
Time: 1570 seconds
 σ : 3.5 MPa
 P_{Target} : 4.0 MPa
 P : 4.031 MPa
 V : 0.2211 cm³

Crack Initiation & Propagation

Tensile crack A(T) was the first crack to propagate past the flaw seal boundary. Pressure remained stable during the initial propagation of A(T).

Sketch 3



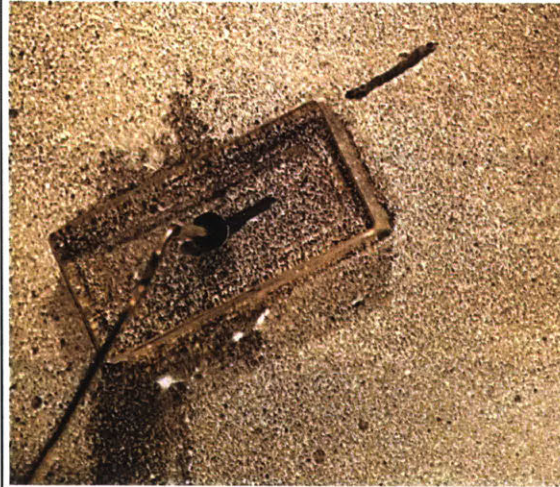
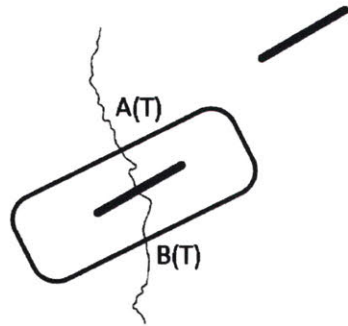
Frame: HR 1401
Time: 1590 seconds
 σ : 3.5 MPa
 P_{Target} : 4.0 MPa
 P : 4.023 MPa
 V : 0.2230 cm³

Crack Initiation & Propagation

Shortly after A(T) propagated past the flaw seal boundary, B(T) propagated downwards past the flaw seal boundary as well.

Both A(T) and B(T) propagated past the flaw seal boundary, but the crack tips of each did not advance while holding the target pressure of 4 MPa.

Sketch 4

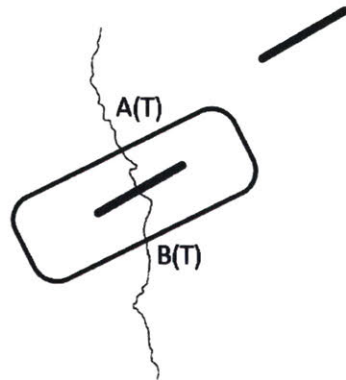


Frame: HR 1462
Time: 1712 seconds
 σ : 3.5 MPa
 P_{Target} : 4.5 MPa
P: 3.797 MPa
V: 0.2915 cm³

Crack Propagation

After pressurizing to 4.5 MPa, the pressure immediately dropped. Both cracks A(T) and B(T) continued propagating up and down, respectively.

Sketch 5



Frame: HR 1468
Time: 1724 seconds
 σ : 3.5 MPa
 P_{Target} : 4.5 MPa
 P : 3.742 MPa
 V : 0.3169 cm³

Crack Propagation

B(T) continued propagating slowly in tension.

After this point, pressure continued to drop and both cracks arrested.

This geometry and loading condition lead to a Category 1: No Coalescence.

OP-HF-2a-30-30-D

11-18-2016

Uniaxial Compression With Hydraulic Fracture of Opalinus Shale

Experimental Procedure Notes:

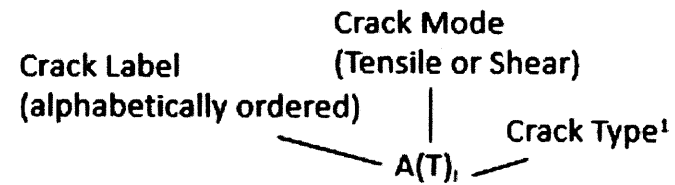
- Flaw saturation phase fills flaw with oil that flows out of bleed hole to expel air from the system. This results in initial pressure build up in flaw shown at time = 0 seconds.
- After flaw saturation, system is closed by attaching pressure transducer to bleed hole.
- Pressurization of flaw is achieved using a PID pressure-control algorithm, where user-defined target pressures (P_{Target}) are defined and PVA injects oil to achieve P_{Target} .
- While holding a constant uniaxial compressive stress, flaw is pressurized in 0.5 MPa increments until specimen failure. Pressure step is held for 1-2 minutes before moving up to the next increment.

OP-HF-2a-30-30 D Dimensions			
Height (h)	Width (w)	Thickness (t)	Area (A=wxt)
[in]	[in]	[in]	[in ²]
3.962	1.843	0.928	1.710

OP-HF-2a-30-30-D Test Summary			
Vertical Load Applied	Vertical Stress Applied	Maximum Hydraulic Pressure	Volume Injected until Loss of Pressure
[kN]	[MPa]	[MPa]	[cm ³]
3.86	3.5	4.03	0.2227

OP-HF-2a-30-30-D Sketch Summary						
Sketch Number	Type of Frame	Frame Number	Time from beginning of closing system	Hydraulic Pressure	Normalized Hydraulic Pressure	Volume Injected
			[s]	[MPa]	(P _{max} =4.03 MPa)	[cm ³]
0	High Resolution	4744	0	0.2564	0.0636	0.0000
1	High Speed	-2631	889.369	3.2615	0.8095	0.2329
2	High Speed	-1187	890.81	3.0277	0.7515	0.2378
3	High Speed	814	892.81	2.8232	0.7007	0.2414
4	High Resolution	5189	896.81	2.6734	0.6635	0.2540
5	High Resolution	5194	906.81	2.5223	0.6260	0.3039
6	High Resolution	5201	920.81	2.3887	0.5929	0.3751

Fracture Analysis Legend



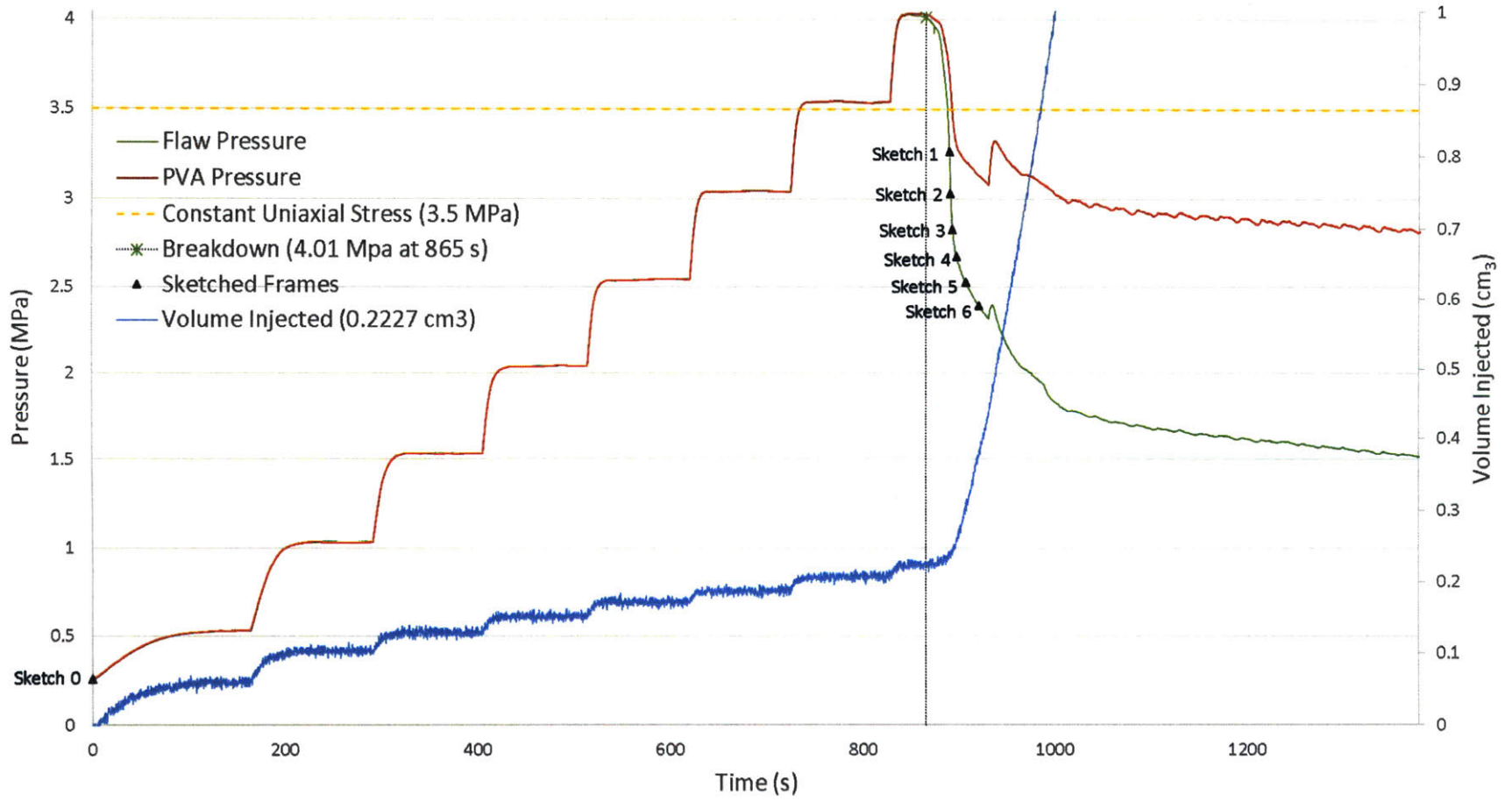
Notes:

- Flow through bedding planes is denoted by a subscript “_b”.
- High-Speed video was not captured for this test.
- Table shows estimated crack initiation.
- Coalescence Category 1: no coalescence

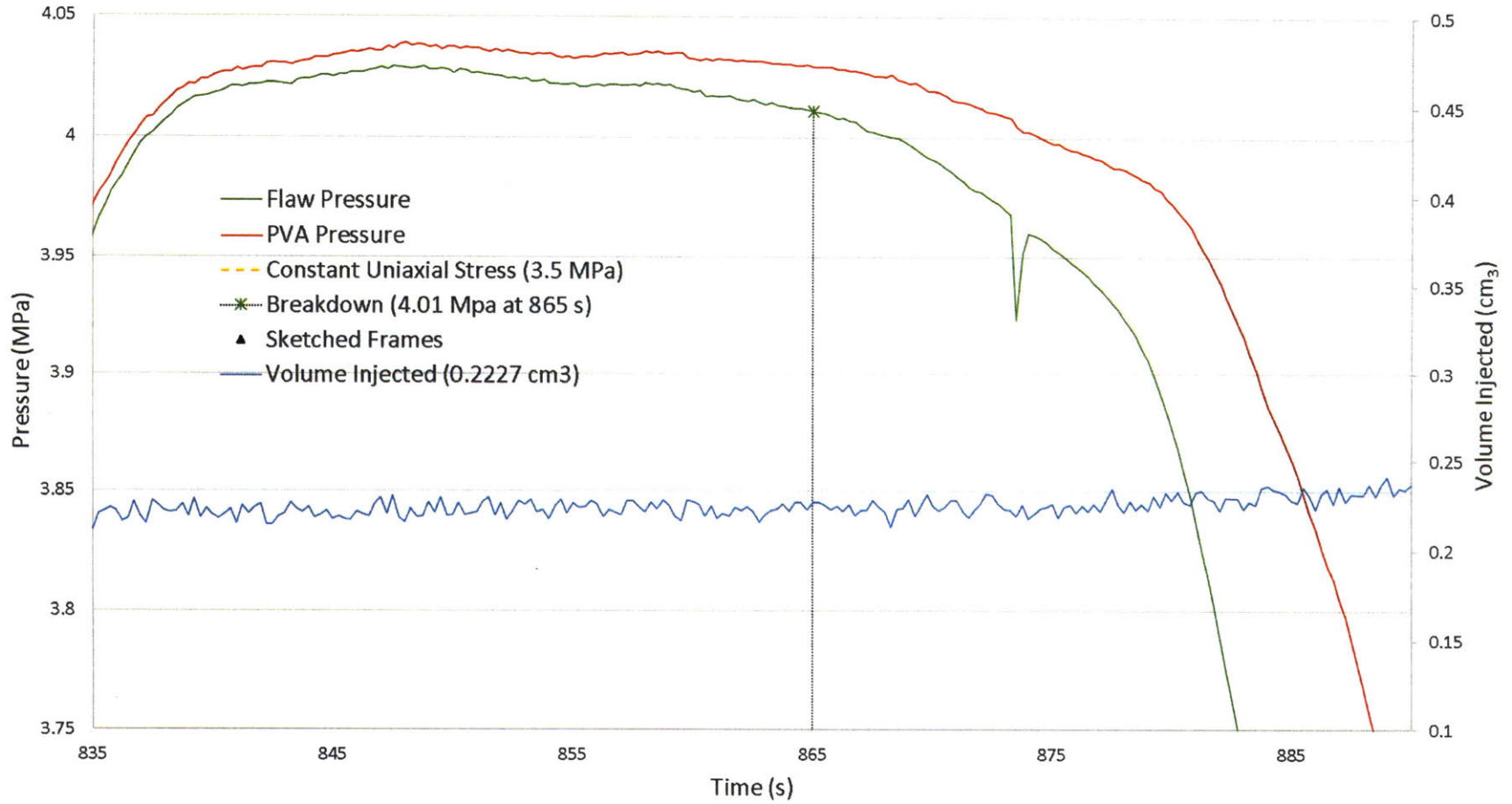
- Pre-existing (cut) Flaw
- Crack
- ↔ Crack Opening
- ↗ Shearing Direction
- Point of Coalescence

OP-2a-30-30-D Fractures Summary				
Crack ID	Crack Type	Hydraulic Pressure at Crack Initiation	Hydraulic Pressure Normalized to the Maximum Hydraulic Pressure	Sketch
		[MPa]		
A(T)	no type	3.0277	0.7515	2
B(T)	no type	2.8232	0.7007	3

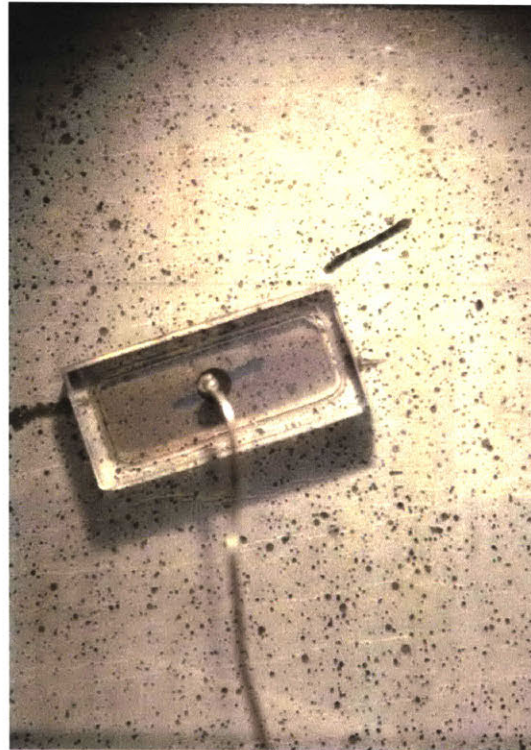
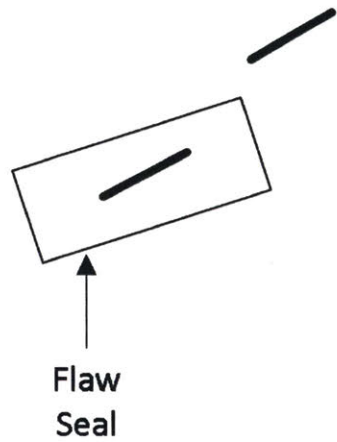
OP-HF-2a-30-30-D Test Data



OP-HF-2a-30-30-D Test Data Close-Up



Sketch 0



Frame: HR 4744 – Initial
Time: 0 seconds
 σ : 3.5 MPa
 P_{Target} : 0.5 MPa
P: 0.271 MPa
V: 0 cm³

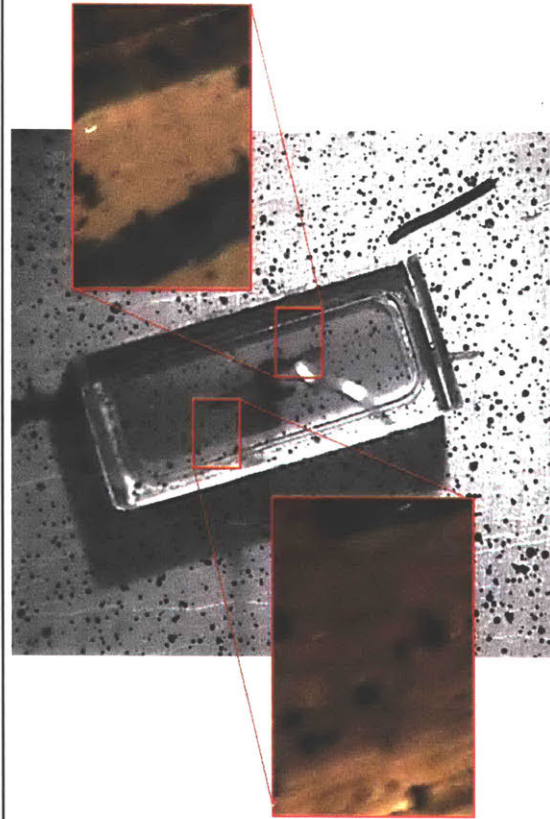
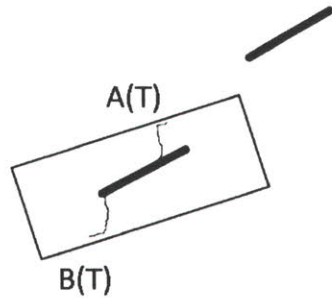
Initial Configuration

Prismatic Specimen: 4"x2"x1"
Flaw: 2a = 3/8"
Ligament Spacing (L): 2a
Flaw Angle (β): 30°
Bridging Angle (α): 30°
Bedding Orientation (ψ): 0°

Pressure Increments: 0.5 MPa
Pressure Hold Time: ~1 min

All cracks are labeled based on their initiation order.

Sketch 1



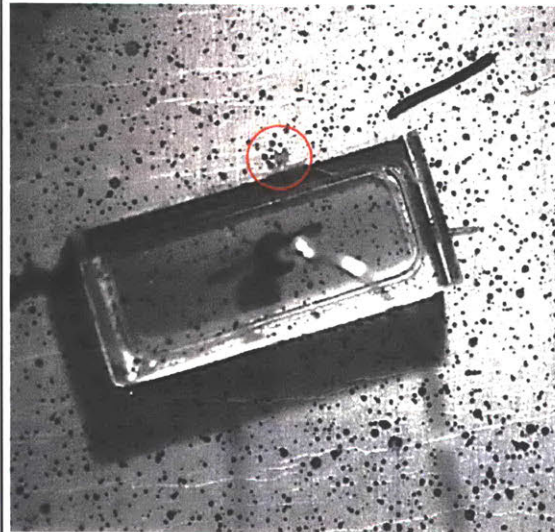
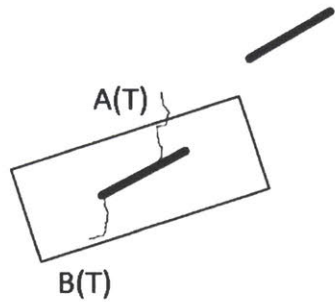
Frame: HS -2631
Time: 889.37 seconds
 σ : 3.5 MPa
 P_{Target} : 4.0 MPa
P: 3.262 MPa
V: 0.2329 cm³

Crack Initiation within Seal

Both tensile cracks A(T) and B(T) appeared during the same frame and were not visible before. A(T) was labelled first because it is the first crack to propagate past the flaw seal boundary. The close-up images were adjusted to show the visible cracks A(T) and B(T) more clearly. Pressure dropped 0.738 MPa from the target pressure with no crack propagation past the flaw seal boundary.

Note: Cracks are labeled alphabetically in chronological order of crack initiation. If the order cannot be determined, then they are labeled chronologically by initiation past flaw seal.

Sketch 2

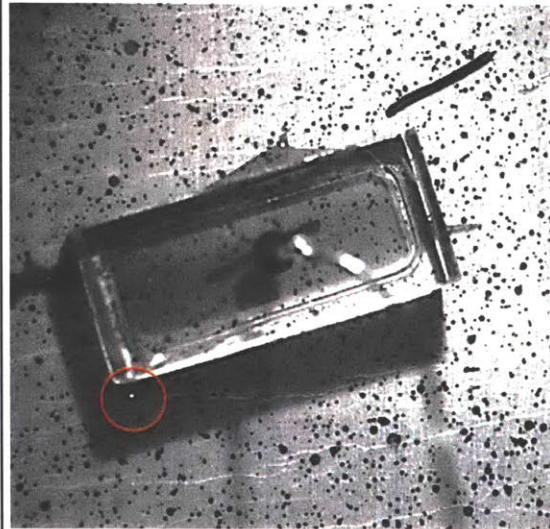
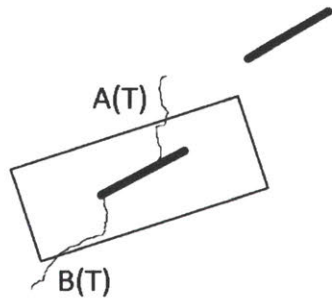


Frame: HS -1187
Time: 890.81 seconds
 σ : 3.5 MPa
 P_{Target} : 4.0 MPa
P: 3.028 MPa
V: 0.2378 cm³

Crack Initiation – Seal Break

Tensile crack A(T) propagated past the flaw seal boundary. This first crack propagation past the flaw seal boundary occurred after pressure dropped 0.972 MPa from target pressure. Note that breakdown pressure did not correspond to immediate cracking events and that pressure had to drop significantly prior to any visible crack initiation or propagation.

Sketch 3

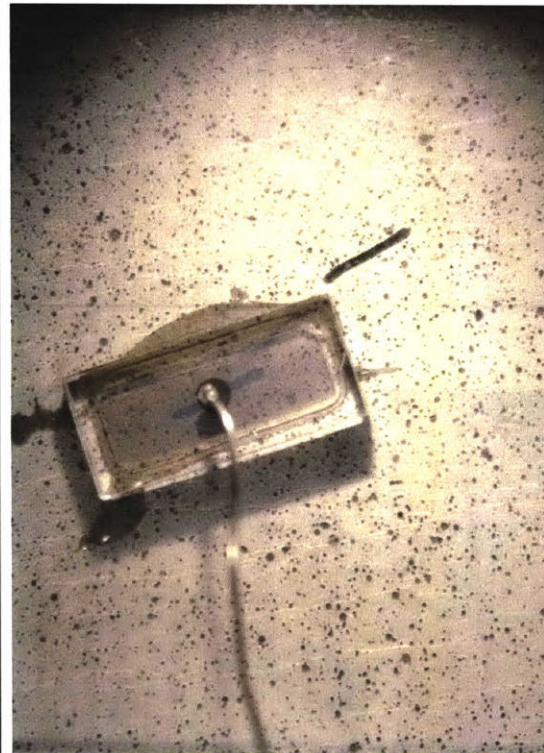
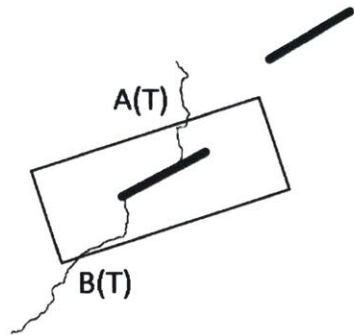


Frame: HS 814
Time: 892.81 seconds
 σ : 3.5 MPa
 P_{Target} : 4.0 MPa
P: 2.823 MPa
V: 0.2414 cm³

Crack Initiation – Seal Break

Tensile crack B(T) propagates past the flaw seal boundary. Tensile crack A(T) continued propagating.

Sketch 4



Frame: HR 5189
Time: 896.81 seconds
 σ : 3.5 MPa
 P_{Target} : 4.0 MPa
P: 2.673 MPa
V: 0.2540 cm³

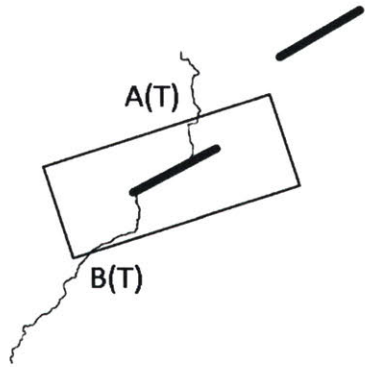
Crack Propagation

Tensile cracks A(T) and B(T) continue propagation.

Throughout propagation, a lag was observed between the advancement of the crack and hydraulic fluid leaking out of the propagating crack behind the crack tip.

Also, the way the cracks propagated was a repetition of the pressurized crack propagating in tension across bedding planes, then through a bedding plane, then across bedding planes again.

Sketch 5



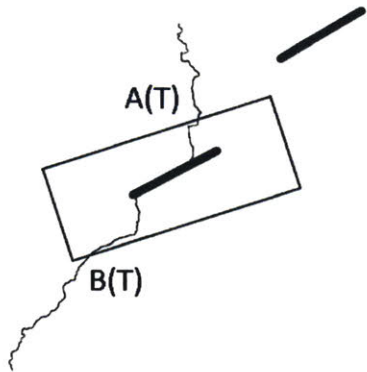
Frame: HR 5194
Time: 906.81 seconds
 σ : 3.5 MPa
 P_{Target} : 4.0 MPa
P: 2.522 MPa
V: 0.3039 cm³

Crack Propagation

In the time between Sketch 4 and Sketch 5, tensile cracks A(T) and B(T) had continued propagation.

However, tensile crack B(T) stopped propagating from this sketch onwards. Tensile crack B(T) propagated for 14 seconds since propagating past the flaw seal boundary.

Sketch 6



Frame: HR 5201
Time: 920.81 seconds
 σ : 3.5 MPa
 P_{Target} : 4.0 MPa
 P : 2.389 MPa
 V : 0.3751 cm³

End of Crack Propagation

In the time between Sketch 5 and Sketch 6, tensile crack A(T) slightly propagated and then stopped. Crack A(T) propagated for 30 seconds since propagating past the flaw seal boundary. After this point in the test, propagation of the current cracks ceased, and no new cracks initiated.

This geometry and loading condition resulted in no coalescence.

OP-HF-2a-30-60-A

11-17-2016

Uniaxial Compression With Hydraulic Fracture of Opalinus Shale

Experimental Procedure Notes:

- Flaw saturation phase fills flaw with oil that flows out of bleed hole to expel air from the system. This results in initial pressure build up in flaw shown at time = 0 seconds.
- After flaw saturation, system is closed by attaching pressure transducer to bleed hole.
- Pressurization of flaw is achieved using a PID pressure-control algorithm, where user-defined target pressures (P_{Target}) are defined and PVA injects oil to achieve P_{Target} .
- While holding a constant uniaxial compressive stress, flaw is pressurized in 0.5 MPa increments until specimen failure. Pressure step is held for 1-2 minutes before moving up to the next increment.

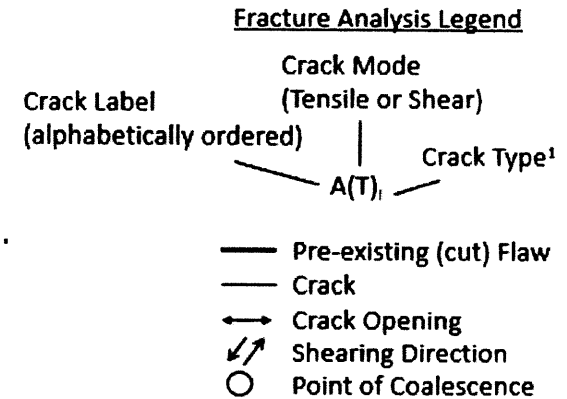
OP-HF-2a-30-60-A Dimensions			
Height (h)	Width (w)	Thickness (t)	Area (A=w x t)
[in]	[in]	[in]	[in ²]
3.953	1.973	1.022	2.015

OP-HF-2a-30-60-A Test Summary			
Vertical Load Applied	Vertical Stress Applied	Maximum Hydraulic Pressure	Volume Injected until Loss of Pressure
[kN]	[MPa]	[MPa]	[cm ³]
4.55	3.5	4.99	0.3817

OP-HF-2a-30-60-A Sketch Summary						
Sketch Number	Type of Frame	Frame Number	Time from beginning of closing system	Hydraulic Pressure	Normalized Hydraulic Pressure (Pmax = 4.98 MPa)	Volume Injected
			[s]	[MPa]		[cm ³]
0	High Resolution	2391	-	-	-	-
1	High Resolution	2422	212.04	0.5357	0.1074	0.0000
2	High Resolution	2994	1360.04	2.4644	0.4940	2.0639
3	High Speed	-741	1362.04	2.4636	0.4938	2.0833
4	High Resolution	2998	1368.04	2.4480	0.4907	2.1514
5	High Resolution	3004	1380.04	2.4227	0.4856	2.2780
6	High Resolution	3006	1384.04	2.4300	0.4871	2.3304
7	High Resolution	3021	1414.04	2.3764	0.4763	2.6578

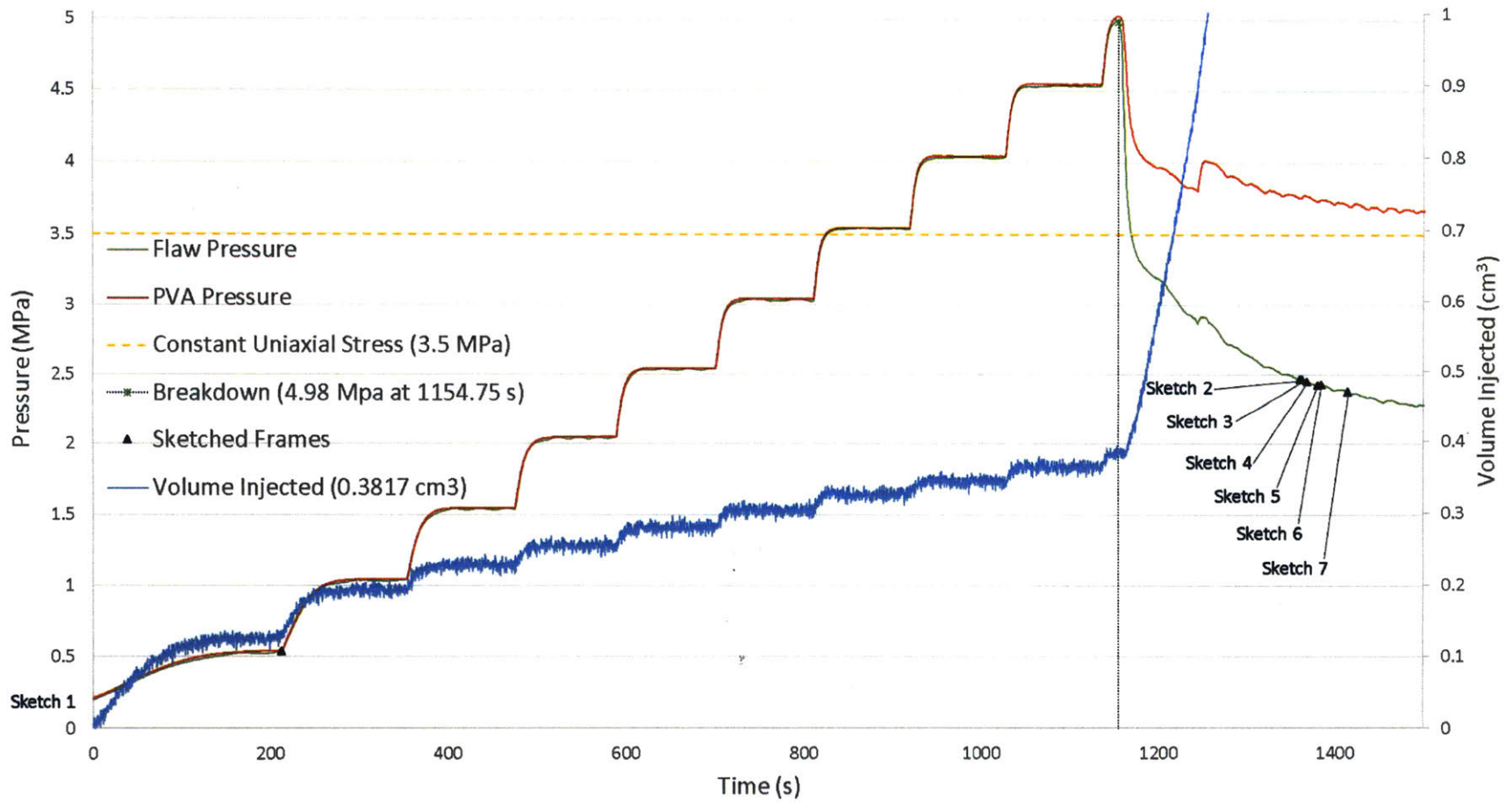
Notes:

- Cracks A-B occurred before pressurization where hydraulic fluid flowed through the bedding planes and pre-existing natural fractures.
- Flow through bedding planes is denoted by a subscript “_b”
- Table shows estimated crack initiation
- Coalescence Category 2: indirect coalescence by multiple cracks

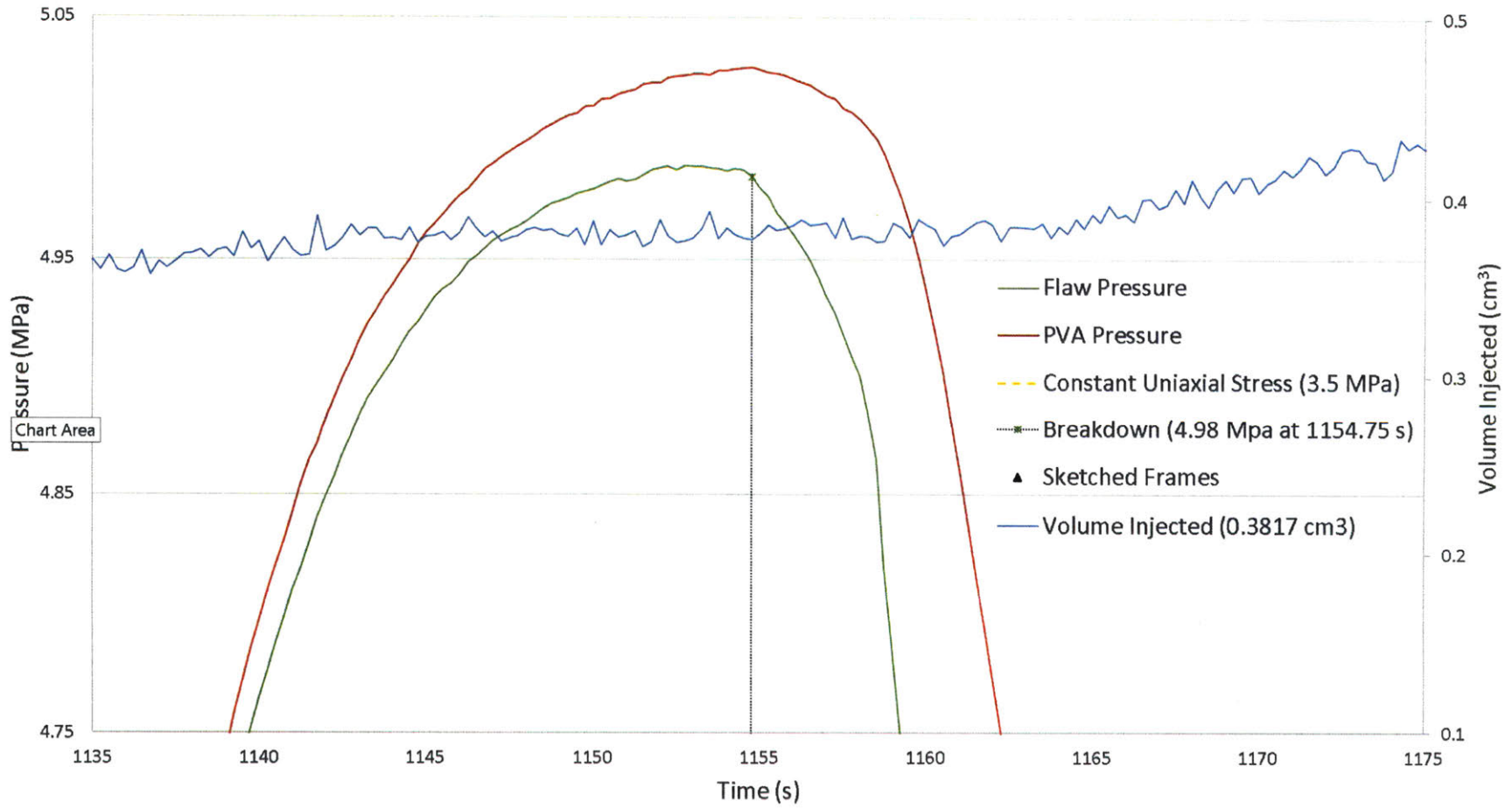


OP-HF-2a-30-60-A Fractures Summary							
Crack Label	Crack Type	Type of Frame	Frame Number	Time from beginning of closing system	Hydraulic Pressure	Normalized Hydraulic Pressure (P _{max} = 4.99 MPa)	Volume Injected
				[s]	[MPa]		[cm ³]
A(T)	Tensile – No Type	High Resolution	2391	-1805.964	-	-	-
B(T) _b	Tensile – Bedding Flow	High Resolution	2391	-1805.964	-	-	-
Test Start	-	-	-	0	0.2029	0.0709	0.0000
C(T) _i	Tensile – Type 1	High Resolution	2994	1360.04	2.4644	-	2.0639
D(T)	Tensile – No Type	High Speed	-741	1362.04	2.4636	-	2.0833
E(T) _b	Tensile – Bedding Flow	High Resolution	3001	1374.04	2.4336	-	2.2292
F(T) _b	Tensile – No Type	High Resolution	3005	1382.04	2.4252	0.0721	2.3085
Coalescence Category 2: Indirect Coalescence		High Resolution	3021	1144.691	2.5319	0.6278	1.1757

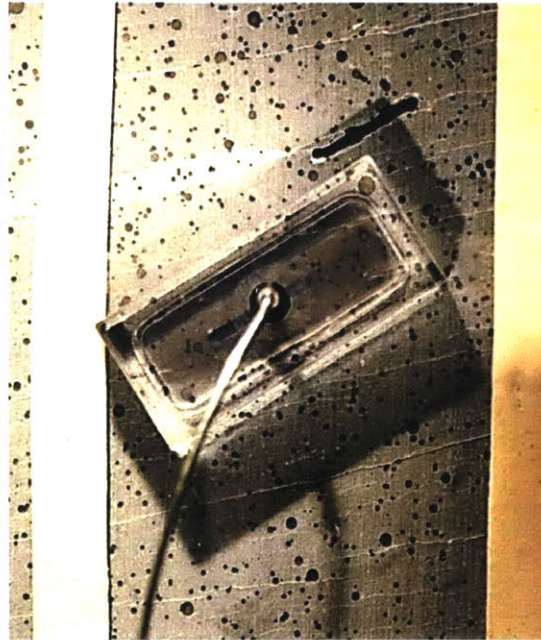
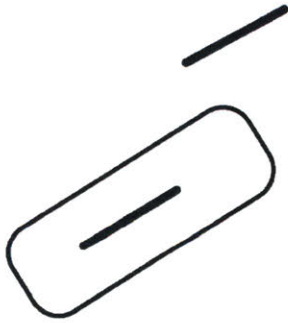
OP-HF-2a-30-60-A Test Data



OP-HF-2a-30-60-A Test Data Close-Up



Sketch 0



Frame: HR 2391 – Initial

Time: 0 seconds

σ : 3.5 MPa

P_{Target} : 0.5 MPa

P: - MPa

V: - cm^3

Initial Configuration

Prismatic Specimen: 4"x2"x1"

Flaw: $2a = 3/8$ "

Ligament Spacing (L): 2a

Flaw Angle (β): 30°

Bridging Angle (α): 60°

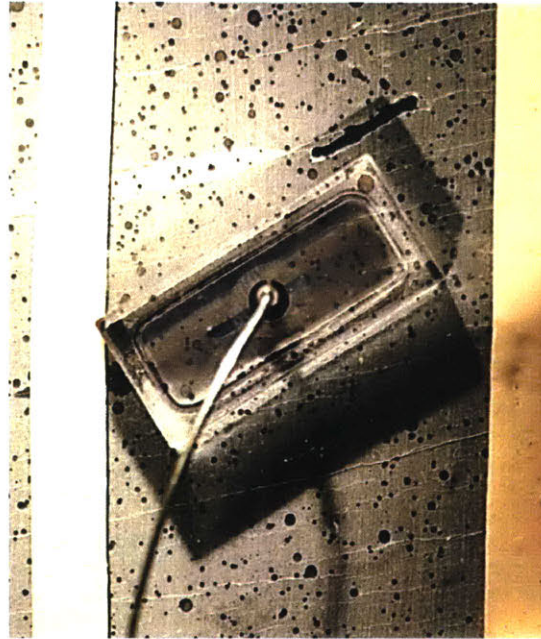
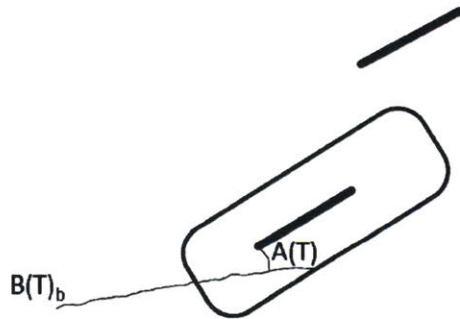
Bedding Orientation (ψ): 0°

Pressure Increments: 0.5 MPa

Pressure Hold Time: ~1 min

Note: Image was taken during saturation phase.

Sketch 1



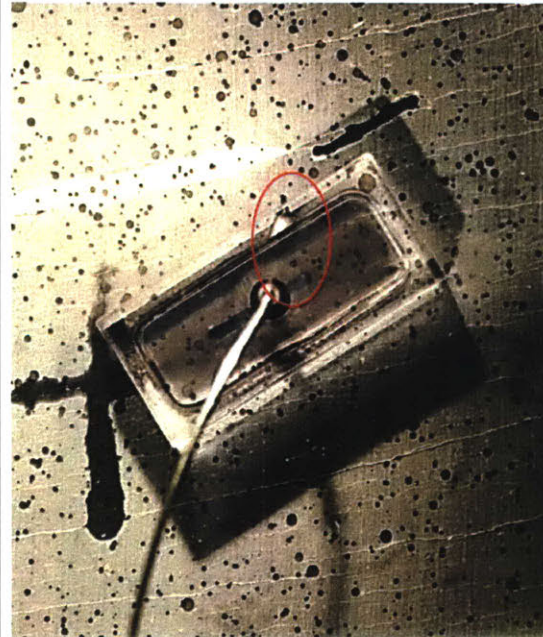
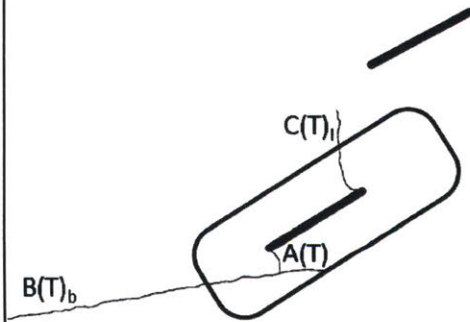
Frame: HR 2422
Time: 0 seconds
 σ : 3.5 MPa
 P_{Target} : 0.5 MPa
 P : 0.203 MPa
 V : 0 cm³

Crack Initiation prior to Pressurization

This shale specimen had a pre-existing natural fracture A(T) coinciding with the outer tip of the left flaw at one end, and a bedding plane B(T)_b at the other. Throughout the flaw saturation phase, oil filled and pressurized the natural fracture and bedding plane. A(T) was filled with oil first. A(T) connected the flaw to bedding plane B(T)_b through which the pressurized oil flowed.

Note: Cracks are labeled alphabetically in chronological order of crack initiation. If the order cannot be determined, then they are labeled chronologically by initiation past flaw seal.

Sketch 2

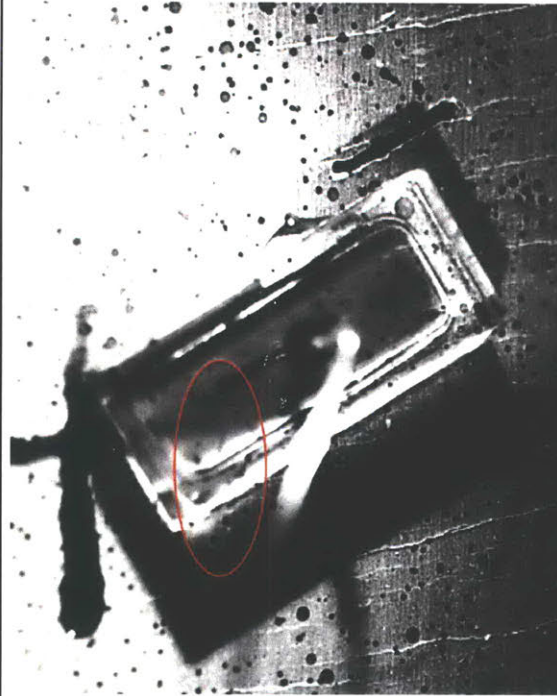
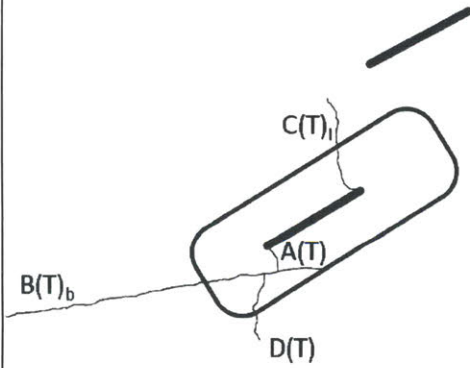


Frame: HR 2994
Time: 1360.04 seconds
 σ : 3.5 MPa
 P_{Target} : 5.0 MPa
 P : 2.464 MPa
 V : 2.0639 cm³

Crack Initiation & Propagation

$C(T)_i$ was the first crack to initiate and propagate. It initiated at the inner tip of the left flaw and propagated as a wing crack. Oil continued flowing through bedding plane $B(T)_b$ until the specimen edge.

Sketch 3

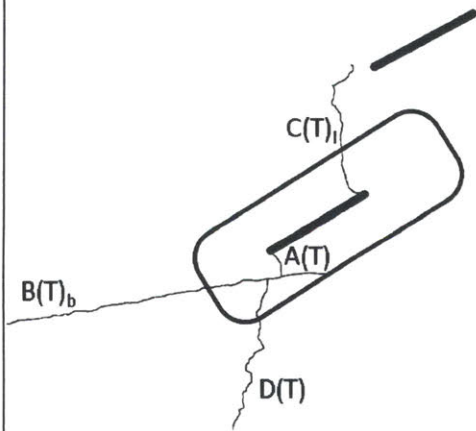


Frame: HS -741
Time: 1362.04 seconds
 σ : 3.5 MPa
 P_{Target} : 5.0 MPa
 P : 2.464 MPa
 V : 2.0833 cm³

Crack Initiation & Propagation

D(T) is a tensile crack that initiated from the pressurized bedding plane B(T)_b within the flaw seal boundary. D(T) propagated in tension instantly past the flaw seal boundary.

Sketch 4

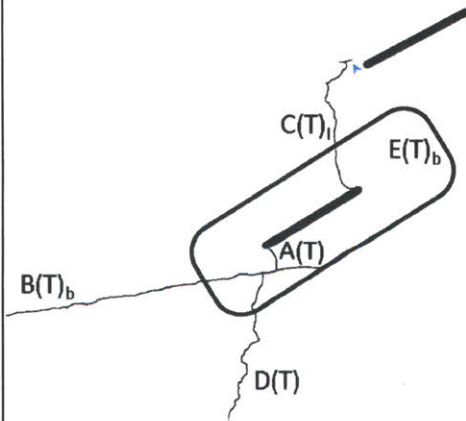


Frame: HR 2998
Time: 1368.04 seconds
 σ : 3.5 MPa
 P_{Target} : 5.0 MPa
 P : 2.448 MPa
 V : 2.1514 cm³

Crack Propagation & Arrest

$C(T)_1$ and $D(T)$ continued propagating.
 $C(T)_1$ arrested at a bedding plane to the left of the right flaw.

Sketch 5

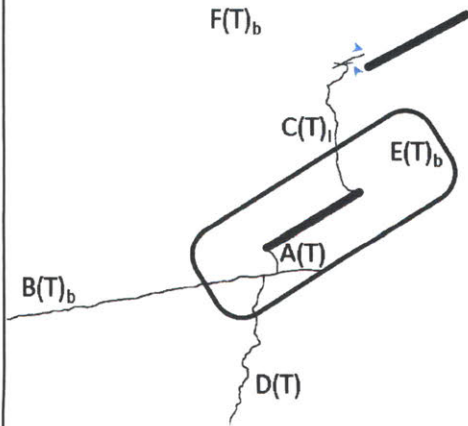


Frame: HR 3004
Time: 1380.04 seconds
 σ : 3.5 MPa
 P_{Target} : 5.0 MPa
 P : 2.423 MPa
 V : 2.2780 cm³

Bedding Plane Pressurization

Bedding Plane $E(T)_b$ starting filling with oil upon the arrest of $C(T)_i$. The oil flowed in both directions across the bedding plane.

Sketch 6



Frame: HR 3006
Time: 1384.04 seconds
 σ : 3.5 MPa
 P_{Target} : 5.0 MPa
 P : 2.430 MPa
 V : 2.3304 cm³

Bedding Plane Flow

$F(T)_b$ is a bedding plane that pinches into $E(T)_b$. After oil flowed into $E(T)_b$, it eventually started flowing into and through $F(T)_b$ as well.

OP-HF-2a-30-60-B 11-17-2016

Hydraulic Fracture of Opalinus Shale

Experimental Procedure Notes:

- Flaw saturation phase fills flaw with oil that flows out of bleed hole to expel air from the system. This results in initial pressure build up in flaw shown at time = 0 seconds.
- After flaw saturation, system is closed by attaching pressure transducer to bleed hole.
- Pressurization of flaw is achieved using a PID pressure-control algorithm, where user-defined target pressures (P_{Target}) are defined and PVA injects oil to achieve P_{Target} .
- While holding a constant uniaxial compressive stress, flaw is pressurized in 0.5 MPa increments until specimen failure. Pressure step is held for 1-2 minutes before moving up to the next increment.

OP-HF-2a-30-60-B Dimensions			
Height (h)	Width (w)	Thickness (t)	Area (A=w x t)
[in]	[in]	[in]	[in ²]
4.158	2.140	0.970	2.076

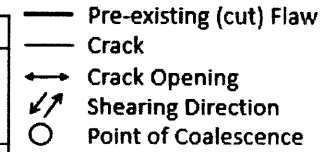
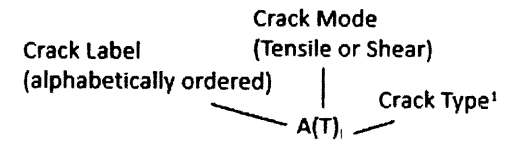
OP-HF-2a-30-60-B Test Summary			
Vertical Load Applied	Vertical Stress Applied	Maximum Hydraulic Pressure	Volume Injected until Loss of Pressure
[kN]	[MPa]	[MPa]	[cm ³]
4.69	3.5	4.03	0.2707

OP-HF-2a-30-60-B Sketch Summary						
Sketch Number	Type of Frame	Frame Number	Time from beginning of closing system	Hydraulic Pressure	Normalized Hydraulic Pressure (Pmax = 4.03 MPa)	Volume Injected
			[s]	[MPa]		[cm ³]
0	High Resolution	3151	-901.309	NA	NA	NA
1	High Resolution	3331	2.691	0.2906	0.0721	0.0007
2	High Resolution	3532	426.691	1.5304	0.3795	0.1683
3	High Resolution	3843	1049.691	2.8752	0.7129	0.5947
4	High Resolution	3844	1051.691	2.8716	0.7120	0.5973
5	High Resolution	3847	1057.691	2.8549	0.7079	0.6375
6	High Resolution	3850	1063.691	2.8450	0.7054	0.6672
7	High Resolution	3852	1067.691	2.8319	0.7022	0.6904
8	High Resolution	3853	1069.691	2.8204	0.6993	0.6955
9	High Speed	-2309	1077.691	2.7949	0.6930	0.7448
10	High Resolution	3869	1101.691	2.7139	0.6729	0.8929
11	High Resolution	3884	1131.691	2.6376	0.6540	1.0943
12	High Resolution	3887	1144.691	2.5319	0.6278	1.1757

Notes:

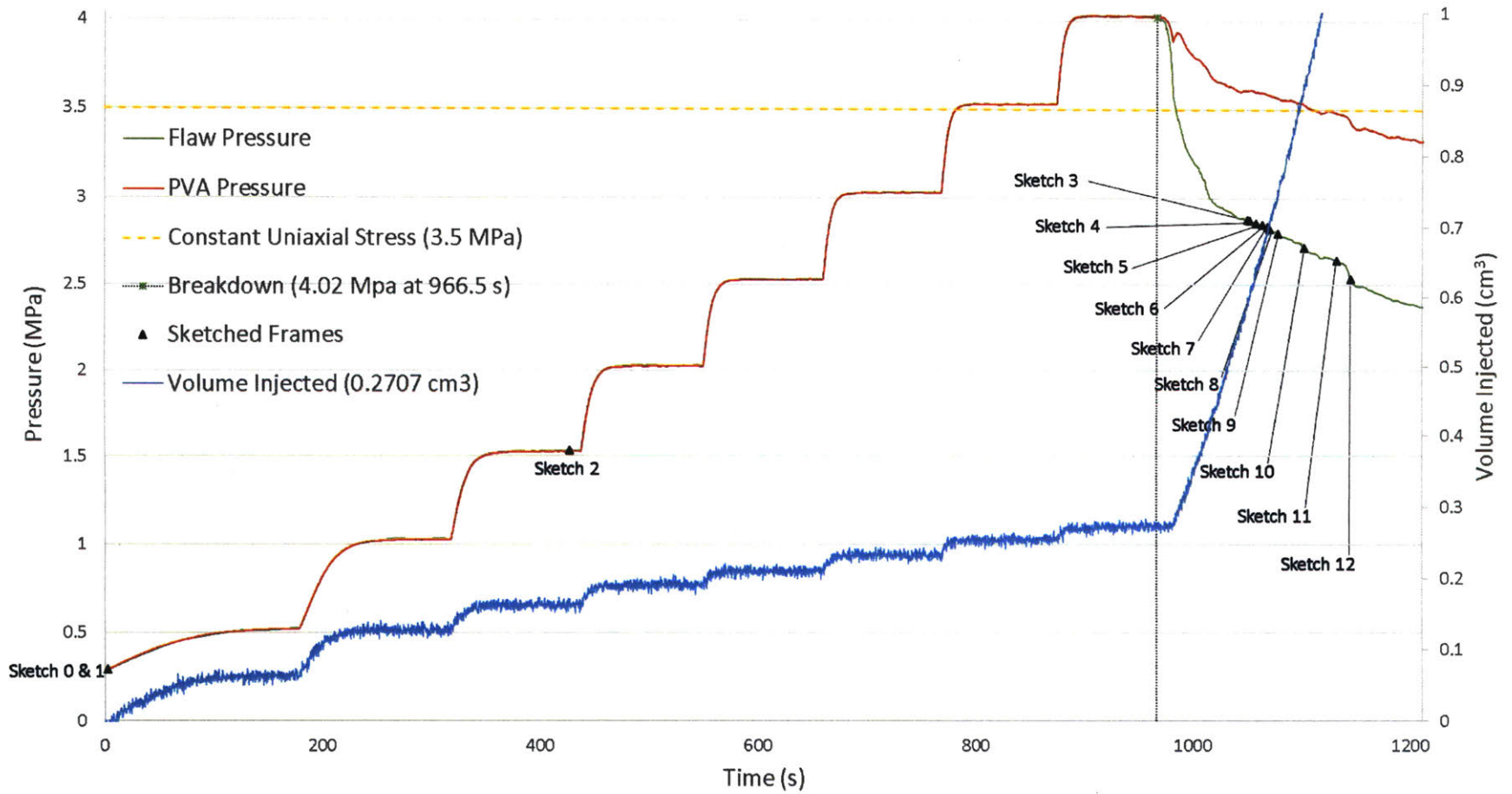
- Cracks A-E occurred before pressurization where hydraulic fluid flowed through the bedding planes and pre-existing natural fractures.
- Flow through bedding planes is denoted by a subscript “_b”
- Coalescence Category 2: indirect coalescence by multiple cracks

Fracture Analysis Legend

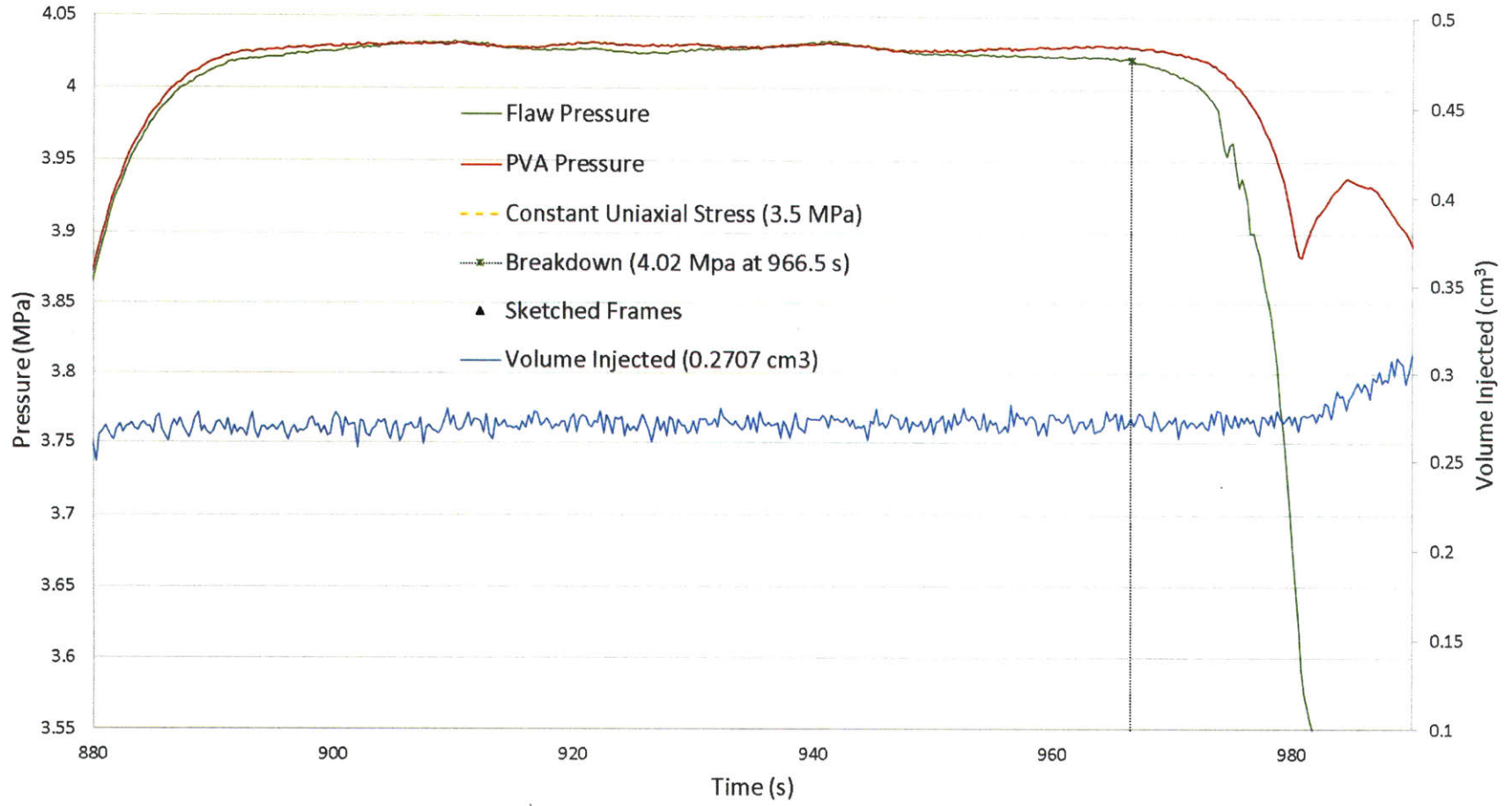


OP-HF-2a-30-60-B Fractures Summary							
Crack Label	Crack Type	Type of Frame	Frame Number	Time from beginning of closing system	Hydraulic Pressure	Normalized Hydraulic Pressure (Pmax = 4.03 MPa)	Volume Injected
				[s]	[MPa]		[cm ³]
A(T)	Tensile – No Type	High Resolution	3151	-901.309	-	-	-
B(T)	Tensile – No Type	High Resolution	3153	-891.309	-	-	-
C(T) _b	Tensile – Bedding Flow	High Resolution	3158	-866.309	-	-	-
D(T) _b	Tensile – Bedding Flow	High Resolution	3160	-856.309	-	-	-
E(T) _b	Tensile – Bedding Flow	High Resolution	3325	-27.309	-	-	-
Test Start	-	-	-	0	0.2860	0.0709	0.0000
F(T)	Tensile – No Type	High Resolution	3331	2.691	0.2906	0.0721	0.0007
G(T)	Tensile – No Type	High Resolution	3532	426.691	1.5304	0.3795	0.1683
H(T)	Tensile – No Type	High Resolution	3800	963.691	4.0226	0.9974	0.2655
I(T) _b	Tensile – Bedding Flow	High Resolution	3844	1051.691	2.8716	0.7120	0.5973
J(T)	Tensile – No Type	High Speed	3845	1053.691	2.8673	0.7109	0.6108
K(T)	Tensile – No Type	High Resolution	3850	1063.691	2.8450	0.7054	0.6672
L(T)	Tensile – No Type	High Resolution	3852	1067.691	2.8319	0.7022	0.6904
M(T) _b	Tensile – Bedding Flow	High Resolution	3853	1069.691	2.8204	0.6993	0.6955
N(T)	Tensile – No Type	High Resolution	3854	1071.691	2.8156	0.6981	0.7188
O(T) _b	Tensile – Bedding Flow	High Speed	-309	1079.691	2.7834	0.6901	0.7620
P(T)	Tensile – No Type	High Resolution	3870	1103.691	2.7027	0.6701	0.9066
Q(T)	Tensile – No Type	High Resolution	3885	1133.691	2.6362	0.6536	1.1036
Coalescence Category 2: Indirect		High Resolution	3887	1144.691	2.5319	0.6278	1.1757

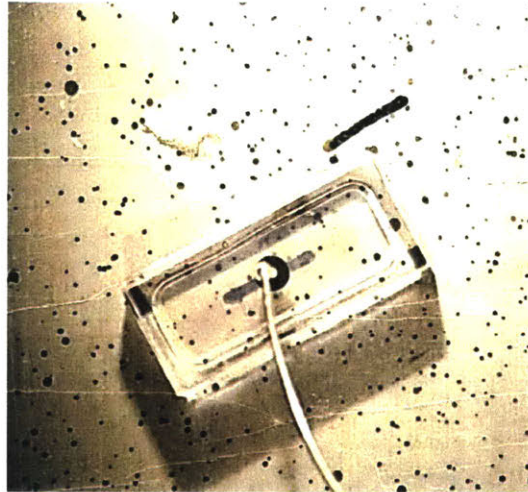
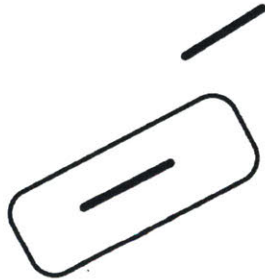
OP-HF-2a-30-60-B Test Data



OP-HF-2a-30-60-B Test Data Close-Up



Sketch 0



Frame: HR 3151 – Initial
Time: 0 seconds
 σ : 3.5 MPa
 P_{Target} : 0.5 MPa
P: 0.286 MPa
V: 0 cm³

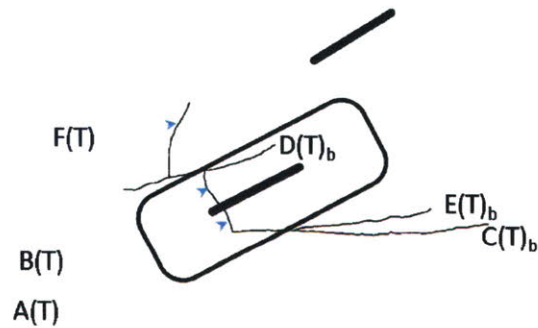
Initial Configuration

Prismatic Specimen: 4"x2"x1"
Flaw: 2a = 3/8"
Ligament Spacing (L): 2a
Flaw Angle (β): 30°
Bridging Angle (α): 60°
Bedding Orientation (ψ): 0°

Pressure Increments: 0.5 MPa
Pressure Hold Time: ~1 min

All cracks are labeled based on their initiation order.

Sketch 1



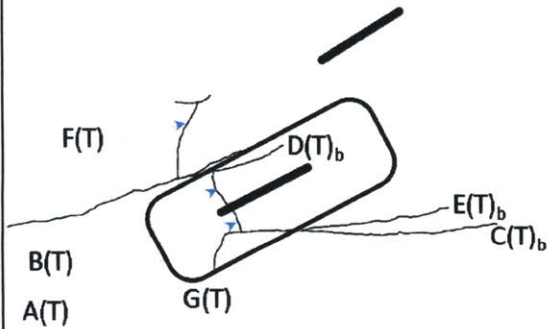
Frame: HR 3331
Time: 2.691 seconds
 σ : 3.5 MPa
 P_{Target} : 0.5 MPa
P: 0.291 MPa
V: 0.0007 cm³

Crack Initiation prior to Pressurization

This shale specimen had many natural fractures and the bedding planes seemed weakly bonded. Throughout the flaw saturation phase, oil filled the natural fractures and bedding planes. A(T) and B(T) were natural fractures that were filled with oil first. A(T) connected the flaw to bedding plane C(T)_b through which the oil flowed. B(T) connected the flaw to bedding plane D(T)_b similarly. Bedding plane E(T)_b pinches into C(T)_b, so when oil reached the end of C(T)_b, it started flowing through E(T)_b. Finally, F(T) is a natural fracture through which oil flowed via D(T)_b. The photograph shows the state of the specimen at the start of pressurization.

Note: Cracks are labeled alphabetically in chronological order of crack initiation. If the order cannot be determined, then they are labeled chronologically by initiation past flow seal.

Sketch 2

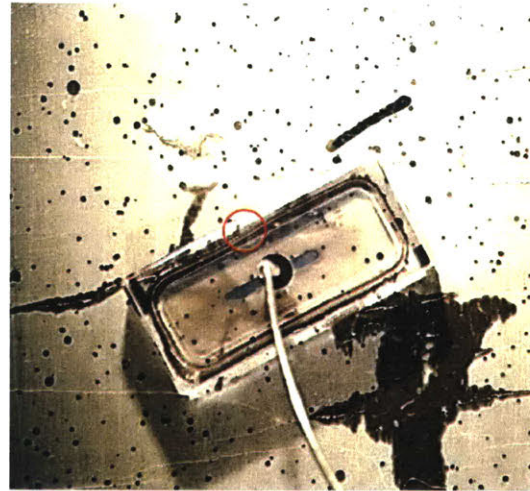
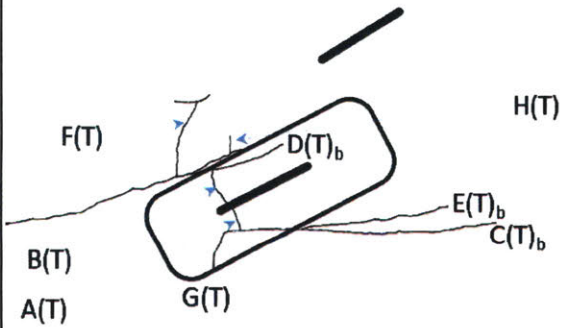


Frame: HR 3532
Time: 426.691 seconds
 σ : 3.5 MPa
 P_{Target} : 1.5 MPa
P: 1.530 MPa
V: 0.1683 cm³

Crack Propagation within Seal

G(T) is a natural fracture that filled with oil during the pressurization process. Oil continued flowing through D(T)b. Note that there is a spherical intrusion/fossil above the outer tip of the right flaw. F(T) is a natural fracture connecting D(T)b to this intrusion, and oil starts to flow through F(T) into the matrix/fossil boundary.

Sketch 3

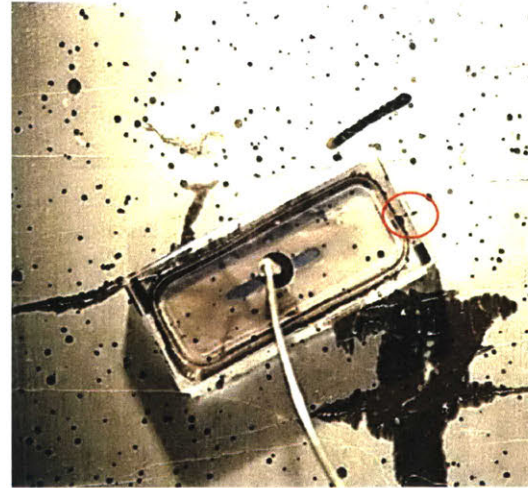
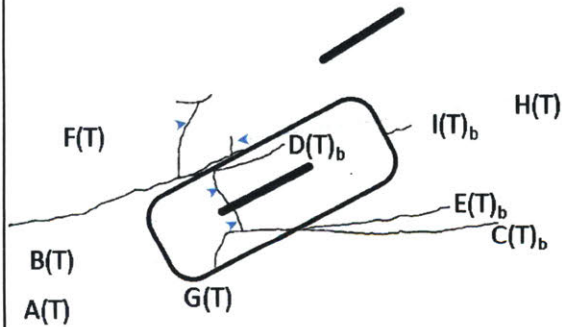


Frame: HR 3843
Time: 1049.691 seconds
 σ : 3.5 MPa
 P_{Target} : 4.0 MPa
 P : 2.875 MPa
 V : 0.5947 cm³

Crack Initiation post-Breakdown

H(T) is the first crack to initiate outside the seal boundary. H(T) initiated from the pressurized bedding plane D(T)_b. Note that there was significant pressure drop before observable crack initiation.

Sketch 4

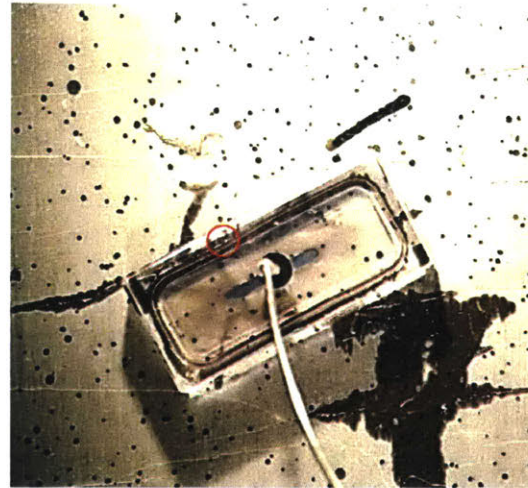
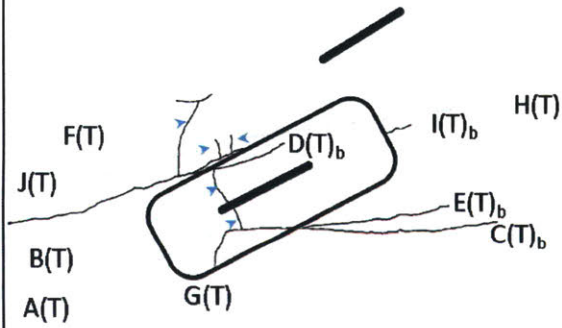


Frame: HR 3844
Time: 1051.691 seconds
 σ : 3.5 MPa
 P_{Target} : 4.0 MPa
 P : 2.872 MPa
 V : 0.5973 cm³

Crack Propagation

$I(T)_b$ appeared to initiate outside the flaw sea boundary. However, $I(T)_b$ is an extension of bedding plane $D(T)_b$. Although the bedding plane does not seem filled within the flaw seal, it is likely that oil was flowing through the bedding plane $D(T)_b$ and beyond the flaw seal boundary through a path not visible on the surface.

Sketch 5

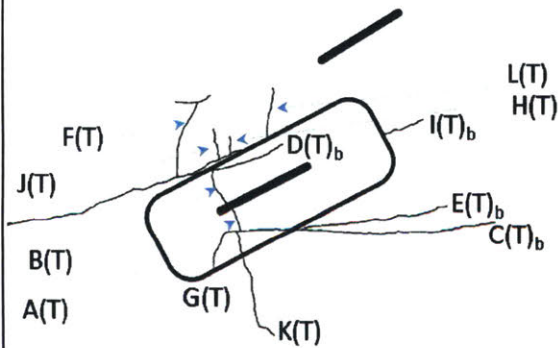


Frame: HR 3847
Time: 1057.691 seconds
 σ : 3.5 MPa
 P_{Target} : 4.0 MPa
P: 2.855 MPa
V: 0.6375 cm³

Crack Initiation

J(T) initiated in the same way that H(T) did, from the pressurized bedding plane D(T)_b.

Sketch 7

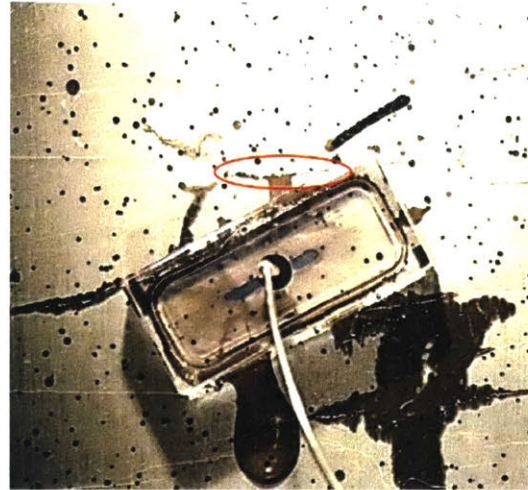
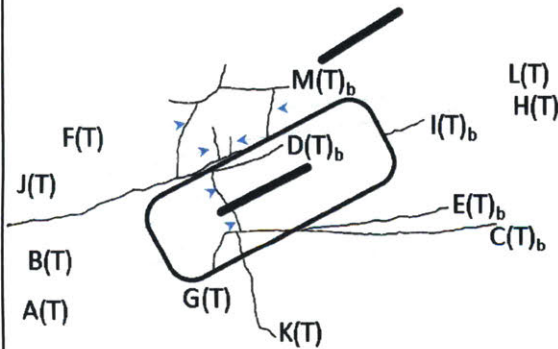


Frame: HR 3852
Time: 1067.691 seconds
 σ : 3.5 MPa
 P_{Target} : 4.0 MPa
P: 2.832 MPa
V: 0.6904 cm³

Crack Initiation & Propagation

L(T) initiated at the flaw seal boundary, but may have initiated at pressurized bedding plane D(T)_b from within the specimen thickness rather than the observable specimen surface. L(T) propagated up and arrested at a bedding plane. K(T) continued propagation.

Sketch 8

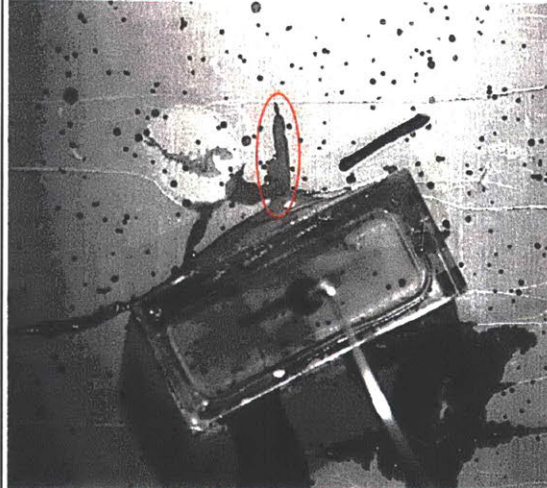
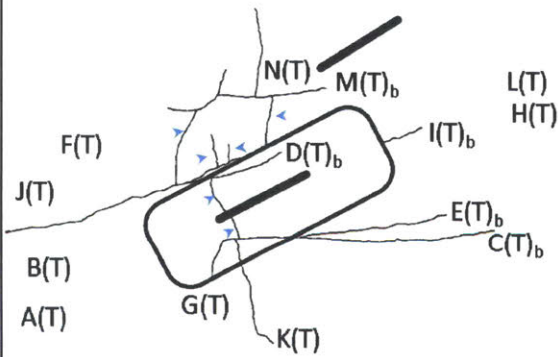


Frame: HR 3853
Time: 1069.691 seconds
 σ : 3.5 MPa
 P_{Target} : 4.0 MPa
P: 2.820 MPa
V: 0.6955 cm³

Crack Propagation

Upon the arrest of L(T), the pressurized oil began filling bedding plane M(T)_b. The oil flowed through the bedding plane, right and left. The oil flowing through the left leg of M(T)_b reached the fossil and started flowing between the matrix/fossil boundary, connecting to the pressurized natural fracture F(T).

Sketch 9

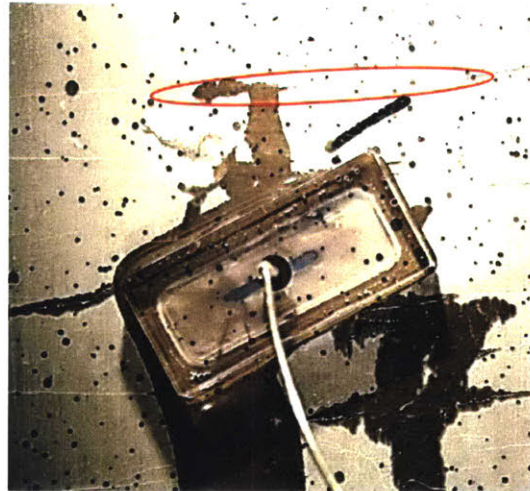
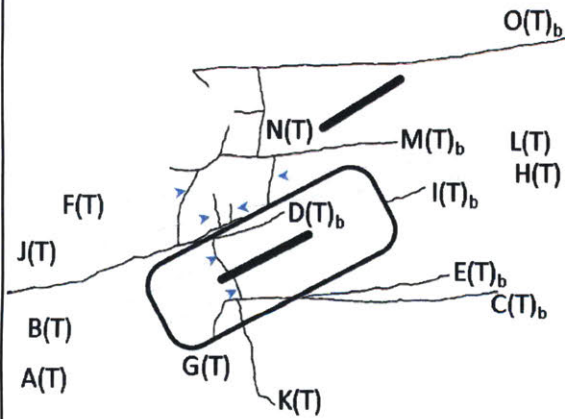


Frame: HS -2309
Time: 1077.691 seconds
 σ : 3.5 MPa
 P_{Target} : 4.0 MPa
P: 2.795 MPa
V: 0.7448 cm³

Crack Initiation & Propagation

N(T) initiated from the right leg of bedding plane M(T)b, between the arrest point of L(T) and the fossil boundary. N(T) propagated up and arrested at a bedding plane, similar to the initiation and propagation of L(T).

Sketch 10

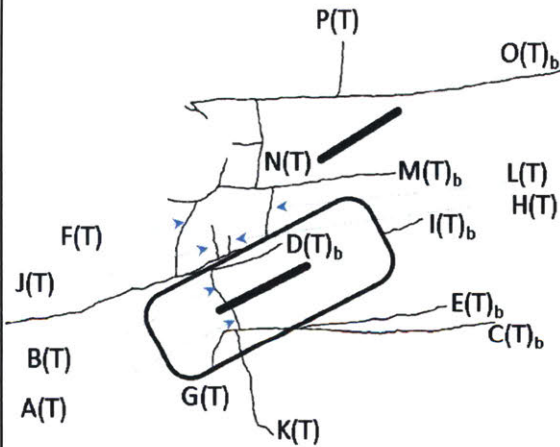


Frame: HR 3869
Time: 1101.691 seconds
 σ : 3.5 MPa
 P_{Target} : 4.0 MPa
P: 2.714 MPa
V: 0.0.8929 cm³

Crack Propagation

Similar to L(T) arresting at M(T)_b, oil started flowing into and filling bedding plane O(T)_b at the arrest point of N(T). The oil also started flowing through a bedding plane connecting N(T) to the fossil boundary.

Sketch 11

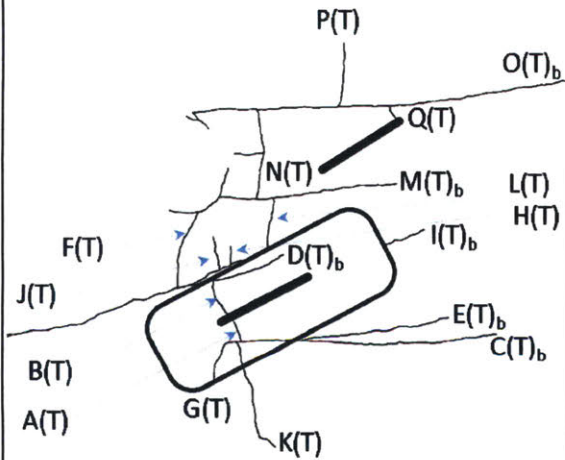


Frame: HR 3884
Time: 1131.691 seconds
 σ : 3.5 MPa
 P_{Target} : 4.0 MPa
P: 2.638 MPa
V: 1.0943 cm³

Crack Initiation & Propagation

P(T) initiated at the pressurized bedding plane O(T)_b above the middle of the right flaw. P(T) propagated upwards and arrested at a bedding plane. P(T) initiated and propagated similar to L(T) and N(T).

Sketch 12



Frame: HR 3887
Time: 1144.691 seconds
 σ : 3.5 MPa
 P_{Target} : 4.0 MPa
P: 2.532 MPa
V: 1.1757 cm³

Coalescence

Q(T) initiated from the pressurized bedding plane O(T)_b close the outer tip of the right flaw. Q(T) propagated towards the flaw tip until coalescence.

This geometry and loading condition lead to a Category 2: Indirect Coalescence by multiple cracks.

OP-HF-2a-30-60-C

11-18-2016

Uniaxial Compression With Hydraulic Fracture of Opalinus Shale

Experimental Procedure Notes:

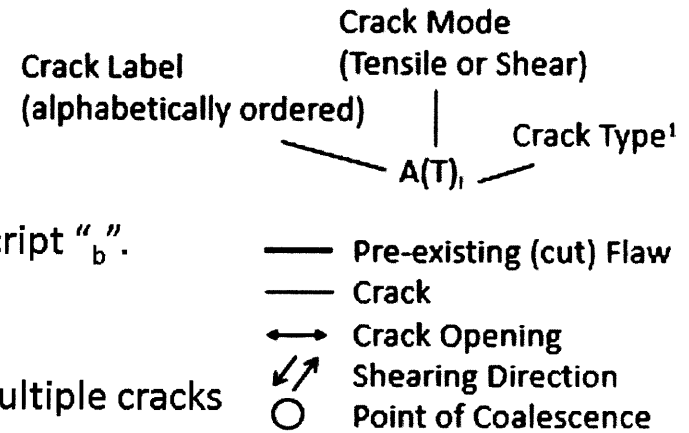
- Flaw saturation phase fills flaw with oil that flows out of bleed hole to expel air from the system. This results in initial pressure build up in flaw shown at time = 0 seconds.
- After flaw saturation, system is closed by attaching pressure transducer to bleed hole.
- Pressurization of flaw is achieved using a PID pressure-control algorithm, where user-defined target pressures (P_{Target}) are defined and PVA injects oil to achieve P_{Target} .
- While holding a constant uniaxial compressive stress, flaw is pressurized in 0.5 MPa increments until specimen failure. Pressure step is held for 1-2 minutes before moving up to the next increment.

OP-HF-2a-30-60 C Dimensions			
Height (h)	Width (w)	Thickness (t)	Area (A=w x t)
[in]	[in]	[in]	[in ²]
4.073	2.185	1.026	2.24

OP-HF-2a-30-60-C Test Summary			
Vertical Load Applied	Vertical Stress Applied	Maximum Hydraulic Pressure	Volume Injected until Loss of Pressure
[kN]	[MPa]	[MPa]	[cm ³]
5.06	3.5	3.53	0.2388

OP-HF-2a-30-60-C Sketch Summary						
Sketch Number	Type of Frame	Frame Number	Time from beginning of closing system	Hydraulic Pressure	Normalized Hydraulic Pressure (Pmax = 3.53 MPa)	Volume Injected
			[s]	[MPa]		[cm ³]
0	High Resolution	4064	0	0.2771	0.0784	0.0000
1	High Resolution	4065	1.502	0.2820	0.0798	0.0000
2	High Resolution	4451	777.502	3.5331	1.0000	0.2471
3	High Resolution	4453	781.502	3.5324	0.9998	0.2380
4	High Resolution	4454	783.502	3.5319	0.9996	0.2409
5	High Speed	-998	787.502	3.5329	0.9999	0.2429
6	High Speed	1002	789.502	3.5322	0.9997	0.2349
7	High Resolution	4458	791.502	3.5296	0.9990	0.2372
8	High Resolution	4460	795.502	3.5211	0.9966	0.2314
9	High Resolution	4463	801.502	3.4772	0.9842	0.2246
10	High Resolution	4488	861.502	1.7374	0.4917	0.5328

Fracture Analysis Legend

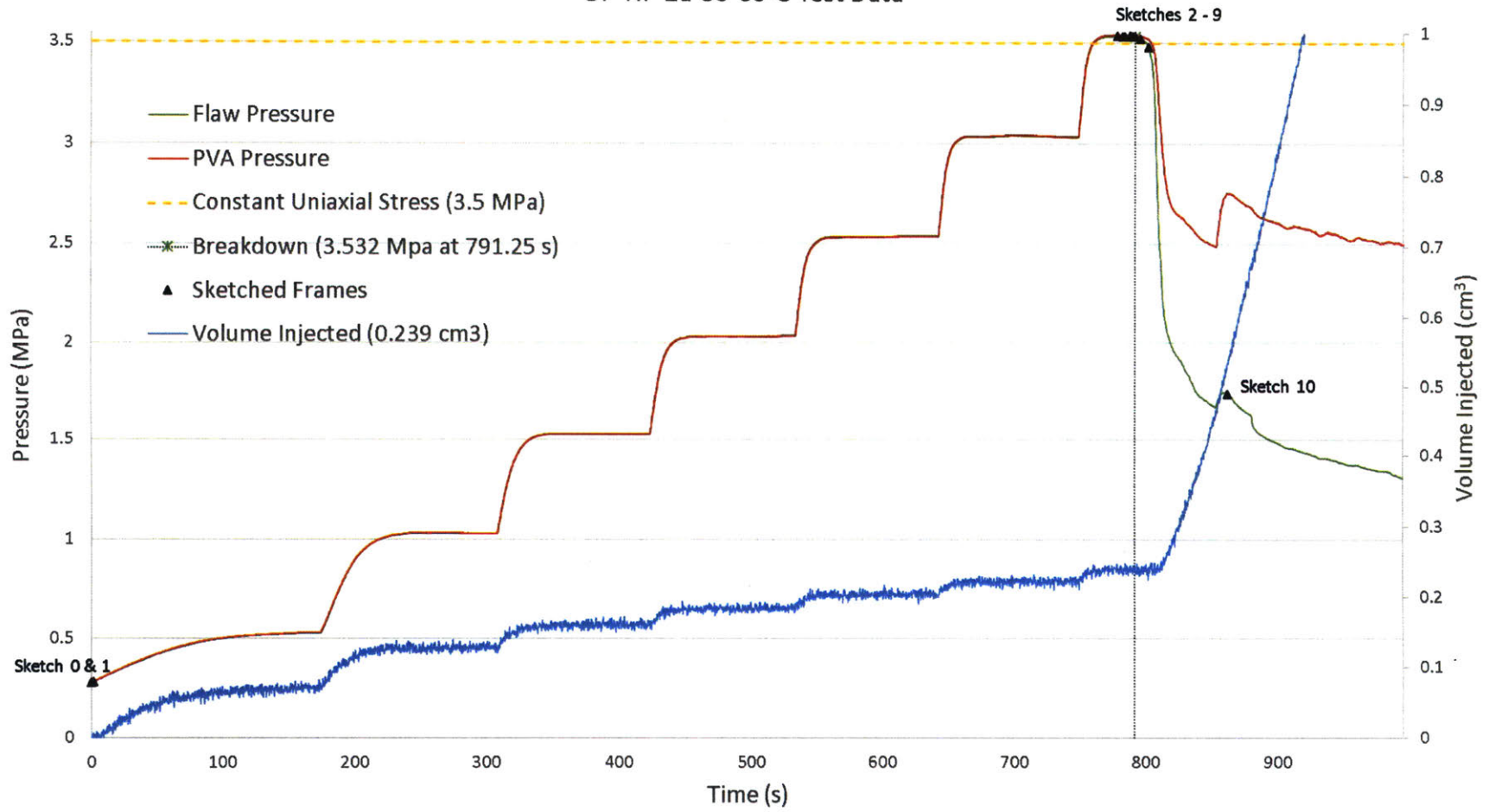


Notes:

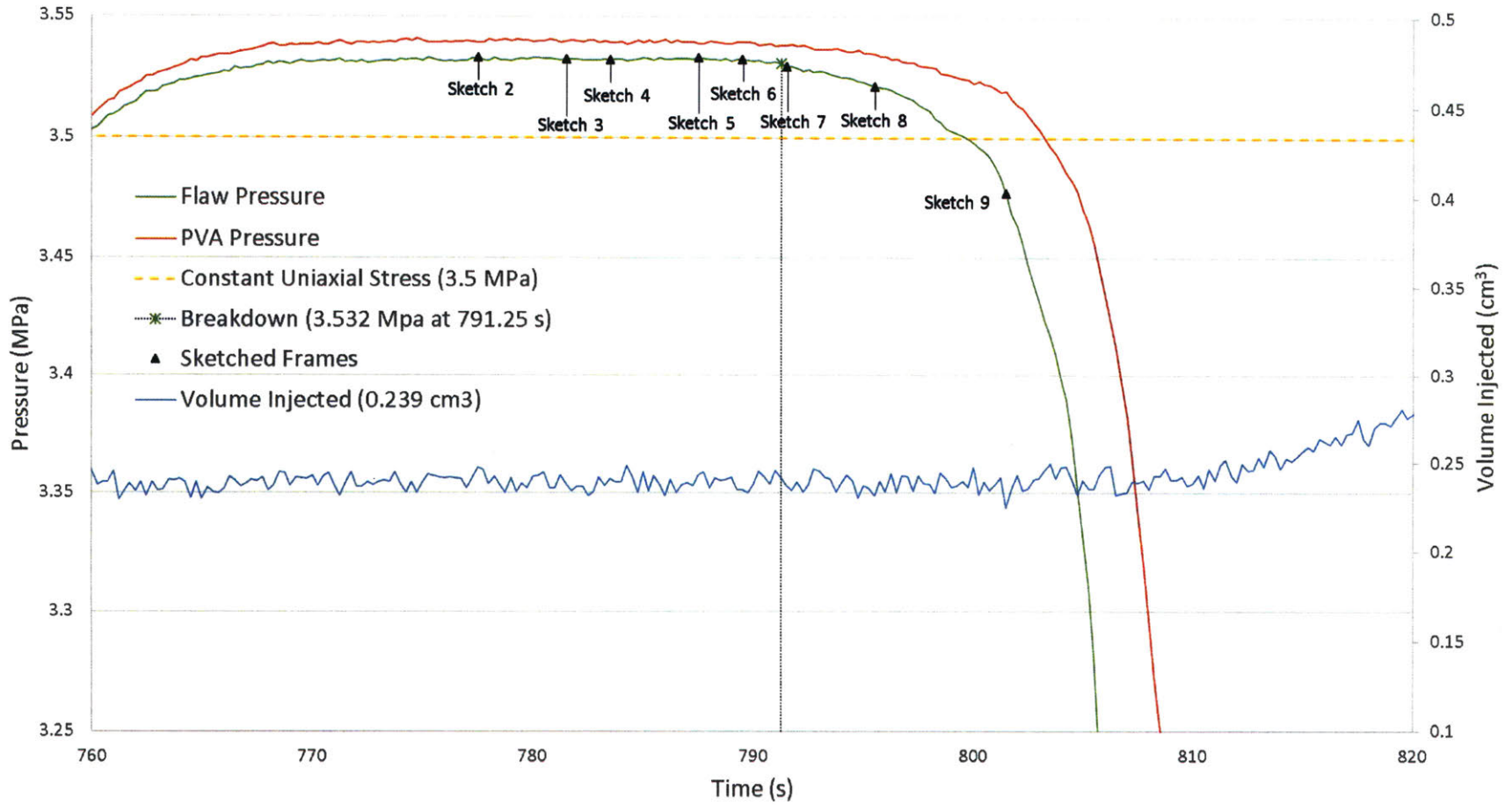
- Flow through bedding planes is denoted by a subscript “_b”.
- High-Speed video was not captured for this test.
- Table shows estimated crack initiation.
- Coalescence Category 2: indirect coalescence by multiple cracks

OP-2a-30-60-C Fractures Summary				
Crack ID	Crack Type	Hydraulic Pressure at Crack Initiation	Hydraulic Pressure Normalized to the Maximum Hydraulic Pressure	Sketch
		[MPa]		
B(T) _i	Type 1 – Tensile	3.5331	1.0000	2
A(T) _i	Type 1 – Tensile	3.5324	0.9998	3
C(T) _i	Type 1 – Tensile	3.5211	0.9966	8

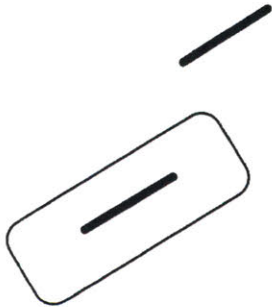
OP-HF-2a-30-60-C Test Data



OP-HF-2a-30-60-C Test Data Close-Up



Sketch 0



Frame: HR 4064 – Initial
Time: 0 seconds
 σ : 3.5 MPa
 P_{Target} : 0.5 MPa
 P : 0.277 MPa
 V : 0 cm³

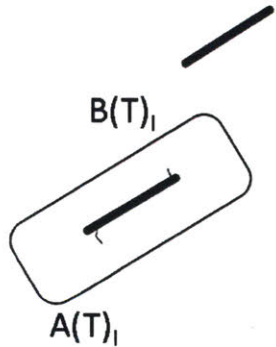
Initial Configuration

Prismatic Specimen: 4"x2"x1"
Flaw: 2a = 3/8"
Ligament Spacing (L): 2a
Flaw Angle (β): 30°
Bridging Angle (α): 60°
Bedding Orientation (ψ): 0°

Pressure Increments: 0.5 MPa
Pressure Hold Time: ~1 min

All cracks are labeled based on their initiation order.

Sketch 1



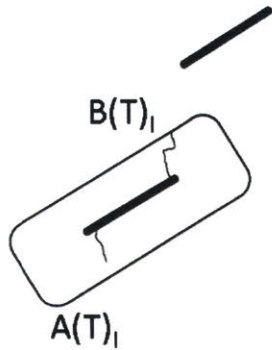
Frame: HR 4065
Time: 1.052 seconds
 σ : 3.5 MPa
 P_{Target} : 0.5 MPa
 P : 0.282 MPa
 V : 0.0013 cm³

Crack Initiation within Seal

Tensile crack A(T)_i initiated during the saturation phase prior to pressurization. The outer tip of the left flaw coincided with a bedding plane at the initiation point of A(T)_i, which developed into a crack upon filling with oil. Tensile crack B(T)_i initiated at this time in the test; i.e. the beginning of the pressurization phase. The inner tip of the left flaw also coincides with a bedding plane at the initiation point of B(T)_i.

Note: Cracks are labeled alphabetically in chronological order of crack initiation. If the order cannot be determined, then they are labeled chronologically by initiation past flaw seal.

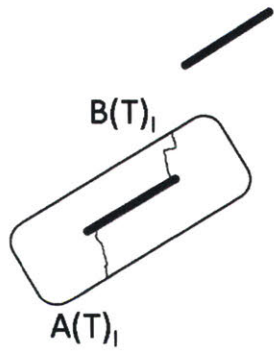
Sketch 2



Frame: HR 4451
Time: 777.502 seconds
 σ : 3.5 MPa
 P_{Target} : 3.5 MPa
 P : 3.533 MPa
 V : 0.2471 cm³

Crack Propagation within Seal
First, $A(T)_1$ propagated slightly within the flaw seal boundary and then arrested at a bedding plane. Afterwards, $B(T)_1$ propagated and arrested at a bedding plane as well. However, as the pressure increased, $B(T)_1$ propagated horizontally through the bedding plane it was arrested at, and then vertically upwards across bedding planes to the flaw seal boundary (this frame). Upon reaching the flaw seal boundary, a very small droplet of oil was observed to form at this point. However, pressure remained stable.

Sketch 3

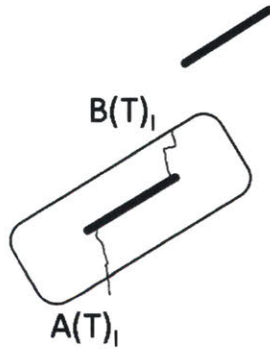


Frame: HR 4453
Time: 781.502 seconds
 σ : 3.5 MPa
 P_{Target} : 3.5 MPa
P: 3.532 MPa
V: 0.2380 cm³

Crack Propagation within Seal

Tensile crack B(T)₁ remained arrested at the flaw seal boundary. Tensile crack A(T)₁ continued propagating and arrested at the flaw seal boundary as well.

Sketch 4



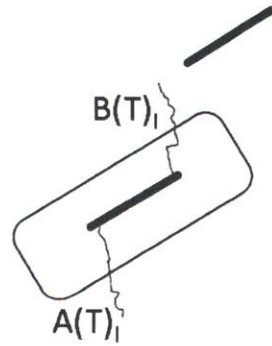
Frame: HR 4454
Time: 783.502 seconds
 σ : 3.5 MPa
 P_{Target} : 3.5 MPa
 P : 3.532 MPa
 V : 0.2409 cm³

Crack Propagation Past Seal Boundary

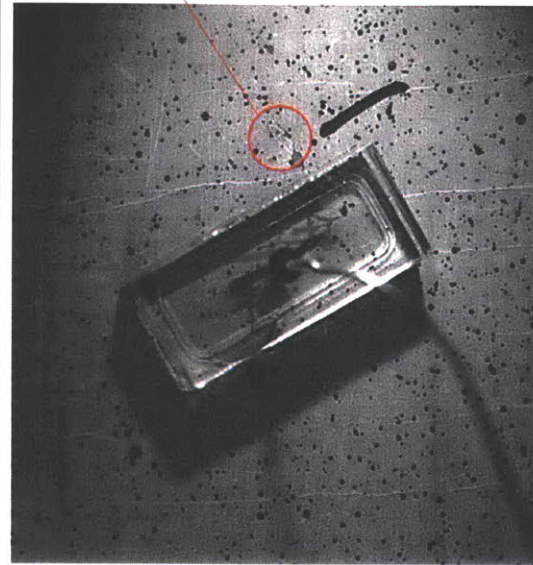
As pressure remained constant at this point. As pressure was held, tensile crack $A(T)_1$ began propagating past the flaw seal boundary.

Despite $B(T)_1$ reaching the flaw seal boundary first, $A(T)_1$ propagated past the boundary first.

Sketch 5



fossil

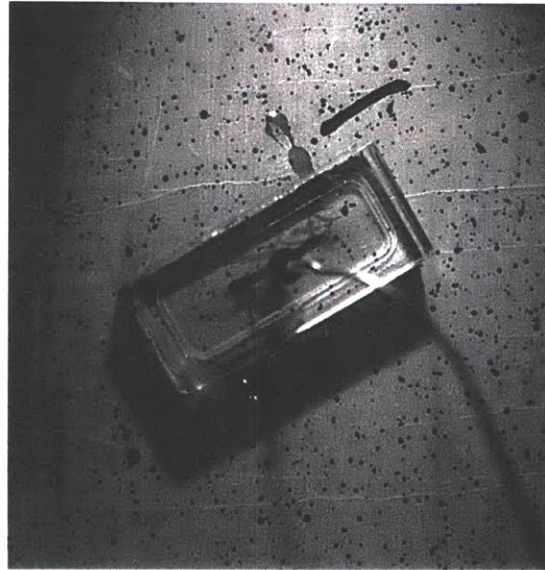
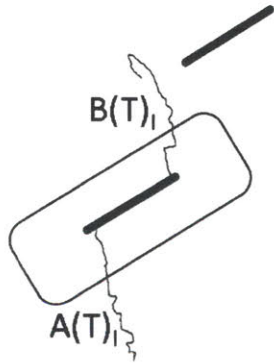


Frame: HS -998
Time: 787.502 seconds
 σ : 3.5 MPa
 P_{Target} : 3.5 MPa
P: 3.533 MPa
V: 0.2429 cm³

Crack Propagation Past Seal Boundary

Tensile crack $A(T)_i$ continued to propagate in a series of advancements and arrests at bedding plane boundaries, displaying a propagation path that is particularly jagged. $B(T)_i$ propagated past the flaw seal boundary towards an angular fossil embedded in the shale matrix.

Sketch 6

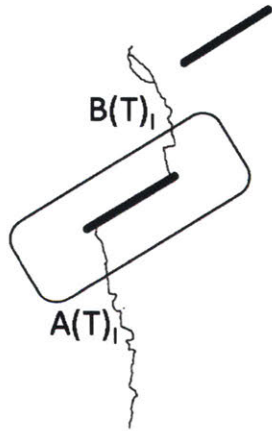


Frame: HS 1002
Time: 789.502 seconds
 σ : 3.5 MPa
 P_{Target} : 3.5 MPa
 P : 3.532 MPa
 V : 0.2349 cm³

Crack Propagation

Rather than propagate through the fossil, $B(T)_I$ propagated around the fossil boundary. $A(T)_I$ continued propagating in the same manor as stated in the previous sketch.

Sketch 7



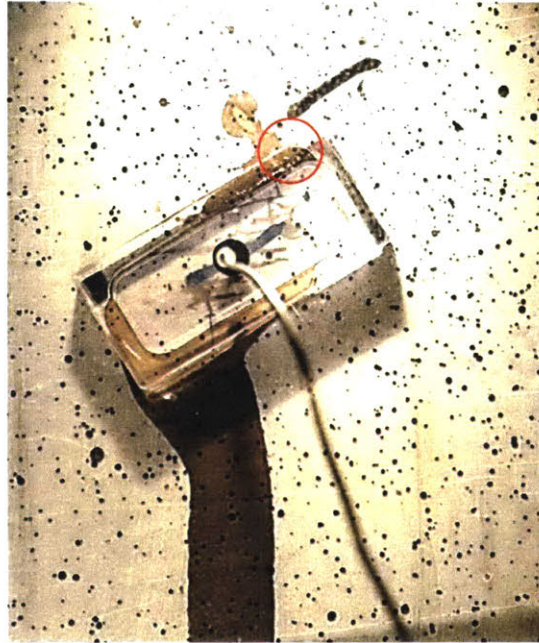
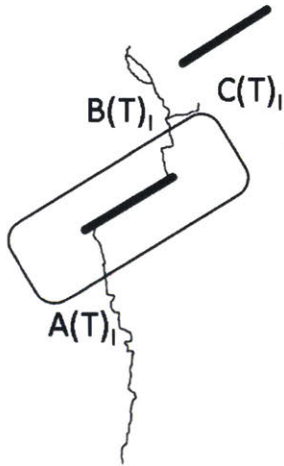
Frame: HR 4458
Time: 791.502 seconds
 σ : 3.5 MPa
 P_{Target} : 3.5 MPa
 P : 3.530 MPa
 V : 0.2372 cm³

Crack Propagation

After $B(T)_1$ completed propagation around the perimeter of the fossil, it continued propagating upwards past the fossil. This fossil is only on the specimen surface and does not penetrate through the entire thickness of the specimen, whereas $B(T)_1$ does (observed post experiment).

It is likely that $B(T)_1$ did not propagate around the perimeter of the fossil, rather it propagated behind the fossil, and the oil flowing out of the fossil perimeter. $B(T)_1$ arrested at this point. Crack $A(T)_1$ continued propagating.

Sketch 8



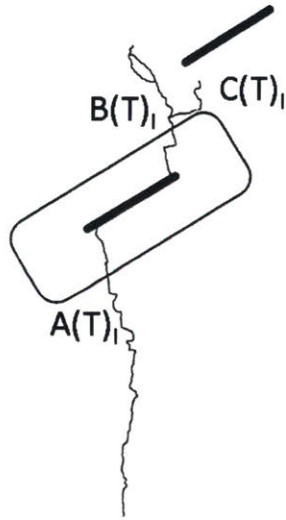
Frame: HR 4460
Time: 795.502 seconds
 σ : 3.5 MPa
P_{Target}: 3.5 MPa
P: 3.521 MPa
V: 0.2314 cm³

Crack Initiation & Propagation

Although B(T)₁ stopped propagating, a new tensile crack, C(T)₁, branched off of B(T)₁ at a bedding plane. C(T)₁ propagated along the bedding plane towards the right flaw.

Crack A(T)₁ continued propagating.

Sketch 9



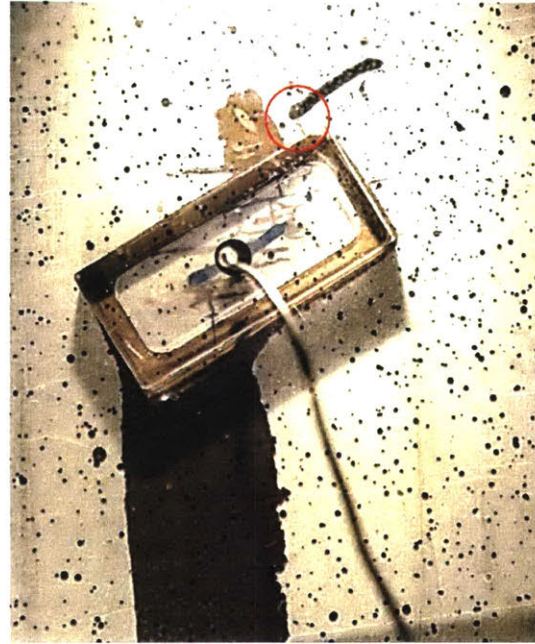
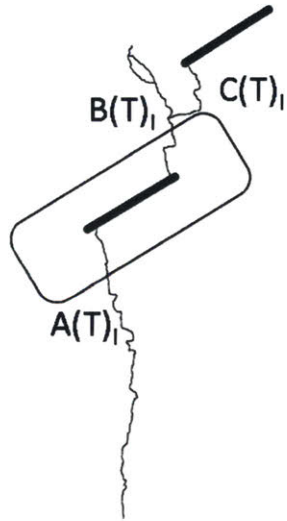
Frame: HR 4463
Time: 801.502 seconds
 σ : 3.5 MPa
 P_{Target} : 3.5 MPa
 P : 3.477 MPa
 V : 0.2246 cm³

Crack Propagation

Once $C(T)_1$ reached a point below the inner tip of the right flaw, its propagation mechanism changed from propagating along a bedding plane to propagating across bedding planes upwards towards the inner tip of the right flaw.

Crack $A(T)_1$ continued propagating and stopped at this point.

Sketch 10



Frame: HR 4488
Time: 861.502 seconds
 σ : 3.5 MPa
 P_{Target} : 3.5 MPa
 P : 1.737 MPa
 V : 0.5328 cm³

Coalescence

B(T)₁ and A(T)₁ remained arrested throughout the duration between Sketch 9 and Sketch 10. C(T)₁ continued propagating slowly across bedding planes in a jagged series of advancements and arrests towards the inner tip of the right flaw until coalescing.

This geometry and loading condition lead to a Category 2: Indirect Coalescence by multiple cracks.

Appendix B – Shale Mineralogy Analysis

Appendix B1 – Opalinus Shale Bulk Mineralogy and Clay fraction



Report Number: 2014-20795

ANALYTICAL LABORATORY SERVICES
Assured Analytical Excellence
www.claysandminerals.com

Report on the Whole Rock Mineralogy of Four Samples and <2 µm Clay Fraction Mineralogy of Six Samples by X-Ray Powder Diffraction (XRPD)

FOR:
Chunwei Ge
MIT
77 Massachusetts Avenue,
Building 1, Room 353,
Cambridge,
Massachusetts,
02139-4307
USA



REPORT AUTHORS:

Nia Gray, MChem (Analyst)
(e-mail: nia.gray@hutton.ac.uk T: 01224 395346)



Prof. Stephen Hillier

**Report Authorisation
Aberdeen**

2015.01.13 15:15:17 Z

Tests marked "N/A" are not covered by the UKAS Schedule for this laboratory.
Opinions and interpretations expressed herein are outside the scope of UKAS Accreditation.
This report shall not be reproduced, except in full, without written approval of the laboratory.

Craigiebuckler, Aberdeen AB15 8QH, Scotland
T: +44 (0)844 928 5428 F: +44 (0)1224 395010 W: www.hutton.ac.uk

Page 1 of 14

Job and Sample Information:			
Job No(s):	2014-20795		
Client Order No/Reference:	5510057544		
Date Sample(s) Received:	11 th -December-2014		
Lab Code	Client Code	Whole Rock	Clay
1189849	1-Yellow-Pierre Shale	✓	✓
1189850	2-Blue-Opalinus Shale from core BSO-34	✓	✓
1189851	3-Purple-Opalinus Shale from core BSO-36	✓	✓
1189852	4-Orange-Opalinus Shale from core FE-A	✓	✓
1189853	5-Orange-Opalinus Shale from core BSO-36-targeting calcitic material		✓
1189854	IS Trans O2		✓

Introduction

Six samples were forwarded for <2 µm clay fraction analysis by X-ray powder diffraction, in addition four of these samples were requested for whole rock mineralogical analysis by X-ray powder diffraction. For sample 'IS Trans O2' (1189854) the client requested that its clay size fraction should be analysed in a Mg²⁺ saturated form.

Methods

Methods	Accreditation Reference
Identification and Quantification of Whole Rock Mineralogy by XRPD	GM003 and GM004
Identification and Quantification of Clay Minerals by XRPD	GM001 and GM002
Saturation by a known cation	N/A

XRPD

The whole rock samples were wet ground (in ethanol) in a McCrone mill and then spray dried to produce a random powder. The X-ray powder diffraction (XRPD) patterns were recorded from 4-70°2θ using Copper Kα radiation. Quantitative analysis was done by a normalised full pattern reference intensity ratio (RIR) method. Unless stated otherwise, expanded uncertainty using a coverage factor of 2, i.e. 95% confidence, is given by $\pm X^{0.95}$, where X = concentration in wt.%, e.g. 30 wt.% ± 3.3 . Note also that for phases present at the trace level (<1%) there may also be uncertainty as to whether or not the phase is truly present in the sample. This is both phase and sample dependent. It arises because at trace concentrations identification is often based on the presence of a single peak and the judgement of the analyst in assigning that peak to a likely mineral.

The clay fractions of <2µm were obtained by timed sedimentation, prepared as oriented mounts using the filter peel transfer technique and scanned using Copper Kα radiation from 3-45°2θ in the air-dried state, after glycolation, and after heating to 300°C for one hour. Clay minerals identified were quantified using a mineral intensity factor approach based on calculated XRPD patterns. Unless otherwise stated, for clay minerals present in amounts >10wt.% uncertainty is estimated as better than ± 5 wt.% at the 95% confidence level.

For one sample the clay fraction was analysed in magnesium saturated form achieved by repeated exchange with 1 M MgCl₂ and subsequent rinsing in deionised water.

XRPD patterns are identified by labcodes and by names based on customer supplied identifiers plus the suffix, 'A' for Air-dried, 'G' for Glycolated, 'H3' for Heated to 300°C and 'B' for bulk sample.

Results

XRPD whole rock results are presented in Table 1 and clay fraction results in Table 2. Additionally XRPD patterns, with the main phases identified in the bulk samples by reference to patterns from the International Centre for Diffraction Database (ICDD), are provided for reference.

Comments and opinions

Whole rock mineralogical analysis indicates that the samples contain quartz, K-feldspar, plagioclase, calcite, pyrite, chlorite, muscovite, illite + mixed layer illite/smectite (undifferentiated in the whole rock), kaolinite and potentially dolomite, siderite, apatite and possible traces of gypsum, halite and anatase.

Clay fraction analysis indicates that the samples are dominated by mixed layer illite/smectite, and also contain illite, chlorite and kaolinite, apart from sample 'IS Trans O2' (1189854), where kaolinite was not detected. The expandability of the mixed layer clays is estimated at around 20% in the four Opalinus samples 60% in the '1-Yellow-Pierre-Shale' (1189849), and about 15% in sample 'IS Trans O2'.

Based on the minor amounts of illite observed in the clay fractions it would be a reasonable assumption that most of the undifferentiated illite + illite/smectite in the whole rock analyses is mixed-layer illite/smectite.

Note:

Samples will be stored for a period of eight weeks following completion of analysis and acceptance of analytical report(s) at no extra cost after which samples will be disposed of unless a specific instruction is given (with the sample analysis request/order) to store the sample beyond this period. Extended storage charges will apply.

Table 1: XRPD Bulk Mineralogy (weight %) by RIR Method

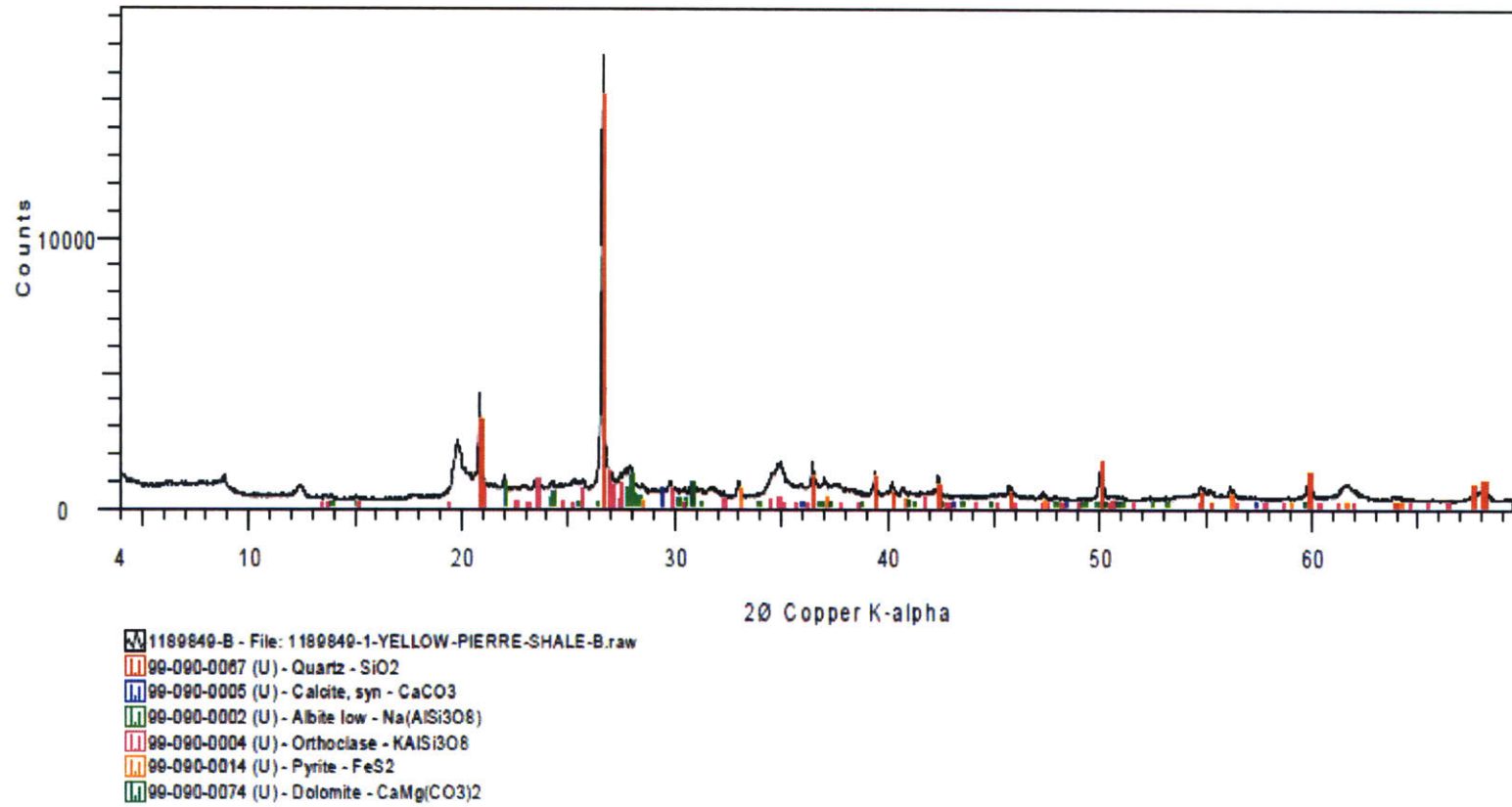
Labcode	Sample ID	Quartz	K-feldspar	Plagioclase	Calcite	Dolomite	Siderite	Gypsum	Hallite	Anatase	Apatite	Pyrite	Chlorite (Tr)	Muscovite	I/S-ML	Kaolinite	TOTAL
1189849	1-YELLOW-PIERRE-SHALE-B	20.4	3.8	7.0	0.9	1.1	0.3	0.5	0.5	0.1	0.7	1.3	3.7	1.0	50.5	8.3	100
1189850	2-BLUE-OPALINUS-SHALE-CORE-BSO-34-B	34.0	2.3	1.4	6.5	0.7	0.7	0.3	0.0	0.4	1.1	1.2	2.6	2.0	31.5	15.6	100
1189851	3-PURPLE-OPALINUS-SHALE-CORE-BSO-36-B	15.9	0.5	0.9	5.4	0.5	0.3	0.0	0.0	0.5	1.1	2.2	3.6	2.0	45.4	21.6	100
1189852	4-ORANGE-OPALINUS-SHALE-CORE-FE-A-B	13.5	0.5	1.1	12.8	1.3	0.7	0.0	0.0	0.4	0.9	0.9	3.4	2.2	44.2	18.1	100

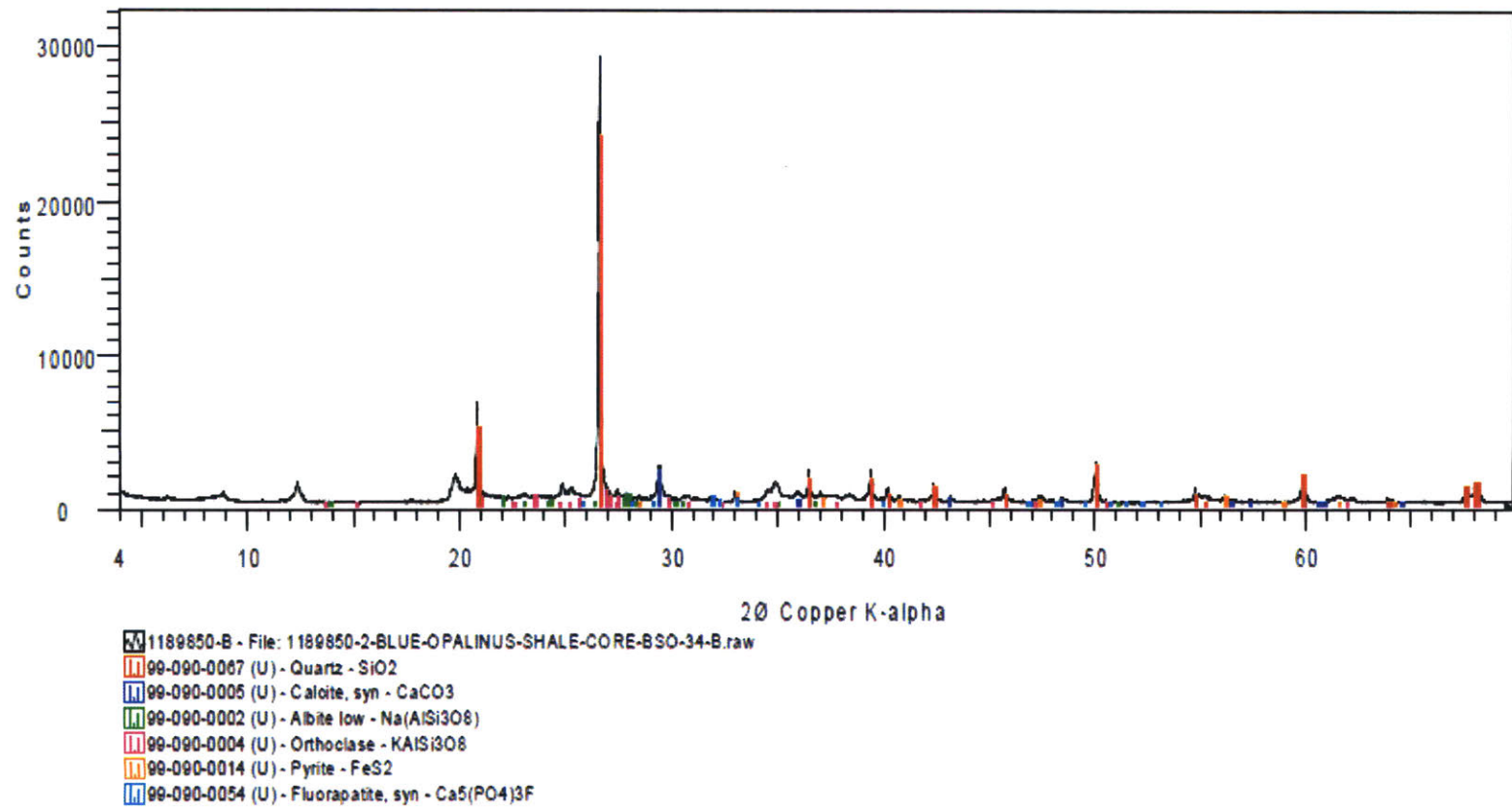
I/S-ML = Illite + Mixed Layer Illite-Smectite

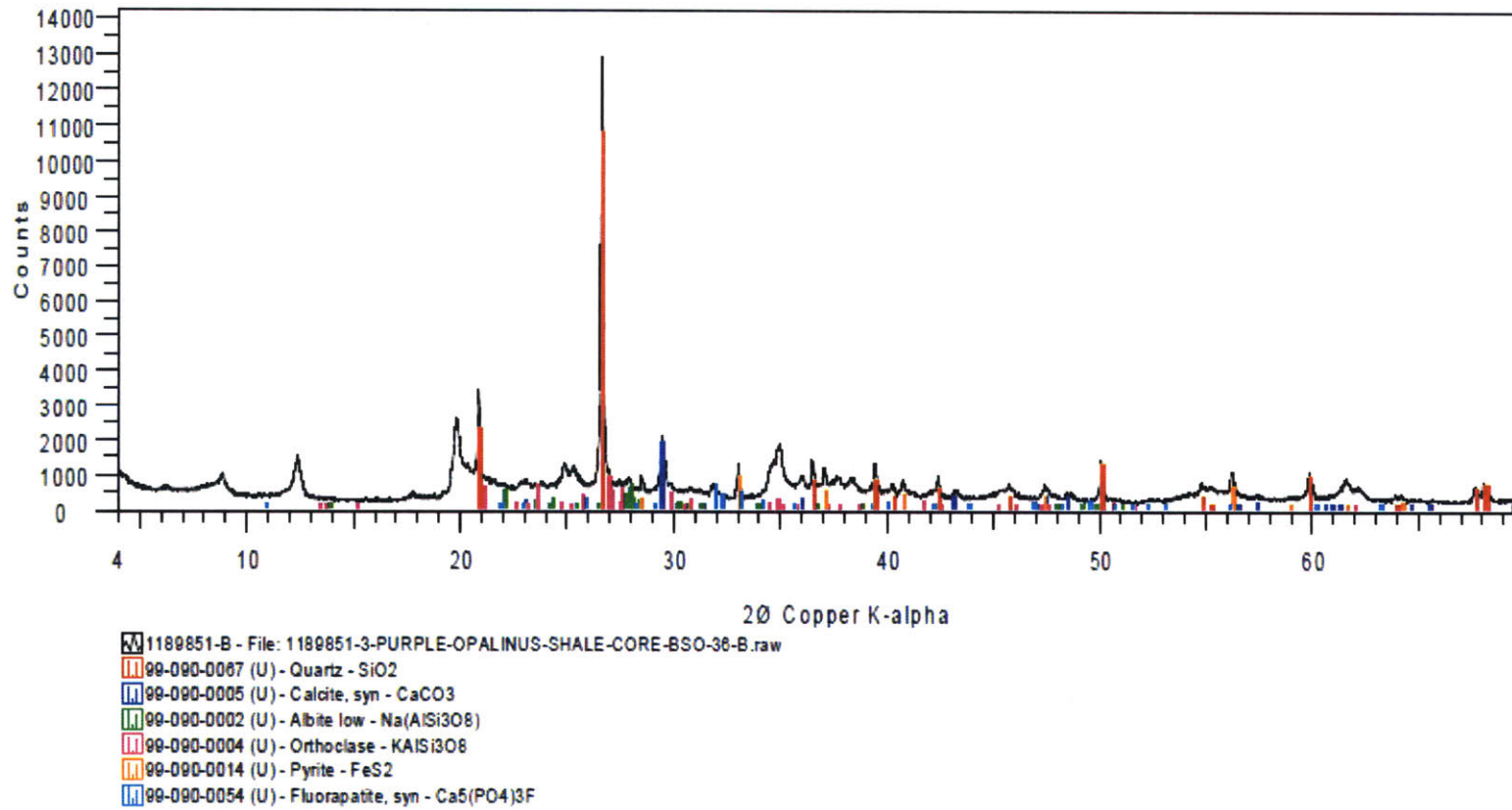
Table 2: Relative percentage of clay minerals in the <2µm clay size fraction

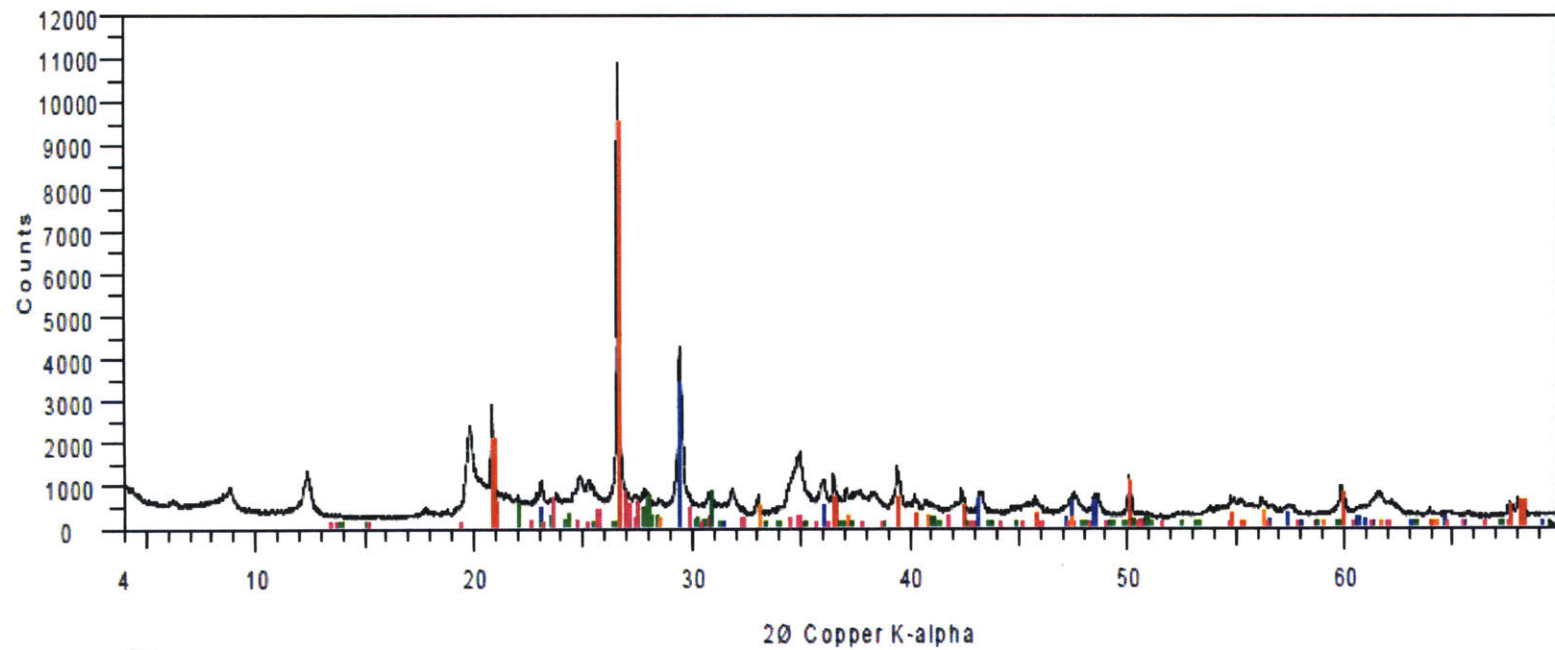
Labcode	Sample ID	Chlorite(Tr)%	Kaolinite%	Illite%	I/S-ML%	%Exp
1189849	1-YELLOW-PIERRE-SHALE	2	5	5	88	60
1189850	2-BLUE-OPALINUS-SHALE-CORE-BSO-34	4	19	4	73	20
1189851	3-PURPLE-OPALINUS-SHALE-CORE-BSO-36	3	17	4	76	20
1189852	4-ORANGE-OPALINUS-SHALE-CORE-FE-A	4	11	4	81	20
1189853	5-ORANGE-OPALINUS-SHALE-CORE-BSO-36-TARGETING-CALCITIC-MATERIAL	4	15	5	76	20
1189854	IS-TRANS-O2-MG-SAT	1	0	5	94	15

%Exp = Expandability of mixed-layer illite-smectite

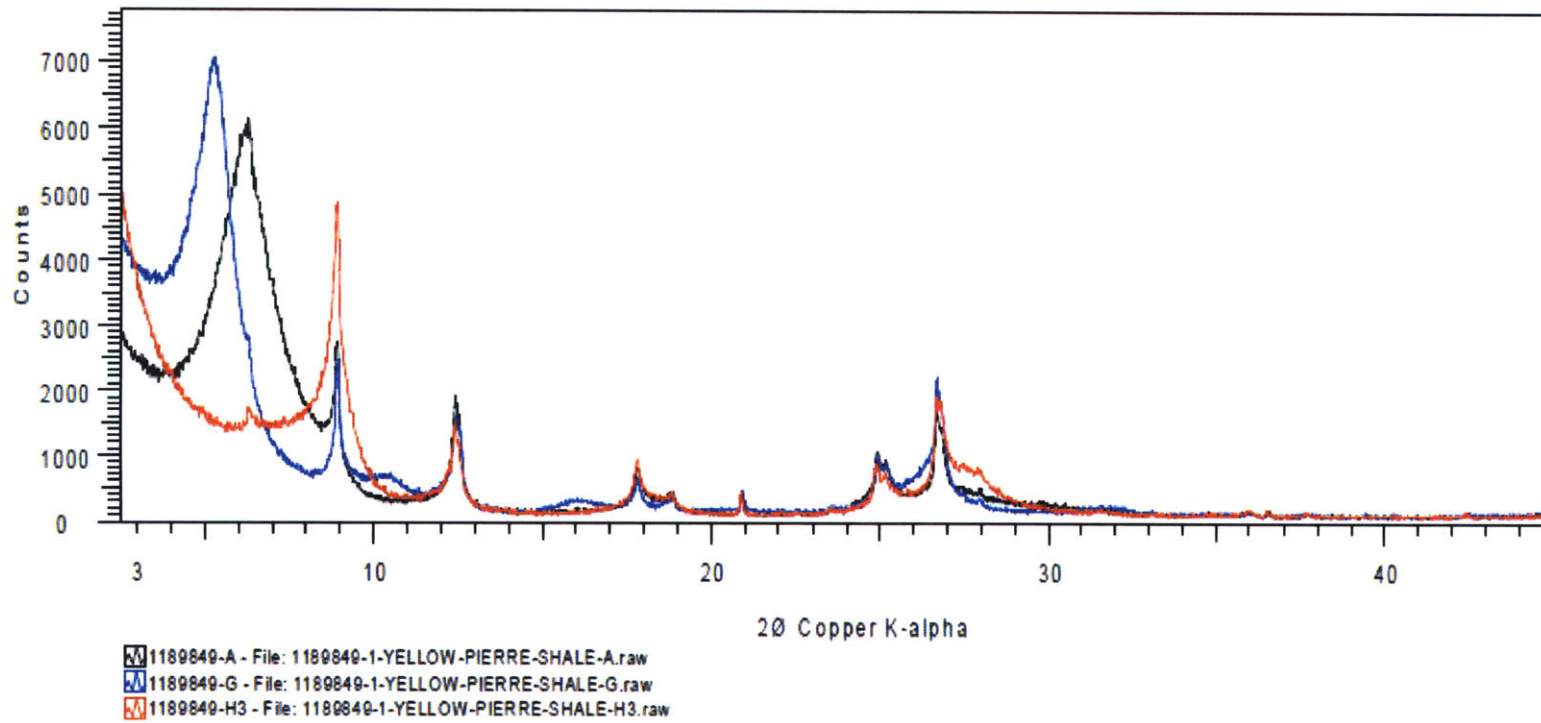


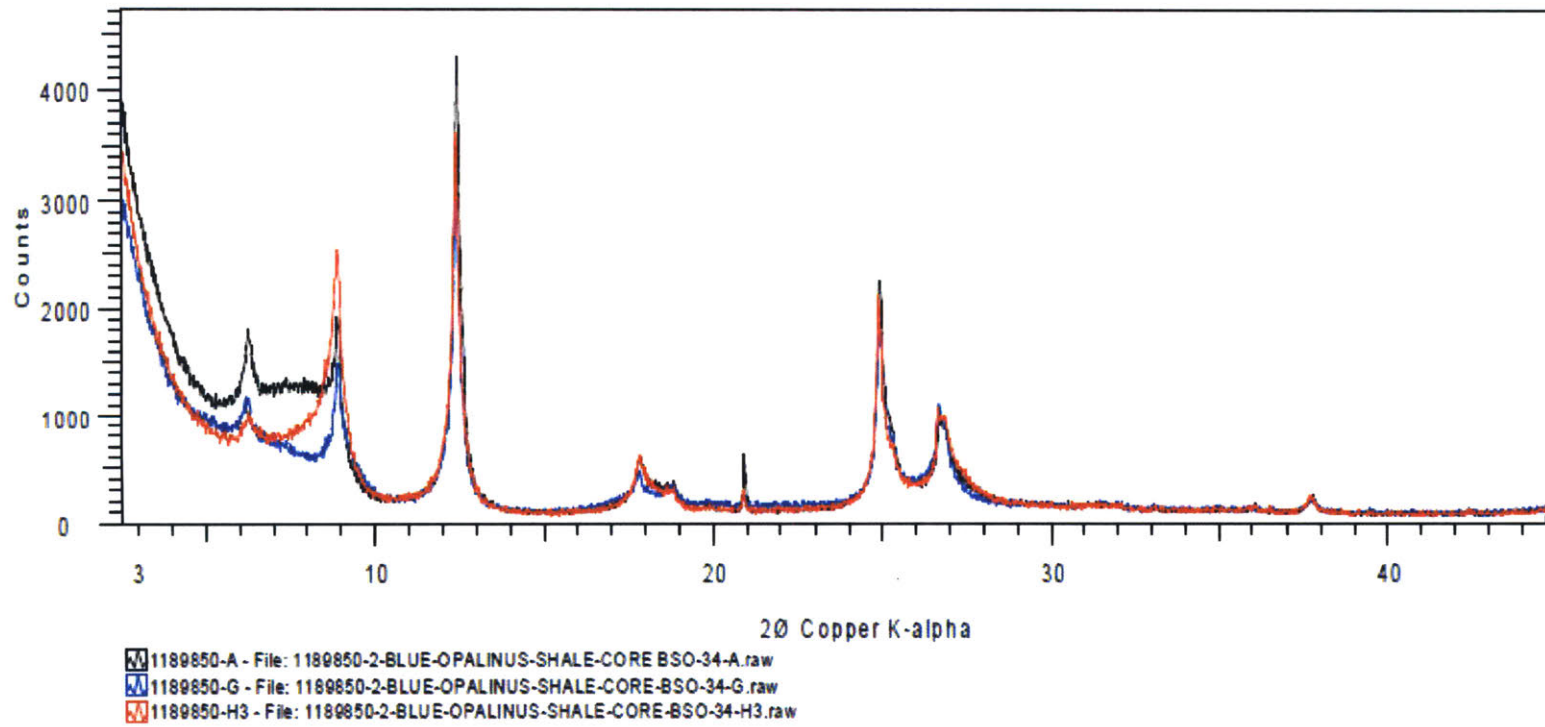


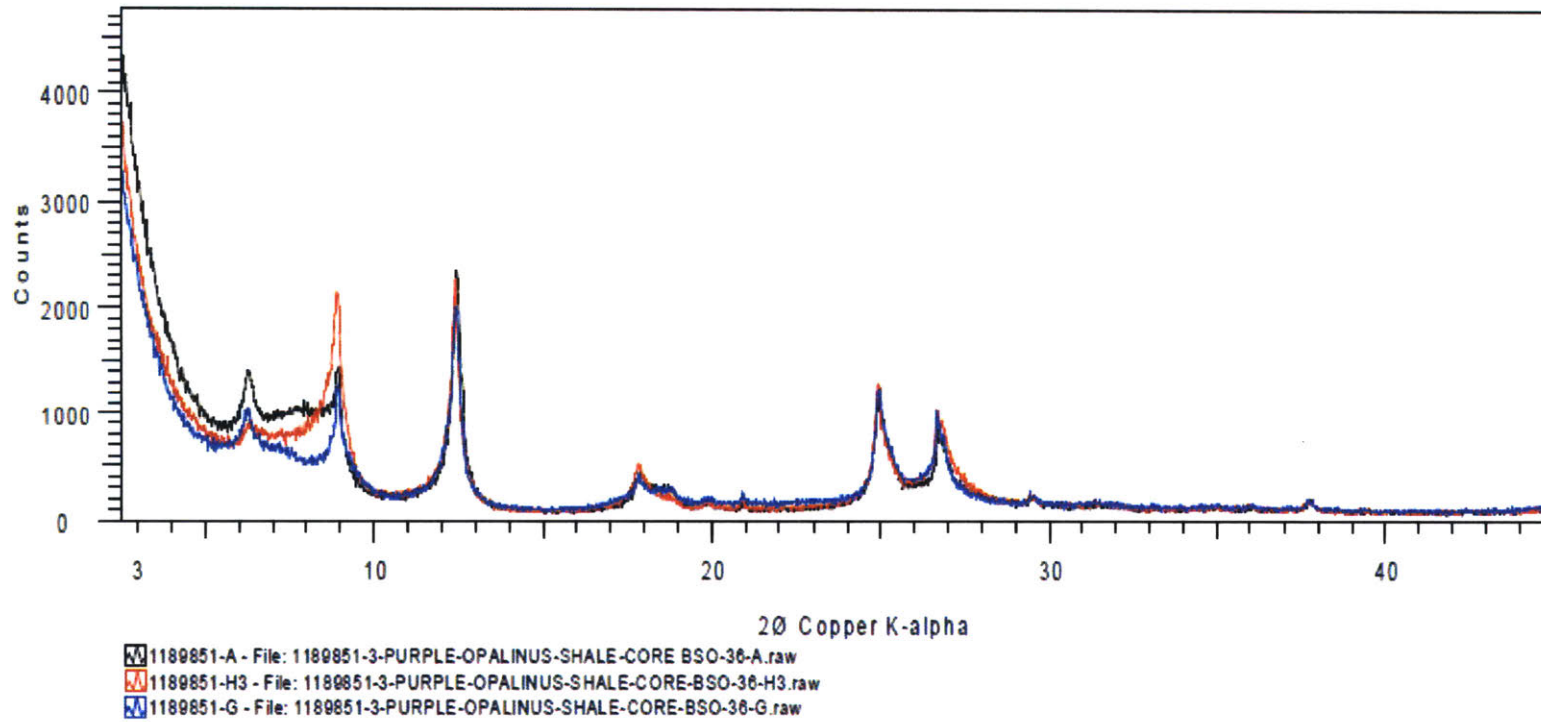


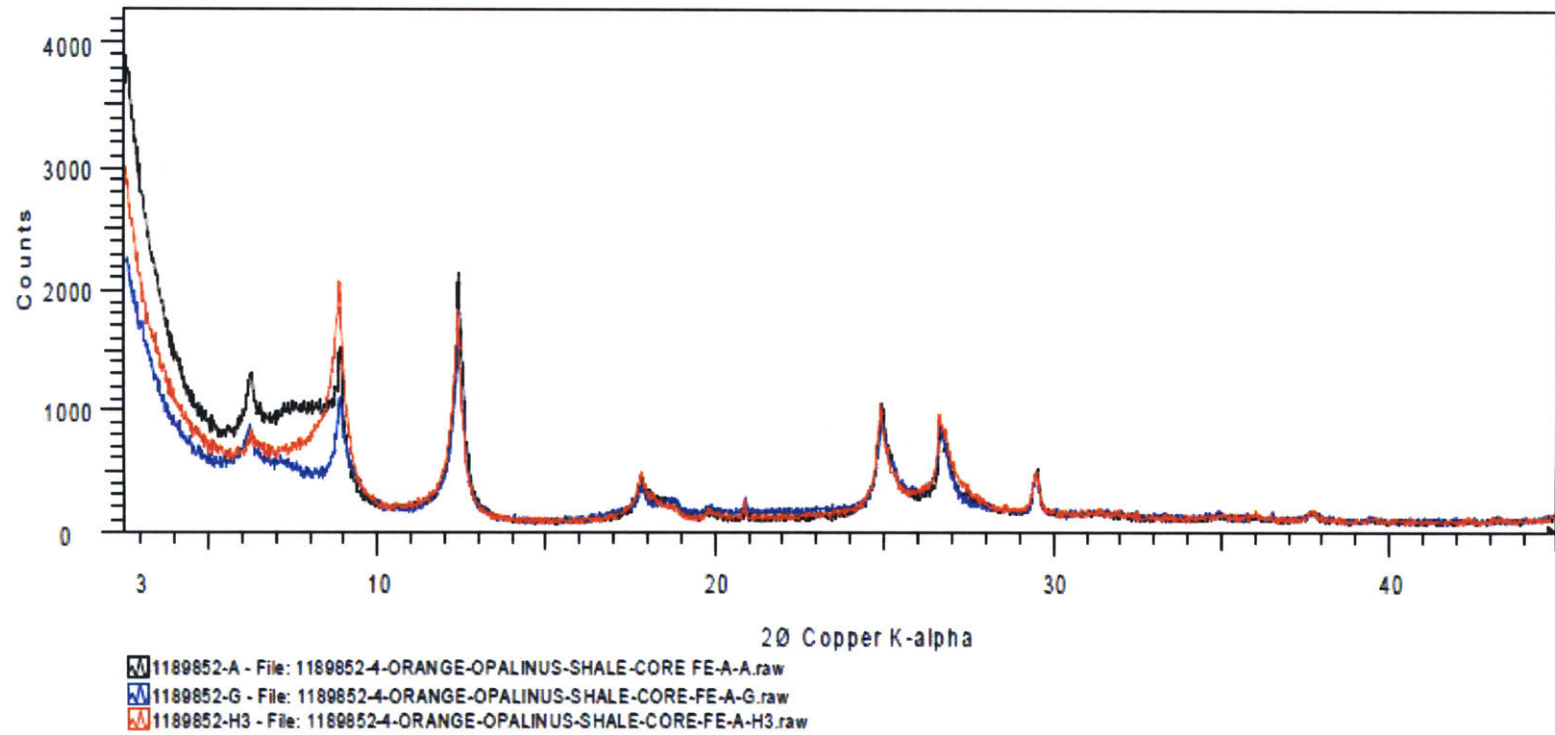


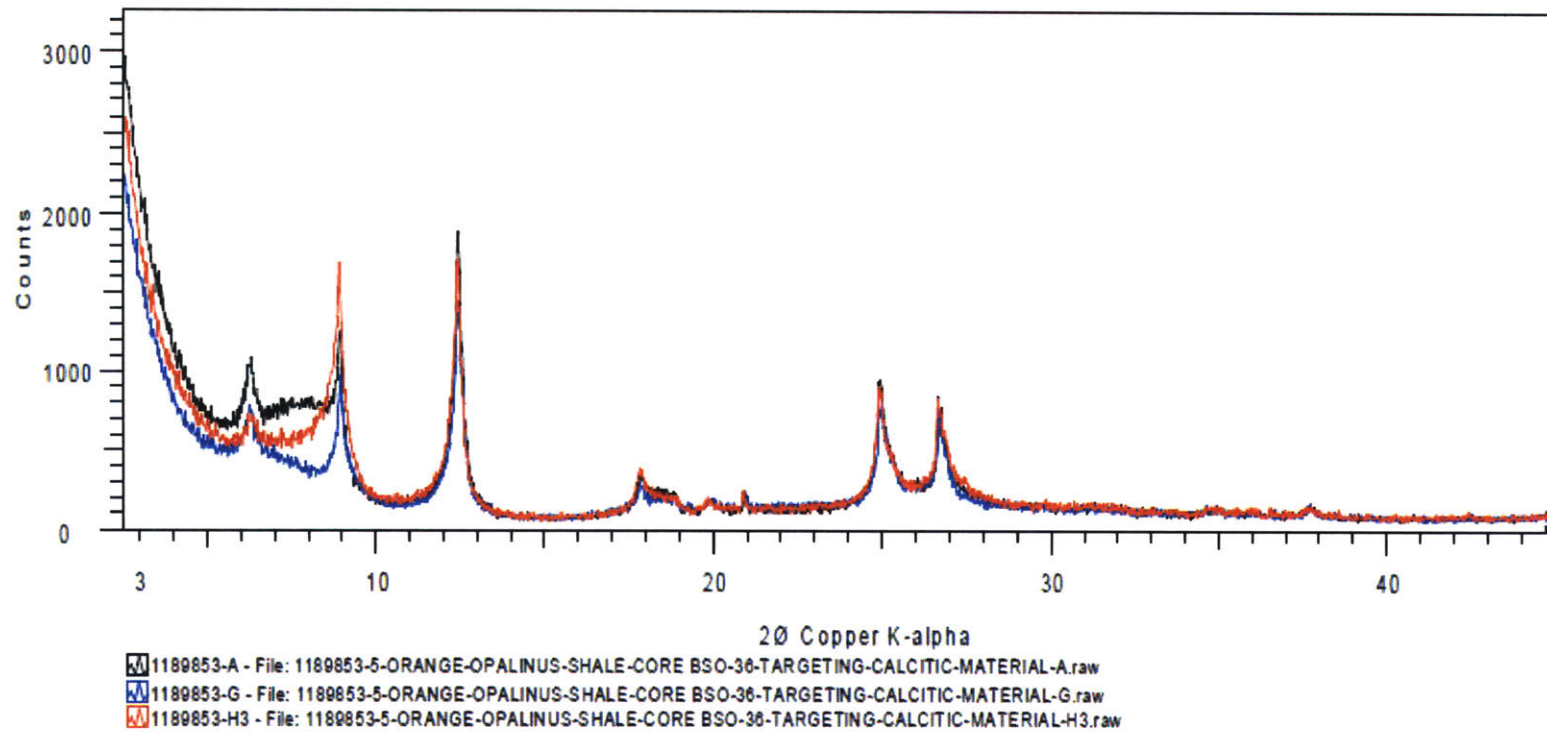
- 1189852-B - File: 1189852-4-ORANGE-OPALINUS-SHALE-CORE-FE-A-B.raw
- 99-090-0067 (U) - Quartz - SiO₂
- 99-090-0005 (U) - Calcite, syn - CaCO₃
- 99-090-0002 (U) - Albite low - Na(AlSi₃O₈)
- 99-090-0004 (U) - Orthoclase - KAlSi₃O₈
- 99-090-0014 (U) - Pyrite - FeS₂
- 99-090-0074 (U) - Dolomite - CaMg(CO₃)₂

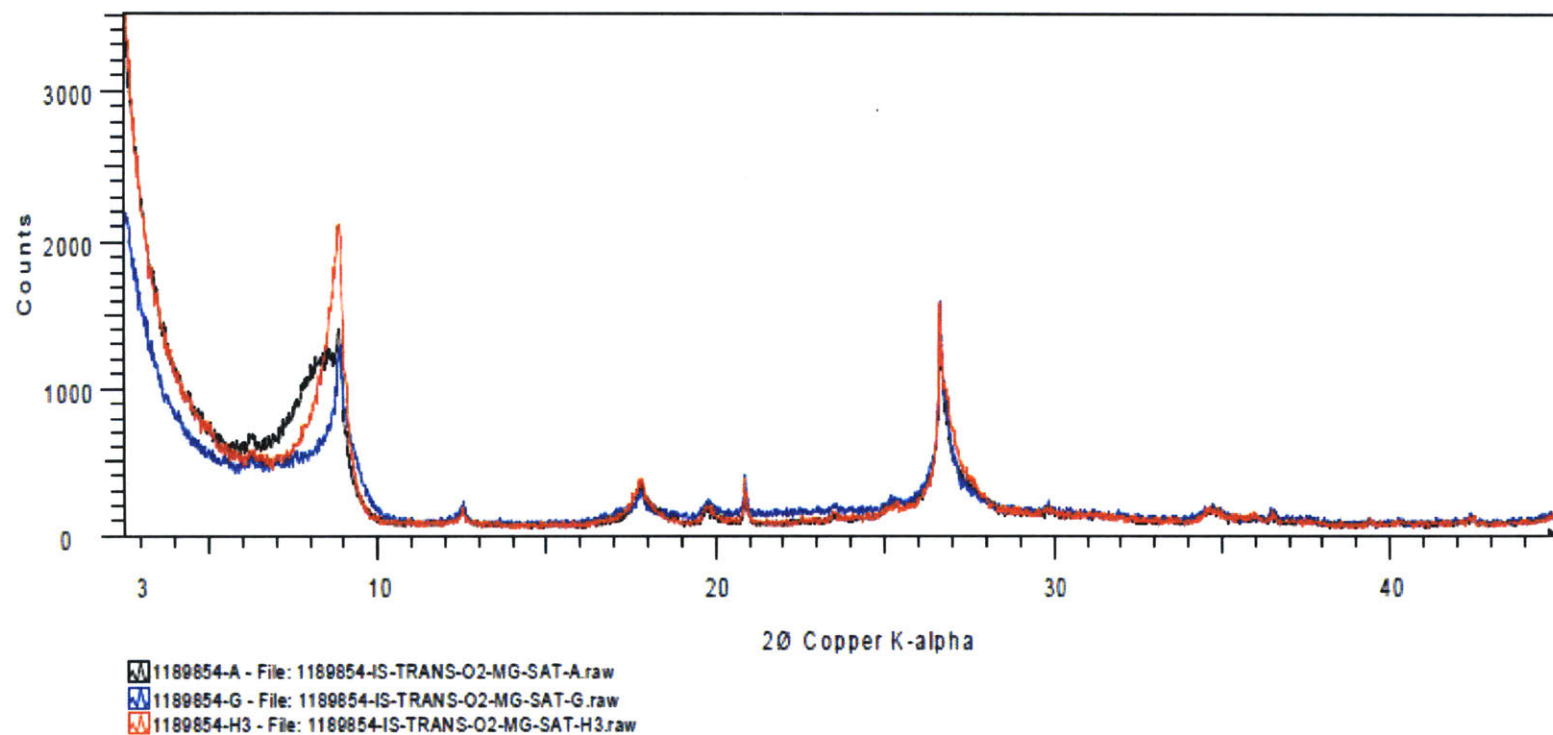














Report Number: 2015-21653

ANALYTICAL LABORATORY SERVICES
Assured Analytical Excellence
www.claysandminerals.com

Report on the Whole Rock Mineralogy, <2 µm Clay Fraction Analysis by X-Ray Powder Diffraction (XRPD) and Cation Exchange Capacity (CEC) of Three Vaca Muerta Shale Samples

FOR:

Omar Al Dajani,
MIT,
77 Massachusetts Avenue,
Building 1 Room 353,
Cambridge,
Massachusetts,
02139-4307
USA



REPORT AUTHORS:

Nia Gray, MChem (Analyst)
(e-mail: nia.gray@hutton.ac.uk T: 01224 395346)



 Digitally signed by Ian Phillips
Reason: Report Authorisation
Date: 2015.07.15 07:41:16
+01'00'

Tests marked "N/A" are not covered by the UKAS Schedule for this laboratory.
Opinions and interpretations expressed herein are outside the scope of UKAS Accreditation.
This report shall not be reproduced, except in full, without written approval of the laboratory.

Job and Sample Information:	
Job No(s):	2015-21653
Client Order No/Reference:	email
Date Sample(s) Received:	25-May-2015
Lab Code	Client Code
1201331	Vaca Muerta Shale - AR X3 @ 2596.4 m air dried, ground with pestle and mortar, and then passed through No. 90 sieve.
1201332	Vaca Muerta Shale - AR X3 @ 2596.4 m air dried, ground with pestle and mortar, and then passed through No. 90 sieve.
1201333	Vaca Muerta Shale - AR X4 @ 2897.37 m air dried, ground with pestle and mortar, and then passed through No. 90 sieve.
1201334	Vaca Muerta Shale - AR X4 @ 2897.37 m air dried, ground with pestle and mortar, and then passed through No. 90 sieve.
1201335	Vaca Muerta Shale - AR X5 @ 2685.98 m air dried, ground with pestle and mortar, and then passed through No. 90 sieve.
1201336	Vaca Muerta Shale - AR X5 @ 2685.98 m air dried, ground with pestle and mortar, and then passed through No. 90 sieve.

Introduction

Three samples were forwarded for bulk mineralogical analysis and <2 µm clay fraction analysis by X-ray powder diffraction (XRPD). Cation exchange capacity measurements (CEC) were also carried out on the samples. Each sample type was sent in two separately named vials by the client, the first of each was for bulk mineralogy and cation exchange capacity and the second was for clay fraction analysis.

Methods

Methods	Accreditation Reference
Identification and Quantification of Whole Rock Mineralogy by XRPD	GM003 and GM004
Identification and Quantification of Clay Minerals by XRPD	GM001 and GM002
Cation Exchange Capacity by Cobalt hexamine Method	GM006

XRPD

The whole rock samples were wet ground (in ethanol) in a McCrone mill and then spray dried to produce a random powder. The X-ray powder diffraction (XRPD) patterns were recorded from 4-70°2θ using Copper Kα radiation. Quantitative analysis was done by a normalised full pattern reference intensity ratio (RIR) method. Unless stated otherwise, expanded uncertainty using a coverage factor of 2, i.e. 95% confidence, is given by $\pm X^{0.35}$, where X = concentration in wt.%, e.g. 30 wt.% ± 3.3 . Note also that for phases present at the trace level (<1%) there may also be uncertainty as to whether or not the phase is truly present in the sample. This is both phase and sample dependent. It arises because at trace concentrations identification is often based on the presence of a single peak and the judgement of the analyst in assigning that peak to a likely mineral.

The clay fractions of <2µm were obtained by timed sedimentation, prepared as oriented mounts using the filter peel transfer technique and scanned using Copper Kα radiation from 3-45°2θ in the air-dried state, after glycolation, and after heating to 300°C for one hour. Clay minerals identified were quantified using a mineral intensity factor approach based on calculated XRPD patterns. Unless otherwise stated, for clay minerals present in amounts >10wt.% uncertainty is estimated as better than ± 5 wt.% at the 95% confidence level.

XRPD patterns are identified by labcodes and by names based on customer supplied identifiers plus the suffix, 'A' for Air-dried, 'G' for Glycolated, 'H3' for Heated to 300°C and 'B' for bulk sample.

CEC

Cation exchange capacity (CEC) was measured using a cobalt hexamine trichloride method based on the ISO 23470 standard, wherein the exchangeable cations on the sample are replaced by trivalent cobalt hexamine ions and the CEC of the sample is determined by absorption colorimetry.

Results

XRPD whole rock results are presented in Table 1, clay fraction results in Table 2 and cation exchange capacity results in Table 3. Additionally, XRPD patterns, with the main non clay phases identified in the bulk samples by reference to patterns from the International Centre for Diffraction Database (ICDD), are provided for reference.

Comments and Opinions

Minerals identified and quantified include quartz, plagioclase and illite + mixed layer illite/smectite. Some of the samples may contain K-feldspar, calcite, dolomite, hematite, apatite, pyrite, chlorite and muscovite along with possible traces of halite, anatase, marcasite and kaolinite.

Clay fraction analysis indicates that the samples are dominated by low expandable mixed layer illite/smectite while samples Vaca Muerta Shale - AR X4 @ 2897.37 m (1201334) and Vaca Muerta Shale - AR X5 @ 2685.98 m (1201336) also contain low levels of illite and chlorite.

Cation exchange capacity measurements range from 0 – 7.9 $\text{cmol}\cdot\text{kg}^{-1}$ and a good correlation can be observed between the CEC as predicted by mineralogy and the measured CEC as shown in Table 3.

Note:

Samples will be stored for a period of eight weeks following completion of analysis and acceptance of analytical report(s) at no extra cost after which samples will be disposed of unless a specific instruction is given (with the sample analysis request/order) to store the sample beyond this period. Extended storage charges will apply.

Table 1: XRPD Bulk Mineralogy (weight %) by RIR Method

Labcode	Sample ID	Quartz	K-feldspar	Plagioclase	Calcite	Dolomite	Halite	Anatase	Apatite	Hematite	Pyrite	Marcasite	Chlorite (Tri)	I+/S-ML	Muscovite	Kaolinite	TOTAL
1201331	VACA-MUERTA-AR-X3-2596-4-B	82.6	2.9	4.8	0.2	0.3	0.8	0.0	0.5	3.7	0.2	0.0	0.4	3.6	0.0	0.0	100
1201333	VACA-MUERTA-AR-X4-2897-37-B	37.6	1.8	13.4	15.1	1.2	0.1	0.1	1.5	0.0	2.6	0.7	0.7	20.9	3.6	0.6	100
1201335	VACA-MUERTA-AR-X5-2685-98-B	25.7	0.0	9.6	14.4	1.5	0.2	0.1	0.9	0.1	1.3	0.1	5.6	40.6	0.0	0.0	100

I+/S-ML = Illite + undifferentiated mixed layer illite-smectite

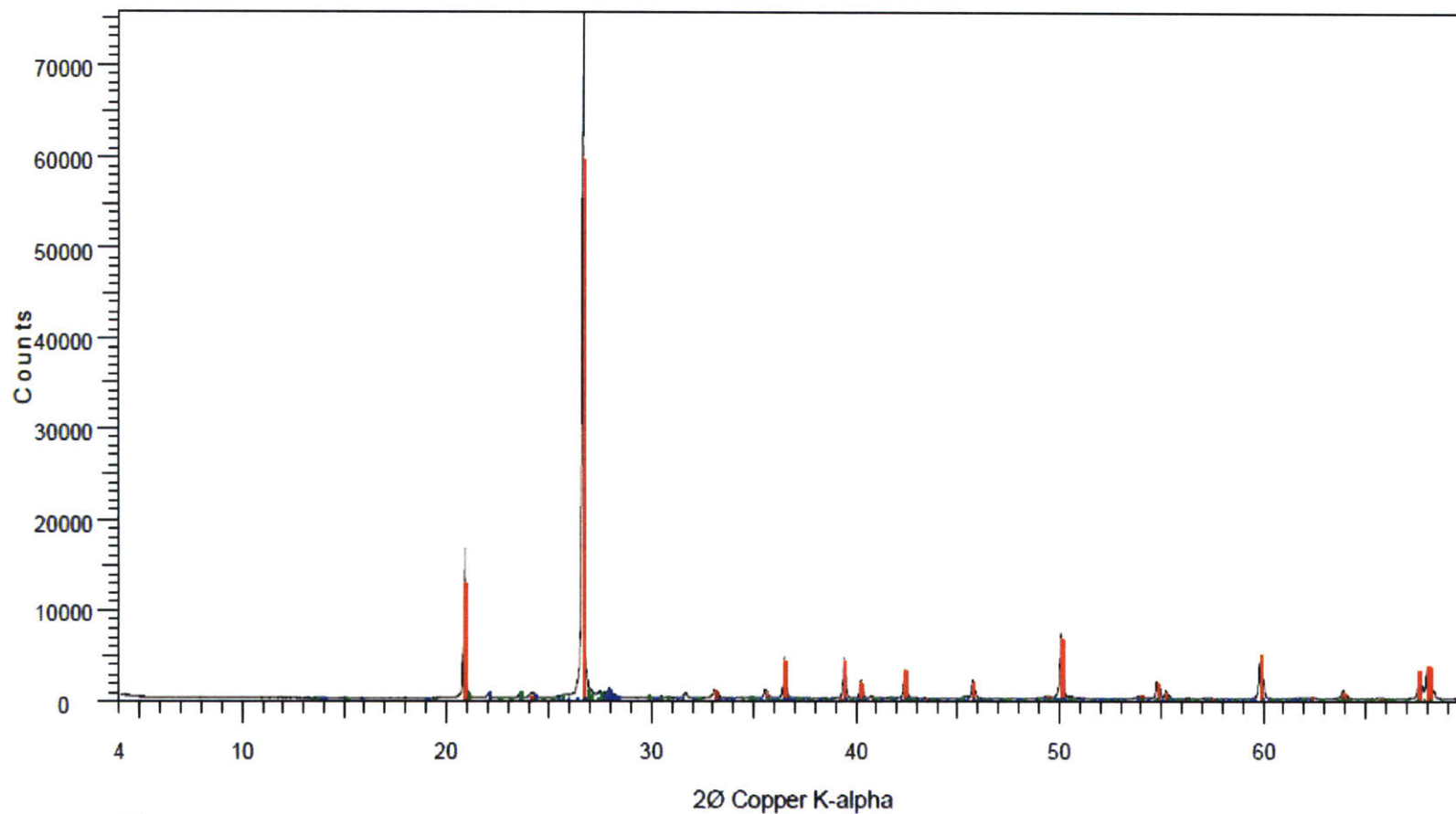
Table 2: Relative percentage of clay minerals in the <2 μ m clay size fraction

Labcode	Sample ID	ChloriteTri [®]	Illite [®]	I/S-ML [®]	%Exp [®]
1201332	VACA-MUERTA-AR-3-296-4	0	0	100	10
1201334	VACA-MUERTA-AR-4-2897-37	4	14	82	20
1201336	VACA-MUERTA-AR-5-285-98	2	8	90	20

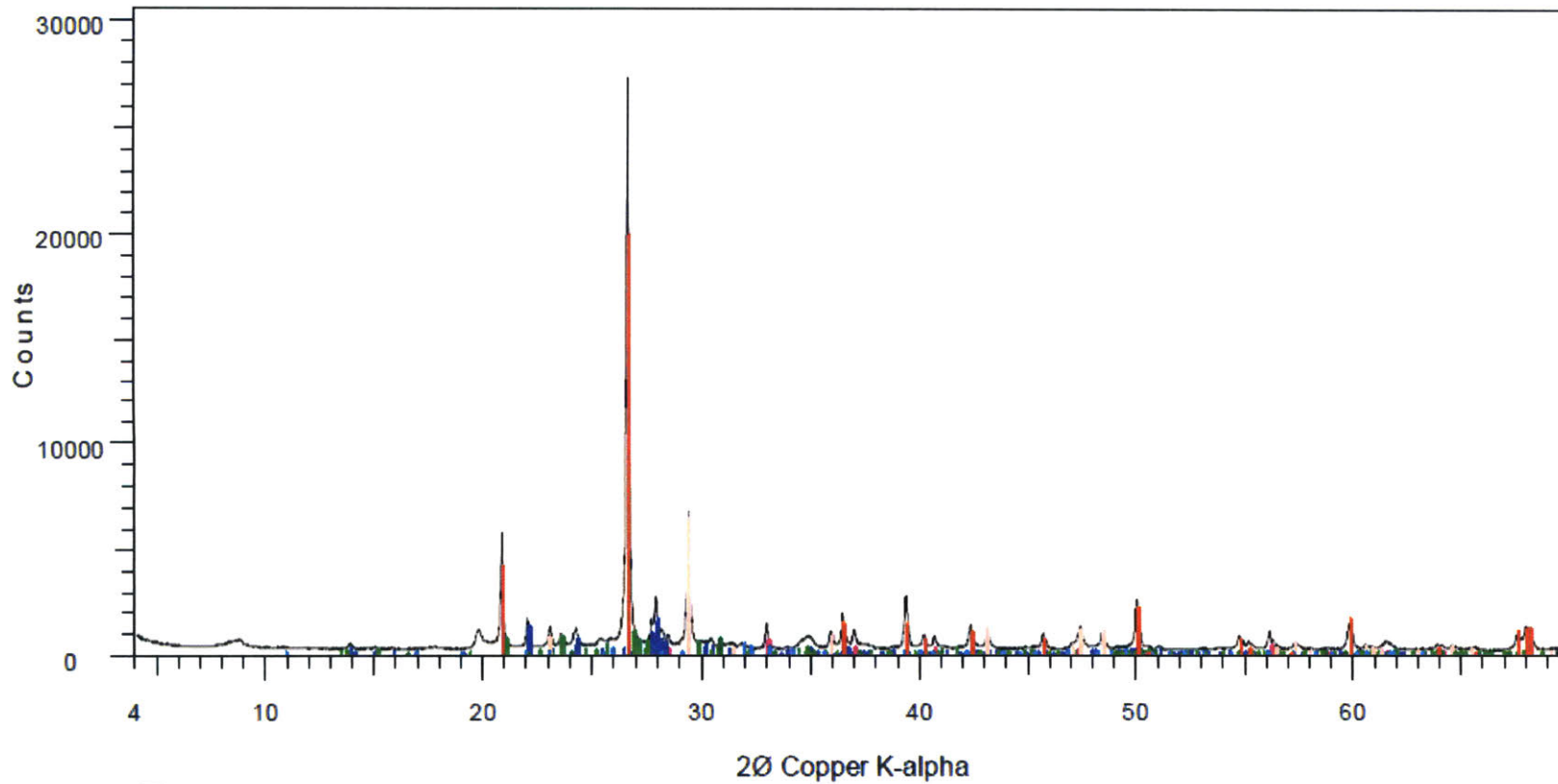
I/S-ML[®] = mixed layer illite-smectite%Exp[®] = expandability of clays

Table 3: Cation Exchange Capacity by Cobalt hexamine at 105°C

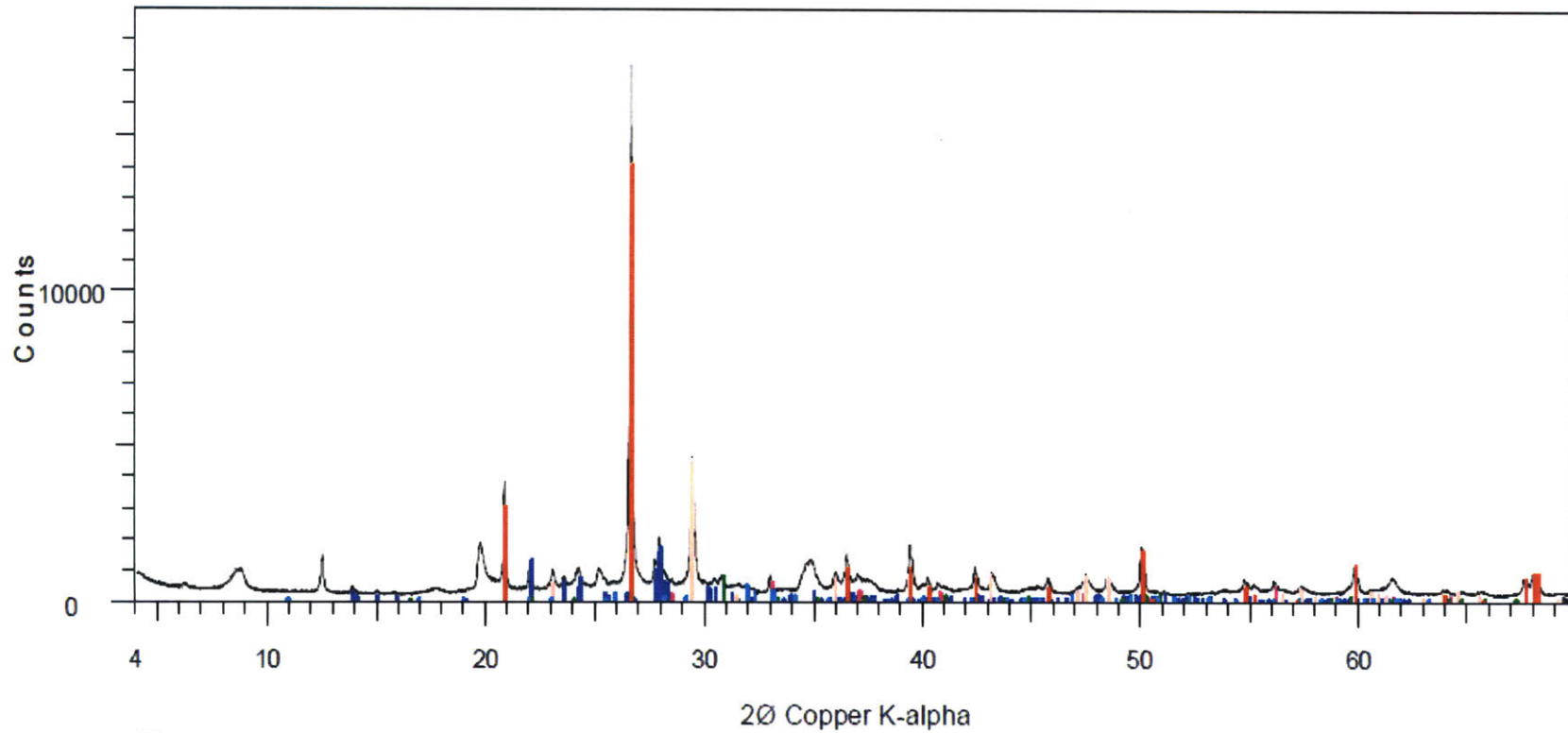
Labcode	Sample ID	CEC (cmol+kg-1)	CEC calculated from Mineralogy (cmol+kg-1)
1201331	VACA-MUERTA-AR-X3-2596-4	0.0	0.4
1201333	VACA-MUERTA-AR-X4-2897-37	6.7	4.2
1201335	VACA-MUERTA-AR-X5-2685-98	7.9	8.1










- 1201331-B - File: 1201331-VACA-MUERTA-AR-X3-2596-4-B.raw
- 99-090-0067 (U) - Quartz - SiO₂
- 99-090-0002 (U) - Albite low - Na(AlSi₃O₈)
- 99-090-0004 (U) - Orthoclase - KAlSi₃O₈
- 99-090-0011 (U) - Hematite, syn - Fe₂O₃



- 1201333-B - File: 1201333-VACA-MUERTA-AR-X4-2897-37-B.raw
- 99-090-0067 (U) - Quartz - SiO₂
- 99-090-0002 (U) - Albite low - Na(AlSi₃O₈)
- 99-090-0004 (U) - Orthoclase - KAlSi₃O₈
- 99-090-0014 (U) - Pyrite - FeS₂
- 99-090-0005 (U) - Calcite, syn - CaCO₃
- 99-090-0074 (U) - Dolomite - CaMg(CO₃)₂
- 99-090-0054 (U) - Fluorapatite, syn - Ca₅(PO₄)₃F



-  1201335-B - File: 1201335-VACA-MUERTA-AR-X5-2685-98-B.raw
-  99-090-0067 (U) - Quartz - SiO₂
-  99-090-0002 (U) - Albite low - Na(AlSi₃O₈)
-  99-090-0014 (U) - Pyrite - FeS₂
-  99-090-0005 (U) - Calcite, syn - CaCO₃
-  99-090-0074 (U) - Dolomite - CaMg(CO₃)₂
-  99-090-0054 (U) - Fluorapatite, syn - Ca₅(PO₄)₃F

